

**Development of a QMC code to tackle interacting
electronic systems in 2D with application to TMD
nanoribbons**

Francisco Monteiro de Oliveira Brito

Thesis to obtain the Master of Science Degree in
Physics Engineering

Supervisor(s): Prof. Eduardo Filipe Vieira de Castro
Prof. João Manuel Viana Parente Lopes

Examination Committee

Chairperson: Prof. Pedro Domingos Santos do Sacramento
Supervisor: Prof. Eduardo Filipe Vieira de Castro
Co-Supervisor: Prof. João Manuel Viana Parente Lopes
Members of the Committee: Prof. Pedro José Gonçalves Ribeiro

October 2018

The behavior of large and complex aggregates of elementary particles, it turns out, is not to be understood in terms of a simple extrapolation of the properties of a few particles.

P. W. Anderson

Cover picture credit: University of Manchester
www.graphene.manchester.ac.uk (accessed on 12 June 2018)

Acknowledgments

I want to start by thanking my parents Laura and João, and the rest of my family, biological, and non-biological. They did everything they could (and more) to ensure that I had the opportunities that led me to develop this work. They taught me to do things out of love, and that is a lesson I carry with me every day of my life.

Then, I want to thank Beatriz for supporting me unconditionally in everything I do, for always being so kind and sincere, for brightening up my life and making me smile so much, and for the great love and understanding she shows everyday. Quoting Carl Sagan, “In the vastness of space and the immensity of time, it is my joy to share a planet and an epoch” with her.

Of course, I would also like to thank my supervisors Prof. Eduardo Filipe Vieira de Castro, and Prof. João Manuel Viana Parente Lopes for the openness, support, and tireless will to teach me, and learn with me. Not only did they provide valuable scientific insight, but they also showed great humaneness in guiding me through the journey I embarked on during the last year.

I also want to express the gratitude and admiration I feel for my colleagues at Centro de Física do Porto, the Theoretical Physics Center at University of Porto. They worked beside me almost daily, discussing and criticizing my work, providing great help, be it by cheering me up in darker times, or by celebrating even the tiniest achievements in my work. I also want to thank Centro de Física do Porto for granting me access to use the High Performance Computing Cluster located in the Faculty of Engineering of the University of Porto.

I am grateful for having had great teachers, who inspired me to seek knowledge over the years. I wish to thank all of them. I would like to thank Dr. Miklós Lajkó, Dr. Jon Demidio for what they taught me during my stay in Lausanne, and Prof. Frédéric Mila for introducing me to many currents topics of research in condensed matter theory, and sharing valuable insight.

Lastly, I want to thank a number of close friends who constantly support me, of which I will mention a few: Mateus, Carol, Marta, Bárbara, Andreia, Inês Lopes, Inês Viegas, Nuno, Samuel, Glênio, Raquel, Tiago, Miguel, Branca, Pedro, and Isabela.

Abstract

Cooperative behavior has been at the forefront of condensed matter physics research for the most part of the last half-century. This complex systems era has brought about a concept called emergence, which is now overarching. In particular, in strongly correlated electron systems, emergent phenomena lead to a variety of exotic properties that defy intuition.

The discovery of two-dimensional materials, has renewed interest in the many-electron problem since electron-electron interactions play an important role in the description of many of the properties of these systems. Moreover, the rapid increase in computational power, and algorithmic sophistication has made it possible to attack many problems in the field that were previously intractable. In this work, we focus on a particular class of two-dimensional materials showing a wealth of fascinating electronic and optical properties: Transition Metal Dichalcogenides.

We investigate emerging edge-state magnetism in a type of nanostructure called a nanoribbon, so called because it resembles a ribbon, being much longer on direction than on the other. To study this phenomenon, we consider a recently introduced symmetry-based tight-binding model that is found to capture most properties related to the edge physics of the problem. Then, we generalize it to the interacting case by considering intra-orbital Hubbard-type interactions.

Our approach to this problem is two-fold. We start by performing original numerical mean field calculations and build an approximate physical picture of the system at hand. Then, we use our own implementation of the unbiased, state-of-the-art Determinant Quantum Monte Carlo algorithm to simulate this interacting, quantum many-fermion system.

Keywords

2D Materials, Hubbard Model, Strongly Correlated Electrons, Transition Metal Dichalcogenide Nanoribbons, Mean Field Theory, Determinant / Auxiliary Field Quantum Monte Carlo (QMC) (English)

Resumo

O comportamento coletivo tem estado na linha da frente da investigação feita em física da matéria condensada durante grande parte do último século. Esta era dos sistemas complexos trouxe-nos um conceito denominado emergência que tem, atualmente, uma natureza transversal. Em particular, em sistemas de eletrões fortemente correlacionados, fenómenos emergentes conduzem a uma enorme variedade de propriedades exóticas que desafiam a intuição.

A descoberta de materiais bidimensionais renovou o interesse no problema a N eletrões dado que as interações eletrão-eletrão têm um papel determinante na descrição de muitas das propriedades destes sistemas. Além disso, o rápido aumento de poder computacional e de sofisticação algorítmica tornou possível atacar problemas que eram até então inacessíveis. Neste trabalho, focamo-nos numa classe particular de materiais bidimensionais, mostrando uma grande riqueza de propriedades óticas e eletrónicas: os dicalcogenetos de metais de transição.

Neste contexto, investigamos a emergência de magnetismo associado a estados de fronteira, num tipo de nanoestrutura chamado de nanofita, dada a sua semelhança a uma fita, por ser muito mais longa numa direção que na outra. Para estudar este fenómeno, consideramos um modelo de tight-binding baseado em considerações de simetria que captura a maioria das propriedades relacionadas com a “física de fronteiras” do problema. Depois, generalizamos este modelo para o caso interatuante, considerando interações do tipo Hubbard intra-orbitais.

A nossa abordagem ao problema divide-se em duas partes. Começamos por levar a cabo cálculos numéricos originais na aproximação de campo médio para construir uma imagem física aproximada do sistema. Depois, usamos a nossa própria implementação de um algoritmo de ponta, livre de enviesamento estatístico - o método do determinante de Monte Carlo Quântico - para simular o sistema interatuante a N fermiões em estudo.

Palavras Chave

Materiais Bidimensionais, Modelo de Hubbard, Eletrões Fortemente Correlacionados, Nanofitas de Dicalcogenetos de Metais de Transição, Teoria de Campo Médio, Monte Carlo Quântico: Método do Determinante ou Campo Auxiliar (Português)

Contents

1	Introduction	1
1.1	Motivation	1
1.2	Strongly correlated electron systems	2
1.3	Beyond graphene: TMD nanoribbons	4
1.3.1	Electronic properties	5
1.3.2	Nanoribbons	6
1.3.3	Effective three-band minimal tight-binding model	8
1.4	Introduction to Quantum Monte Carlo	9
1.4.1	Variational Monte Carlo	11
1.4.2	Diffusion Monte Carlo and projective methods	11
1.4.3	Auxiliary Field QMC and the Fermion Sign Problem	12
1.5	Original Contributions	14
1.6	Outline	14
2	Minimal models of electron correlations	15
2.1	Modelling electron correlations in energy bands	15
2.2	Hubbard model	16
2.2.1	Electron correlations in narrow d -bands	17
2.2.2	Hubbard Hamiltonian	18
2.2.3	Particle-hole symmetry	19
2.3	Exact solutions for simple cases	20
2.3.1	The purely atomic ($\frac{U}{t} \rightarrow \infty$), single site limit	22
2.3.2	The non-interacting ($\frac{U}{t} = 0$) limit	25
2.4	Effective $\frac{U}{t} \gg 1$ Heisenberg Model	27
2.4.1	Two-site calculation	28
2.4.2	Degenerate perturbation theory	29
2.5	Green's functions	30
2.5.1	Single site case	30
2.5.2	Non-interacting case	31
2.6	Magnetism and mean field theory	32
2.6.1	Stoner criterion for ferromagnetism	32

2.6.2	Mean field theory of the Hubbard model	33
2.6.3	Self-consistent solution in the Grand-canonical ensemble (GCE)	35
2.7	Simulatable variants of the Hubbard model and TMDs	36
3	Auxiliary Field Quantum Monte Carlo	38
3.1	Monte Carlo Method in Classical Statistical Physics	38
3.2	Theoretical Framework and Mathematical Formulation	44
3.2.1	Trotter-Suzuki Decomposition	45
3.2.2	Hubbard-Stratonovich transformation	46
3.2.3	Single-particle propagators and the fermionic trace	47
3.2.4	Monte Carlo sampling of the Hubbard Stratonovich field	49
3.2.5	Checkerboard Breakup	51
3.3	Measurements	52
3.3.1	Obtaining observables in terms of Green's functions	53
3.3.2	Correlation functions	54
3.3.3	Imaginary-time displaced Green's functions and susceptibilities	55
3.4	Stabilization	55
3.4.1	Stable matrix multiplication	57
3.4.2	Inverting to obtain the Green's function	58
3.4.3	Storing partial products and time-displaced Green's function	60
4	Applications and original results	62
4.1	One-dimensional Chain	62
4.2	Square lattice	64
4.3	Nanoribbons	66
4.3.1	Graphene	66
4.3.2	Transition Metal Dichalcogenides (TMDs)	69
5	Conclusions and Future Work	77
Bibliography		78
Appendix A Obtaining the Hubbard Model. Approximate Solutions		A-1
A.1	Hartree-Fock Approximation and the Self Consistent Field	A-1
A.2	Mott insulators	A-3
A.3	Computing the partition function for a quadratic Hamiltonian	A-6
A.4	Density of states for a 1D tight binding model	A-7
A.5	Effective Heisenberg model as the atomic limit of the Hubbard model	A-7
A.6	On Wick's theorem	A-9
A.7	Mean field theory and the variational principle	A-10

Appendix B Formulating Auxiliary Field Quantum Monte Carlo	B-1
B.1 Casting the fermionic trace as a determinant	B-1
B.2 Rank-one updates of the Green's function	B-3
B.3 Particle-hole symmetry and the sign problem	B-5

List of Figures

1.1	Graphene monolayer; graphene's dispersion relation.	4
1.2	Transition Metal Dichalcogenide (TMD) monolayer condensing in its 2H phase. $M - X$ honeycomb lattice. Unit cell of the trigonal prismatic (2H) phase of a TMD monolayer. High symmetry points of the corresponding hexagonal lattice's reciprocal space.	5
1.3	Structure and electronic properties of TMD monolayers.	6
1.4	(TEM) images of graphene nanoribbons. Fabrication of TMD nanoribbons.	7
1.5	Zigzag edges of a nanoribbon and magnetism. Orbital projected band structures for monolayer MoS ₂ obtained from first principles.	7
2.1	Graphical comparison between the Ising and the Hubbard models.	16
2.2	Hydrogen atomic wave functions.	17
2.3	Electron density in the purely atomic limit of the Hubbard model. Magnetization as a function of temperature $\langle m^2 \rangle(T)$ in the single site Hubbard model for varying chemical potential μ .	24
2.4	Magnetization as a function of the on-site interaction $\langle m^2 \rangle(U)$, and vice-versa, in the single site Hubbard model for varying temperature T .	24
2.5	Dispersion relations for the 1D chain and the square lattice in the non-interacting case.	27
2.6	Density of states of the 1D tight-binding model.	32
2.7	Mean field results for the 1D Hubbard model.	34
3.1	Evolution of the probability of accepted configurations.	49
3.2	Exponentially divergent diagonal entries of \mathbf{D}' , showing the orders of magnitude spanned by the matrix elements of the stabilized matrix product.	58
3.3	Condition number of $\mathbf{M}_l = \prod_l \mathbf{B}_l$ obtained by multiplying \mathbf{B} -matrices naively. Absolute values of the diagonal entries of \mathbf{D}' and corresponding condition number of the matrix to invert to obtain the Green's function.	59
4.1	Spin-spin correlation function, magnetic structure factor, and susceptibility for a 64 site Hubbard chain at $\beta t = 25$, for $U = 4t$.	63
4.2	The magnetic structure factor and the susceptibility have a peak at $q = \pi$ that increases as $T \rightarrow 0$, indicating <i>antiferromagnetic ordering</i> . Divergence of the staggered susceptibility near $T_c = 0$, signaling the transition to the antiferromagnetic ground state.	63

4.3	Comparison of the magnetic structure factor with that obtained using QUEST. Run time comparison.	64
4.4	Convergence of some of the measured observables to the value given by exact diagonalization for $N = 2$, $\beta t = 2$, $U = 4t$. Comparison with the results of QUEST.	64
4.5	Mean field phase diagram of the Hubbard model. Quantum Monte Carlo (QMC) data showing the decrease of the double occupancy with increasing U	64
4.6	Spin-spin correlations on the square lattice. Magnetic structure factors showing a peak at $\mathbf{q} = \pi$. Color maps of the structure factor $S(\mathbf{q})$, and susceptibility $\chi(\mathbf{q})$, both showing peaks at $\mathbf{q} = \pi$	65
4.7	Left: Infinite system extrapolation of long range order. Right: $S(\pi)$ for varying system size and inverse temperature.	66
4.8	Boundary conditions on the nanoribbon. Spin-spin correlations of a strained zig-zag graphene nanoribbon.	67
4.9	Spin-spin correlation function profile along the longitudinal direction x of the ribbon. Magnetization parameter along each row, as a function of the transverse coordinate y	68
4.10	Magnetic structure factor $S(\mathbf{q})$ for a strained graphene nanoribbon: bulk and edges.	68
4.11	Divergence of the edge susceptibility when approaching the critical temperature. Linear fit used to obtain the critical temperature of the transition to the edge-magnetized phase.	69
4.12	Filling ν as a function of the Fermi energy ε_F for a TMD monolayer and a nanoribbon. MoS ₂ . TMDNR band structure obtained by the 3-band model.	70
4.13	Comparison between the zero temperature MF solutions of the Hubbard model for a graphene nanoribbon(GNR) and a TMDNR.	71
4.14	Mean field phase diagram at zero temperature. Zoom-in of the first phase transition.	72
4.15	Zoom-in of the second phase transition (as U is increased). Band structure of the free-fermion problem.	72
4.16	$T = 0$ mean field band structure for a Transition Metal Dichalcogenide Nanoribbon (TMDNR) of width $N_y = 16$ in the ordered phase, at $U = 20 t_0 $	72
4.17	Spin-resolved band structures for varying U and β , compared with the tight-binding bands.	74
4.18	Localized edge states on the top and on the bottom of the ribbon for the different orbitals. Resulting magnetization profile along the ribbon's transverse direction due to higher spin up than spin down occupation.	75
4.19	Comparison of the band structures at $U = 15.2 t_0 $, and $U = 15.4 t_0 $	75
4.20	Mean field phase diagram for varying U and β . Average sign as a function of electron density, obtained by running our determinant QMC code for a 9×4 TMDNR at $\beta t_0 = 2$, $U = 16 t_0 $	75
4.21	Longitudinal profile (along the x direction) of orbital-resolved S^z spin-spin correlation functions we measured, for two lattice sizes: 9×4 and 9×6	76

A.1 Configuration of the Hubbard model on the square lattice with a hole and a doubly occupied site.	A-5
A.2 Example of the minimization of the grandpotential functional.	A-12
B.1 Average sign as a function of chemical potential/electron density for a 4-site Hubbard chain.	B-6
B.2 Electron density as a function of chemical potential for a 4-site Hubbard chain. Average sign as a function of chemical potential for a simulation of a 9×4 TMD nanoribbon using the minimal model described in chapter 2.	B-6
B.3 Average sign as a function of electron density for the minimal Hubbard model of TMDNRs. Electron density as a function of chemical potential.	B-6
B.4 Average sign as a function of chemical potential for the same system, and for a system at lower temperature ($\beta t_0 = 2$), and fixed on-site/orbital interaction $U = 16 t_0 $	B-7
B.5 Electron density as a function of the chemical potential for the 9×4 TMD nanoribbon, with $\beta t_0 = 2$ and $U = 16 t_0 $. Sign of the accepted configuration as a function for a few space-time sweeps of the algorithm.	B-7

List of Tables

4.1 Nearest neighbors on the graphene nanoribbon. The neighbors in gray are only for sites that are not on the edges. % refers to the remainder of integer division.	67
--	----

Abbreviations

QMC Quantum Monte Carlo

TMD Transition Metal Dichalcogenide

LG Landau-Ginzburg

2D Two-dimensional

1D One-dimensional

PBC Periodic Boundary Condition

OBC Open Boundary Condition

PHS Particle-hole symmetry

AF Antiferromagnetic

PHT Particle-hole transformation

AFM Atomic Force Microscopy

BSS Blankenbecler, Scalapino and Sugar

FFT Fast Fourier Transform

GCE Grand-canonical ensemble

TMDNR Transition Metal Dichalcogenide Nanoribbon

1

Introduction

Contents

1.1	Motivation	1
1.2	Strongly correlated electron systems	2
1.3	Beyond graphene: TMD nanoribbons	4
1.4	Introduction to Quantum Monte Carlo	9
1.5	Original Contributions	14
1.6	Outline	14

The isolation of graphene in 2004 has led to a growing interest of the scientific community in Two-dimensional (2D) materials revealing extraordinary properties. Among them are Transition Metal Dichalcogenides (TMDs), appearing in the form of a variety of nanostructures. Unlike in graphene, where the effects of electron-electron interactions are relatively weak, in TMDs, electrons are strongly correlated, and one cannot overlook the interactions between them. Analytical approaches to the solution of the problem are either hopeless, or rely on possibly unrealistic approximations. In fact, the increased complexity of the models describing such highly correlated materials, compared to their graphene counterparts, calls for sophisticated computer simulation methods, most notably Quantum Monte Carlo (QMC). In this introductory chapter, we start by reviewing the literature on the physics of TMDs, focusing on their basic properties. Then, we present a survey of simulation methods belonging to the Quantum Monte Carlo class. We introduce some basic concepts, and motivate the choice of the particular used method. Finally, we summarize our original contributions, and outline the structure of the thesis.

1.1 Motivation

It might seem surprising that 2D systems were not considered as a real possibility before the discovery of graphene since they are often idealized in thought experiments, for example when investigating toy models of more complex higher dimensional systems. In fact, while thin film deposition on comparably thicker substrates was commonplace long before 2004, 2D layers were thought not to exist independently from their 3D base. Their existence was not expected *a priori* because at first sight they seem to violate the Mermin-Wagner-Hohenberg theorem [1–3], a no-go theorem that forbids ordering below three dimensions at finite temperature¹.

The discovery of graphene paved the way for the search for similarly stable 2D materials and a plethora of these has been discovered since [4]. A vast set of open problems remains to be solved within the realm of the fascinating and counterintuitive properties of the now huge variety of existing 2D systems. In particular, in some of these, the effect of electron-electron interactions is not negligible, leading to emergent phenomena. These are collective effects which emerge as a result of the interactions between the individual components of a macroscopic system. The properties of the system's components do not

¹On graphene sheets, ripples appear, which implies that the material is not strictly 2D, and thus can be stabilized. This issue is subtle, and is beyond the scope of this work.

directly percolate up; instead, they shape the interactions that dictate the system’s properties sometimes in rather unexpected ways, leading to unusual behavior.

Interacting electron systems are often tackled by carrying out computer simulations. QMC is a family of numerical methods that are amply applicable to condensed matter physics problems, and that are particularly well suited to study strongly correlated electrons. Despite the system size being constrained due to limited simulation time, reliable, accurate and unbiased solutions are provided to the otherwise intractable quantum many-body problem. The class of QMC algorithms that is used in this work was introduced in the 1980’s in a series of seminal papers by Hirsch and Blankenbecler, Scalapino and Sugar² [5–11], but it saw a recent surge [12–24] due to the increase in computational power, and algorithmic development. Method optimization can prove crucial in applications to widely studied physical models of electron-electron interactions. In particular, recent computational and algorithmic developments opened the door to study both larger and lower temperature systems [15, 25–27]. In this work, an implementation of determinant QMC based on the BSS algorithm is used to simulate a TMD zigzag-edged nanoribbon, a nanostructure made of this recent member of the 2D materials family. Early mean field studies show that this type of nanostructures have a tendency towards magnetism in graphene [28], which makes them good candidates for use in nanospintronics. Our mean field calculations for TMDs show a similar trend, motivating our subsequent QMC study, in an attempt to test how realistic the mean field predictions are. QMC is a complementary, more accurate, and unbiased approach that can shed light upon not only magnetic, but also other phenomena, like the formation of charge density waves and superconductivity in the context of generic interacting electron models. Hence QMC has acquired a far-reaching importance as a flexible, and accurate numerical tool.

1.2 Strongly correlated electron systems

Condensed matter physics is concerned with the emergence of the properties of quantum materials from complexity. The central concept within this approach is that of symmetry breaking. When a phase transition occurs, a system is said to condense into a phase of lower symmetry. A simple pictorial example is the transition from a gas to a solid.

A framework that is commonly used to identify symmetry breaking is the Landau-Ginzburg (LG) theory of phase transitions. This theory gives a prescription to discover phase transitions. More precisely, it gives criteria for a symmetry to become manifest. Symmetry breaking gives rise to emergent phenomena. The idea of emergence rests on a constructionist, rather than a reductionist hypothesis: that the behavior of the many does not trivially follow from the behavior of the few. As P.W. Anderson puts it, “The ability to reduce everything to simple fundamental laws does not imply the ability to start from those laws and reconstruct the universe.” [29]

The broad scope of condensed matter comes from the sheer number of possibilities that the symmetry breaking approach affords. For the specific case of the LG theory, one can study the emergence of magnetism, superconductivity, or superfluidity, just to name a few. However, as we shall see, sometimes the LG theory fails to capture a system’s behavior, and we must resort to other theories to identify these,

²After whom the Blankenbecler, Scalapino and Sugar (BSS) algorithm, on which we based the implementation used in this work, is named.

or other eventual properties that might arise. The Landau-Ginzburg procedure can be summarized as follows: identify an order parameter reflecting the underlying symmetry of the system, and minimize the free energy in order to deduce conditions for the symmetry to become manifest, leading to a phase transition. The drawback of this *variational* approach is that it might be difficult to identify an order parameter in the first place. Moreover, even if we do manage to find one, the usual procedure may be impossible to perform. It can easily happen that the degree of complexity of the order parameter is simply too high. Additionally, and perhaps more importantly, *not all* phase transitions can be described by the LG paradigm.

On the one hand, there are systems where a different kind of order arises. A prominent example is that of fractional quantum Hall effect, where (rather surprisingly!) the *quasi-particles* describing the excitations of the quantum Hall fluid carry *fractions* of the electron charge. There is an intimate connection between charge fractionalization and topology, which may be understood in terms of the properties of the Laughlin states describing the quantum Hall fluid. However, while it is tempting to try to characterize the latter in terms of the LG paradigm, it must actually be regarded as a distinct type of matter, where “topological order” arises [30].

On the other hand, for the so called *strongly correlated* systems we shall focus on in this work, there are phenomena which emerge specifically due to the interacting nature of the problem. They are elusive because a description within the LG paradigm does not yield a behavior consistent with what is observed. The LG theory fails because it ignores these interactions by disregarding fluctuations in the microscopic configuration of the system. This approximation consists of reducing the complex interactions to an effective *mean field*, which is normally determined self-consistently. Strongly correlated systems require an approach beyond mean field, which makes them both extremely interesting and notoriously difficult to treat. In fact, the failure of mean field theory is not limited to correlated systems, and its success in describing a given system depends, for example, on the dimensionality³ and on the range of the particular type of interaction that is considered.

In many cases, mean field theory is too extreme an approximation. Nonetheless, its occasional failure at capturing the whole of a system’s properties does not deem it useless. Actually, it is quite the contrary. Mean field is often used as a first approach to build an intuitive physical picture for the general properties of the system, while keeping in mind that the description it provides is intrinsically insufficient. In this work, we will use mean field theory to gain intuition about the problem at hand.

A central piece in the understanding of correlated matter is the Hubbard model, a model which we will use extensively in this thesis. It was introduced to bridge a gap between metals and magnetic insulators, building on the earlier work of Mott. The model is extremely simple. Electrons hop from atom to atom on a lattice, paying an energy penalty when they occupy the same site. This repulsive effect results in correlations beyond those that are always present due to the fermionic nature of the particles obeying the Pauli exclusion principle. In the limit of weak repulsion, the electrons are nearly free, and the system behaves like a metal. Otherwise, the electrons become localized at fixed atomic positions resulting in magnetic insulating behavior. The model is simple to formulate, but already includes highly nontrivial

³Normally, there is an upper critical dimension d_c above which mean field is exact. Below d_c , its predictions might be useful qualitatively, but not quantitatively.

correlation effects between all electrons in the solid. Thus, it is not surprising that an exact solution exists only in 1D [31], and higher dimensional versions are still being studied more than 50 years after the model appeared [32].

1.3 Beyond graphene: TMD nanoribbons

Planar materials have steadily been drawing the attention of the community since graphene was isolated from a graphite sample by mechanical exfoliation [33] (Fig.(1.1), left). Since then, numerous studies have been made concerning the interesting as-yet-unseen phenomena occurring within these materials. For example, in the case of graphene, we have: unconventional quantum Hall effect, absence of localization, and electrons behaving like massless relativistic particles at low energies (Fig.(1.1), right), providing a bridge between condensed matter physics and quantum electrodynamics [34]. In spite of its undeniable potential both from a fundamental and an application point of view, graphene has some shortcomings. This motivated the community to study other more complex graphene-like materials, which could have other desirable properties, while maintaining most of graphene's potential.

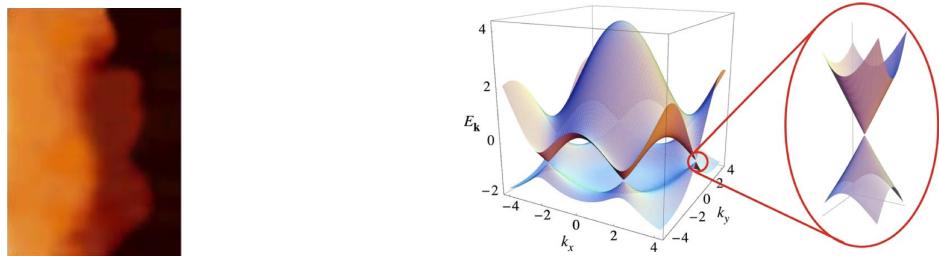


Figure 1.1: Left: Atomic Force Microscopy (AFM) picture of a graphene monolayer (from [35]). The black area is a substrate used for fabrication purposes. The dark orange area is a monolayer of graphene. Right: Dispersion relation of graphene. Close to the charge neutrality point, the dispersion relation is linear, corresponding to massless excitations (taken from [36]).

Transition Metal Dichalcogenides are prominent examples of such novel members of the 2D materials family [37–39]. An excellent review of their properties, experimental results and applications is given in [40]. Much like graphite which is essentially constituted by stacked monolayers of carbon atoms bound by weak Van der Waals forces, 3D TMD structures are also formed by weakly bound layers. However, instead of carbon, the layers contain transition metals M , and chalcogens X , in a $1 - 2$ proportion. Thus, group 6 TMDs are denoted MX_2 , where $M = \text{Mo, W, ...}$ (respectively Molybdenum and Tungsten) and $X = \text{S, Se, Te}$ (respectively Sulfur, Selenium and Tellurium). Each TMD monolayer contains a layer of M atoms organized in a triangular lattice sandwiched between two layers of X atoms, unlike graphene. Each M atom is coordinated with six X atoms, in a stacked structure with various possible coordinations for the X atoms. The most common phases are trigonal prismatic (2H) and octahedral (1T), typically in the few Å range (for Molybdenum disulfide, MoS_2 , the width is around 6.5Å). Here we will consider the 2H configuration, whose planar honeycomb lattice is depicted in the top-down view of Fig (1.2a). The valence bands arise out of the hybridization of the d_{xy} and $d_{x^2-y^2}$ orbitals of the transition metal with the $p_{x,y}$ orbitals of the chalcogen, while conduction bands have a main contribution from the $d_{3z^2-r^2}$ orbitals of the M atoms with only a minor contribution from the $p_{x,y}$ orbitals of the X atoms.

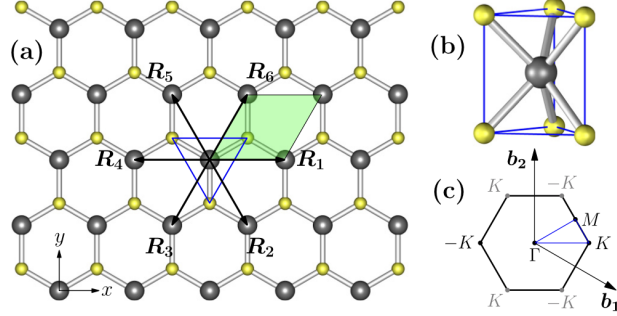


Figure 1.2: (a) The 2H phase of a TMD monolayer may be viewed simply as a $M - X$ honeycomb lattice. Here we represent the six nearest neighbors of a point on the M triangular lattice by the real space vectors $\mathbf{R}_{i=1,2,\dots,6}$. (b) Unit cell of the trigonal prismatic (2H) phase of a TMD monolayer. (c) High symmetry points Γ, M, K of the first Brillouin zone ($\mathbf{b}_{1,2}$ are the reciprocal basis vectors).

Two-dimensional TMDs have been attracting interest because they seem to overcome some of the drawbacks of graphene in technological applications. For example, monolayer graphene is gapless, while its bilayer counterpart has a tunable, but small gap of the order of a tenth of an eV. Contrastingly, monolayer TMDs are semiconductors, having an intrinsic gap in excess of 1 eV, which lies at the inequivalent K points of the hexagonal Brillouin zone (see Fig.(1.2)). Thus, TMDs are more promising for designing, for example, transistors. More generally, since the direct band gap lies in the visible frequency range, and room temperature mobility is good, these semiconducting analogues of graphene are promising for electronic and optoelectronic applications. Perhaps even more striking is the appearance of an extra so called *valley* degree of freedom. Since the valence and conduction band edges both lie at the two corners ($\pm K$) of the first Brillouin zone, electrons and holes can acquire an extra degree of freedom which can be used to encode and process information.

On a more fundamental level, hole-doped TMDs are expected to show topological superconductivity [41]. While the superconducting phase of graphene has been predicted, it is not easily attained. Superconductivity in graphene-like 2D materials is important because it could boost high speed nanoelectronics. Moreover, the presence of transition metal atoms in TMDs suggests the possibility of magnetic ordering [42], which could be very relevant in nanospintronics applications. Both superconductivity and magnetic ordering may arise due to the effect of strong electron correlations. Thus, to investigate these properties of TMDs reliably, we need a computational method that can capture the effects of strong electron-electron interactions accurately. As we shall see, auxiliary field QMC fulfills this criterion.

1.3.1 Electronic properties

The electronic properties of TMD monolayers depend crucially on X-coordination. In particular, for the 2H phase, they may ultimately be attributed to the lack of inversion symmetry relative to the M atoms. This leads to the spin splitting of the electronic bands driven by spin-orbit coupling. Time-reversal symmetry implies that the splitting is opposite at the K and K' points, where the top of the valence band and the bottom of the conduction band occur (the so called valleys), leading to the band structure of Fig. (1.3d) (we show the part relevant for realistic charge-carrier concentrations). This property, known as spin-valley coupling, implies that the valley polarization of charge carriers directly translates into spin polarization, leading to an intrinsic property of TMDs that could allow the design of spintronic devices

without resorting to magnetic materials [40]. More broadly, the possibilities afforded by the different compositions and structural phases listed in Fig.(1.3) lead to a vast array of electronic properties. On the one hand, the band structure and its metallic/insulating character vary quite substantially among TMDs. On the other hand, both highly nontrivial correlated and topological phases arise within these materials. In this work, we investigate the properties of correlated phases in zigzag edged TMD nanoribbons.

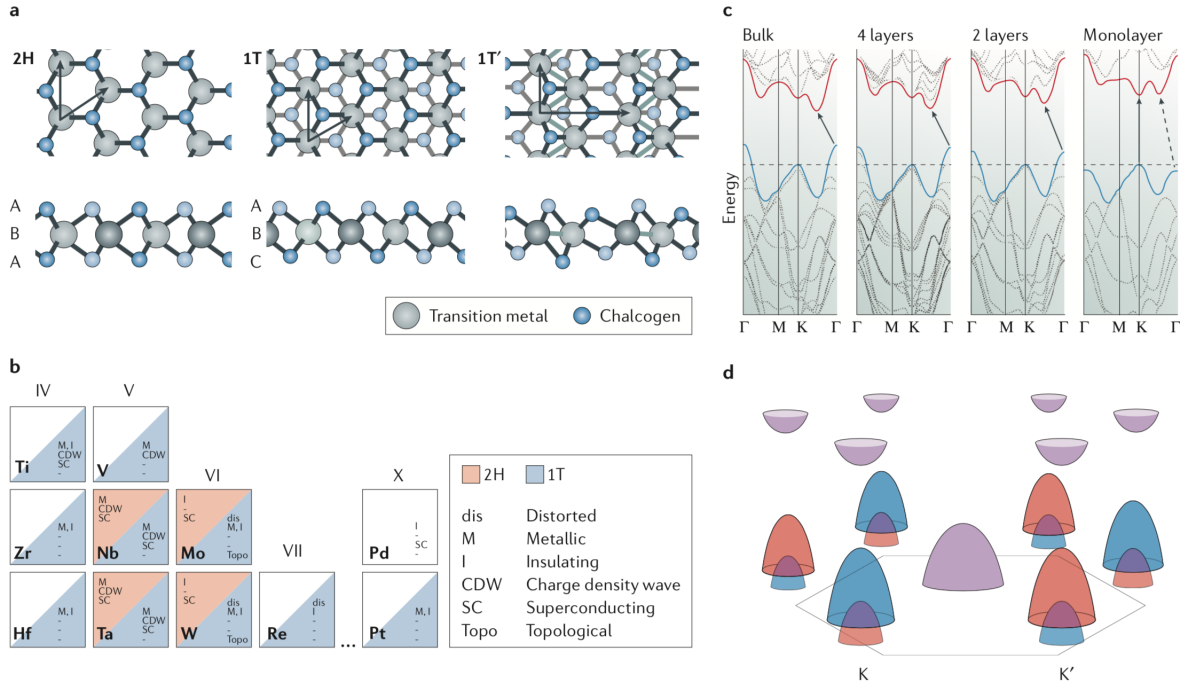


Figure 1.3: (a) Some of the possible structural phases of TMD monolayers: trigonal prismatic (2H) with ABA stacking, distorted octahedral (1T), and dimerized octahedral (1T'), showing ABC stacking. (b) A periodic table of known TMD layers. Shown are the transition metals involved, the existing phases (2H and/or 1T), and the possible electronic phases. (c) Calculated band structure (from density functional theory [43]) of 2H – MoS₂ for samples of decreasing thickness. (d) Representation of the band structure of monolayer 2H – MoS₂, showing the spin splitting (red for spin-up, blue for spin-down) of the bands near the corners of the Brillouin zone (K and K') (taken from [40])

1.3.2 Nanoribbons

Nanoribbons are a particularly promising type of 2D nanostructure. They consist of 2D layers that can be regarded as infinitely long on one direction, but not on the other (Fig.(1.4)), so that the edge-states become relevant in their physical properties. For simulation purposes, we assume translational invariance along the ribbon's longitudinal direction, by the use of Periodic Boundary Conditions (PBCs). On the transverse direction, we use Open Boundary Conditions (OBCs), considering zigzag edges (see Fig.(1.5), left).

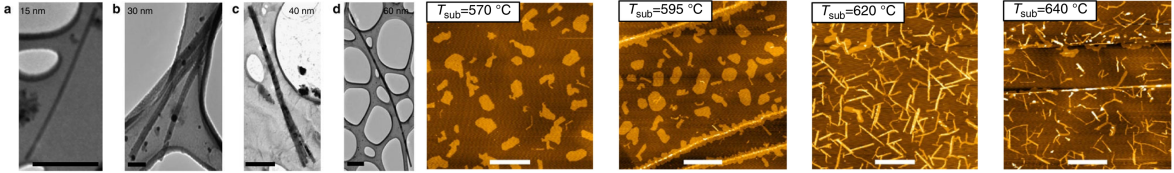


Figure 1.4: Left: (a) to (d) - Transmission electron microscopy (TEM) images of graphene nanoribbons (GNRs) of widths 15, 30, 40, and 60 nm (adapted from [44]). Right: Fabrication of TMD nanoribbons. Left to right: AFM images showing the appearance of nanostructures ranging from 2D nanoislands to nanoribbons, as the temperature of the substrate is increased. The nanoribbons are grown by taking advantage of the temperature dependence of shape transformations occurring during the nonequilibrium growth of surface-based nanostructures (taken from [45])

For graphene, ab initio calculations indicate that a large density of low-energy electronic states is localized at the zigzag edges, decaying quickly in the bulk, which suggests the possibility of magnetic ordering [28]. In fact, a mean field solution of the Hubbard model for a graphene nanoribbon shows that magnetic moments are localized at the edges [28] (see Fig.(1.5), left). QMC has been used to investigate edge-state magnetism beyond mean field in graphene [46–50]. However, edge-state magnetism in zigzag-edged TMD nanoribbons remains unexplored [51], and we would like to investigate, for example, whether edge-state magnetism is stabilized at finite temperature in such systems, following the tendency that was identified for their graphene counterparts. In fact, several studies suggest that zero temperature long range order can be found at the zigzag edges of graphene nanoribbons.

However, at finite temperature, the presence of the $SU(2)$ symmetry and the 1D nature of the edge implies that no true long range order exists. However, the high value for the spin wave stiffness for the domain wall creation energy implies a crossover temperature $T_X \approx 10K$ below which the spin correlation length ξ grows exponentially with decreasing temperature. Below T_X , $\xi \propto T^{-1}$ limits the long-range magnetic order to $\sim 1nm$ at $300K$ [52]. In TMDs $SU(2)$ symmetry is broken, as the sizable spin-orbit coupling forces the spin to be perpendicular to the plane.

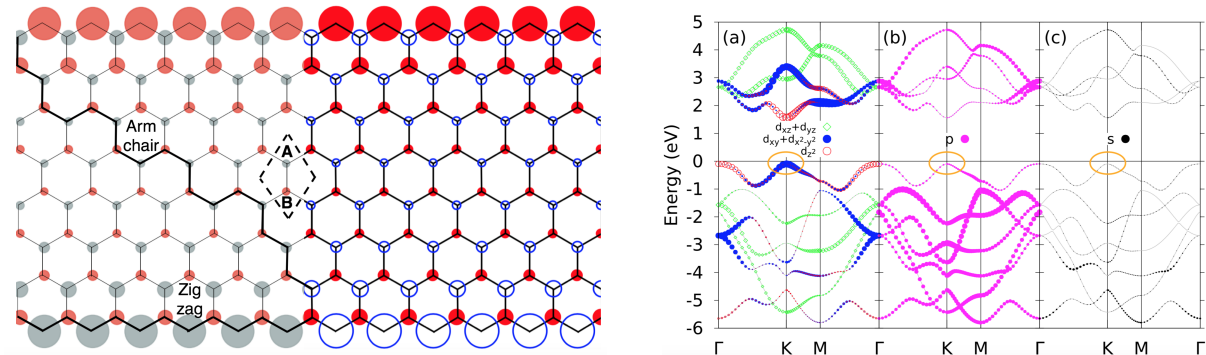


Figure 1.5: Left: Two possible terminations of a honeycomb nanoribbon, and an example of a mean field result for a graphene nanoribbon. Local magnetic moments tend to develop significantly on zigzag edges. The area of the circles is proportional to the magnitude of the magnetic moment. The red circles correspond to a spin up density, and the blue ones to a spin down density. The particular arrangement of the electronic edge states leads to an AF ground state (opposite edges with opposite magnetic moment). The results on the right part of the picture are taken from [28], while the left part corresponds to our original results clearly reproducing the ones on the literature). Right: Orbital projected band structures for monolayer MoS₂ obtained from first principles. The Fermi energy is set to 0, and the symbol size is proportional to the population of the state. The panels represent the contributions from: (a) Mo d-orbitals; (b) All p-orbitals, dominated by S atoms; (c) All s-orbitals.

1.3.3 Effective three-band minimal tight-binding model

In this section, we present a minimal model describing the low energy physics of group 6 TMD monolayers [53]. To obtain this tight-binding model, one uses the symmetries of the monolayer, and the fact that at low energies, both band edges have major contributions from d_{z^2} , d_{xy} , and $d_{x^2-y^2}$ orbitals of M-atoms and the p -orbitals of the X-atoms (which contribute very little at the band edges). This is illustrated for MoS₂ in Fig.(1.5). Near the Fermi energy, the Mo d -orbitals are clearly more populated at the K point (circled in orange), hence these atomic orbitals contribute more to the Bloch states near that point.

The existence of mirror symmetry through the $x - y$ plane (see Fig.(1.2)) imposes that no hybridization can occur between the sets of orbitals $\{d_{z^2}, d_{xy}, d_{x^2-y^2}\}$ and $\{d_{xz}, d_{yz}\}$ ⁴. At low energies, the former are known to be the most relevant for the band structure of TMDs (see (1.5)). These considerations motivate us to construct a three-band tight-binding model. Moreover, the remaining point-symmetry operations impose a constraint on the number of independent hopping parameters. By fitting to first principles results obtained from density functional theory for the materials' energy bands, the hopping parameters can be obtained. The strategy that is chosen to do the fit in [53] is to fit the band energies at the high-symmetry \mathbf{k} -points Γ , K , and M , and the energies of the valence and conduction bands near K by least-squares. This procedure leads to a non-uniform nearest neighbor (NN) hopping matrix on the M-atom triangular lattice. Note that since the argument is purely based on symmetry, in general, the $d - d$ hoppings include both direct $d - d$ interactions of M atoms, and indirect ones, mediated by $X - p$ orbitals. These M-M hoppings suffice to describe the band-edge properties near the $\pm K$ valleys. By including third nearest neighbor hoppings, one can reproduce the energy dispersion in the entire first Brillouin zone. We start by introducing the “spinless” model, and then generalize it to include spin-orbit coupling. Let the greek indices represent orbital space, except for σ , meaning spin. Then, the Hamiltonian reads

$$\mathcal{H} = \sum_{i,j,\sigma} \sum_{\alpha,\beta} c_{i,\alpha}^\dagger t_{\alpha\beta}^\sigma (\mathbf{R}_i - \mathbf{R}_j) c_{j,\beta} \text{ and } t_{\alpha\beta}^\dagger(\mathbf{R}) = t_{\alpha\beta}^\dagger(\mathbf{R}) \quad (1.1)$$

where we consider the basis set $\{|\alpha\rangle\}_{\alpha=1}^3 = \{(d_{z^2}), (d_{xy}, d_{x^2-y^2})\}$. Here, we split the basis into two orbital categories based on which irreducible representation of the D_{3h} group they belong to. Let index j run through the orbital categories, and μ through the basis elements, so that the orbitals $|\phi_\mu^j\rangle$ are

$$|\phi_1^1\rangle = d_{z^2} \quad |\phi_1^2\rangle = d_{xy} \quad |\phi_2^2\rangle = d_{x^2-y^2}$$

By symmetry, there are eight independent parameters, which can be written in terms of only a few of all the hopping integrals $t_{\mu\nu}^{jk}(\mathbf{R}_i) = \langle \phi_\mu^j(\mathbf{r}) | \mathcal{H} | \phi_\nu^k(\mathbf{r} - \mathbf{R}_i) \rangle$ [53, 54]. Let

$$\begin{aligned} \varepsilon_1 &= t_{11}^{11}(\mathbf{0}) & \varepsilon_2 &= t_{22}^{11}(\mathbf{0}) = t_{22}^{22}(\mathbf{0}) & t_0 &= t_{11}^{11}(\mathbf{R}_1) & t_1 &= t_{11}^{12}(\mathbf{R}_1) \\ t_2 &= t_{12}^{12}(\mathbf{R}_1) & t_{11} &= t_{11}^{22}(\mathbf{R}_1) & t_{12} &= t_{12}^{22}(\mathbf{R}_1) & t_{22} &= t_{22}^{22}(\mathbf{R}_1) \end{aligned}$$

The on-site energies ε_j corresponding to the atomic orbitals $|\phi_\mu^j\rangle$ appear through a diagonal hopping

⁴ d_{yz} and d_{xz} orbitals are not symmetric under reflection upon the $x - y$ plane.

matrix in orbital space $\mathbf{t}(\mathbf{0}) \equiv \mathbf{t}^0 = \text{diag}(\varepsilon_1, \varepsilon_2, \varepsilon_2)$, while the NN hoppings are (see Fig.(1.2))

$$\mathbf{t}(\mathbf{R}_{1,4}) \equiv \mathbf{t}^{1,4} = \begin{pmatrix} t_0 & \pm t_1 & t_2 \\ \mp t_1 & t_{11} & \pm t_{12} \\ t_2 & \mp t_{12} & t_{22} \end{pmatrix} \quad (1.2)$$

$$\mathbf{t}(\mathbf{R}_{2,5(3,6)}) \equiv \mathbf{t}^{2,5(3,6)} = \begin{pmatrix} t_0 & \pm \left(\pm \frac{1}{2}t_1 - \frac{\sqrt{3}}{2}t_2 \right) & \mp \frac{\sqrt{3}}{2}t_1 - \frac{1}{2}t_2 \\ \mp \left(\mp \frac{1}{2}t_1 - \frac{\sqrt{3}}{2}t_2 \right) & \frac{1}{4}(t_{11} + 3t_{22}) & \pm \left(\frac{\sqrt{3}}{4}(t_{22} - t_{11}) \mp t_{12} \right) \\ \pm \frac{\sqrt{3}}{2}t_1 - \frac{1}{2}t_2 & \pm \left(\frac{\sqrt{3}}{4}(t_{22} - t_{11}) \pm t_{12} \right) & \frac{1}{4}(3t_{11} + t_{22}) \end{pmatrix} \quad (1.3)$$

The heavy transition metal M-atoms have large spin-orbit coupling, which persists in MX₂ monolayers. We model it by a minimal on-site term $\lambda \mathbf{L} \cdot \mathbf{S}$ for M-atoms that does not mix up and down-spins. Thus, the “on-site matrices” become spin-dependent, while the $t_{\alpha\beta}^\sigma (\mathbf{R}_i \neq \mathbf{0})$ remain unchanged. This is shown by acting with $\lambda \mathbf{L} \cdot \mathbf{S}$ upon our basis states explicitly. Although this produces states outside of the Hilbert space, these can be safely projected out since they are not allowed by symmetry [53, 54].

$$\mathbf{t}^\sigma(\mathbf{0}) \rightarrow \mathbf{t}^\sigma(\mathbf{0}) + \frac{\sigma\lambda}{2} \mathbf{L}_0, \quad \mathbf{L}_0 = \begin{pmatrix} 0 & 0 & 0 \\ 0 & 0 & 2i \\ 0 & -2i & 0 \end{pmatrix}, \quad \text{where } \sigma = \pm 1 \quad (1.4)$$

Spin-orbit coupling is important because it is responsible for the splitting of the valence band maximum by $\Delta_{\text{SOC}}^v = 2\lambda$. The conduction band minimum remains degenerate (although a small splitting Δ_{SOC}^c arises when considering perturbations due to the *d* orbitals that are not considered in our minimal model).

The minimal model we presented is very rich, and can be used to study many-body physics, for example by adding Hubbard-type interaction terms. Moreover, it can be used to study edge state physics by imposing appropriate boundary conditions on the hopping matrix. We will follow this route by numerically solving an interacting extension of the model for a nanoribbon using QMC, and comparing it with our own results obtained in the mean field approximation.

1.4 Introduction to Quantum Monte Carlo

Solving the many-body problem remains one of the greatest challenges in physics. Following the wealth of attempts at such pursuit, certain phenomena arising due to the strong interactions in quantum systems are explained in different theoretical frameworks, namely superconductivity, the Mott metal-insulator transition, and fractional quantum Hall effect. However, only in very limited cases does an actual analytical solution exist for the Schrödinger equation for a system of interacting particles, and one must resort to sophisticated approximation methods to obtain information about the role played by the competing interactions. Thus, numerical methods have become prominent as a tool for extracting information about this type of systems. Quantum Monte Carlo is amongst the most accurate and extensively studied methods. It differs from “Classical” Monte Carlo because in the quantum version, instead of measuring thermal averages, one measures expectations of operators over the Hilbert space of the system, corresponding to physical observables that have both quantum dynamical and thermal fluctuations. In fact, the dynamics of a quantum system are encoded in the Hamiltonian operator. In the

case of graphene-like 2D materials, such as TMDs, electron-electron interactions can be substantial, and we need accurate picture of the many-body phenomena that occur within them due to these interactions.

The idea of all QMC methods is to reduce the interacting problem to solving a set of integrals, which can be evaluated numerically through a standard stochastic procedure. But there is a myriad of methods to evaluate integrals numerically. Why is Monte Carlo the best one for this case? Multi-dimensional integrals are plagued by the curse of dimensionality. Although the Newton-Cotes quadrature formulas (including, for example the Newton method, and Simpson's rules), Gaussian quadrature formulas, or Romberg's method all scale polynomially with the number of integration points, they become impractical as the dimension increases. To use them, one would invoke Fubini's theorem to reduce the multi-dimensional integral to a series of one-dimensional integrals. However, the number of function evaluations required to compute the whole integral grows exponentially with its dimension. Monte Carlo preserves the polynomial scaling, thus yielding comparable accuracy with far less function evaluations. It is natural to use it since typically the state space of our quantum system is huge, leading to high dimensional integrals.

The Monte Carlo method is ubiquitous, and is based on using randomness to produce accurate estimates of deterministic integrals. The term was coined by Metropolis in 1949, although it was used as early as 1777 in an experiment known as Buffon's needle - where one obtains an estimate of the constant π by repeatedly throwing a needle randomly onto a sheet of paper with evenly spaced lines. The method is particularly useful when one wants to sample from a probability distribution in an exponentially large state space (like the huge Hilbert space of an interacting electron system), but it can, in principle, be used to solve any problem allowing a probabilistic formulation. Using the Monte Carlo approach to study a many-fermion system implies overcoming a significant obstacle common to all QMC methods - the so called *fermion sign problem*. Pauli's exclusion principle implies that the many-fermion wave function is anti-symmetric, which leads to a sign oscillation that greatly impedes the accurate evaluation of averages of quantum observables. The anti-symmetry constraint implies that a straightforward weight interpretation of the wave function is not possible. In the case of the finite temperature algorithm, the cancellations that occur when computing the average of any physical observable lead to poor statistical properties of the corresponding estimators. This means that a massive amount of samples requiring enormous computer time are needed to obtain meaningful results. In the case of the zero temperature algorithms, the situation is even worse. It might not even be possible to design a stochastic process carrying the system to its ground state, as normally is done in "projective" methods⁵: the wave function that is used as an initial proposal turns out to converge to a bosonic one, and the fermionic character of the system is lost. As was proven by Troyer, the *fermion sign problem* has NP⁶ computational complexity [55]. One of the greatest open questions in computer science is whether $P = NP$. Solving the *fermion sign problem* would imply finding a solution to $P = NP$, which would constitute a major breakthrough.

⁵Methods that iteratively project a trial wave function onto the ground state.

⁶NP or nondeterministic polynomial time, meaning that one can devise an algorithm that verifies the "yes" answer to a decision problem in polynomial time in the system size. Note that the class P - of polynomial time algorithms - is a subclass of NP.

1.4.1 Variational Monte Carlo

Variational techniques rely on an educated guess for the wave function of the system. A set of variational parameters α are tuned according to a variational principle, and we use the optimized trial wave function to compute physical quantities of interest using Monte Carlo. The method is used to simulate zero temperature systems, and requires prior knowledge to propose an approximate wave function in the first place. A particularly relevant observable is the variational energy E_V associated to a trial ground state. Let \mathbf{r} be the $3N$ spatial coordinates of the N electrons. For simplicity, let us ignore all other degrees of freedom, such as spin. Given the Hamiltonian of the system \mathcal{H} , and a trial wave function $\psi_T(\mathbf{r})$ - a “guess” of the ground state - one can compute its associated variational energy by averaging over a “local” energy:

$$E_V = \frac{\langle \psi_T | \mathcal{H} | \psi_T \rangle}{\langle \psi_T | \psi_T \rangle} = \frac{\int d\mathbf{r} |\psi_T(\mathbf{r})|^2 E_L(\mathbf{r})}{\int d\mathbf{r} |\psi_T(\mathbf{r})|^2} = \int d\mathbf{r} \rho(\mathbf{r}) E_L(\mathbf{r}), \text{ where } E_L = \frac{\mathcal{H} \psi_T(\mathbf{r})}{\psi_T(\mathbf{r})}, \rho(\mathbf{r}) = \frac{|\psi_T(\mathbf{r})|^2}{\int d\mathbf{r}' |\psi_T(\mathbf{r}')|^2} \quad (1.5)$$

We casted the variational energy as an average of the *local* energy E_L over the distribution ρ . This may be computed using Monte Carlo by sampling M points \mathbf{r}_k from the distribution $\rho(\mathbf{r})$: $E_V \approx \bar{E}_L = \frac{1}{M} \sum_{k=1}^M E_L(\mathbf{r}_k)$. Then, the trial ground state ψ_α is optimized by tuning the variational parameters α , according to how close the trial state’s energy is to the ground state energy E_0 , via the variational principle:

$$E_V(\alpha) = \frac{\langle \psi_\alpha | \mathcal{H} | \psi_\alpha \rangle}{\langle \psi_\alpha | \psi_\alpha \rangle} \geq E_0, \quad (1.6)$$

We use the optimized ground state wave function to compute averages of other observables. Since $E_V(\alpha)$ is bounded from below, the optimization procedure is equivalent to minimizing it in the hope that the bound is tight: $E_V(\alpha_{min}) \gtrsim E_0$. The finite sampling size M , of course, introduces a statistical error common to all Monte Carlo methods. However, the use of an approximate wave function introduces a systematic error that is hard to control since trial wave functions are generally introduced based on approximate, or heuristic arguments.

1.4.2 Diffusion Monte Carlo and projective methods

Variational Monte Carlo is severely limited by the use of a trial wave function $\psi_T(\mathbf{r})$ because we may not even have enough information to construct a reliable variational wave function in the first place. Diffusion QMC allows the simulation of a many-body system while having only a limited knowledge of the system’s physical properties. The idea is to map the Schrödinger equation onto an imaginary-time diffusion equation. Excited states are then filtered out by a diffusion process as we advance in imaginary-time. In imaginary-time $\tau = it$, the solution to the Schrödinger equation in terms of a formal series expansion in the eigenfunctions of the Hamiltonian becomes a series of “transient” wavefunctions weighted by $e^{-E_n \tau}$, $n \in \mathbb{N}$. Within precision and accuracy constraints, the longest lasting of these in imaginary-time is the ground state [56]. Thus, the idea of the diffusion method is to generate samples using the exact ground state wave function $\psi_0(\mathbf{r})$ [57]. The associated exact energy E_0 is the matrix

element of the Hamiltonian calculated using a trial wave function and the ground state.

$$E_0 = \frac{(\langle \psi_0 | E_0 \rangle (I | \psi_T \rangle))}{\langle \psi_0 | \psi_T \rangle} = \frac{\langle \psi_0 | \mathcal{H} | \psi_T \rangle}{\langle \psi_0 | \psi_T \rangle} = \frac{\int d\mathbf{r} \psi_0^*(\mathbf{r}) \psi_T(\mathbf{r}) E_L(\mathbf{r})}{\int d\mathbf{r} \psi_0^*(\mathbf{r}) \psi_T(\mathbf{r})} \quad (1.7)$$

Note that using this trick we avoid the computation of $\mathcal{H}\psi_0 = E_0\psi_0$, that is, the ground state energy. Instead, we approximate the integral by considering M configurations $\mathbf{r}_{k=1,\dots,M}$. The local energy of the trial wave function $E_L(\mathbf{r}) = \frac{\mathcal{H}\psi(\mathbf{r})}{\psi(\mathbf{r})}$ is averaged over a mixed distribution from which we draw a sample:

$$f(\mathbf{r}) = \frac{\psi_0^*(\mathbf{r}) \psi_T(\mathbf{r})}{\int d\mathbf{r} \psi_0(\mathbf{r}) \psi_T(\mathbf{r})} \quad (1.8)$$

Although the method is, of course, aimed at probing many-body systems, let us consider a single particle in 1D to illustrate its use. Performing a Wick rotation - effectively going to imaginary time - and shifting the energy, the Schrödinger equation becomes (with $\hbar = 1$)

$$\frac{\partial \psi_T(x, \tau)}{\partial \tau} = -\frac{1}{2m} \frac{\partial^2 \psi_T(x, \tau)}{\partial x^2} - [V(x) - E_T] \psi_T(x, \tau) \rightsquigarrow \psi_T(x, \tau) = \sum_{n=0}^{\infty} c_n \psi_n(x) e^{-(E_n - E_T)\tau} \quad (1.9)$$

The exact ground state wave function $\psi_0(x)$ is obtained as the longest lasting transient state in imaginary time: we are interested in the asymptotic behavior of the series expansion constituting the formal solution of the Schrödinger equation. For long times, the evolution of $|\psi_T(\tau)\rangle$ is given by

$$|\psi_T(\tau \rightarrow \infty)\rangle = \lim_{\tau \rightarrow \infty} \sum_n e^{-(E_n - E_T)\tau} |\psi_n\rangle \langle \psi_n | \psi_T \rangle = \lim_{\tau \rightarrow \infty} e^{-(E_0 - E_T)\tau} |\psi_0\rangle \langle \psi_0 | \psi_T \rangle \quad (1.10)$$

If $E_T > E_0$ the wave function diverges exponentially fast: $\lim_{\tau \rightarrow \infty} \psi_T(x, \tau) = \infty$. Similarly, for $E_T < E_0$ it vanishes exponentially fast: $\lim_{\tau \rightarrow \infty} \psi_T(x, \tau) = 0$. However, if $E_T = E_0$ the wave function converges to the ground state up to a constant factor, $c_0 = \langle \psi_0 | \psi_T \rangle$: $\lim_{\tau \rightarrow \infty} \psi_T(x, \tau) = c_0 \psi_0(x)$. Diffusion QMC makes use of this relation, approximating $\psi_0(x)$ by $\psi_T(x, \tau)$ for sufficiently long time. An important requirement is that $\psi_T(x, \tau)$ and $\psi_0(x)$ overlap significantly so that c_0 is large enough to be numerically measurable.

We can only use Monte Carlo to integrate Eq.(1.7) if $f(\mathbf{r})$ is positive and real. The second constraint is usually satisfied since we typically consider time-reversal symmetric Hamiltonians, for which we may choose real eigenstates. However, since many-electron wave functions are anti-symmetric, the trial wave function ψ_T might have different plus and minus sign domains (nodal cells) than those of the ground state wave function ψ_0 , changing the sign of $f(\mathbf{r})$, and hindering Monte Carlo integration.

1.4.3 Auxiliary Field QMC and the Fermion Sign Problem

As we have seen, the major drawback of the variational method was that it demanded *a priori* knowledge of a reasonable variational wave function describing, at least partly, some of the physics of the problem. Diffusion QMC demands less: we need only propose a trial wave function that overlaps with the ground state. However, none of these methods allow us to probe systems at finite temperature. Moreover, they both require some prior knowledge about the system, which may not always be available.

An alternative method is based on introducing an additional lattice field that mediates the electron-electron interaction. The interacting problem then becomes a problem of independent fermions coupled to this external field, and the fermionic part of the partition function can be traced out explicitly, leaving

the contribution of a *discrete*⁷ classical field, \mathbf{h} . This contribution can be evaluated numerically by employing importance sampling over the field configurations. Auxiliary field QMC relies on a mapping to a so called “classical” system (in quotes because there may be no actual classical analogue):

$$Z = \text{Tr}[e^{-\beta\mathcal{H}}] = \sum_{\{\mathbf{h}\} \text{ fermionic}} \sum_c e^{-S} = \sum_c p(c), \quad (1.11)$$

but some of the “probabilities” $p(c)$ can actually be negative due to the antisymmetry of the many-electron wavefunction under electron exchange. Here, S is a fermion-field action that we shall write out explicitly later. For a fixed configuration of the \mathbf{h} field, we sum over the fermionic part exactly to obtain the weight of each configuration, $p(c)$. The sum over \mathbf{h} is carried out stochastically. The negative weight problem can be circumvented when computing the average of an observable A :

$$\langle A \rangle = \frac{\sum_c A(c)p(c)}{\sum_c p(c)} = \frac{\sum_c A(c)|p(c)|\text{sign}[p(c)]/\sum_c |p(c)|}{\sum_c |p(c)|\text{sign}[p(c)]/\sum_c |p(c)|} \equiv \frac{\langle As \rangle_{|p|}}{\langle s \rangle_{|p|}}, \quad (1.12)$$

where $s(c) = \text{sign}[p(c)]$, and $|p(c)|$ corresponds to an auxiliary bosonic system (also coupled to the classical field) corresponding to the original fermionic system, and for which there is no sign problem.

The relative error $\Delta s / \langle s \rangle$ increases exponentially with system size, inverse temperature, and possibly other parameters of the specific model to be studied [55, 58]. To see this, we start by noting that the average sign is the ratio between the partition functions of the fermionic ($Z = \sum_c p(c)$) and bosonic systems ($Z' = \sum_c |p(c)|$). In terms of the difference in free energy densities, $\langle s \rangle = Z/Z' = e^{-\beta N \Delta f}$, implying that for M samples, the error of the denominator of Eq. (1.12) becomes

$$\frac{\Delta s}{\langle s \rangle} = \frac{\sqrt{(\langle s^2 \rangle - \langle s \rangle^2)/M}}{\langle s \rangle} = \frac{\sqrt{1 - \langle s \rangle^2}}{\sqrt{M} \langle s \rangle} \propto \frac{e^{\beta N \Delta f}}{\sqrt{M}}, \quad (1.13)$$

and similarly for the numerator of Eq. (1.12).

Auxiliary field, or determinant QMC can also be formulated to probe ground state properties, and a sign problem arises similarly. In fact, this problem plagues all QMC methods, even though we showed it only for the determinant method⁸. The latter is the most robust, unbiased, and reliable method, with a generally modest sign problem, hence we choose it to carry out our simulations.

Furthermore, in general, it suffices to use the finite temperature auxiliary field method with β large enough to probe ground state properties (for example, this is shown numerically for the Hubbard model on the square lattice in [59]). In this case, the inverse temperature may be regarded as being analogous to a projective parameter Θ , characterizing convergence to the ground state, within statistical uncertainty. Projector QMC, the zero temperature version of auxiliary field QMC is based on an equation similar to Eq.(1.10). Any observable A is computed by use of a trial wave function with some overlap with the ground state, i.e. $\langle \psi_T | \psi_0 \rangle \neq 0$ (see [60] for more details on the projector method; in this work we focus on the finite temperature version since it is more general):

$$\langle A \rangle = \lim_{\Theta \rightarrow \infty} \frac{\langle \psi_T | e^{-\Theta \mathcal{H}} A e^{-\Theta \mathcal{H}} | \psi_T \rangle}{\langle \psi_T | e^{-2\Theta \mathcal{H}} | \psi_T \rangle} \quad (1.14)$$

⁷The introduced field is discrete (and *binary*) because each fermionic state can only have occupations $n = 0, 1$. Although, there is a finite number of field configurations, the number grows exponentially with the number of sites on the lattice.

⁸So called because, as we shall show later, $p(c)$ boils down to a product of determinants that depends on the energy scales of the problem.

Auxiliary field QMC is more powerful than the variational and diffusion methods outlined before since it requires much less *a priori* information about the system. Perhaps more importantly, recent work suggests that it can be used in conjunction with neural networks to discover quantum phase transitions in correlated systems [61] in what could be a revolution in the field.

1.5 Original Contributions

In this work, we focus on the study of emerging magnetic ordering in TMD nanoribbons due to electron-electron interactions. To carry out this study, we use our own original implementation of the auxiliary field QMC algorithm in C++. To validate the built software, we consider previously well known models (such as the Hubbard model on the 1D chain, and the square lattice), and benchmark our results by comparing them with those of existing implementations (namely ALF [62] and QUEST [63]) and early seminal studies [5, 59]. We obtain original mean field results, which we use as a guide to approach the problem via QMC. The code we wrote can be used to simulate low-dimensional Hubbard-like models with different geometries, thus extending this work further. Additionally, using our code, we compare different options to stabilize the matrix products needed to perform the simulations, and characterize the fermion sign problem.

To study TMD nanoribbons, we extend a minimal three-band tight binding model [53] of TMDs to the interacting case. Then, we find emerging edge-state magnetism in TMD nanoribbons via original mean field calculations, and we compare those with QMC results.

1.6 Outline

We started this introductory chapter with the concept of emergence in strongly correlated electron systems. Then, we proceeded to discuss the particular example we study in this thesis: the 2D TMD nanoribbon. The strong electron correlations in this system suggest the existence of emergent edge-state magnetism, which to our knowledge was unexplored numerically before this work. To tackle this interacting fermion system, we resort to a numerical iterative solution of the mean field self consistent equation and a state-of-the-art determinant QMC algorithm.

In chapter 2, we introduce the Hubbard model, an ubiquitous model of electron correlations. We discuss analytical solutions for simple limiting cases, outline some approximation methods, and introduce Green's functions, which turn out to be the main object of our simulations. Moreover, we formulate the mean field theory of the Hubbard model.

In chapter 3, we start by summarizing the main ideas about how to apply the Monte Carlo method to statistical physics problems. In this context, we use original results of our simulations to illustrate the concepts in the specific context of our problem. Still in chapter 3, we introduce the auxiliary field method, and its various challenges, namely low temperature, and large size stabilization.

In chapter 4, we apply the code we implemented for a variety of systems, benchmarking our code, and carrying out some original calculations both at the mean field level and using QMC for TMDs.

Finally, in chapter 5, we conclude by discussing the results obtained in the previous chapter in the context of the literature, and propose future work to be done on the topic.

2

Minimal models of electron correlations

Contents

2.1	Modelling electron correlations in energy bands	15
2.2	Hubbard model	16
2.3	Exact solutions for simple cases	20
2.4	Effective $\frac{U}{t} \gg 1$ Heisenberg Model	27
2.5	Green's functions	30
2.6	Magnetism and mean field theory	32
2.7	Simulatable variants of the Hubbard model and TMDs	36

We start with an overview of the Hubbard model and in the following chapters we provide details on how to simulate it numerically using Quantum Monte Carlo. We discuss the original motivation provided by Hubbard to introduce the model and show how its Hamiltonian arises as an approximate representation of the Coulomb repulsion between electrons in an energy band. Then, we present exact solutions for particular limiting cases, which are used to crosscheck our simulations. In particular, we show that, in the limit where the interaction is large, the effective Hamiltonian at half filling corresponds to an atomic Heisenberg model defined in the appropriate Hilbert space with one electron per site. Then, we introduce Green's functions and explain how they relate to Wick's theorem. We proceed by formulating the mean field theory of the Hubbard model, and comparing results for a 1D chain with those obtained from Stoner's criterion. Finally, we show how one can generalize the Hubbard Hamiltonian and finish by discussing what type of interaction terms may be recast in a way that is more prone to simulation.

2.1 Modelling electron correlations in energy bands

The interactions between the electrons in a solid give rise to effects that arise specifically due to the many-body nature of the system. These strong electron correlations are often studied in the context of the Hubbard model. The latter goes beyond the periodic ionic potential perturbation to the free electron gas or tight binding approaches, which lead to band theory, by adding an interaction term to the tight binding Hamiltonian. Using it, we can make predictions about properties of a strongly correlated system, namely magnetic and superconducting behavior, and metal-insulator transitions.

Appearing in 1963 as one of the first attempts to include electron interaction effects in a quantum mechanical description of a solid, the Hubbard model was originally introduced to explain the behavior of the electrons in the narrow, partially filled d -bands of transition metals [32]. Correlation phenomena due to the Coulomb repulsion between the electrons in these bands lead to a behavior reminiscent of the atomic picture of a solid. In fact, the model may simply be regarded as a minimal model of interacting electrons in an energy band of a solid, where only on-site interactions penalizing double occupancy are considered. We have come a long way since the introduction of the Hubbard model and it is now arguably as paradigm-defining in many-body theory as the Ising model in statistical physics [64–66]. Although it was initially applied to transition metal monoxides like FeO, NiO, and CoO, which are antiferromagnetic

insulators (and not metallic, as was initially thought)¹, it gives insight on insulating, magnetic, and even superconducting phases arising due to the effect of electron interactions in a variety of quantum systems.



Figure 2.1: Unlike the Ising model, where either an up or a down spin live at each site, in the Hubbard model, there are four possible states at each site: a "hole" (absence of an electron), either an up spin electron or a down spin electron, or two electrons of opposite spins. The idea behind the model is to consider that the electrons interact, repelling each other (or attracting, in the case of superconductivity), only when they are on the same site (taken from [67]).

Fig.(2.1) is only a simplified view presented for comparison with a classical model of magnetism. The Hubbard Hamiltonian acts on electron wave functions centered on the sites of a lattice, leading to simultaneous charge and spin fluctuations. Ultimately, we wish to determine, or at least approximate, the wave function describing the full electronic system. Due to the many-body effects of electron correlations, this wave function is not a simple combination of products of one electron wave functions (a Slater determinant), as in the interaction-free case, or for nearly free electrons.

In the 1950's, the community was working on a theory of correlation effects in the free electron gas [68–73], which motivated Hubbard to devise a simple model for the (at the time) seemingly intractable problem of interacting electrons in a band. It became popular because it is generally realistic, yet relatively amenable to both analytical and numerical computations after some controlled approximations are introduced. Notably, it has been shown to be very relevant in the description of Mott insulators, and high T_c superconductors². In fact, the Hubbard model has found many applications, describing successfully a variety of quantum systems [74]; nonetheless, even the simplified picture it offers is in general difficult to approach analytically. There exists an exact solution in one dimension via Bethe ansatz [31], however the more general higher dimensional case is often solved numerically. An example of particular relevance for this work is the study carried out by Hirsch [8]. In the following chapters, we will discuss how to simulate the Hubbard model using a numerical approach that is based on this seminal paper, and essentially follows the ideas introduced in it.

2.2 Hubbard model

The nearly free electron gas models the conduction bands of metals and alloys fairly accurately. The high mobility of the electrons compared to the ions justifies two equivalent approximations, both giving essentially the same results [75]. The first idea is to treat the periodic potential created by the *virtually* fixed ions (compared to the electrons) as a perturbation on the free electron gas. Equivalently, we may imagine the system as a collection of tightly bond atoms, in which the electrons in the higher energy band hop from atom to atom. Both these approaches lead to band theory, a framework which allows us to predict whether a material is a conductor or a insulator. From the tight binding point of view, the effect of the electron mobility is the broadening of the atomic energy levels: the electrons in the solid occupy energy bands, rather than levels. The partially filled band of highest energy is called the

¹They were predicted to be metals by band theory until they were found not to behave like metals empirically.

²In this context, T_c is the critical temperature associated with the transition to a superconducting phase.

conduction band, since it is the band occupied by conduction electrons hopping from atom to atom. However, in transition metal and rare-earths, as in some compounds containing these elements, apart from the conduction bands there are partially filled d - or f -bands. The electron correlations within these partially filled bands are responsible for the characteristic properties of these solids. Some of these are not explained by band theory, namely the Mott metal-insulator transition [76–78].

2.2.1 Electron correlations in narrow d -bands

First, note that the effects of correlations cannot possibly be the same in narrow energy bands and in the free electron gas. To see this, we may simply recall the shape of a d -wave function (see Fig.(2.2)).

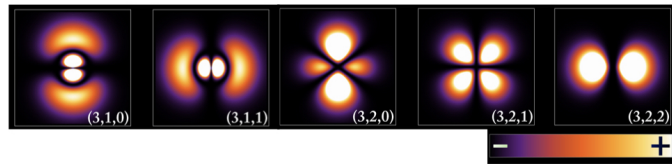


Figure 2.2: Probability density plots for different hydrogen orbital wave functions corresponding to quantum numbers (n, l, m) for $n = 3$. d -wave functions correspond to $l = 2$. We compare them with p -wave functions ($l = 1$). The probability density is higher in a region near the nucleus, and its shape leads to a non-uniform distribution of electronic charge, as opposed to the case of the free electron gas. (adapted from [79])

In a d -orbital, the electron charge density is concentrated near the nucleus. In a solid, the electronic charge density should then also be concentrated near the nuclei, as long as the atomic description is useful, even if not completely correct³. For a d -band, we assume this description to hold to some extent since the band is narrow. The fact that we may speak with some meaning of an electron belonging to a particular atom motivates a description from which the atomic characteristics of the solid emerge, in spite of the fact that the bandwidth of a d -band is still appreciable. The point is that electrons in d -bands are certainly not well described by a nearly free electron model nor by a tight binding model, which cannot possibly account for atomic-like behavior.

Experimentally, d -electrons of transition metals show hybrid behavior: sometimes they are accurately described by an ordinary band model, but there are occasions in which the atomic model is better. For example, we see spin wave phenomena in ferromagnetic transition metals, and the susceptibilities of some of these metals depend strongly on temperature. This is characteristic of an atomic (Heisenberg) model. On the other hand, the d -electrons contribute significantly to the low temperature specific heat and sometimes the magnetic moments per atom of some transition metal ferromagnets are not integer multiples of the Bohr magneton. This is characteristic of band theory⁴. Our theory of correlations should describe this balance between band-like and atomic-like behavior.

A theory of electron correlations in a narrow energy band should reduce to an atomic model in the

³The electronic charge density is, of course, not actually defined in terms of a squared norm of the d -wave function for a narrow band. There is some broadening of the corresponding atomic energy level, and the wave function describing an electron is a Bloch wave function. Since the band is narrow, we assume that the atomic wave function description is still somewhat useful in a given range and we use it to provide a heuristic motivation for the non validity of the free electron assumption.

⁴Think, for example, of a tight binding model. Electrons hop from atom to atom, and in general the spin of each atom depends on the particular electrons “belonging” to it at a given time. If we take an average of the total spin of each atom, we will in general not necessarily obtain an integer multiple of the Bohr magneton. If we simply had a collection of atoms, Hund’s rule would apply, and each atom would have its spin aligned in a given direction. The average spin would then tend to be an integer multiple of the Bohr magneton.

appropriate limit, for example atoms that are so far apart on a lattice that they interact only very weakly. Although we always keep in mind that we are focusing on d -electrons, we shall consider s -electrons in what follows for the sake of simplicity. The important conclusions will not differ significantly. We will use the "atomicity" of the electronic distribution to introduce an approximate representation of the electron interaction. It turns out that this representation is mathematically much simpler to handle than the Coulomb interaction itself.

In short, our picture is the following: electrons hop rapidly from atom to atom in a band-like fashion, but their motion is correlated in such a way that atomic characteristics emerge. The extent of atomic behavior depends, of course, on the strength of the interaction.

2.2.2 Hubbard Hamiltonian

Imagine a hypothetical partially filled narrow s -band with n electrons per atom. Suppose you have obtained Bloch wave functions $\psi_{\mathbf{k}}$ corresponding to energies $\varepsilon_{\mathbf{k}}$ by solving the Schrödinger equation for some spin-independent Hartree-Fock potential that accounts for the average interaction of the s -band electrons with electrons on other bands, and the interaction with the other s -electrons. The electrons on the band evolve according to the Hamiltonian:

$$\mathcal{H} = \sum_{\mathbf{k}\sigma} \left(\varepsilon_{\mathbf{k}} - \sum_{\mathbf{k}'} (2V_{\mathbf{k}\mathbf{k}'}^{\mathbf{k}\mathbf{k}'} - V_{\mathbf{k}'\mathbf{k}'}^{\mathbf{k}\mathbf{k}'}) \nu_{\mathbf{k}'} \right) c_{\mathbf{k}\sigma}^\dagger c_{\mathbf{k}\sigma} + \frac{1}{2} \sum_{\substack{\mathbf{k}_1 \mathbf{k}_2 \\ \mathbf{k}'_1 \mathbf{k}'_2 \sigma_1 \sigma_2}} V_{\mathbf{k}'_1 \mathbf{k}'_2}^{\mathbf{k}_1 \mathbf{k}_2} c_{\mathbf{k}_1 \sigma_1}^\dagger c_{\mathbf{k}_2 \sigma_2}^\dagger c_{\mathbf{k}'_2 \sigma_2} c_{\mathbf{k}'_1 \sigma_1}, \quad (2.1)$$

where the \mathbf{k} -sums run over the first Brillouin zone. The integrals are defined by

$$V_{\mathbf{k}'_1 \mathbf{k}'_2}^{\mathbf{k}_1 \mathbf{k}_2} \equiv \left\langle \mathbf{k}_1 \mathbf{k}_2 \left| \frac{e^2}{r} \right| \mathbf{k}'_1 \mathbf{k}'_2 \right\rangle = e^2 \int \frac{\psi_{\mathbf{k}_1}^*(\mathbf{x}) \psi_{\mathbf{k}'_1}(\mathbf{x}) \psi_{\mathbf{k}_2}^*(\mathbf{x}') \psi_{\mathbf{k}'_2}(\mathbf{x}')}{|\mathbf{x} - \mathbf{x}'|} d\mathbf{x} d\mathbf{x}' \quad (2.2)$$

The first term represents the band energies of the electrons minus their potential energy in the part of the Hartree-Fock field due to the electrons of the s -band itself. The latter ensures that we do not overestimate the magnitude of the interactions between the electrons of the band: the Hartree-Fock field that specifies $\varepsilon_{\mathbf{k}}$ is computed taking into account these interactions, so if we didn't subtract it, we would count the energy of these interactions twice since they reappear in the last term, which represents the interactions among all electrons in the system. Furthermore, we assume that up and down spins are occupied equally, and $\nu_{\mathbf{k}}$ are the occupation numbers of the states of the band in the Hartree-Fock calculation. The term that we subtract in equation (2.1) corresponds to the part of the interaction term which is already accounted for by the first diagonal "mean field" term. Thus, it corresponds to the mean field expansion of the interaction term. A generic way of writing the interaction term by gathering the \mathbf{k}, σ indexes into a single index μ is $V_{\text{int}} = \frac{1}{2} V_{\nu' \mu'}^{\nu \mu} c_{\nu}^\dagger c_{\mu'}^\dagger c_{\mu'} c_{\nu}$, where the summation over repeated indexes is implied. In appendix A, we obtain the form of V_{int} in the Hartree-Fock approximation.

We may write the Bloch states $\psi_{\mathbf{k}}$ as a combination of Wannier functions localized at each atom.

$$\psi_{\mathbf{k}}(\mathbf{x}) = N^{-1/2} \sum_i e^{i\mathbf{k} \cdot \mathbf{R}_i} \phi(\mathbf{x} - \mathbf{R}_i), \text{ where } \phi(\mathbf{x}) = N^{-1/2} \sum_{\mathbf{k}} \psi_{\mathbf{k}}(\mathbf{x}), \quad (2.3)$$

and where N is the number of atoms. The sum runs over all atomic positions \mathbf{R}_i . Introducing the annihilation (creation) operators of an electron of spin σ in the Wannier state $\phi(\mathbf{x} - \mathbf{R}_i)$ localized at site

i , $c_{i\sigma}^{(\dagger)}$, we may write $c_{i\sigma}^{(\dagger)} = N^{-1/2} \sum_i e^{i\mathbf{k}\cdot\mathbf{R}_i} c_{i\sigma}^{(\dagger)}$, so that the Hamiltonian becomes

$$\mathcal{H} = \sum_{ij} K_{ij} c_{i\sigma}^\dagger c_{j\sigma} + \sum_{\substack{ijkl \\ \sigma\sigma'}} \left[\frac{1}{2} V_{kl}^{ij} c_{i\sigma}^\dagger c_{j\sigma'}^\dagger c_{l\sigma'} c_{k\sigma} - \left(2V_{kl}^{ij} - V_{lk}^{ij} \right) \nu_{jl} c_{i\sigma}^\dagger c_{k\sigma} \right], \quad (2.4)$$

where

$$K_{ij} = N^{-1} \sum_{\mathbf{k}} \varepsilon_{\mathbf{k}} e^{i\mathbf{k}\cdot(\mathbf{R}_i - \mathbf{R}_j)}, \text{ and } \nu_{jl} = N^{-1} \sum_{\mathbf{k}} e^{i\mathbf{k}\cdot(\mathbf{R}_j - \mathbf{R}_l)} \quad (2.5)$$

Now comes the crucial approximation. For a narrow energy band, the Wannier functions ϕ nearly coincide with atomic s -functions. For small bandwidth, these s -functions form an atomic shell whose radius is small compared with the spacing between atoms, that is, the lattice constant. Thus, the integral $U = \langle ii | e^2/r | ii \rangle$ should turn out to be much larger than all other integrals. This suggests the seemingly crude approximation of neglecting all other integrals. However, this approximation is not so radical as it could seem at first sight since the other integrals are indeed much smaller than U . In fact, for example, for $3d$ electrons of transition metals they are smaller by about two orders of magnitude [32]. Keeping only the terms in U in the interaction part, we obtain

$$\mathcal{H} = \sum_{i,j,\sigma} K_{ij} c_{i\sigma}^\dagger c_{j\sigma} + \frac{U}{2} \sum_{i\sigma} n_{i\sigma} n_{i,-\sigma} - U \sum_{i,\sigma} \nu_{i,i} n_{i,\sigma} \quad (2.6)$$

where $n_{i\sigma} = c_{i\sigma}^\dagger c_{i\sigma}$. Note that $\nu_{i,i} = N^{-1} \sum_{\mathbf{k}} \nu_{\mathbf{k}} = n/2$, where n is the electron density, which means that the last term is constant and may be dropped. Now, the hopping matrix \mathbf{K} can, in principle, be found by inverse Fourier transforming the dispersion relation $\varepsilon_{\mathbf{k}}$ of the interaction-free system, that we can assume to be obtained experimentally or numerically. From the tight binding view (with no U -term), we have a well defined crystal wavevectors that depend on the symmetry of the lattice, which may be written as Fourier transforms $|\mathbf{k}\rangle \equiv \frac{1}{N} \sum_{\mathbf{r}} e^{i\mathbf{k}\cdot\mathbf{r}} |\mathbf{r}\rangle$, and, recalling the form of the hopping Hamiltonian (or the kinetic energy part in the Hubbard model): $\mathcal{H}_K = - \sum_{\mathbf{r}\mathbf{r}'} K(\mathbf{r} - \mathbf{r}') |\mathbf{r}'\rangle \langle \mathbf{r}|$, we can cast the dispersion relation as the (negative) Fourier transform of the hopping

$$-\mathcal{H}_K |\mathbf{k}\rangle = \frac{1}{\sqrt{N}} \sum_{\mathbf{r}\mathbf{r}'} K(\mathbf{r} - \mathbf{r}') e^{i\mathbf{k}\cdot\mathbf{r}} |\mathbf{r}'\rangle = \frac{1}{\sqrt{N}} \left(\sum_{\mathbf{R}} K(\mathbf{R}) e^{i\mathbf{k}\cdot\mathbf{R}} \right) \left(\sum_{\mathbf{r}'} e^{i\mathbf{k}\cdot\mathbf{r}'} |\mathbf{r}'\rangle \right) = \varepsilon_{\mathbf{k}} |\mathbf{k}\rangle \quad (2.7)$$

This gives us an interpretation of the \mathbf{K} matrix: given the dispersion relation, and considering the solid to be well described by a tight binding model, we can easily obtain the matrix elements K_{ij} .

Let us now suppose that we have the simplest uniform nearest neighbor hopping model with Hubbard-type electron interactions. Going back to equation (2.5), and recalling that the sum on \mathbf{k} is restricted to the first Brillouin zone, we obtain the usual tight binding result: $K_{\langle ij \rangle} = -t \in \mathbb{R}$ and 0 otherwise (i.e. \mathbf{K} is a very sparse matrix that is only non-zero for i, j nearest neighbors). Thus, the full Hamiltonian reads

$$\mathcal{H} = -t \sum_{\langle i,j \rangle, \sigma} \left(c_{i,\sigma}^\dagger c_{j,\sigma} + c_{j,\sigma}^\dagger c_{i,\sigma} \right) + U \sum_i n_{i,\uparrow} n_{i,\downarrow} - \mu \sum_i \left(n_{i,\uparrow} + n_{i,\downarrow} \right), \quad (2.8)$$

where, for generality, we included the chemical potential, thus taking the Grand-canonical ensemble.

2.2.3 Particle-hole symmetry

In this section we examine a particularly relevant and unique symmetry of the Hubbard model. The main idea is that, at half filling, the Hubbard Hamiltonian is invariant under a transformation which

turns particles into holes and vice-versa. Particle-hole symmetry (PHS) allows us to relate the properties of the Hubbard Hamiltonian at different values of the parameters. Moreover, it allows us to devise a mapping between the attractive ($U < 0$) and the repulsive ($U > 0$) models. We will see later that this mapping is important in QMC simulations [80]. We start our discussion with the concept of a bipartite lattice. A lattice is said to be bipartite if it can be divided into two sublattices \mathcal{A} and \mathcal{B} , such that the set of neighbors of a site in sublattice \mathcal{A} belongs to sublattice \mathcal{B} . For example, the square and honeycomb lattices are bipartite, whereas the triangular lattice is not. In a bipartite lattice, antiferromagnetic (AF) order is favored. In contrast, AF order is frustrated on the triangular and other non bipartite lattices.

Introducing a Particle-hole transformation (PHT),

$$d_{i,\sigma}^\dagger = (-1)^i c_{i,\sigma}, \quad (2.9)$$

we exchange the role of annihilation and creation operators. In fact, particles become holes and vice-versa: $d_{i,\sigma}^\dagger d_{i,\sigma} = 1 - c_{i,\sigma}^\dagger c_{i,\sigma}$, and the occupations $n = 0, 1$ are interchanged. Consider a bipartite lattice. Since in that case the factor $(-1)^i$ takes on -1 on one sublattice and 1 on the other, the kinetic part of the Hamiltonian is invariant under a PHT: $c_{i,\sigma}^\dagger c_{j,\sigma} + c_{j,\sigma}^\dagger c_{i,\sigma} \mapsto (-1)^{i+j} (d_{i,\sigma}^\dagger d_{j,\sigma}^\dagger + d_{j,\sigma}^\dagger d_{i,\sigma}^\dagger) = d_{j,\sigma}^\dagger d_{i,\sigma} + d_{i,\sigma}^\dagger d_{j,\sigma}$.

The PHS form of the kinetic term can be incorporated into the interaction term by a shift in the chemical potential and by adding a constant to the Hamiltonian. First, note that the interaction term $U(n_{i,\uparrow} - \frac{1}{2})(n_{i,\downarrow} - \frac{1}{2})$ is unchanged under a PHT. Expanding it, we get $U n_{i,\uparrow} n_{i,\downarrow} - \frac{U}{2}(n_{i,\uparrow} + n_{i,\downarrow}) + \frac{U}{4}$, which indeed differs from the original interaction term by a shift in the chemical potential ($\mu \rightarrow \mu + U/2$) plus a constant. Thus, the particle-hole symmetric Hamiltonian is equivalent to the original one.

$$\mathcal{H} = -t \sum_{\langle i,j \rangle, \sigma} \left(c_{i,\sigma}^\dagger c_{j,\sigma} + c_{j,\sigma}^\dagger c_{i,\sigma} \right) + U \sum_i \left(n_{i,\uparrow} - \frac{1}{2} \right) \left(n_{i,\downarrow} - \frac{1}{2} \right) - \mu \sum_i \left(n_{i,\uparrow} + n_{i,\downarrow} \right) \quad (2.10)$$

Under a PHT, the density, $\rho = \langle n_\uparrow + n_\downarrow \rangle$, transforms as $\rho \mapsto 2 - \rho$. The Hamiltonian changes only in the chemical potential term: $\mu \mapsto -\mu$. Thus, we have that $\rho(\mu) = 2 - \rho(-\mu)$, and at $\mu = 0$, we have half filling: $\rho = 1$. This reasoning is valid for any β , t , or U , which implies that the phase diagram of the Hubbard model must be symmetric about half filling. Suppose you added next nearest neighbor (NNN) hoppings t' ⁵. Then, PHS would be broken, and the phase diagram would no longer be symmetric about $\mu = 0$. Indeed, a modified version of the Hubbard model with NNN hoppings is often used to model cuprate superconductors, and this lack of symmetry is consistent with the fact that hole- and electron-doped cuprates have different properties. PHS is also broken for the triangular lattice with non uniform hoppings we shall consider later when modelling Transition Metal Dichalcogenides (TMDs).

2.3 Exact solutions for simple cases

In PHS form, the Hubbard Hamiltonian may then be written as a sum of kinetic and chemical, and potential energy terms $\mathcal{H} = \mathcal{H}_K + \mathcal{H}_V$. Let indexes i and j label sites on a lattice, and define

$$\mathcal{H}_K = -t \sum_{\langle i,j \rangle, \sigma} \left(c_{i,\sigma}^\dagger c_{j,\sigma} + c_{j,\sigma}^\dagger c_{i,\sigma} \right) - \mu \sum_i \left(n_{i,\uparrow} + n_{i,\downarrow} \right), \quad \mathcal{H}_V = U \sum_i \left(n_{i,\uparrow} - \frac{1}{2} \right) \left(n_{i,\downarrow} - \frac{1}{2} \right), \quad (2.11)$$

⁵On the square lattice, this corresponds to connecting sites across the diagonal of each square.

where $c_{i,\sigma}^{(\dagger)}$ is an operator that annihilates (creates) an electron with spin σ on site i ; $n_{i,\sigma}$ is the number operator counting the number of electrons of spin σ on site i (either 0 or 1); t is the hopping parameter related to the kinetic energy of the electrons: it is determined by the overlap of the atomic wave functions on neighboring sites $\langle i, j \rangle$; U is the on-site Coulomb repulsion between electrons: whenever a site i has two electrons, there is a local repulsion between them corresponding to an energy cost $Un_{i\uparrow}n_{i\downarrow}$ (up to an additive constant); μ is the chemical potential controlling the electron number (or density).

A given physical observable of interest \mathcal{O} , such as the spin-spin correlation, or the magnetic susceptibility may be computed formally by using the projection operator \mathcal{P} defined below

$$\langle \mathcal{O} \rangle = \text{Tr}[\mathcal{O}\mathcal{P}], \text{ where } \mathcal{P} \equiv \frac{1}{Z}e^{-\beta\mathcal{H}}, \text{ with } Z = \text{Tr}[e^{-\beta\mathcal{H}}] \quad (2.12)$$

The trace is taken over the Hilbert space corresponding to all possible configurations of the lattice occupation. Defining an orthonormal basis of this Hilbert space $\{|\psi_\alpha\rangle | \alpha = 1, \dots, D\}$, where D is the dimension of the Hilbert space, the partition function reads

$$Z = \text{Tr}[e^{-\beta\mathcal{H}}] = \sum_{\alpha} \langle \psi_{\alpha} | e^{-\beta\mathcal{H}} | \psi_{\alpha} \rangle \quad (2.13)$$

There are four possible states at each site in the Hubbard model: $| \rangle$, $|\uparrow\rangle$, $|\downarrow\rangle$, $|\uparrow\downarrow\rangle$, corresponding, respectively, to no electron, a spin up or spin down electron, and two electrons of opposite spin occupying the site. The potential energy operator acts as follows

$$U(n_{i\uparrow} - \frac{1}{2})(n_{i\downarrow} - \frac{1}{2}) \begin{cases} | \rangle = \frac{U}{4} | \rangle \\ |\uparrow\rangle = -\frac{U}{4} |\uparrow\rangle \\ |\downarrow\rangle = -\frac{U}{4} |\downarrow\rangle \\ |\uparrow\downarrow\rangle = \frac{U}{4} |\uparrow\downarrow\rangle \end{cases} \quad (2.14)$$

Singly occupied states ($|\uparrow\rangle$, $|\downarrow\rangle$) have lower energy and are thus more likely to occur. They correspond to nonzero magnetization $m = n_{\uparrow} - n_{\downarrow}$, which is favored by the Hubbard interaction U . A relevant question is whether or not the spins order in space when $t \neq 0$ and to what extent.

Let us now establish our notations for second quantized operators to introduce a different representation of electronic states on the lattice. The fermionic annihilation and creation operators anticommute: $\{c_{j\sigma}, c_{l\sigma'}^{\dagger}\} = \delta_{jl}\delta_{\sigma\sigma'}$. The c -operator algebra is further defined by the vanishing of all other anticommutators: $\{c_{j\sigma}^{(\dagger)}, c_{l\sigma'}^{(\dagger)}\} = 0$. Note that taking $l = j$ and $\sigma = \sigma'$ in this equation for the c^{\dagger} -operators, we recover Pauli's exclusion principle since $(c_{j\sigma}^{\dagger})^2 = 0$. If we omit the site i and spin σ indices, a convenient way of specifying states on the lattice is $|0\rangle$: unoccupied state - no electron, $|1\rangle$: occupied state - one electron, so that a generic state may be written as a product of the states above $\otimes_{i=1}^N \otimes_{\sigma=\pm 1/2} |n_{i,\sigma}\rangle$ at each site for each spin state, where $n = 0, 1$. For example, one such state is $|0\rangle_{1,\uparrow} |1\rangle_{1,\downarrow} |1\rangle_{2,\uparrow} |1\rangle_{2,\downarrow} |0\rangle_{3,\uparrow} |0\rangle_{3,\downarrow} \dots |1\rangle_{N,\uparrow} |0\rangle_{N,\downarrow}$, where N is the number of sites on the lattice. Site 1 has a single spin-down electron, while site 2 is doubly occupied, site 3 is unoccupied, and so on, until we reach site N , which has a single spin-up electron. The creation and annihilation operators act as follows

$$c|0\rangle = 0 \quad c^{\dagger}|0\rangle = |1\rangle \quad c|1\rangle = |0\rangle \quad c^{\dagger}|1\rangle = 0 \quad (2.15)$$

Thus, the eigenstates of the number operator are $|0\rangle, |1\rangle$: $n|0\rangle = 0, n|1\rangle = |1\rangle$. Moreover, the

operator $c_i^\dagger c_{i+1}^\dagger$, corresponding to the hopping from site $i + 1$ to i , i.e. to the kinetic energy of the electrons on neighboring sites, annihilates the particle at $i + 1$ and creates it back at i , i.e. the electron hops from $i + 1$ to i . Ignoring spin, the only nonzero kinetic energy term is $c_i^\dagger c_{i+1}^\dagger |01\rangle = |10\rangle$. When acting upon the other three states we get 0.

2.3.1 The purely atomic ($\frac{U}{t} \rightarrow \infty$), single site limit

When $t = 0$, the site index may be omitted since the Hamiltonian is a sum of operators solely at site i . Hence, we have $[\mathcal{H}, n_{i,\sigma}] = 0 \forall i = 1, 2, \dots, N$, and the eigenstates of \mathcal{H} are also eigenstates of all number operators at the different sites in the lattice. Thus, in the single site limit, we obtain

$$\mathcal{H} = U \left(n_\uparrow - \frac{1}{2} \right) \left(n_\downarrow - \frac{1}{2} \right) - \mu \left(n_\uparrow + n_\downarrow \right) \quad (2.16)$$

which acts as follows (using the eigenstates of n_σ)

$$\mathcal{H} \begin{cases} |\rangle = \frac{U}{4} |\rangle \\ |\uparrow(\downarrow)\rangle = \left(\frac{U}{4} - (\mu + \frac{U}{2}) \right) |\uparrow(\downarrow)\rangle \\ |\uparrow\downarrow\rangle = \left(\frac{U}{4} - 2\mu \right) |\uparrow\downarrow\rangle \end{cases} \quad (2.17)$$

Thus, the Hamiltonian is diagonal in the basis $\{|\psi_\alpha\rangle\} = |\rangle, |\uparrow\rangle, |\downarrow\rangle, |\uparrow\downarrow\rangle$:

$$\mathcal{H} \rightsquigarrow \mathbf{H} = \text{diag} \left(\frac{U}{4}, \frac{U}{4} - (\mu + \frac{U}{2}), \frac{U}{4} - (\mu + \frac{U}{2}), \frac{U}{4} - 2\mu \right), \quad (2.18)$$

which means that $e^{-\beta\mathcal{H}}$ is also diagonal:

$$e^{-\beta\mathcal{H}} \rightsquigarrow e^{-\beta U/4} \text{diag} \left(1, e^{\beta(\mu+\frac{U}{2})}, e^{\beta(\mu+\frac{U}{2})}, e^{2\beta\mu} \right) \quad (2.19)$$

and this is one of the rare situations in which it is possible to explicitly write down a closed form for the partition function.

$$Z = \text{Tr}[e^{-\beta\mathcal{H}}] = \sum_\alpha \langle \psi_\alpha | e^{-\beta\mathcal{H}} | \psi_\alpha \rangle = e^{-\beta U/4} \left(1 + 2e^{\beta(\mu+\frac{U}{2})} + e^{2\beta\mu} \right) \quad (2.20)$$

Moreover, the aforementioned observables are explicitly computable. This is due to the diagonal form of \mathcal{H} , and to the low-dimensional Hilbert space.

$$\begin{aligned} \mathcal{H}e^{-\beta\mathcal{H}} &\rightsquigarrow e^{-\beta U/4} \text{diag} \left(\frac{U}{4}, (-\mu - \frac{U}{4})e^{\beta(\mu+\frac{U}{2})}, (-\mu - \frac{U}{4})e^{\beta(\mu+\frac{U}{2})}, (\frac{U}{4} - 2\mu)e^{2\beta\mu} \right) \\ n_\uparrow e^{-\beta\mathcal{H}} &\rightsquigarrow e^{-\beta U/4} \text{diag} \left(0, e^{\beta(\mu+\frac{U}{2})}, 0, e^{2\beta\mu} \right) \quad n_\downarrow e^{-\beta\mathcal{H}} \rightsquigarrow e^{-\beta U/4} \text{diag} \left(0, 0, e^{\beta(\mu+\frac{U}{2})}, e^{2\beta\mu} \right) \\ n_\uparrow n_\downarrow e^{-\beta\mathcal{H}} &\rightsquigarrow e^{-\beta U/4} \text{diag} \left(0, 0, 0, e^{2\beta\mu} \right) \end{aligned} \quad (2.21)$$

From these we can compute some traces we shall find useful to obtain averages of some observables.

$$\begin{aligned} \text{Tr} \left[\mathcal{H}e^{-\beta\mathcal{H}} \right] &= e^{-\beta U/4} \left(\frac{U}{4} + 2(-\mu - \frac{U}{4})e^{\beta(\mu+\frac{U}{2})} + (\frac{U}{4} - 2\mu)e^{2\beta\mu} \right) \\ \text{Tr} \left[(n_\uparrow + n_\downarrow)e^{-\beta\mathcal{H}} \right] &= e^{-\beta U/4} \left(2(-\mu - \frac{U}{4})e^{\beta(\mu+\frac{U}{2})} + (\frac{U}{4} - 2\mu)e^{2\beta\mu} \right), \quad \text{Tr} \left[n_\uparrow n_\downarrow \right] = e^{-\beta U/4} e^{2\beta\mu} \end{aligned} \quad (2.22)$$

The bottom line is that we are able to obtain *exact* expressions for:

1. The one-site density $\rho = \langle n_{\uparrow} \rangle + \langle n_{\downarrow} \rangle$, measuring the average occupation of each site,

$$\rho = \frac{\text{Tr}[(n_{\uparrow} + n_{\downarrow})e^{-\beta\mathcal{H}}]}{Z} = \frac{2e^{\beta(\frac{U}{2}+\mu)} + 2e^{2\beta\mu}}{1 + 2e^{\beta(\mu+\frac{U}{2})} + e^{2\beta\mu}}. \quad (2.23)$$

Note that when there is no chemical potential $\mu = 0$, we have $\rho = 1$ for any U , or β . This corresponds to half filling: the density of electrons is half its maximum possible value.

In Fig.(2.3), we plot $\rho(\mu)$ for varying temperature, and fixed on-site interaction. It allows us to get some insight into the Mott insulating gap. From now on, we take $k_B = 1$. At $T = 0.25$, the curve owes its step-like shape to the small thermal fluctuations. As T increases, the curve starts losing this tendency, and by $T = 2.0$, it is no longer possible to identify it. This is a consequence of the now larger thermal fluctuations that are present at higher temperature. We denote the flat region between $\mu = -U/2$ and $\mu = U/2$ “Mott Plateau”. As the chemical potential is increased, the density remains small until a threshold is exceeded at $\mu = -\frac{U}{2}$. Then, it rises very rapidly to $\rho = 1$ (half filling), and again stays almost constant. It is not until μ jumps by U that we fill the site ($\rho = 2$). This Mott insulating gap appears because the presence of a fermion in the site blocks the addition of a second one due to the on-site interaction. One needs a sufficiently large chemical potential to overcome this effect. As we shall see, this feature of the model remains present as the number of sites increases. Note that in the Mott gap, the compressibility vanishes: $\kappa = \frac{\partial\rho}{\partial\mu} = 0$, leading to the appearance of the Mott Plateau. Just as thermal fluctuations can destroy the sharp jumps corresponding to the gap, so can quantum fluctuations. The hopping term in the Hamiltonian introduces such fluctuations, leading to an effect similar to that of Fig.(2.3).

2. The one-site energy $E = \langle \mathcal{H} \rangle$,

$$\begin{aligned} E &= \frac{\text{Tr}\left(\mathcal{H}e^{-\beta\mathcal{H}}\right)}{Z} = \frac{\frac{U}{4} + 2(-\mu - \frac{U}{4})e^{\beta(\frac{U}{2}+\mu)} + (\frac{U}{4} - 2\mu)e^{2\beta\mu}}{1 + 2e^{\beta(\frac{U}{2}+\mu)} + e^{2\beta\mu}} \\ &= \frac{\frac{U}{4}(1 + 2e^{\beta(\frac{U}{2}+\mu)} + e^{2\beta\mu})}{1 + 2e^{\beta(\frac{U}{2}+\mu)} + e^{2\beta\mu}} + \frac{2(-\mu - \frac{U}{4})e^{\beta(\frac{U}{2}+\mu)} - 2\mu e^{2\beta\mu} - 2\frac{U}{4}e^{\beta(\frac{U}{2}+\mu)}}{1 + 2e^{\beta(\frac{U}{2}+\mu)} + e^{2\beta\mu}} \\ &= \frac{U}{4} - \frac{(2\mu - U)e^{\beta(\frac{U}{2}+\mu)} + 2\mu e^{2\beta\mu}}{1 + 2e^{\beta(\frac{U}{2}+\mu)} + e^{2\beta\mu}} \end{aligned} \quad (2.24)$$

which at half filling becomes $E = \frac{U}{4} - \frac{U}{2}(1 + e^{-\beta U/2})^{-1}$.

3. The double occupancy $\langle n_{\uparrow}n_{\downarrow} \rangle$,

$$\langle n_{\uparrow}n_{\downarrow} \rangle = \frac{\text{Tr}[n_{\uparrow}n_{\downarrow}]}{Z} = \frac{e^{2\beta\mu}}{1 + 2e^{\beta(\frac{U}{2}+\mu)} + e^{2\beta\mu}} \quad (2.25)$$

which, at half filling, simplifies to $\langle n_{\uparrow}n_{\downarrow} \rangle = \frac{1}{2}(1 + e^{\beta U/2})^{-1}$.

Note that as either U or β increase the double occupancy tends to zero.

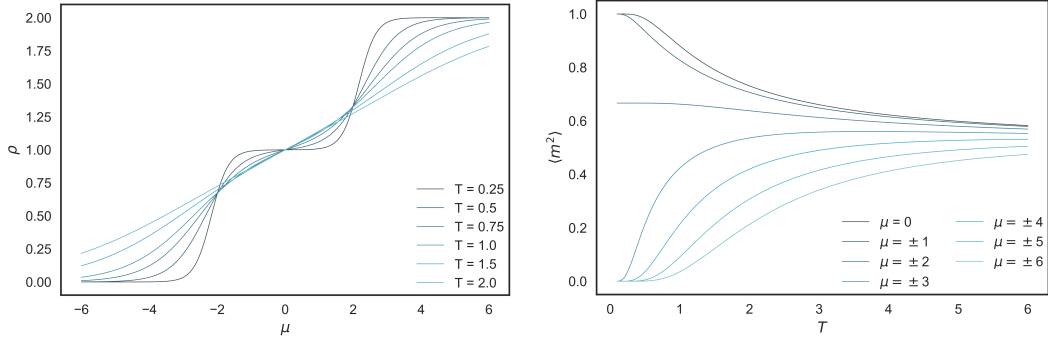


Figure 2.3: Left: Electron density ρ for varying chemical potential μ and temperature $T = \beta^{-1}$, but fixed $U = 4$. As the temperature decreases, a “Mott plateau” sets in. The Mott insulating gap already seen here is an important feature of the Hubbard model. Right: Magnetization as a function of temperature $\langle m^2 \rangle(T)$ in the single site Hubbard model for varying chemical potential μ . Local moments develop at lower temperature. However, as we increase the magnitude of the chemical potential, the situation is reversed. At low temperatures, the site is either doubly occupied or empty, and so the magnetization goes to zero. Thermal fluctuations allow the occupation of the site to fluctuate, and the magnetization to become nonzero.

As was motivated in the previous chapter, we are interested in studying magnetism in correlated systems. For the Hubbard model, the relevant quantity is the sum of the squared local moments

$$\langle m^2 \rangle = \langle (n_\uparrow - n_\downarrow)^2 \rangle = \langle n_\uparrow + n_\downarrow \rangle - 2 \langle n_\uparrow n_\downarrow \rangle = \rho - 2 \langle n_\uparrow n_\downarrow \rangle \quad (2.26)$$

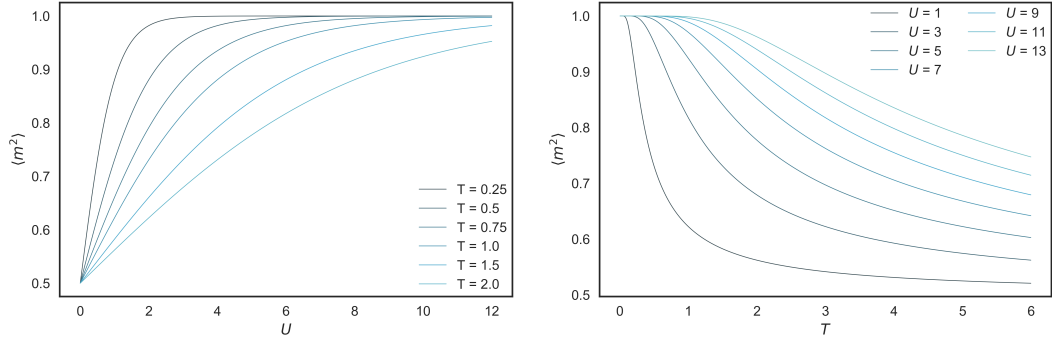


Figure 2.4: Magnetization as a function of the on-site interaction $\langle m^2 \rangle(U)$ (left), and vice-versa (right), in the single site Hubbard model for varying temperature T . Local moments are favored by the on-site interaction, and are more likely to develop at lower temperatures, when thermal fluctuations are smaller. Here we consider half filling: $\mu = 0$.

In Figs.(2.3,2.4), we respectively show how $\langle m^2 \rangle$ varies with T for different values of the chemical potential, and how $\langle m^2 \rangle$ varies as a function of U for different temperatures, and vice-versa. At low temperature or for large on-site interaction, local moments tend to develop, which leads to magnetic ordering: $\langle m^2 \rangle \rightarrow 1$ (in the half-filled case). Since the double occupancy is zero in this case, if we do not consider thermal fluctuations, the magnetization corresponds to the spin of the electron occupying the site.

In Fig.(2.4), we see thermal fluctuations destroying magnetic ordering. As what happens for the Mott plateau, quantum fluctuations (i.e. introducing a hopping term in the Hamiltonian) change the behavior of the magnetization, and perfect moments ($\langle m^2 \rangle = 1$) do not form anymore at zero temperature for finite on-site interaction.

2.3.2 The non-interacting ($\frac{U}{t} = 0$) limit

In the $\frac{U}{t} = 0$ limit, the spin sectors become independent (since the opposite spin electrons do not interact via the on-site term) and they may be considered separately. Thus, we omit the spin indexes of the operators in the Hamiltonian:

$$\mathcal{H} = -t \sum_{\langle i,j \rangle} \left(c_i^\dagger c_j + c_j^\dagger c_i \right) - \mu \sum_i n_i = \mathbf{c}^\dagger \left(-t\mathbf{K} - \mu\mathbf{I} \right) \mathbf{c}, \quad (2.27)$$

where we casted the Hamiltonian as a bilinear form, and defined $\mathbf{c} = \begin{bmatrix} c_1 & c_2 & \dots & c_N \end{bmatrix}^T$, $\mathbf{c}^\dagger = \begin{bmatrix} c_1^\dagger & c_2^\dagger & \dots & c_N^\dagger \end{bmatrix}$, and where \mathbf{I} is the identity matrix. We also defined a matrix of zeros and ones specifying the hopping geometry, \mathbf{K} . The elements of the hopping matrix are simply defined by the indicator function: $K_{ij} = \mathbb{1}_{j(i)}(i)$, where $j(i)$ is the set of neighbors j of site i . When writing down \mathbf{K} , we must specify the boundary conditions. Periodic Boundary Conditions (PBCs) preserve a system's translational invariance and are advantageous because they reduce finite size effects. An example of a quantity which is measured more accurately is energy. In the thermodynamic limit, $N \rightarrow \infty$, the measured energy differs from the actual value by a correction of order $\mathcal{O}(\frac{1}{N^2})$ with PBCs, while for Open Boundary Conditions (OBCs), the correction is of order $\mathcal{O}(\frac{1}{N})$ [58]. Additionally, PBCs have the property of giving site independent observables. For example, the electron density per site does not vary with the distance to the edges of the lattice with PBCs, but it does when we use OBCs.

For concreteness, let us consider a rectangular two-dimensional lattice with $N_x \times N_y$ sites. Then, we have $\dim(\mathbf{K}) = N_x N_y \times N_x N_y$, and

$$\mathbf{K} = \mathbf{I}_y \otimes \mathbf{K}_x + \mathbf{I}_x \otimes \mathbf{K}_y, \quad (2.28)$$

where $\mathbf{I}_{x,y}$ are identity matrices of dimension $N_{x,y} \times N_{x,y}$, respectively, and $\mathbf{K}_{x,y}$ are the hopping matrices in the x and y -directions. For lattices in 1D or 2D, it is possible to find an exact eigendecomposition

$$\mathbf{K} = \mathbf{F}^T \boldsymbol{\Lambda} \mathbf{F} \quad \text{with} \quad \mathbf{F}^T \mathbf{F} = \mathbf{I}, \quad (2.29)$$

where $\boldsymbol{\Lambda} = \text{diag}(\lambda_{\mathbf{k}})$ is a diagonal matrix of eigenvalues of \mathbf{K} . The Hamiltonian is diagonalized:

$$\mathcal{H} = \tilde{\mathbf{c}}^\dagger \left(-t\mathbf{K} - \mu\mathbf{I} \right) \tilde{\mathbf{c}} = \sum_{\mathbf{k}} \varepsilon_{\mathbf{k}} \tilde{n}_{\mathbf{k}}, \quad (2.30)$$

where $\tilde{\mathbf{c}} = \mathbf{F}\mathbf{c}$ and $\tilde{\mathbf{c}}^\dagger = (\mathbf{F}\mathbf{c})^\dagger$, and $\varepsilon_{\mathbf{k}} = -t\lambda_{\mathbf{k}} - \mu$, $\tilde{n}_{\mathbf{k}} = \tilde{c}_{\mathbf{k}}^\dagger \tilde{c}_{\mathbf{k}}$.

This is equivalent to performing a canonical transformation on the annihilation (creation) operators, that preserves not their Poisson brackets, as in classical mechanics, but their anti-commutators. Finding the eigendecomposition is equivalent to changing to Fourier space:

$$\tilde{c}_{\mathbf{k}}^\dagger = \frac{1}{\sqrt{N}} \sum_j e^{i\mathbf{k} \cdot \mathbf{R}_j} c_j^\dagger, \quad (2.31)$$

a transformation which indeed preserves the anti-commutation relations, and the total number operator, i.e., $n = \sum_j n_j = \tilde{n} = \sum_{\mathbf{k}} n_{\mathbf{k}}$. The $\tilde{c}_{\mathbf{k}}$ -operators are equally valid electron creation/annihilation operators, obeying the same anticommutation relations as the original operators c_i , and the total number operator is unchanged under our transformation. However, while the original operators create/annihilate particles at

specific (spatial) sites, the new ones create/annihilate particles with momentum \mathbf{k} . Both sets of operators describe the same physics. Why can't this procedure be applied to the interacting case? The interaction term in the Hubbard model takes on a fairly complex form in momentum space so it is not possible to apply a similar transformation to diagonalize it.

Now, it turns out that it is easy to evaluate the partition function for quadratic Hamiltonians, once we have diagonalized them. If $\mathcal{H} = \mathbf{c}^\dagger \mathbf{H} \mathbf{c}$, where \mathbf{H} is a $N \times N$ Hermitian matrix, then we have that

$$\text{Tr}[e^{-\beta \mathcal{H}}] = \prod_{i=1}^N (1 + e^{-\beta \lambda_i}), \quad (2.32)$$

where λ_i are the eigenvalues of \mathbf{H} . We present a proof of this result in appendix A. It suggests that if we are able to devise some approximation to transform the quartic term of the interacting Hubbard model in a quadratic form, then we can solve it. While this idea is essentially correct, the procedure is not straightforward. We explore it in the next chapter to derive the simulation method that is at the basis of this work. To complete the solution of the non-interacting case we apply the result of equation (2.32) to compute the partition function corresponding to the quadratic Hamiltonian defined in equation (2.30):

$$Z = \prod_{\mathbf{k}} (1 + e^{-\beta(\varepsilon_{\mathbf{k}} - \mu)}), \quad (2.33)$$

where $\varepsilon_{\mathbf{k}}$ is just the dispersion relation for a tight binding model, a standard result. A related quantity is the density of states, counting the number of states with a given energy. For a single spin species:

$$N(E) = \frac{1}{N} \sum_{\mathbf{k}} \delta_{E, \varepsilon_{\mathbf{k}}} \rightarrow \frac{1}{(2\pi)^d} \int d\mathbf{k} \delta(E - \varepsilon_{\mathbf{k}}) \text{ when } N \rightarrow \infty. \quad (2.34)$$

In 1D, we have $\varepsilon_k = -2t \cos k$, which gives $N(E) = (\pi\sqrt{4t^2 - E^2})^{-1}$ (see appendix A).

Now that we have found a closed form solution for Z , it is again possible to find closed form expressions for observables of interest as well, namely:

1. The density, or average occupation of each site, ρ ,

$$\rho = \langle n \rangle = \langle \tilde{n} \rangle = \frac{1}{N} \sum_{\mathbf{k}} \langle \tilde{n}_{\mathbf{k}} \rangle = \frac{1}{N} \sum_{\mathbf{k}} \frac{1}{1 + e^{\beta(\varepsilon_{\mathbf{k}} - \mu)}} = \frac{1}{N} \sum_{\mathbf{k}} f(\mathbf{k}), \quad (2.35)$$

where $f(\mathbf{k}) = (1 + e^{\beta(\varepsilon_{\mathbf{k}} - \mu)})^{-1}$ is the Fermi-Dirac distribution (at half filling: $\mu = 0$).

2. The energy $E = \langle \mathcal{H} \rangle$,

$$E = \frac{1}{N} \sum_{\mathbf{k}} \frac{\varepsilon_{\mathbf{k}} - \mu}{1 + e^{\beta(\varepsilon_{\mathbf{k}} - \mu)}} = \sum_{\mathbf{k}} (\varepsilon_{\mathbf{k}} - \mu) f(\mathbf{k}). \quad (2.36)$$

3. The equal-time Green's function, which will be introduced later, in section 2.5, and plays a key role in computing other quantities, such as correlation functions,

$$G_{\mathbf{l}\mathbf{j}} = \langle c_{\mathbf{l}} c_{\mathbf{j}}^\dagger \rangle = \frac{1}{N} \sum_{\mathbf{k}} e^{i\mathbf{k} \cdot (\mathbf{l} - \mathbf{j})} (1 - f(\mathbf{k})). \quad (2.37)$$

Note that the Green's function, like the Hamiltonian, is translationally invariant: $G_{\mathbf{l}\mathbf{j}} = G_{\mathbf{l}-\mathbf{j}}$. If we use PBCs, no site is singled out, they are all equivalent and this behavior of the Green's function should become apparent in our simulations.

The properties of a fermionic system are dominated by particles near the Fermi surface. On the square lattice, a unique feature called perfect nesting appears. For example, in 2D, the wavevector⁶ $\mathbf{k} = (\pi, \pi)$ connects symmetric regions of the Fermi surface. This suggests that this wavevector could have a crucial role in the description of the model in the square lattice. Indeed, as we will see, a large magnetic structure factor at $\mathbf{k} = (\pi, \pi)$ signals antiferromagnetic order. This is a feature of the Hubbard model at half filling down to $U = 0$ on the square lattice. A similar effect happens in 1D, at $k = \pi$.

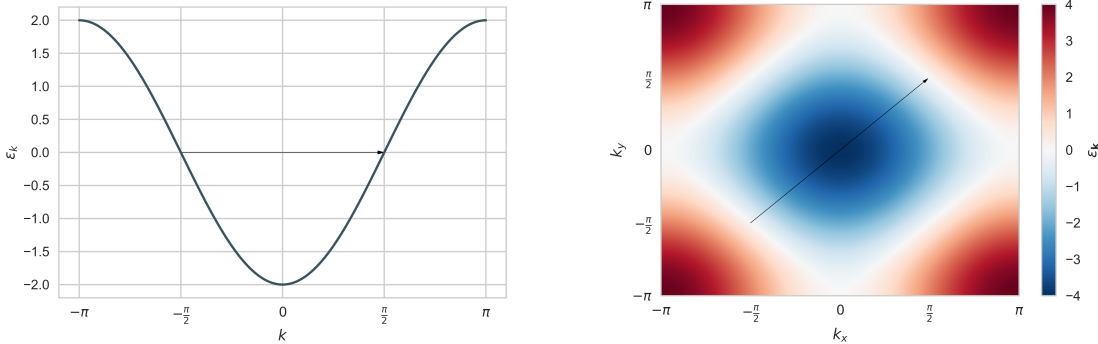


Figure 2.5: Dispersion relations for the 1D chain and the square lattice in the non-interacting case. For the square lattice, the surfaces separating the different colors are Fermi surfaces for different fillings of the lattice. In particular, for half filling ($\rho = 1, \mu = 0$), we obtain the rotated square in the white region.

From our analysis, we draw an important conclusion: that solving the single-particle problem, that is, obtaining $\varepsilon_{\mathbf{k}}$, gives us all the information we need about all particle sectors (any number of particles, which is controlled via the chemical potential). When the on-site interaction is “turned off”, the fermions simply occupy the one-particle states according to Pauli’s exclusion principle. The single-particle sector allows us to extrapolate to obtain the behavior of a system for any number of particles simply because $U = 0$; even if the hoppings were not uniform, this would hold. The hoppings need not even be only between nearest neighbors, and in general we could even consider a chemical potential varying from site to site. All we require is that the Hamiltonian is a quadratic form of the fermion operators.

2.4 Effective $\frac{U}{t} \gg 1$ Heisenberg Model

In appendix A, we argue that Mott insulators allow low energy magnetic excitations (spin flips) without incurring into any energy cost whatsoever. Their insulating phase corresponds to a configuration where each atom has an odd number of electrons, let’s say one. This electron may have its spin up or down. In the purely atomic limit $\frac{U}{t} \rightarrow \infty$, the atoms are infinitely far, and the excitation spectrum is very simple. The ground state is highly degenerate: every configuration with one electron per site is a ground state. As a matter of fact, the ground state is 2^N -fold degenerate. The first excited state corresponds to configurations with a hole and a doubly occupied site. Let us set the energy of the ground state to zero in our conventions. The energy of these configurations is then U , and there are $N(N - 1)2^{N-2}$ of them. This process of generating higher energy excitations may be continued. When the atoms are brought together, the first effect is the lifting of the degeneracy of the ground state, i.e. the splitting of the subspace of energy $E = 0$. The effective Hamiltonian describing the lifting of the degeneracy of the

⁶We take unit lattice constant, $a = 1$ throughout.

lowest energy band is obtained by applying degenerate perturbation theory [81] to the kinetic term of the Hubbard Hamiltonian⁷ $\mathcal{H}_0 = -t \sum_{\langle i,j \rangle, \sigma} (c_{i\sigma}^\dagger c_{j\sigma} + c_{j\sigma}^\dagger c_{i\sigma})$.

2.4.1 Two-site calculation

The effect of the hopping term is best understood in a minimal two-site example. There are four one-particle quantum states, represented by the action of the operators $c_{1,\uparrow}^\dagger, c_{1,\downarrow}^\dagger, c_{2,\uparrow}^\dagger, c_{2,\downarrow}^\dagger$ on the vacuum state. There are six two-particle states in the Fock space represented by $|n_{1\uparrow} n_{1\downarrow} n_{2\uparrow} n_{2\downarrow}\rangle$:

$$\begin{aligned} |1\rangle &\equiv |1,0,1,0\rangle = c_{1\uparrow}^\dagger c_{2\uparrow}^\dagger |0\rangle & |2\rangle &\equiv |0,1,0,1\rangle = c_{1\downarrow}^\dagger c_{2\downarrow}^\dagger |0\rangle & |3\rangle &\equiv |1,0,0,1\rangle = c_{1\uparrow}^\dagger c_{2\downarrow}^\dagger |0\rangle \\ |4\rangle &\equiv |0,1,1,0\rangle = c_{1\downarrow}^\dagger c_{2\uparrow}^\dagger |0\rangle & |5\rangle &\equiv |1,1,0,0\rangle = c_{1\uparrow}^\dagger c_{1\downarrow}^\dagger |0\rangle & |6\rangle &\equiv |0,0,1,1\rangle = c_{2\uparrow}^\dagger c_{2\downarrow}^\dagger |0\rangle \end{aligned} \quad (2.38)$$

The two-site Hamiltonian $\mathcal{H}_2 = -t(c_{1\uparrow}^\dagger c_{2\uparrow} + c_{2\uparrow}^\dagger c_{1\uparrow} + c_{1\downarrow}^\dagger c_{2\downarrow} + c_{2\downarrow}^\dagger c_{1\downarrow}) + U(n_{1\uparrow} n_{1\downarrow} + n_{2\uparrow} n_{2\downarrow})$ acts on the states of the Fock space as follows

$$\begin{aligned} \mathcal{H}_2 |1\rangle &= 0 & \mathcal{H}_2 |3\rangle &= -t(c_{2\uparrow}^\dagger c_{1\uparrow} + c_{1\downarrow}^\dagger c_{2\downarrow}) c_{1\uparrow}^\dagger c_{2\downarrow}^\dagger |0\rangle = -t(|5\rangle + |6\rangle) \\ \mathcal{H}_2 |2\rangle &= 0 & \mathcal{H}_2 |4\rangle &= -t(c_{1\uparrow}^\dagger c_{2\uparrow} + c_{2\downarrow}^\dagger c_{1\downarrow}) c_{1\downarrow}^\dagger c_{2\uparrow}^\dagger |0\rangle = t(|5\rangle + |6\rangle) \\ \mathcal{H}_2 |5\rangle &= \left[-t(c_{2\uparrow}^\dagger c_{1\uparrow} + c_{2\downarrow}^\dagger c_{1\downarrow}) + Un_{1\uparrow} n_{1\downarrow} \right] c_{1\uparrow}^\dagger c_{1\downarrow}^\dagger |0\rangle = U|5\rangle - t(|3\rangle - |4\rangle) \\ \mathcal{H}_2 |6\rangle &= \left[-t(c_{1\uparrow}^\dagger c_{2\uparrow} + c_{1\downarrow}^\dagger c_{2\downarrow}) + Un_{2\uparrow} n_{2\downarrow} \right] c_{2\uparrow}^\dagger c_{2\downarrow}^\dagger |0\rangle = U|6\rangle - t(|3\rangle - |4\rangle) \end{aligned} \quad (2.39)$$

When we act on the first two states we obtain 0 because every term of the Hamiltonian gives a term $(c^\dagger)^2$, which is 0 due to Pauli's exclusion principle. The minus signs that appear on the hopping terms stem from the fermion anticommutation relations.

Let us now diagonalize the Hamiltonian in the subspace spanned by $\{|3\rangle, |4\rangle, |5\rangle, |6\rangle\}$. If we add states $|3\rangle$ and $|4\rangle$, we get 0 when acting with the Hamiltonian. $\mathcal{H}_2(|3\rangle + |4\rangle) = 0$. On the other hand, if we subtract $|5\rangle$ and $|6\rangle$, we obtain $\mathcal{H}_2(|5\rangle - |6\rangle) = U(|5\rangle - |6\rangle)$. We have found two more eigenvalues (the first two were trivially found to be zero). The others are found by subtracting $|3\rangle$ and $|4\rangle$ and adding $|5\rangle$ and $|6\rangle$: $\mathcal{H}_2(|3\rangle + |4\rangle) = -2t(|5\rangle + |6\rangle)$ $\mathcal{H}_2(|5\rangle - |6\rangle) = -2t(|3\rangle - |4\rangle) + U(|5\rangle + |6\rangle)$. The characteristic equation allowing us to find the rest of the eigenvalues in the rotated subspace spanned by $\{|3\rangle \pm |4\rangle, |5\rangle \pm |6\rangle\}$ is $E(E - U) - 4t^2 = 0 \iff E_\pm = \frac{1}{2}(U \pm \sqrt{U^2 + 16t^2})$. Taylor expanding the square root up to second order, we obtain $E_- = -\frac{4t^2}{U}$ $E_+ = U + \frac{4t^2}{U}$. Thus, we have obtained the complete energy spectrum. The ground state is a non-degenerate state of energy $-\frac{4t^2}{U}$, while the first excited state is a 3-fold degenerate state with energy 0. The two other excited states have energies of the order of U , the first one being exactly U and the second $U + \frac{4t^2}{U}$. There are four states for which the energy would be 0 if the hopping term vanished, corresponding to the four states with one electron per site. The effect of the hopping term is to lift the degeneracy by splitting the 4-fold degenerate zero energy state into a singlet of energy $-\frac{4t^2}{U}$ and a triplet of energy 0. This is what we obtain by minimizing a Heisenberg Hamiltonian of the form $\mathcal{H}_{\text{Heis}} = \frac{4t^2}{U}(\mathbf{S}_1 \cdot \mathbf{S}_2 - \frac{1}{4})$ for two spins- $\frac{1}{2}$. However, it turns out that this result is yet more general. For an arbitrary number of sites, this is the form of the effective Hamiltonian at second order (see appendix A for details).

It is easy to extend this analysis beyond half filling to compare it to our solution for the single site case.

⁷An alternative method would be to use a canonical transformation technique.

The latter gave us some insight into how the on-site interaction gives rise to magnetic ordering, and about the development of the Mott plateau. Adding in the hopping we can understand the interplay between kinetic and potential energy, and the magnetic correlations between sites. In fact, we will outline the simplest nontrivial method to solve Hubbard-type Hamiltonians: *exact diagonalization*, which is a competitor of QMC, but is limited to very small system sizes. Since the two-site Hamiltonian commutes with n_σ , it conserves the number of up and down fermions, and the $2^4 = 16$ states can be divided into 9 sectors of varying dimension d : $(n_\uparrow, n_\downarrow, d) = (0, 0, 1), (1, 0, 2), (2, 0, 1), (0, 1, 2), (1, 1, 4), (2, 1, 2), (0, 2, 1), (1, 2, 2), (2, 2, 1)$. There are four sectors of dimension 1: the empty and the fully filled lattices, and the lattices with two like-spin fermions. All these sectors have zero kinetic energy: in the first, there are no electrons present to hop, and in the second Pauli's exclusion principle blocks hopping. The sectors with $n_\sigma = 2$ have energy $-U/2$, while the ones with $n_\uparrow = n_\downarrow$ have energy $U/2$.

The four sectors of dimension 2 are also simple. One and three particle sectors must have the same energy spectrum due to Particle-hole symmetry (PHS). They have eigenenergies $\pm t$. A single fermion can hop between sites, while out of the three fermions, the two with like-spin are blocked and can't hop to the same site, leaving a single fermion free to hop. We have already solved the most complicated $n_\uparrow = n_\downarrow = 1$ sector, while tackling the half filled case. By determining the complete spectrum of the two-site Hubbard model, we demonstrated that the eigenenergies in the $U \neq 0$ case can't be deduced solely from considering the single-particle sector. The low temperature properties of the model are determined by the lowest energy eigenvalues, which all seem to fall in the half filled sectors. Subtracting $U/2$ to the energies we obtained in the half filled sectors is equivalent to considering the PHS form of the Hamiltonian. At half filling, we end up with four states with energies around $-U/2$ (the so called lower Hubbard band), and two states with energies around $U/2$ (upper band). The lower band controls the low temperature physics. In the next section, we show that the Heisenberg Hamiltonian that seems to govern the behavior of the electrons in the lower Hubbard band is in fact the effective $U/t \gg 1$ model.

2.4.2 Degenerate perturbation theory

To first order in \mathcal{H} , the matrix elements of its effective Hamiltonian coincide in the ground state subspace, by definition: $\langle m | \mathcal{H}_{\text{eff}} | n \rangle = \langle m | \mathcal{H}_0 | n \rangle$, where $|m\rangle$, and $|n\rangle$ belong to the ground state subspace. Since we are considering the system to be at half filling in our calculations, $|m\rangle$, and $|n\rangle$ must have one electron per site. The hopping Hamiltonian \mathcal{H}_0 makes an electron hop, leaving its previous site empty, and the site it hops to doubly occupied. This implies that to first order all the matrix elements are 0.

To second order, the matrix elements of the effective Hamiltonian are

$$\langle m | \mathcal{H}_{\text{eff}} | n \rangle = \sum_{|k\rangle} \frac{\langle m | \mathcal{H}_0 | k \rangle \langle k | \mathcal{H}_0 | n \rangle}{E_0 - E_k} = -\frac{1}{U} \sum_{|k\rangle} \langle m | \mathcal{H}_0 | k \rangle \langle k | \mathcal{H}_0 | n \rangle, \quad (2.40)$$

where $|k\rangle$ are the states that are not in the ground state subspace. In the second equality we simply noted that \mathcal{H}_0 creates a doubly occupied site. The energy cost of creating a doubly occupied site is U .

In appendix A, we find the Heisenberg model as the effective Hamiltonian in this $\frac{U}{t} \gg 1$ limit. This

is consistent since the Heisenberg model couples spins on different sites, thus it is an *atomic* model.

$$\mathcal{H}_{\text{eff}} = J \sum_{\langle i,j \rangle} \mathbf{S}_i \cdot \mathbf{S}_j, \quad (2.41)$$

with $J = 4t^2/U$. Since $J > 0$, the model favors configurations with antiparallel adjacent spins.

There is an intuitive physical picture for this result: if two electrons on neighboring sites have parallel spins, none of the two can hop to the neighboring site due to Pauli's exclusion principle. If adjacent sites have antiparallel spins, however, it is possible for any of the two electrons to hop to the neighboring site, and an exchange process allows the system to lower its energy. First, a fermion hops to a neighboring site already occupied with an opposite spin fermion. The intermediate state has a higher energy by U . Then, the fermion hops back to its original site, in a process that decreases the energy by $E^{(2)} \propto -t^2/U$.

2.5 Green's functions

Green's functions are the core of the first perturbative, diagrammatic approaches to the Hubbard model. They are very useful in reducing the enormous amount of variables that come into play in correlated systems to a manageable number. Here we try do give some intuition about how they work since they are the central quantity in the QMC method we will use. Considering the imaginary-time variable of the previous chapter $\tau = it$, for $\tau > 0$, the Green's function is defined as

$$G_{ij}(\tau, 0) = \left\langle c_i(\tau) c_j^\dagger(0) \right\rangle, \text{ with } c_i(\tau) = e^{\mathcal{H}\tau} c_i(0) e^{-\mathcal{H}\tau} \quad (2.42)$$

2.5.1 Single site case

The Hubbard Hamiltonian does not distinguish between spin-up and spin-down sectors. Thus, without loss of generality, let us consider the spin-up sector, and compute $G_\uparrow(\tau, 0) = \left\langle c_\uparrow(\tau) c_\uparrow^\dagger(0) \right\rangle$. Only the states $|n_\uparrow n_\downarrow\rangle = |00\rangle, |01\rangle$ contribute to the expectation due to the creation operator on the right, which gives 0, unless there is no spin up electron already in the state it acts upon.

$$\begin{aligned} c_\uparrow(\tau) c_\uparrow^\dagger(0) |00\rangle &= e^{\mathcal{H}\tau} c_\uparrow(0) e^{-\mathcal{H}\tau} c_\uparrow^\dagger(0) |00\rangle = e^{\mathcal{H}\tau} c_\uparrow(0) e^{-\mathcal{H}\tau} |01\rangle \\ &= e^{\mathcal{H}\tau} c_\uparrow(0) e^{U\tau/4+\mu\tau} |10\rangle = e^{\mathcal{H}\tau} e^{U\tau/4+\mu\tau} |00\rangle = e^{U\tau/2+\mu\tau} |00\rangle \\ c_\uparrow(\tau) c_\uparrow^\dagger(0) |01\rangle &= e^{\mathcal{H}\tau} c_\uparrow(0) e^{-\mathcal{H}\tau} c_\uparrow^\dagger(0) |01\rangle = e^{\mathcal{H}\tau} c_\uparrow(0) e^{-\mathcal{H}\tau} |11\rangle \\ &= e^{\mathcal{H}\tau} c_\uparrow(0) e^{-U\tau/4+2\mu\tau} |11\rangle = e^{\mathcal{H}\tau} e^{-U\tau/4+2\mu\tau} |01\rangle = e^{U\tau/2+\mu\tau} |01\rangle \end{aligned} \quad (2.43)$$

Using the expression for the partition function that we obtained in equation (2.20), we arrive at

$$G_\uparrow(\tau, 0) = \frac{e^{\tau(U/2+\mu)} e^{-\beta U/4} + e^{-\tau(U/2-\mu)} e^{\beta(U/4+\mu)}}{e^{-\beta U/4}(1 + 2e^{\beta(U/2+\mu)} + e^{2\beta\mu})}, \quad (2.44)$$

which, at half filling becomes

$$G_\uparrow(\tau, 0) = \frac{e^{\tau U/2} e^{-\beta U/4} + e^{-\tau U/2} e^{\beta U/4}}{2e^{-\beta U/4} + 2e^{\beta U/4}}, \quad (2.45)$$

There is a well known relation between the Green's function and the spectral density $A(\omega)$, which may be regarded as a local density of states:

$$G(\tau, 0) = \int_{-\infty}^{+\infty} A(\omega) \frac{e^{-\omega\tau}}{e^{-\beta\omega} + 1} d\omega, \quad (2.46)$$

If we replace the following expression for the spectral density in equation (2.46), we recover the result for the half filled case: $A(\omega) = \frac{1}{2} \left(\delta(\omega - \frac{U}{2}) + \delta(\omega + \frac{U}{2}) \right)$. We could do a similar calculation for $\mu \neq 0$ by changing the spectral density adequately, but the algebra is slightly more cumbersome, and the result does not bring additional insight. The spectral density consists of two delta functions separated by U , which is reminiscent of our result for the Mott insulating gap. In the same way that the gap softens (eventually disappearing) when we introduce hopping, the spectral function for the full Hubbard Hamiltonian changes accordingly, reflecting the same information about the system as the Green's function, only encoded in a different manner. In QMC, we can access $G(\tau, 0)$ and deduce the properties of the system from it.

2.5.2 Non-interacting case

In this limit, we can compute $G_{ij}(\tau, 0)$ analytically by going to momentum space.

$$c_{\mathbf{k}}(\tau) = e^{\mathcal{H}\tau} c_{\mathbf{k}}(0) e^{-\mathcal{H}\tau} = e^{-\varepsilon_{\mathbf{k}}\tau} c_{\mathbf{k}}(0) \quad (2.47)$$

This equation can be verified by acting with the left hand side and with right hand side on the states $|0\rangle$ and $|1\rangle$, and noting that the result is the same. Alternatively, one can use the equation of motion $\partial_{\tau} \hat{A}(\tau) = [\mathcal{H}, \hat{A}(\tau)]$. To generalize the result of equation (2.37) for the *equal-time* Green's function to *unequal-time* we transform the fermionic operators in G to momentum space, and use $\langle c_{\mathbf{k}} c_{\mathbf{k}}^\dagger \rangle = 1 - f(\mathbf{k})$:

$$G_{ij}(\tau, 0) = \frac{1}{N} \sum_{\mathbf{k}} e^{i\mathbf{k} \cdot (\mathbf{R}_i - \mathbf{R}_j)} (1 - f_{\mathbf{k}}) e^{-\varepsilon_{\mathbf{k}}\tau}, \quad (2.48)$$

which is translationally invariant corresponding to the symmetry of the Hamiltonian.

We can generalize our definition of the Green's function by using the time-ordering operator \mathcal{T} :

$$G_{\mathbf{k}}(\tau, 0) = -\langle \mathcal{T} c_{\mathbf{k}}(\tau) c_{\mathbf{k}}^\dagger(0) \rangle, \text{ where } \mathcal{T} c_{\mathbf{k}}(\tau) c_{\mathbf{k}}^\dagger(0) = \begin{cases} c_{\mathbf{k}}(\tau) c_{\mathbf{k}}^\dagger(0), & \tau > 0 \\ -c_{\mathbf{k}}^\dagger(0) c_{\mathbf{k}}(\tau), & \tau < 0 \end{cases} \quad (2.49)$$

An important property follows immediately from this definition: $G(\tau + \beta, 0) = -G(\tau, 0)$ for $-\beta < \tau < 0$. The imaginary-time anti-periodicity constraint implies that the frequencies that appear when we Fourier transform are the so called (fermionic) Matsubara frequencies $\omega_n = \frac{(2n+1)\pi}{\beta}$.⁸

$$G(i\omega_n) = \int_0^{\beta} \frac{d\tau}{\beta} G(\tau, 0) e^{i\omega_n \tau} \quad G(\tau, 0) = \sum_n G(i\omega_n) e^{-i\omega_n \tau} \quad (2.50)$$

In momentum space, and imaginary time, the Green's function then becomes

$$G_{\mathbf{k}}(\tau, 0) = \begin{cases} -e^{-\varepsilon_{\mathbf{k}}} (1 - f_{\mathbf{k}}), & 0 < \tau < \beta \\ e^{-\varepsilon_{\mathbf{k}}} f_{\mathbf{k}}, & -\beta < \tau < 0, \end{cases} \quad \text{or} \quad G_{\mathbf{k}}(i\omega_n) = \frac{1}{i\omega_n - \varepsilon_{\mathbf{k}}} \quad (2.51)$$

in frequency space. This result may also be obtained by taking the partial derivative of the time-ordered Green's function written in the form $G_{\mathbf{k}}(\tau, 0) = \langle c_{\mathbf{k}}(\tau) c_{\mathbf{k}}^\dagger(0) \rangle \theta(\tau) - \langle c_{\mathbf{k}}(0) c_{\mathbf{k}}^\dagger(\tau) \rangle \theta(-\tau)$ and Fourier transforming both sides to solve for $G(i\omega_n)$. Taking a time derivative of G implies computing commutators of \mathcal{H} with the fermionic operators. The equation closes for quadratic Hamiltonians, which we, of course, know to be soluble.

As was emphasized in section 2.3, the key concept that will be used in deriving the auxiliary field method is a mapping to a single-particle problem defined in terms of a quadratic Hamiltonian. Thus,

⁸Analogously, for bosons, imaginary-time periodicity implies that $\omega_n = 2n\pi/\beta$

Wick's theorem may be applied to simplify products of fermionic operators. In [82], the theorem is rigorously proven for both the ground state and the finite temperature cases. Later, we will apply it to our case of interest, and leave a more detailed discussion following [83] to appendix A.

In general, Green's functions are a much more complicated object than in the simple examples treated so far. Fortunately, our mapping to a single particle problem allows us to express many-particle Green's functions as a function of single particle Green's functions sampled over the auxiliary field's configurations. The latter will turn out to play a crucial role in the sampling process itself. Moreover, any observable may be written in terms of these single particle Green's functions (for a given auxiliary field configuration) by using Wick's theorem. Thus, measuring any observable requires simply gathering the necessary elements of the single particle Green's function, since the latter must be computed already to sample the auxiliary field's configurations. This observation stems solely from the fact that the electrons are decoupled once the auxiliary field is introduced, reducing the interacting problem to a single particle problem.

2.6 Magnetism and mean field theory

In this section we will build a picture of magnetism in the Hubbard model in increasing level of sophistication. As our degenerate perturbation theory calculation of section (2.4) showed, the on-site interaction favors opposite spin neighboring fermions through an Heisenberg type interaction. A different approach leads to the Stoner criterion for ferromagnetism. The argument is based on creating an imbalance between the numbers of spin-up and spin-down fermions, and analyzing the interplay between the resulting increase in kinetic energy, and decrease in potential energy. Finally, we formulate the Hubbard model in the mean field approximation, and discuss how it relates to the non-interacting case.

2.6.1 Stoner criterion for ferromagnetism

Pauli's exclusion principle gives a prescription on how to fill fermionic energy levels so as to yield the lowest possible total energy. Start from the lowest level, and start filling each level of higher energy consecutively with two electrons, one of each spin, until reaching the Fermi energy. This procedure requires the number of spin-up and spin-down electrons to be the same. Otherwise, there is an energy cost, since we are obliged to fill higher energy levels with the excess electrons. An unequal number of spin-up and spin-down electrons also decreases the potential energy. An extreme example is a completely polarized lattice. In that case, the potential energy is zero. More generally, partial spin polarization makes double occupation unlikely, lowering the potential energy.

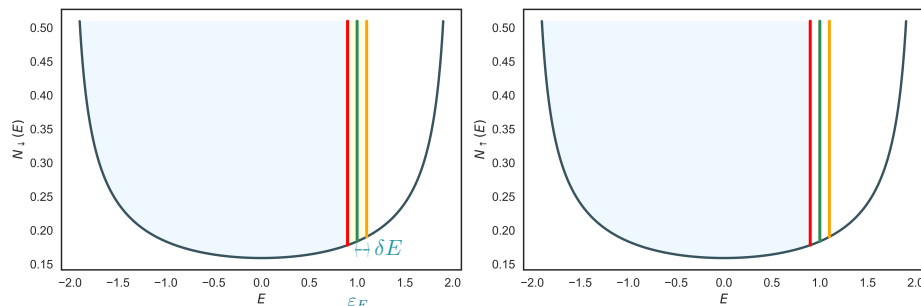


Figure 2.6: Density of states of the 1D tight-binding model. Here we represent a polarization of the spins, which leads to an increase in kinetic energy, since the imbalance of spins forces higher energy levels to be filled.

A system with density of states $N(E)$ has equal densities of spin-up and spin-down electrons, n , filling the energy levels up to the Fermi energy, ε_F . When we reduce, say the spin-up electron density by δn , the potential energy is lowered by $\delta P = U(n + \delta n)(n - \delta n) - Un^2 = -U(\delta n)^2$.

The extra density of electrons δn that is added to the down sector will occupy levels with energy greater than ε_F , so that $\delta n = N(\varepsilon_F)\delta E$. Some spin-up levels below ε_F that used to be occupied are now empty, which makes δn fermions per site increase their energy by δE , leading to a change in kinetic energy $\delta K = \delta n\delta E = \frac{(\delta n)^2}{N(\varepsilon_F)}$. The global change in energy is

$$\delta E = \delta P + \delta K = \left(-U + \frac{1}{N(\varepsilon_F)} \right) (\delta n)^2 = \left(-UN(\varepsilon_F) + 1 \right) \frac{(\delta n)^2}{N(\varepsilon_F)} \quad (2.52)$$

If $UN(\varepsilon_F) > 1$, then $\delta E < 0$, and the imbalance of spin densities becomes more favorable. Thus, magnetism is favored by a large on-site interaction and a large density of states near the Fermi energy.

2.6.2 Mean field theory of the Hubbard model

We have already encountered an example of a mean field theory when deriving the Hubbard Hamiltonian (see appendix A, where we provide motivation both heuristically and via a more rigorous variational approach). In mean field theory, we give a systematic procedure to derive the most plausible quadratic Hamiltonian (which, as we know by now, is soluble) capturing some of the physics of our system. We do this variationally in appendix A. Here we provide the heuristic explanation. In the case of the Hubbard model, to find the best possible approximation for the quartic term we start by expressing the number operators in terms of an average plus fluctuations: $n = \langle n \rangle + (n - \langle n \rangle) \equiv \langle n \rangle + \delta n$. Then, we make this substitution in the interaction term and neglect the term that is second order in the fluctuations:

$$\begin{aligned} n_\uparrow n_\downarrow &= (\langle n_\uparrow \rangle + \delta n_\uparrow)(\langle n_\downarrow \rangle + \delta n_\downarrow) = \langle n_\uparrow \rangle \langle n_\downarrow \rangle + \langle n_\downarrow \rangle (n_\uparrow - \langle n_\uparrow \rangle) + \langle n_\uparrow \rangle (n_\downarrow - \langle n_\downarrow \rangle) + \mathcal{O}((\delta n)^2) \\ &= n_\uparrow \langle n_\downarrow \rangle + n_\downarrow \langle n_\uparrow \rangle - \langle n_\uparrow \rangle \langle n_\downarrow \rangle, \end{aligned} \quad (2.53)$$

and from equation (2.53), we obtain the quadratic mean field Hamiltonian

$$\mathcal{H}_{\text{MF}} = -t \sum_{\langle i,j \rangle, \sigma} \left(c_{i,\sigma}^\dagger c_{j,\sigma} + c_{j,\sigma}^\dagger c_{i,\sigma} \right) + U \sum_i \left(n_{i,\uparrow} \langle n_{i,\downarrow} \rangle + n_{i,\downarrow} \langle n_{i,\uparrow} \rangle - \langle n_{i,\uparrow} \rangle \langle n_{i,\downarrow} \rangle \right), \quad (2.54)$$

where we consider a “mean field” in the sense that the average density of spin-up electrons interacts with the spin-down electrons and vice-versa. The last term subtracts the overcounted interaction term. To solve \mathcal{H}_{MF} , one merely has to diagonalize the corresponding matrix. In the ferromagnetic case, the average occupation is independent of the specific site, but can vary with the spin species: $n_{i,\uparrow(\downarrow)} = n \pm m$, where m is the magnetization, the order parameter of the transition to a ferromagnetic phase. Similarly, for the AF case on a bipartite lattice, we consider $n_{i,\uparrow(\downarrow)} = n \pm (-1)^i m$, signaling to a staggered potential.

Now we take on a Landau-Ginzburg theory kind of approach. We compute the energy E for fixed n as a function of m , and inspect the system for ferromagnetic ordering: if the minimum lies at $m = 0$, the system is paramagnetic, otherwise it is ferromagnetic. For simplicity, let us now consider the 1D model. Since the average densities are site-independent, we can easily write down the polarized dispersion relations (up to an additive constant), and add these levels up for the various possible fillings of the lattice.

$$\varepsilon_{\uparrow,k} = U(n - m) - 2t \cos k \quad \varepsilon_{\downarrow,k} = U(n + m) - 2t \cos k, \quad (2.55)$$

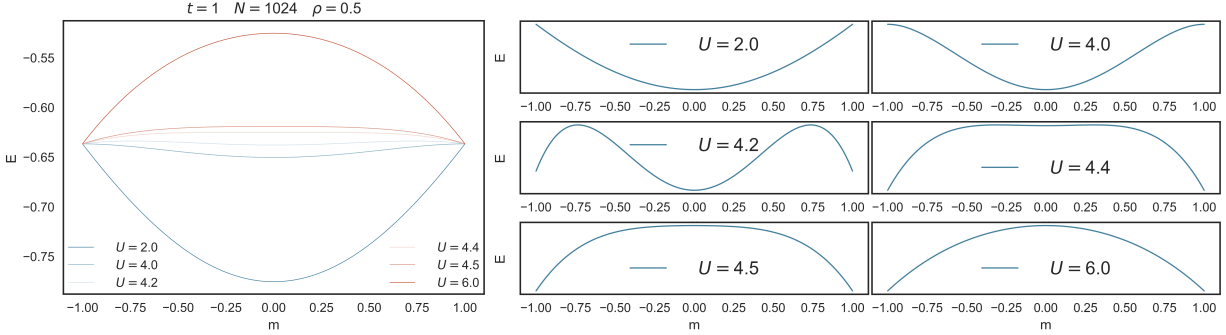


Figure 2.7: Mean field results at quarter filling for a 1024-site chain. U is in units of t . As the on-site interaction is increased, we see a transition from a paramagnetic to a ferromagnetic phase. On the right, we close in on the phase transition: plots of each energy curve separately giving evidence of a phase transition.

The computational procedure to perform mean field computations goes as follows: fix the lattice size N , the total particle number N_p , and the on-site interaction U ; set the possible densities by iterating $N_\uparrow = 0, 1, \dots, N_p/2$, and $N_\downarrow = N_p - N_\uparrow$ (we only need half the values since the values are symmetric under $N_\uparrow \leftrightarrow N_\downarrow$), and setting $n_{\uparrow,\downarrow} = N_{\uparrow,\downarrow}/N$; fill the lowest N_\uparrow , and N_\downarrow energy levels, by looping over the allowed momentum states $k = \frac{2\pi}{N} \{-\frac{N}{2} + 1, -\frac{N}{2}, \dots, \frac{N}{2}\}$, and using Eq.(2.55). Normalize the energy to N and add in the additive constant $-\langle n_\uparrow \rangle \langle n_\downarrow \rangle$. This step is altered for the AF case since we are assuming the up and down densities to be identical over the whole lattice. In such case, we fix $n = N_p/2$ and loop over $m = 1/N, 2/N, \dots$, staying within the first Brillouin zone. Out of the energies computed in this way for varying $N_{\uparrow,\downarrow}$, the lowest gives the magnetization for the chosen values of N_p and U .

Focus on Fig.(2.7). At $U = 2$, the phase is paramagnetic since the energy is minimized at $m = 0$. By $U = 4$, the phase transition is yet to occur, but looking at the energy scale on the left, one sees that the energy of the spin polarized solutions has decreased dramatically. At $U = 4.2$, the large $|m|$ energies have turned down, although $m = 0$ is still the lowest energy solution. At $U = 4.4$, the phase transition occurs, and the solutions with $|m| = 1$ become the lowest energy solutions, signaling the appearance of the ferromagnetic phase.

Are these results consistent with Stoner's criterion: $UN(\varepsilon_F) > 1$? First, we use the density of states obtained in section (2.3) to find a relation between the density ρ and the Fermi energy ε_F :

$$\rho(\varepsilon_F) = 2 \int_{-2t}^{\varepsilon_F} dE N(E) \rightsquigarrow \rho_{1D}(\varepsilon_F) = \frac{2}{\pi} \arccos \left(\frac{-\varepsilon_F}{2t} \right), \quad (2.56)$$

which behaves as expected, i.e. $\rho(-2t) = 0$, $\rho(0) = 1$, $\rho(2t) = 2$. In terms of the electron density:

$$N(\rho) = \frac{1}{2\pi t \sin(\pi\rho/2)}, \quad (2.57)$$

and in particular we can obtain the critical value U_c at which the transition to the ferromagnetic phase takes place. At quarter filling, we have $N(1/2) = 1/\sqrt{2\pi t}$, giving $U_c = \sqrt{2\pi t} \approx 4.44t$, which is about what we obtained at the mean field level⁹.

An example of the success of mean field is the discovery of striped phases of the Hubbard model, which are crucial in cuprate superconductors. Recently, these phases have been probed by the Quantum Monte Carlo (QMC) method we shall use in this thesis [84]. In fact, mean field theory is insightful, but uncontrolled. It tends to overestimate the possibility of ordering since it always predicts a phase

⁹Here, there can be finite size effects due to the finite size of the chain, $N = 1024$.

transition. Even if the transition does occur, generally its details are not perfectly captured (the critical temperature, the critical exponents, ...).

2.6.3 Self-consistent solution in the Grand-canonical ensemble (GCE)

In this section, we solve the mean field Hamiltonian in an iterative, self-consistent manner.

$$\mathcal{H}_{\text{MF}} = \mathcal{H}_{\uparrow} + \mathcal{H}_{\downarrow} + \mathcal{C}, \quad \mathcal{H}_{\sigma} = -t \sum_{\langle i,j \rangle} \left(c_{i,\sigma}^{\dagger} c_{j,\sigma} + c_{j,\sigma}^{\dagger} c_{i,\sigma} \right) + U \sum_i n_{i,\sigma} \langle n_{i,-\sigma} \rangle, \quad \mathcal{C} = -U \sum_i \langle n_{i,\uparrow} \rangle \langle n_{i,\downarrow} \rangle \quad (2.58)$$

We seek the most energetically favorable self-consistent solution iteratively¹⁰: the up and down-spin electron densities are updated successively until convergence occurs.

Since the interacting problem is turned into a single particle problem, the solution basically consists of diagonalizing two $N \times N$ matrices, where N is the size of the system. By varying the $2N$ mean field parameters, which are essentially the average local densities $\langle n_{i,\sigma} \rangle$, we can find the ground state, or other excited states, at the mean field level. The mean field approach has several advantages: the Hilbert space is reduced from exponential to linear in the system size, which allows the study of relatively large systems; we can do the computation in real space; we can arbitrarily change the system geometry (introducing OBCs, defects, nonuniform hoppings); the model is flexible: tight-binding, and interaction terms are easily added to the Hamiltonian. However, $SU(2)$ symmetry is broken, and electron correlations are neglected. Only long range order is captured and its stability is often overestimated. While the mean field solution approaches the exact solution at weak coupling U , it can give only qualitative behavior at best, when U increases significantly.

The iterative method starts with the initialization of the mean field parameters. This initial condition cannot be completely arbitrary because it affects convergence. Typical choices are the random initial condition or the paramagnetic state. Then, we repeat the following steps until convergence.

First, we diagonalize \mathcal{H}_{σ} , obtaining the one-particle spectrum $\varepsilon_{\alpha,\sigma}$ and the corresponding eigenvectors.

$$\mathcal{H}_{\text{MF}} = \sum_{\alpha,\sigma} \varepsilon_{\alpha,\sigma} d_{\alpha,\sigma}^{\dagger} d_{\alpha,\sigma} + \mathcal{C}, \quad d_{\alpha,\sigma} = \sum_i Q_{\alpha i,\sigma}^* c_{i,\sigma} \quad (2.59)$$

Given a number of electrons per unit cell, n_e , compute the chemical potential corresponding to that filling implicitly through $\frac{1}{N} \sum_{\alpha,\sigma} (e^{\beta(\varepsilon_{\alpha,\sigma} - \mu)} + 1)^{-1} = n_e$ (we use the bisection method).

Recompute mean field parameters, and check for convergence: at iteration I , $\langle n_{i,\sigma} \rangle_I \approx \langle n_{i,\sigma} \rangle_{I-1}$.

$$\langle n_{i,\sigma} \rangle = \sum_{\alpha} |Q_{\alpha i,\sigma}|^2 (1 + e^{\beta(\varepsilon_{\alpha,\sigma} - \mu)})^{-1} \quad (2.60)$$

As we explain in appendix A, a self-consistent solution is not necessarily the mean field one, thus one must continually check if the functional F of Eq.(A.43) is being minimized (of, in the case of the GCE, the functional Ω of Eq.(A.52)). Moreover, we must repeat the calculation above several times by varying the initial conditions, and then select the lowest energy solution that minimizes F as the mean field one. This is illustrated in appendix A.

To compare with the results of our QMC simulations, we may compute other observables, such as the spin-spin correlation, by inverting the transformation above: $c_{i,\sigma} = \sum_{\alpha} Q_{\alpha i,\sigma} d_{\alpha,\sigma}$, yielding $\langle c_{i,\sigma}^{\dagger} c_{j,\sigma} \rangle =$

¹⁰One must pay attention so as not to get stuck in metastable states.

$\sum_{\alpha,\beta} Q_{\beta i,\sigma}^* Q_{\alpha j,\sigma} \langle d_{\beta,\sigma}^\dagger d_{\alpha,\sigma} \rangle = \sum_{\alpha} Q_{\alpha i,\sigma}^* Q_{\alpha j,\sigma} f(\varepsilon_{\alpha,\sigma})$, where $f(\varepsilon_{\alpha,\sigma})$ is the Fermi function.

$$\begin{aligned} \langle S_i^z S_j^z \rangle &= \langle (n_{i,\uparrow} - n_{i,\downarrow})(n_{j,\uparrow} - n_{j,\downarrow}) \rangle = \sum_{\sigma} \left(\langle c_{i,\sigma}^\dagger c_{i,\sigma} c_{j,\sigma}^\dagger c_{j,\sigma} \rangle - \langle c_{i,-\sigma}^\dagger c_{i,-\sigma} c_{j,\sigma}^\dagger c_{j,\sigma} \rangle \right) \\ &= \sum_{\sigma} \left(\langle n_{i,\sigma} \rangle \langle n_{j,\sigma} \rangle - \langle n_{i,-\sigma} \rangle \langle n_{j,\sigma} \rangle + \langle c_{i,\sigma}^\dagger c_{j,\sigma} \rangle \langle c_{i,\sigma} c_{j,\sigma}^\dagger \rangle \right), \text{ by Wick's theorem} \\ &= \begin{cases} \sum_{\sigma} (\langle n_{i,\sigma} \rangle \langle n_{j,\sigma} \rangle - \langle n_{i,-\sigma} \rangle \langle n_{j,\sigma} \rangle - \sum_{\alpha,\beta} f(\varepsilon_{\beta,\sigma}) f(\varepsilon_{\alpha,\sigma}) Q_{\alpha i,\sigma}^* Q_{\alpha j,\sigma} Q_{\beta j,\sigma}^* Q_{\beta i,\sigma}) & \text{if } i \neq j \\ \langle n_{i,\uparrow} \rangle + \langle n_{i,\downarrow} \rangle - 2 \langle n_{i,\uparrow} \rangle \langle n_{i,\downarrow} \rangle & \text{if } i = j \end{cases} \end{aligned} \quad (2.61)$$

Now, we discuss how to circumvent the convergence issues that may arise when applying the self-consistent procedure. First, there are many possible initial conditions, most notably: the random one, which is the most unbiased, but may be slow or not converge at all; the paramagnetic state $\langle n_{i,\sigma} \rangle = \text{const.}$, which, when combined with the annealing method we shall describe below, emulates the random initial condition; a specific state, such as the antiferromagnetic one, which is a biased choice, which limits the accessible part of parameter space, and potentially gives a misleading mean field solution, but can have good convergence properties.

In some cases, the symmetry of the system dramatically slows down convergence. By starting the procedure at a higher temperature than the desired one, we can improve convergence. The temperature is then gradually lowered until the desired one is achieved, and this procedure is applied at that temperature. There are a lot of possible annealing schemes, namely keeping β fixed for some iterations and then adjusting it to the desired $\beta = \beta_0$, or smoothly reducing β until it reaches β_0 .

A common convergence issue is the oscillation between two configurations $\langle n_{i,\sigma} \rangle_I \leftrightarrow \langle n_{i,\sigma} \rangle_{I+1}$. This is solved by averaging the values obtained at the current and previous iterations: $\langle n_{i,\sigma} \rangle_{I+1} \leftarrow \frac{1}{2} \langle n_{i,\sigma} \rangle_I + \frac{1}{2} \langle n_{i,\sigma} \rangle_{I+1}$. The weights attributed to each configuration can be also be different, or even vary with the iteration: $\langle n_{i,\sigma} \rangle_{I+1} \leftarrow P(I) \langle n_{i,\sigma} \rangle_I + (1 - P(I)) \langle n_{i,\sigma} \rangle_{I+1}$, if we make sure that $P(I) > \delta$, the latter being the convergence parameter.

Finally, the number of parameters may be reduced. This is done while taking into account the symmetry of the system. For example, one may take only the number of sublattices, say 2 for a square lattice with PBCs. This corresponds to the uniform density ansatz $\langle n_{i,\sigma} \rangle = n_X = \frac{1}{N_X} \sum_{i \in X} \langle n_{i,\sigma} \rangle$ for all sites in the X sublattice. If this reduction is not done correctly, we will obtain biased self-consistent solutions that do not necessarily reflect the nature of the solution.

2.7 Simulatable variants of the Hubbard model and TMDs

More general models than the one considered so far exist. Notwithstanding, a limited basis of single-electron orbitals allows one to describe the essential electronic degrees of freedom. In fact, all the methodology we shall present in the next chapter generalizes for Hamiltonians of the class [85]:

$$\mathcal{H} = - \sum_{i,j,\sigma} K_{ij} \left(c_{i,\sigma}^\dagger c_{j,\sigma} + c_{j,\sigma}^\dagger c_{i,\sigma} \right) + \sum_{i,j} V_{ij} n_i n_j, \quad (2.62)$$

where all the notation has the usual meaning, and V_{ij} , included in the functional of the charge density that models the Coulomb repulsion, already includes the effects of screening, and $n_i = c_{i,\uparrow}^\dagger c_{i,\uparrow} + c_{i,\downarrow}^\dagger c_{i,\downarrow}$.

This generic form includes standard condensed matter models, such as the Hubbard model, its multi-

orbital, and extended variants, and the Anderson model. Various approximation methods at $T = 0$ and $T \neq 0$ aim at studying low-temperature phase transitions perturbatively or by considering simplified interactions. QMC methods are accurate and unbiased, and follow a different route, allowing the exploration of a more vast range of parameter space. In auxiliary field QMC, we start by eliminating the *direct* electron-electron interaction: in the same way that photon fields mediate the electromagnetic interaction, there are fields mediating our simplified screened interaction. In the context of a path integral formulation, we will introduce these fields to eliminate the electron-electron interactions. The complexity of the problem is transferred to the degrees of freedom of the classical, Hubbard Stratonovich field that mediates the interaction. The problem of direct interactions between electrons maps to a free-fermion problem that can be solved formally in terms of field-dependent determinants of single-electron Green's functions. We use Monte Carlo to importance sample configurations of these fields.

The algorithm tends to suffer from a number of difficulties, namely excessive computer time, the sign problem, fermionic wave functions turning bosonic, and, notably, numerical instabilities at low temperatures. Luckily, this last obstacle can be circumvented. In thermodynamic studies of many-electron systems, as we reach the low temperature limit, the lowest energy states are assigned larger weights, whereas high energy states are exponentially suppressed. However, Pauli's exclusion principle implies the existence of a "Fermi energy". The prevalent states are not macroscopically occupied, that is, they are only filled up to the "Fermi energy", which controls the physics of the system. Unfortunately, the information about the states around the Fermi energy is exponentially suppressed with respect to the comparatively unimportant states at the bottom of the band. Numerically, this translates into determining differences of large numbers with great precision. Finite-precision computers impose constraints on this process. Sophisticated algorithms exist to explicitly separate the exponentially diverging numerical scales associated with the different energy scales (electron mobility, doping, Coulomb interaction, ...). Thus, simulations can be stabilized at lower temperature, potentially allowing the study of a wider variety of phases.

The case of interest for simulating TMD nanoribbons comes from considering a particular multi-orbital form of the Hamiltonian of Eq.(2.62). Greek indexes α, β are used to represent different "orbitals" on the same site, and we consider on-site interactions only between electrons on the same orbital:

$$\mathcal{H} = - \sum_{\substack{i,j \\ \alpha,\beta,\sigma}} K_{(i\alpha),(j\beta)} \left(c_{i,\alpha,\sigma}^\dagger c_{j,\beta,\sigma} + c_{j,\beta,\sigma}^\dagger c_{i,\alpha,\sigma} \right) + \frac{U}{2} \sum_{\substack{i,\alpha \\ \sigma \neq \sigma'}} n_{i\alpha,\uparrow} n_{i\alpha,\downarrow} + \frac{U'}{2} \sum_{\substack{i,\alpha \neq \beta \\ \sigma,\sigma'}} n_{i\alpha,\sigma} n_{i\beta,\sigma'}, \quad (2.63)$$

but even when inter-orbital interactions vanish ($U' = 0$), it remains much more expensive to simulate numerically than the simpler Hubbard model since the orbital space increases the overall dimensionality of the problem, and the hopping matrix becomes less sparse. This block matrix specifies the geometry, i.e. the number and position of the neighbors on the spatial lattice, say the triangular lattice. It also relates to the TMD (or other material) at hand via the non-uniform hopping parameters in these blocks, greatly affecting the possibility of simulating the system effectively (due, for example, to the sign problem, whose severity strongly depends on the considered model).

In this work, we focus on the intra-orbital variant of the Hamiltonian of Eq.(2.63).

3

Auxiliary Field Quantum Monte Carlo

Contents

3.1	Monte Carlo Method in Classical Statistical Physics	38
3.2	Theoretical Framework and Mathematical Formulation	44
3.3	Measurements	52
3.4	Stabilization	55

We start with a brief review of the Monte Carlo method in statistical physics, and then explain how the fundamental concepts we present can be generalized to study quantum-many fermion systems. Focusing on the auxiliary field method, we discuss the mapping to the free-fermion problem that reduces the problem to the evaluation of determinants, and show how an efficient algorithm can be designed by successive global updates of the free-fermion Green's functions. Then, we explain how to control the instabilities in this update scheme. In particular, we explain how to circumvent low temperature instabilities due to the ill-conditioning of the matrices representing the free-fermion propagators. We also show that this problem has to do with the coexistence of significantly different energy scales, and tends to get worse as the size increases. Finally, we compute the estimators allowing the measurement of some relevant observables for Transition Metal Dichalcogenide Nanoribbons (TMDNRs).

3.1 Monte Carlo Method in Classical Statistical Physics

Monte Carlo methods form the largest and arguably most useful class of numerical methods used to approach statistical physics problems. Statistical physics often deals with computing quantities that describe the behavior of condensed matter systems. The main difficulty one faces when doing so has to do with the collective nature of these systems. Many identical components comprise them, and while the equations that govern the behavior of the whole may be easy to write down, their solution is in general a remarkably laborious mathematical problem. It is both the sheer number of equations and the coupling between them that deems the task of finding an exact solution either very tough or even impossible. Concomitantly, the exponentially large number of possible configurations of the typical condensed matter system can be daunting. Thus, it is rather striking that we are able to describe a system that is governed by a macroscopically large number of equations in terms of only a few variables. The loss of information in doing so is only apparent. The statistical description is so effective because most of the possible states of the system are extremely improbable when compared to the relevant very narrow part of configuration space. The success of the field is largely attributed to the averaging out that naturally occurs when measuring a property of a macroscopic system.

Suppose you try to sample uniformly from the probability distribution of all possible configurations of one of the aforementioned systems. Chances are your algorithm will not end before the Universe does. This is the computational complexity hurdle. A related issue is that of finite size effects. We are far from being able to simulate a macroscopically sized system. At best we can simulate a system that has only a minuscule fraction of the size of a real system. Amazingly there are techniques that allow

us to efficiently extract information out of relatively small scale simulations. Nonetheless, increasing the system size systematically improves the reliability of a simulation. Thus, it is important to design efficient algorithms to probe larger systems in a fixed computer time frame.

The law of large numbers affords an approximation to integrals which can be written as an expectation of a random variable. Upon drawing enough independent samples from the corresponding distribution, the sample mean gets arbitrarily close to the integral at stake.

$$\mathbb{E}[f(X)] = \int dx f(x)p(x), \quad (3.1)$$

where $p(x)$ is the distribution of X .

We could simply draw M independent and identically distributed samples $x_{1,\dots,M}$ from $p(x)$ and approximate the integral as $\frac{1}{M} \sum_{k=1}^M f(x_k)$, which in most cases converges to the desired expectation, as long as M is large enough. How large?

$$\text{Var}\left(\frac{1}{M} \sum_{k=1}^M f(x_k)\right) = \frac{1}{M} \text{Var}(f(x_1)) \propto \mathcal{O}\left(\frac{1}{M}\right) \quad (3.2)$$

Thus, the estimation error of the mean is of order $\mathcal{O}(\frac{1}{\sqrt{M}})$, as long as $\text{Var}(f(x_1)) \sim 1$. This condition can be achieved by using importance sampling, a variance reduction technique we will shortly discuss.

But how do we sample from an arbitrary distribution $p(X)$? The idea is to start by making an educated choice of a Markov Chain with the prescribed stationary distribution, $p(X)$, from which we desire to sample from. After a sufficiently high number of steps, a Markov Chain Monte Carlo (MCMC) algorithm starts to generate samples from the target distribution. Imposing some conditions on this Markov Chain, namely that it should be irreducible, aperiodic and positive recurrent, the ergodic theorem guarantees that the empirical measures of the aforementioned sampler approach the target stationary distribution. Another important condition to impose on this Markov Chain is detailed balance. Let the transition matrix be $\mathbf{P} = [P_{\mu \rightarrow \nu}]$, and the state space Ω be $\{\pi_\mu | \mu = 1, \dots, |\Omega|\}$, where $|\Omega|$ is the total number of possible states. Then, the condition of detailed balance is defined for all μ, ν as

$$\pi_\mu P_{\mu \rightarrow \nu} = P_{\nu \rightarrow \mu} \pi_\nu \quad (3.3)$$

Consider a system in state μ that makes transitions to state ν at a rate $R_{\mu \rightarrow \nu}$ (that specifies the system's dynamics) and vice-versa. The probability that a system is in state μ at time t , $p_\mu(t)$, such that $\sum_\mu p_\mu(t) = 1$, is given by the master equation(s):

$$\frac{dp_\mu}{dt} = \sum_\nu [p_\nu(t)R_{\nu \rightarrow \mu} - p_\mu(t)R_{\mu \rightarrow \nu}] \quad \forall \mu \in \Omega \quad (3.4)$$

For a physical system, the equilibrium occupation probabilities at finite temperature T follow the Boltzmann distribution.

$$\pi_\mu = \lim_{t \rightarrow \infty} p_\mu(t) = \frac{1}{Z} e^{-E_\mu/k_B T}, \quad (3.5)$$

where E_μ is the energy of state μ , k_B is Boltzmann's constant, and Z is the partition function. From the latter we can extract thermodynamic observables (expectations of physical quantities $\langle Q \rangle$), and response functions (in terms of their variance σ_Q^2).

Imposing the condition of stationarity on Eq.(3.4), $d_t p_\mu = 0$, and noting that $P_{\mu \rightarrow \nu} = R_{\mu \rightarrow \nu} dt$, we obtain the equilibrium condition

$$\sum_\nu \pi_\nu P_{\mu \rightarrow \nu} = \sum_\nu P_{\nu \rightarrow \mu} \pi_\nu \iff \pi_\mu \sum_\nu P_{\mu \rightarrow \nu} = \sum_\nu P_{\nu \rightarrow \mu} \pi_\nu \iff \pi_\mu = \sum_\nu P_{\nu \rightarrow \mu} \pi_\nu \quad (3.6)$$

This condition is enough to ensure the convergence to an equilibrium of the Markov dynamics. However, it does not guarantee that the equilibrium distribution is our desired one, $\boldsymbol{\pi}(\infty)$. In fact, the probability of a state evolves according to

$$\pi_\nu(t+1) = \sum_\mu P_{\mu \rightarrow \nu} \pi_\mu(t) \iff \boldsymbol{\pi}(t+1) = \mathbf{P} \boldsymbol{\pi}(t) \quad (3.7)$$

The stationary distribution of a Markov chain obeys

$$\boldsymbol{\pi}(\infty) = \mathbf{P} \boldsymbol{\pi}(\infty), \quad (3.8)$$

however, condition (3.6) also allows for limit cycles of length n , where $\boldsymbol{\pi}$ rotates around a number of configurations: $\boldsymbol{\pi}(\infty) = \mathbf{P}^n \boldsymbol{\pi}(\infty)$, where \mathbf{P}^n is the n -th power of \mathbf{P} . Detailed balance is a stronger requirement than the equilibrium condition, which eliminates limit cycles, thus ensuring that our sampler draws configurations from the desired distribution. Intuitively, detailed balance corresponds to incorporating time-reversal symmetry in a simulation, and translates into the following constraint on the Markov transition probabilities:

$$\frac{P_{\mu \rightarrow \nu}}{P_{\nu \rightarrow \mu}} = \frac{\pi_\nu}{\pi_\mu} = e^{-\beta(E_\nu - E_\mu)} \quad (3.9)$$

Crucially, Monte Carlo methods employ *importance sampling*. It turns out that we can improve upon our estimate of $\mathbb{E}[f(X)]$ by reducing the variance of the estimator. If we introduce a separate distribution $q(x)$, and define a weight function as $w(x) = p(x)/q(x)$, we can rewrite Eq.(3.1):

$$\mathbb{E}[f(X)] = \int dx f(x) q(x) w(x) = \mathbb{E}[f(Y) w(Y)], \quad (3.10)$$

with $Y \sim q$, i.e. the random variable Y follows the distribution $q(Y)$. It appears as though we didn't gain anything. However, by choosing q wisely, we can actually reduce the variance we computed in Eq.(3.2):

$$\text{Var}\left(\frac{1}{M} \sum_{k=1}^M f(y_k) w(y_k)\right) = \frac{1}{M} \text{Var}\left(f(y_1) w(y_1)\right) \quad (3.11)$$

Since we did not make any assumptions about $q(Y)$, it may be chosen so as to minimize the variance, hence the error of the Monte Carlo estimator, improving the approximation of the expectation. However, note that the error remains proportional to $\frac{1}{\sqrt{M}}$. In practice, we devise a method to select the portion of state space which contains states contributing more significantly to the average. This procedure ensures that $\text{Var}(f(y_1) w(y_1)) \sim 1$, improving the efficiency of our sampler. The choice of the weight function translates to the averaging process by changing the estimator. Explicitly computing averages is only tractable for very small systems. In practice, we choose a subset of states $\{\mu_1, \mu_2, \dots, \mu_M\}$, estimating

$$\langle Q \rangle = \frac{\sum_\mu Q_\mu e^{-\beta E_\mu}}{\sum_\mu e^{-\beta E_\mu}} \quad \text{as} \quad Q_M = \frac{\sum_{i=1}^M Q_{\mu_i} \pi_{\mu_i}^{-1} e^{-\beta E_{\mu_i}}}{\sum_{j=1}^M \pi_{\mu_j}^{-1} e^{-\beta E_{\mu_j}}} \quad (3.12)$$

The estimate improves as N increases, and when $N \rightarrow \infty$, $Q_M \rightarrow \langle Q \rangle$. The accuracy of the estimator

depends on the choice of the probabilities π , which is related to the aforementioned variance. For example, if π corresponds to the uniform distribution, i.e. $\pi_\mu = \frac{1}{|\Omega|} \forall \mu \in \Omega$, we have

$$Q_M = \frac{\sum_{i=1}^M Q_{\mu_i} e^{-\beta E_{\mu_i}}}{\sum_{j=1}^M e^{-\beta E_{\mu_j}}}, \quad (3.13)$$

which turns out to be a poor choice since most of the visited states contribute negligibly to the average, leading to an inaccurate estimate. The sum is dominated by a small subset of states, which we would like to access. The idea of the Quantum (Classical) Monte Carlo method is to simulate the random quantum (thermal) fluctuations of a system, as it oscillates between states in a given time frame [86]. Instead of visiting these states uniformly, the most relevant part of the phase space is sampled more frequently, overcoming the seemingly exponential complexity of computing a sample mean numerically. Even though only a small fraction of the system's states are sampled, we then obtain an accurate estimate of physical quantities of interest, namely energy, and correlation functions. This is implemented via a proposal-acceptance scheme.

To exploit the freedom given by condition (3.9), we note that we can always introduce a non-zero “stay-at-home” probability $P_{\mu \rightarrow \mu} \in [0, 1]$. Regardless of its value, detailed balance is satisfied. Similarly, any adjustment in $P_{\mu \rightarrow \nu}$ must be compensated by changing $P_{\nu \rightarrow \mu}$ to preserve their ratio. Break the transition probability into a selection probability and an acceptance ratio, respectively:

$$\frac{P_{\mu \rightarrow \nu}}{P_{\nu \rightarrow \mu}} = \frac{S_{\mu \rightarrow \nu} A_{\mu \rightarrow \nu}}{S_{\nu \rightarrow \mu} A_{\nu \rightarrow \mu}} \quad (3.14)$$

The Markov process now consists of generating a chain of states according to $S_{\mu \rightarrow \nu}$, which are then accepted or rejected depending on $A_{\mu \rightarrow \nu}$. Since we want to make the algorithm as efficient as possible, we want to make the acceptance ratio as close to one as possible to avoid useless steps. The most common way to do this is to fix the largest of them to one, and adjust the other accordingly. The acceptance ratio will be close to one more often if $S_{\mu \rightarrow \nu}$ includes most of the dependence of $P_{\mu \rightarrow \nu}$ on the characteristics of the states μ, ν . Ideally, states would always be selected with the correct transition probability, and the acceptance ratio would be fixed to unity. Good algorithms approach this situation, and much effort has been directed at optimizing them to do so. By far, the most common sampling scheme choice is the Metropolis-Hastings algorithm, which we now describe.

We select the transition probability to be uniform, and impose detailed balance through the choice of the acceptance ratios:

$$\frac{P_{\mu \rightarrow \nu}}{P_{\nu \rightarrow \mu}} = \frac{A_{\mu \rightarrow \nu}}{A_{\nu \rightarrow \mu}} = e^{-\beta(E_\nu - E_\mu)} \quad (3.15)$$

Suppose that $E_\mu < E_\nu$. Then, $A(\nu \rightarrow \mu) > A(\mu \rightarrow \nu)$, and since only the acceptance ratio is fixed, we may freely set $A(\nu \rightarrow \mu) = 1$, which fixes $A(\mu \rightarrow \nu) = e^{-\beta(E_\nu - E_\mu)}$. This choice maximizes the efficiency of the algorithm. In short, we propose a random new state uniformly, and then we accept it with probability $A_{\mu \rightarrow \nu} = \min(1, e^{-\beta(E_\nu - E_\mu)})$. After we reach the stationary distribution of the Markov process, we can use the states generated by our sampler to measure averages of physical quantities. We consider this condition to be satisfied after a time τ_{eq} , measured in steps of the algorithm. When we consider a lattice model with a discrete set of states at each site $i = 1, 2, \dots, N$, we say that a *sweep* is

completed whenever N Monte Carlo steps are performed. Thus, the number of “warm-up” sweeps is of order $W \sim \tau_{\text{eq}}/N$.

Before running a simulation, we need to decide how many sweeps we need to get an accurate estimate of the average. The problem is that we need uncorrelated samples to average over, while the algorithm generates samples which are correlated in time. To clarify, let us take the paradigmatic case of the Ising model, describing a magnetic solid with N classical spins on a lattice. If each spin takes on two values, say ± 1 , there are 2^N possible states, in total. The Hamiltonian reads

$$H = -J \sum_{\langle i,j \rangle} s_i s_j - B \sum_i s_i, \quad (3.16)$$

where $\langle i,j \rangle$ means that i,j are nearest neighbors on the lattice, and B is an external magnetic field.

A simple strategy to sample configurations of the Ising model is single-spin-flip dynamics. We start with a random configuration of the spins, and then propose new configurations at each step by flipping a single spin at a given site. A sweep is completed after we propose a spin flip at every site on the lattice.

Consecutive configurations generated by this chain differ only slightly. Thus, it takes some time for the system to reach a configuration which is significantly different from the initial one. This characteristic time is called the correlation time τ_c . It can be estimated rigorously through the time-displaced self-correlation function associated to whatever observable is being measured. A relevant quantity for the case of the Ising model is the magnetization per site: $m = \frac{1}{N} \sum_i s_i$. Its associated time-displaced self-correlator (Eq.(3.17)) measures how correlated two magnetization measurements separated by a simulation time t are.

$$\chi_m(t) = \int dt' (m(t') - \langle m \rangle)(m(t'+t) - \langle m \rangle) = \int dt' (m(t')m(t'+t) - \langle m \rangle^2) \quad (3.17)$$

The typical time-scale on which $\chi_m(t)$ falls off is a measure of the correlation time of the simulation. In particular, at long times it falls off exponentially. The definition of τ_c stems from this characteristic long-time behavior: $\chi_m(t) \sim e^{-t/\tau_c}$. In practice, after waiting for $2\tau_c$, the measurements are virtually uncorrelated. Let A be the number of sweeps roughly corresponding to $2\tau_c$ steps. Then, if we make S sweeps of the lattice during the simulation, the number of independent measurements (i.e. with A sweeps between them) is $M = \frac{S-W}{A}$.

There are many ways to estimate τ_c from $\chi_m(t)$. The simplest consists of making an exponential fit in a given range of times. However, this might be unreliable since the estimate depends strongly on the chosen range. An alternative is to compute the “integrated” correlation time:

$$\int_0^\infty dt \frac{\chi_m(t)}{\chi_m(0)} = \int_0^\infty dt e^{-t/\tau_c} = \tau_c, \quad (3.18)$$

which is less sensitive, but not perfect since the assumption that “long-time” behavior has been reached is arbitrary and introduces an uncontrolled error. Moreover, the very long-time behavior of the auto-correlation is rather noisy and must be excluded.

Using measured data for the magnetization at evenly-spaced times, we may construct the time-displaced auto-correlation function up to an unimportant constant, which does not affect the estimate of

the correlation time:

$$\chi_m(t) = \frac{1}{t_{\max} - t} \sum_{t'=0}^{t_{\max}-t} m(t')m(t'+t) - \left(\frac{1}{t_{\max} - t} \sum_{t'=0}^{t_{\max}-t} m(t') \right) \left(\frac{1}{t_{\max} - t} \sum_{t'=0}^{t_{\max}-t} m(t'+t) \right), \quad (3.19)$$

where t_{\max} is the total simulation time in MC steps.

One should be careful when using this expression at very long times. As t approaches t_{\max} , the upper limit of the sums decreases, and the integration interval becomes narrower. Since $m(t)$ fluctuates randomly at very long times, the statistical error associated to $\chi_m(t)$ becomes more prominent as t approaches t_{\max} . This turns out not to be problematic since typical simulations run for many correlation times. Thus, the tails of the auto-correlation may safely be neglected because the correlations will have already vanished, by definition.

To finish our discussion on the issue of computing the time-displaced correlator, we note that if we have a total of N_s samples of, for instance, magnetization data, the complexity of computing χ_m is $\mathcal{O}(N_s^2)$. It is possible to speed up this process by computing its Fourier transform $\tilde{\chi}_m(\omega)$, and inverting to recover $\chi_m(t)$. This can be done via a standard Fast Fourier Transform (FFT) algorithm in $\mathcal{O}(2N_s \log N_s)$ flops. To do this, we apply the following trick, based on time translation invariance:

$$\begin{aligned} \tilde{\chi}_m(\omega) &= \int dt e^{i\omega t} \int dt' \left(m(t') - \langle m \rangle \right) \left(m(t'+t) - \langle m \rangle \right) \\ &= \int dt \int dt' e^{-i\omega t'} \left(m(t') - \langle m \rangle \right) e^{i\omega(t'+t)} \left(m(t'+t) - \langle m \rangle \right) = \tilde{m}'(\omega) \tilde{m}'(-\omega) = |\tilde{m}'(\omega)|^2, \end{aligned} \quad (3.20)$$

where $\tilde{m}'(\omega)$ is the Fourier transform of $m'(t) = m(t) - \langle m \rangle$ ¹.

In practice, when implementing a MC algorithm, we take a measurement say every sweep (which can be less than a correlation time), and then compute the time-displaced correlator at the end of the simulation to estimate the correlation time. How can we estimate the error in the mean of the N_s correlated samples without knowing τ_c in advance? Take again magnetization measurements. Suppose your N_s samples are independent. Then, the standard deviation of their mean are well known:

$$\sigma = \sqrt{\frac{\frac{1}{N_s} \sum_{i=0}^{N_s} (m_i - \bar{m})^2}{N_s - 1}} = \sqrt{\frac{1}{N_s - 1} (\bar{m}^2 - \bar{m}^2)} \quad (3.21)$$

Intuitively, to get the correct result, we could simply replace N_s by $M = \frac{S-W}{A}$, in the last step. This is because the mean shouldn't change very much when including the correlated configurations with nearly the same magnetization. However, the number of uncorrelated samples is certainly smaller than N_s , and can be estimated to be M by auto-correlation studies.

As shown in [87], if the samples are separated by a time interval Δt , the correct expression is

$$\sigma = \sqrt{\frac{1 + 2\tau_c/\Delta t}{N_s - 1} (\bar{m}^2 - \bar{m}^2)}, \quad (3.22)$$

which reduces to Eq.(3.21) when $\Delta t \gg \tau_c$, since in that case the samples are virtually uncorrelated. Also, we now have a rigorous justification for estimating the amount of time between uncorrelated samples as $2\tau_c$, since for much longer times, the samples become uncorrelated.

¹The only difference between $\tilde{m}'(\omega)$ and $\tilde{m}(\omega)$, is that $\tilde{m}'(0) = 0$, while $\tilde{m}(0) \neq 0$. Thus, one can also compute $\tilde{m}(\omega)$ and then set its $\omega = 0$ component to zero.

Often, we work with heavily correlated samples, so that instead we have $\Delta t \ll \tau_c$. In this limit, the 1 in the numerator of Eq.(3.22) can be neglected, and noting that the number of sweeps between measurements corresponding to Δt is $\Delta S = (S - W)/N_s$, we have

$$\sigma \approx \sqrt{\frac{A}{S - W} (\overline{m^2} - \overline{m}^2)}, \quad (3.23)$$

the same result we would obtain by simply replacing N_s by M . What we found, in rigorous terms, was that the presence of many correlated samples does not significantly change the sample mean if $\Delta t \ll \tau_c$. If we take enough correlated samples, their influence on the sample mean averages out. Eq.(3.23) has the advantage of being independent of Δt , which allows us to choose Δt freely, without affecting the final error. This is handy since it allows us to choose Δt small so as not to lose data.

In practice, before we perform our Monte Carlo simulations, we do preliminary auto-correlation studies to ensure that we estimate the error in our measurements correctly.

3.2 Theoretical Framework and Mathematical Formulation

Auxiliary-field, or Determinant QMC is a simulation method that is commonly used to simulate the Hubbard model, allowing one to capture the elusive effects of electron-electron correlations in the two-dimensional graphene-like nanostructures we are concerned with. The sign problem may deem the algorithm exponentially complex in the size of the system and in inverse temperature. The difficulty lies in computing the nearly vanishing average of a random variable X with comparatively large variance, i.e. $\sigma_X / \langle X \rangle \gg 1$. However, it is possible to overcome the sign problem hurdle for a class of models, namely the Hubbard model on a bipartite lattice at half filling. In fact, many interesting phenomena occur at half filling, for example magnetic ordering and the Mott metal-insulator transition.

Ultimately, we seek a computable approximation of the projection operator \mathcal{P} defined in Eq.(2.12). As we shall see, it is found by using a Hubbard-Stratonovich transformation (in either its discrete or continuous form). This transformation introduces an auxiliary field (consisting basically of Ising spins), and we use Monte Carlo to sample configurations from the distribution corresponding to this *classical* configuration space. This approach is equivalent to an exact solution of the integral that is approximated by using the saddle point approximation in mean field, an observation which motivates us to compare our results with the mean field ones. Mean field theory may be formulated by applying the Hubbard Stratonovich (HS) transformation to transform an interacting problem into a one-body problem, and then apply the saddle-point approximation to solve the resulting integrals. In the GCE (where we make $\mathcal{H} \mapsto \mathcal{H} - \mu \mathcal{N}$, \mathcal{N} being the total particle number operator), the grand-partition function may be written in terms of a functional integral over a space-time dependent field of the exponential of a one-body action

$$Z = \text{Tr}[e^{-\beta \mathcal{H}}] = \int \mathcal{D}\mathbf{h} e^{-S(\mathbf{h})} \equiv \text{Tr}_{\mathbf{h}}[e^{-S(\mathbf{h})}], \quad (3.24)$$

which may be computed by Monte Carlo sampling. In mean field, we approximate the integral by replacing the functional integral by a constant times the exponential of the action - evaluated at the field \mathbf{h}^* , for which the action has a minimum: $\partial_{\mathbf{h}} S(\mathbf{h})|_{\mathbf{h}=\mathbf{h}^*} = 0$, and $\partial_{\mathbf{h}}^2 S(\mathbf{h})|_{\mathbf{h}=\mathbf{h}^*} > 0$. This approach depends on the HS decoupling that was used. In contrast, with the auxiliary field Quantum Monte Carlo (QMC)

method, one computes the integral directly. Although it is more expensive in computing time ($\mathcal{O}(\beta N^3)$), it does not rely on any particular choice of the decoupling. Another obstacle of taking into account all the fluctuations around \mathbf{h}^* is the aforementioned fermion sign problem, also referred in chapter 1. However, as we mentioned above, in certain cases, the symmetries of the model (like Particle-hole symmetry (PHS)) may be used to avoid it, as we explain in appendix B.

3.2.1 Trotter-Suzuki Decomposition

In section 2.3, we found exact solutions for particular instances of the Hubbard model by finding a closed form for the partition function [58]. These will be used to calibrate our numerical calculations. Computing the partition function of a quantum system in equilibrium

$$Z_\beta = \text{Tr}[e^{-\beta\mathcal{H}}] = \sum_{\alpha} \langle \psi_\alpha | e^{-\beta\mathcal{H}} | \psi_\alpha \rangle \quad (3.25)$$

is equivalent to studying its imaginary time evolution. One may think of β as the time parameter of the (imaginary) time evolution of the partition function Z_β . In fact, for a zero temperature system, projective methods use this same principle to find the ground state. In that case, the partition function strictly corresponds to the ground state wave function when $\tau \rightarrow \infty$ (in practice, one takes $\tau = \Theta$ large enough).

Eq.(3.25) is not very amenable to numerical computation since it contains an exponential of a sum of non-commuting operators $e^{-\beta(\mathcal{H}_K + \mathcal{H}_V)}$ as per Eq.(2.11). The exponential is not factorizable and involves computing an infinite number of nested commutators containing these two operators, as per the Zassenhaus formula², valid for any two generic operators X and Y :

$$e^{(X+Y)} = e^X e^Y e^{-\frac{1}{2}[X,Y]} e^{\frac{1}{6}(2[Y,[X,Y]]+[X,[X,Y]])} e^{-\frac{1}{24}([[[X,Y],X],X]+3[[[X,Y],X],Y]+3[[[X,Y],Y],Y])} \dots, \quad (3.26)$$

The Trotter-Suzuki decomposition leads to the sought approximate factorization that is used to evaluate the partition function. Dividing the imaginary time interval $[0, \beta]$ into L equal sub-intervals of smaller width $\Delta\tau = \beta/L$, one obtains:

$$Z = \text{Tr} \left[\prod_{l=0}^{L-1} e^{-\Delta\tau\mathcal{H}} \right], \quad (3.27)$$

a form that is more amenable to computation. Actually, by writing the matrix elements of the projection operator \mathcal{P} as path-integrals (here, time-ordering is implicit [5]):

$$\langle \psi | e^{-\beta\mathcal{H}} | \psi' \rangle = \sum_{|\psi_1\rangle, |\psi_2\rangle, \dots, |\psi_{L-1}\rangle} \langle \psi | e^{-\Delta\tau\mathcal{H}} | \psi_1 \rangle \langle \psi_1 | e^{-\Delta\tau\mathcal{H}} | \psi_2 \rangle \dots \langle \psi_{L-1} | e^{-\Delta\tau\mathcal{H}} | \psi' \rangle, \quad (3.28)$$

we see that it is the same as the partition function, if the paths are periodic in imaginary time:

$$Z = \text{Tr}[e^{-\beta\mathcal{H}}] = \sum_{|\psi_0\rangle} \langle \psi_0 | e^{-\beta\mathcal{H}} | \psi_0 \rangle = \sum_{\{|\psi_l\rangle\}} \prod_{l=0}^{L-1} \langle \psi_l | e^{-\Delta\tau\mathcal{H}} | \psi_{l+1} \rangle = \text{Tr} \left[\prod_{l=0}^{L-1} e^{-\Delta\tau\mathcal{H}^l} \right], \quad (3.29)$$

where we have $|\psi_L\rangle = |\psi_0\rangle$. We recover Eq.(3.27) by reorganizing the summations over $\{|\psi_l\rangle\}$, and using closure relations in the Hilbert space of each slice. The “Trotter breakup” follows from truncating Eq.(3.26), and keeping only the first order term in $\Delta\tau$. In the $\Delta\tau \rightarrow 0$ limit, it becomes a trace of a

²This is just the inverse of the well known Baker–Campbell–Hausdorff formula commonly used in quantum mechanics.

time-ordered exponential:

$$Z = \text{Tr} \left[\prod_{l=0}^{L-1} e^{-\Delta\tau \mathcal{H}_K^l} e^{-\Delta\tau \mathcal{H}_V^l} \right] + \mathcal{O}(\Delta\tau^2) \xrightarrow{\Delta\tau \rightarrow 0} \text{Tr} \left[\mathcal{T}_\tau \exp \left(- \int_0^\beta d\tau \underbrace{(\mathcal{H}_K(\tau) + \mathcal{H}_V(\tau))}_{S(\tau)} \right) \right] \quad (3.30)$$

3.2.2 Hubbard-Stratonovich transformation

The kinetic energy term is quadratic in the fermion operators, and spin-independent, meaning that it can be separated into two spin components, independently of the time slice.

$$e^{-\Delta\tau \mathcal{H}_K} = e^{-\Delta\tau \mathcal{H}_{K\uparrow}} e^{-\Delta\tau \mathcal{H}_{K\downarrow}}, \quad (3.31)$$

where $\mathcal{H}_{K\sigma} = \mathbf{c}_\sigma^\dagger (-t_\sigma \mathbf{K}_\sigma - \mu_\sigma \mathbf{I}) \mathbf{c}_\sigma$.

The potential energy term, however, is quartic. Fortunately, it is possible to express it in quadratic form by introducing an extra degree of freedom, the so called *Hubbard-Stratonovich (HS) field* $\tilde{\mathbf{h}} \equiv (h_{l,i})_{i=0, l=0}^{N-1, L-1}$, in which each element is essentially an Ising spin. At each slice, the interaction is eliminated by an N -dimensional HS field $\tilde{\mathbf{h}}$. We start by noting that $[n_{i,\sigma}, n_{j,\sigma'}] = 0 \forall i, j, \sigma, \sigma'$, so that

$$e^{-\Delta\tau \mathcal{H}_V} = e^{-U\Delta\tau \sum_{i=1}^N (n_{i\uparrow} - 1/2)(n_{i\downarrow} - 1/2)} = \prod_i e^{-U\Delta\tau (n_{i\uparrow} - 1/2)(n_{i\downarrow} - 1/2)} \quad (3.32)$$

The HS transformation is based on the well known identity $e^{\frac{a^2}{2}} = \frac{1}{\sqrt{2\pi}} \int_{-\infty}^{\infty} e^{-\frac{z^2}{2} - za} dz \forall a > 0$, which is also valid if a is an operator. Noting that $(n_{i\uparrow} - \frac{1}{2})(n_{i\downarrow} - \frac{1}{2}) = -\frac{1}{2}(n_{i\uparrow} - n_{i\downarrow})^2 + \frac{1}{4}$, we can recast the potential energy term as

$$e^{-\Delta\tau \mathcal{H}_V} = \prod_i e^{\frac{U\Delta\tau}{2} (n_{i\uparrow} - n_{i\downarrow})^2} e^{-\frac{U\Delta\tau}{4}} = \left(\frac{\Delta\tau e^{-\frac{U\Delta\tau}{2}}}{\pi} \right)^{N/2} \int_{-\infty}^{\infty} \prod_i d\tilde{h}_i e^{-\Delta\tau [\tilde{h}_i^2 + \sqrt{2U}(n_{i\uparrow} - n_{i\downarrow})\tilde{h}_i]}, \quad (3.33)$$

so that in the $\tau \rightarrow 0$ limit, the partition function becomes

$$Z \propto \int \mathcal{D}\tilde{\mathbf{h}}(\tau) e^{-\int_0^\beta d\tau \tilde{\mathbf{h}}^2(\tau)} \text{Tr} \left[\mathcal{T}_\tau e^{-\int_0^\beta d\tau [\mathcal{H}_K(\tau) + \sqrt{2U}(\mathbf{n}_\uparrow(\tau) - \mathbf{n}_\downarrow(\tau)) \cdot \tilde{\mathbf{h}}(\tau)]} \right], \quad (3.34)$$

representing a system of noninteracting fermions coupled via spin S^z to an external fluctuating real field.

The fact that $n_{i,\sigma}$ can only take on two possible values suggests an analogous transformation in which the fluctuating field can only take on two possible values. An Ising spin will prove sufficient to eliminate the direct electron-electron interaction. The discrete HS transformation for $U > 0$ allows us to recast Eq.(3.32) in terms of the local spin, a non-interacting quadratic term $n_{i\uparrow} - n_{i\downarrow}$ (at each imaginary-time slice, since the operators live on the Hilbert space of that specific slice). Let $c_U = \frac{1}{2} e^{-\frac{U\Delta\tau}{4}}$ and $\nu = \text{arcosh}(e^{\frac{U\Delta\tau}{2}})$. Then, the sought transformation reads

$$e^{-U\Delta\tau (n_{i\uparrow} - 1/2)(n_{i\downarrow} - 1/2)} = c_U \sum_{\tilde{h}_i = \pm 1} e^{\nu \tilde{h}_i (n_{i\uparrow} - n_{i\downarrow})} \quad (3.35)$$

Notice that $\Delta\tau$ appears explicitly in the coupling constant. This is because we worked with fixed length Ising spins. In the Gaussian formulation we started with (Eq.(3.33)), $\Delta\tau$ can be reabsorbed in the HS field, even though $\Delta\tau$ is still implicit in the integration measure. The parameter $\frac{1}{\Delta\tau}$ can be seen as a high energy cutoff, and it must be larger than all other energy scales in the problem, which is required to make the Trotter breakup error small when discretizing time onto a lattice of $L = \beta/\Delta\tau$ points.

To prove Eq.(3.35), let us write down how the operators $(n_{i\uparrow} - 1/2)(n_{i\downarrow} - 1/2)$ and $(n_{i\uparrow} - n_{i\downarrow})$ act:

$$(n_{i\uparrow} - 1/2)(n_{i\downarrow} - 1/2) \begin{cases} |\rangle = \frac{1}{4} |\rangle \\ |\uparrow\rangle = -\frac{1}{4} |\uparrow\rangle \\ |\downarrow\rangle = -\frac{1}{4} |\downarrow\rangle \\ |\uparrow\downarrow\rangle = \frac{1}{4} |\uparrow\downarrow\rangle \end{cases} \quad (n_{i\uparrow} - n_{i\downarrow}) \begin{cases} |\rangle = 0 |\rangle \\ |\uparrow\rangle = |\uparrow\rangle \\ |\downarrow\rangle = |\downarrow\rangle \\ |\uparrow\downarrow\rangle = 0 |\uparrow\downarrow\rangle \end{cases} \quad (3.36)$$

We can now compare the action of the operators on the LHS and on the RHS of Eq.(3.35) and find the desired relation since we have defined $\cosh \nu = \frac{1}{2}(e^\nu + e^{-\nu}) \equiv e^{\frac{U\Delta\tau}{2}}$.

$$\begin{aligned} e^{-U\Delta\tau(n_{i\uparrow}-1/2)(n_{i\downarrow}-1/2)} |\langle (\uparrow\downarrow)\rangle &= e^{-\frac{U\Delta\tau}{4}} |\langle (\uparrow\downarrow)\rangle & e^{-U\Delta\tau(n_{i\uparrow}-1/2)(n_{i\downarrow}-1/2)} |\langle (\uparrow\downarrow)\rangle &= e^{\frac{U\Delta\tau}{4}} |\langle (\uparrow\downarrow)\rangle \\ c_U \sum_{\tilde{h}_i=\pm 1} e^{\nu\tilde{h}_i(n_{i\uparrow}-n_{i\downarrow})} |\langle (\uparrow\downarrow)\rangle &= e^{-\frac{U\Delta\tau}{4}} |\langle (\uparrow\downarrow)\rangle & c_U \sum_{\tilde{h}_i=\pm 1} e^{\nu\tilde{h}_i(n_{i\uparrow}-n_{i\downarrow})} |\langle (\uparrow\downarrow)\rangle &= \frac{e^\nu + e^{-\nu}}{2} e^{-\frac{U\Delta\tau}{4}} |\langle (\uparrow\downarrow)\rangle \end{aligned} \quad (3.37)$$

We require $U > 0$ to fulfill $\cosh \nu = e^{U\Delta\tau/2}$. A similar reasoning could be made for $U < 0$. Similar transformations that recast other types of quartic terms in terms of quadratic ones exist, but the transformation we derived, following [9], is the one we will use throughout. We have made progress at the expense of introducing L fields $\tilde{\mathbf{h}}$ to which fermions are coupled to at each slice. More precisely, the external field couples to the local spin at each site. Our representation of the interacting problem is *exact*, and is encoded in the configurations of the NL -dimensional HS field \mathbf{h} [58]. The interacting term can be manipulated to arrive at a more compact form.

$$\begin{aligned} e^{-\Delta\tau\mathcal{H}_V} &= \prod_{i=0}^{N-1} \left(c_U \sum_{\tilde{h}_i=\pm 1} e^{\nu\tilde{h}_i(n_{i\uparrow}-n_{i\downarrow})} \right) = (c_U)^N \sum_{\tilde{h}_0=\pm 1} e^{\nu\tilde{h}_0(n_{0\uparrow}-n_{0\downarrow})} \dots \sum_{\tilde{h}_{N-1}=\pm 1} e^{\nu\tilde{h}_{N-1}(n_{N-1\uparrow}-n_{N-1\downarrow})} \\ &= (c_U)^N \sum_{\{\tilde{h}_i=\pm 1\}} e^{\sum_{i=0}^{N-1} [\nu\tilde{h}_i(n_{i\uparrow}-n_{i\downarrow})]} \equiv (c_U)^N \text{Tr}_{\tilde{\mathbf{h}}} \left[e^{\sum_{i=0}^{N-1} [\nu\tilde{h}_i(n_{i\uparrow}-n_{i\downarrow})]} \right] \\ &= (c_U)^N \text{Tr}_{\tilde{\mathbf{h}}} \left[e^{\sum_{i=0}^{N-1} \nu\tilde{h}_i n_{i\uparrow}} e^{-\sum_{i=0}^{N-1} \nu\tilde{h}_i n_{i\downarrow}} \right] = (c_U)^N \text{Tr}_{\tilde{\mathbf{h}}} \left[e^{\mathcal{H}_{V\uparrow}} e^{\mathcal{H}_{V\downarrow}} \right], \end{aligned} \quad (3.38)$$

where the spin up and spin down operators $\mathcal{H}_{V\sigma}$ are defined as $\mathcal{H}_{V\sigma} = \sum_{i=0}^{N-1} \nu\tilde{h}_i n_{i\sigma} = \sigma\nu\mathbf{c}_\sigma^\dagger \mathbf{V}(\tilde{\mathbf{h}}) \mathbf{c}_\sigma$, with $\mathbf{V}(\tilde{\mathbf{h}})$ being simply the HS-field put into a diagonal $N \times N$ matrix: $\mathbf{V}(\tilde{\mathbf{h}}) \equiv \text{diag}(\tilde{h}_0, \tilde{h}_1, \dots, \tilde{h}_{N-1})$.

3.2.3 Single-particle propagators and the fermionic trace

For each imaginary time slice l , we may define a HS-field $\tilde{\mathbf{h}}_l$, which specifies \mathbf{V}_l and $\mathcal{H}_{V_\sigma}^l$. The Hamiltonian acquires a “fictitious” imaginary-time dependence that enforces (imaginary-)time ordering, and independent Hilbert spaces at each slice. We may now replace the result of Eq.(3.38) in Eq.(3.30), and exchange the traces to obtain

$$Z = (c_U)^{NL} \text{Tr}_{\mathbf{h}} \text{Tr} \left[\underbrace{\prod_{l=0}^{L-1} \left(e^{-\Delta\tau\mathcal{H}_{K\uparrow}} e^{\mathcal{H}_{V\uparrow}^l} \right)}_{B_{l,\uparrow}(\tilde{\mathbf{h}}_l)} \underbrace{\left(e^{-\Delta\tau\mathcal{H}_{K\downarrow}} e^{\mathcal{H}_{V\downarrow}^l} \right)}_{B_{l,\downarrow}(\tilde{\mathbf{h}}_l)} \right], \quad (3.39)$$

where all operators are now quadratic in the fermion operators:

$$\mathcal{H}_{K_\sigma} = \mathbf{c}_\sigma^\dagger (-t_\sigma \mathbf{K}_\sigma - \mu_\sigma \mathbf{I}) \mathbf{c}_\sigma \quad \mathcal{H}_{V_\sigma}^l = \sigma\nu\mathbf{c}_\sigma^\dagger \mathbf{V}_l(\tilde{\mathbf{h}}_l) \mathbf{c}_\sigma \quad (3.40)$$

for $\sigma = \pm 1$ and $\mathbf{V}_l(\tilde{\mathbf{h}}_l) = \text{diag}(h_{l,0}, h_{l,1}, \dots, h_{l,N-1})$. Furthermore, we have defined the \mathbf{B} -matrices, representing the imaginary-time propagators between time slices.

$$\mathbf{B}_{l,\sigma}(\tilde{\mathbf{h}}_l) = e^{\Delta\tau(t_\sigma \mathbf{K}_\sigma + \mu_\sigma \mathbf{I})} e^{\sigma\nu \mathbf{V}_l(\tilde{\mathbf{h}}_l)} \quad (3.41)$$

The problem of computing the partition function has been reduced to computing the trace of a product of exponentials of quadratic forms. Thus, we may still rewrite equation (3.39) by making use of the following identity. Let \mathcal{H}_l be quadratic forms of the fermion operators: $\mathcal{H}_l = c_i^\dagger(\mathbf{H}_l)_{ij} c_j$, where the summation is implied, and where \mathbf{H}_l are real matrices. Then, the following identity holds

$$\text{Tr}[e^{-\mathcal{H}_1} e^{-\mathcal{H}_2} \dots e^{-\mathcal{H}_L}] = \det(\mathbf{I} + e^{-\mathbf{H}_L} e^{-\mathbf{H}_{L-1}} \dots e^{-\mathbf{H}_1}) \quad (3.42)$$

For simplicity, in appendix B, we present the proof for a simpler case, corresponding to a single \mathbf{B} -matrix, i.e. a product of exponentials of two quadratic operators [8]. It could then be easily extended to the more general case [85](ch.4, ap. III). The products of up and down spin \mathbf{B} -matrices give rise to a product of two such determinants, which may easily be deduced from the proof of appendix B.

When applied to our problem, Eq.(3.42) essentially makes the computation of the trace possible! That is because it turns the many-fermion problem into a single-particle problem. Note that if we were to compute it naively, we would soon run out of computer memory. The dimension of the Hilbert space of the Hubbard model is exponential in the number of sites N (actually 4^N). Contrastingly, at worst, the determinant can be calculated in $\mathcal{O}(LN^3)$ flops for a matrix whose size is polynomial in N , leading to a naive $\mathcal{O}(L^2N^4)$ algorithm. The computable form of the partition function (3.39) is

$$Z = \text{Tr}_{\mathbf{h}} \left[(c_U)^{NL} \det[\mathbf{M}_\uparrow(\mathbf{h})] \det[\mathbf{M}_\downarrow(\mathbf{h})] \right] = \sum_{\{\mathbf{h}\}} P(\mathbf{h}) \equiv \text{Tr}_{\mathbf{h}}[e^{-S(\mathbf{h})}] \quad (3.43)$$

where the fermion matrices \mathbf{M}_σ are defined in terms of the \mathbf{B} -matrices that depend on the HS-field \mathbf{h} :

$$\mathbf{M}_\sigma(\mathbf{h}) = \mathbf{I} + \mathbf{B}_{L-1,\sigma}(\tilde{\mathbf{h}}_{L-1}) \mathbf{B}_{L-2,\sigma}(\tilde{\mathbf{h}}_{L-2}) \dots \mathbf{B}_{0,\sigma}(\tilde{\mathbf{h}}_0) = \mathbf{I} + \prod_{l=L-1}^0 \mathbf{B}_{l,\sigma}(\tilde{\mathbf{h}}_l) \quad (3.44)$$

By casting the fermionic trace as a product of determinants, we obtained the computable approximation of the distribution operator \mathcal{P} corresponding to Z_β as advertised in Eq.(1.11).

$$P(\mathbf{h}) = \frac{A}{Z_{\mathbf{h}}} \det[\mathbf{M}_\uparrow(\mathbf{h})] \det[\mathbf{M}_\downarrow(\mathbf{h})], \quad (3.45)$$

where $A = (c_U)^{NL}$ is a normalization constant. This is now a distribution function over configurations of the field \mathbf{h} since the problem is “classical” (the quotes serve to emphasize that $P(\mathbf{h})$ can be negative)!

For the particular case of no interactions $U = 0$, we have that $\nu = 0$, and $\mathbf{M}_\sigma(\mathbf{h})$ are independent of the HS-field. The Trotter-Suzuki approximation then becomes exact and the Hubbard Hamiltonian may be simulated exactly after evaluating $\mathbf{M}_\sigma(\mathbf{h})$ a single time. Monte Carlo sampling is not required.

We mapped a d -dimensional quantum problem to a $(d+1)$ -dimensional “classical” problem with an extra imaginary-time dimension. Note that the size of the configuration space remains exponential despite having been increased to 2^{NL} (assuming that $L > 2$). However, it can now be probed more easily: while we might have increased the number of possible configurations by introducing the mapping, we arrived at a form which is tractable by a standard Monte Carlo method, as described in the previous section.

This is because we may now efficiently navigate through the exponentially large state space of the system using importance sampling. Schematically, the degrees of freedom of the quantum problem correspond to the i -indices of the c -operators. In our formulation, an additional imaginary time slice index l was introduced, leading to a mapping that is not specific to the Hubbard model, but applies generally for any quantum system.

3.2.4 Monte Carlo sampling of the Hubbard Stratonovich field

The computational problem is now that of sampling configurations of the \mathbf{h} field drawn from the distribution $P(\mathbf{h})$ using *Classical* Monte Carlo. It remains to choose a dynamics and a sampling scheme. The simplest rule to change from a configuration \mathbf{h} to a new one \mathbf{h}' is single spin-flip dynamics. Choose a random point (l, i) , and flip the spin at that space-time “site”: $h'_{l,i} = -h_{l,i}$, keeping all others unchanged. The most common scheme to ensure that the distribution of the accepted sample is $P(\mathbf{h})$ is the Metropolis-Hastings algorithm, but others exist, such as the heat bath algorithm. After the thermalization steps, we will be correctly sampling from the required distribution, and we may perform measurements.

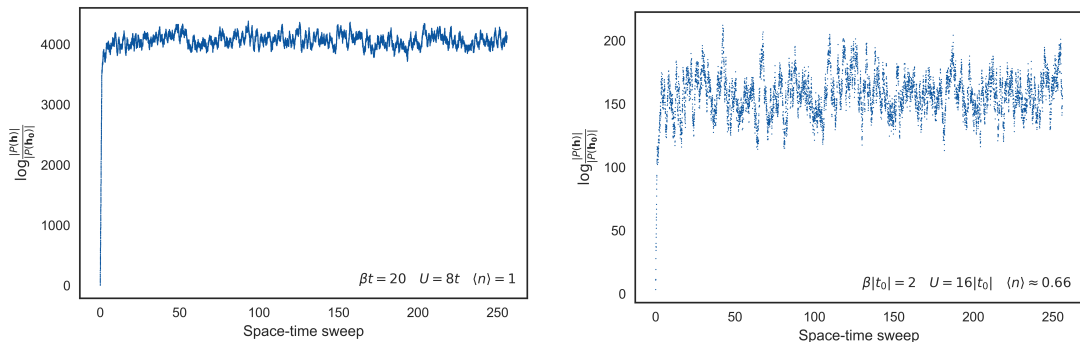


Figure 3.1: Evolution of the probability of accepted HS field configurations, \mathbf{h} , with respect to the probability of the first randomly chosen configuration, \mathbf{h}_0 , for a 8×8 square lattice and for a 9×4 MoS₂ TMDNR.

Algorithm 3.1 Auxiliary Field Quantum Monte Carlo Sampling Scheme

```

Initialize hoppings  $\mathbf{K}$ , and HS field  $\mathbf{h}$ 
 $(h_{l,i}) = (\pm 1)$ ,  $l = 0, \dots L - 1$ ,  $i = 0, \dots N - 1$ ;  $(l, i) \leftarrow (0, 0)$ 
for step = 1 to  $S$  do
    Propose new configuration by flipping a spin:  $h'_{l,i} = -h_{l,i}$ 
    5: Compute the acceptance ratio  $a_{l,i}$ :  $\frac{\det[\mathcal{M}_\uparrow(\mathbf{h}')]\det[\mathcal{M}_\downarrow(\mathbf{h}')]}{\det[\mathcal{M}_\uparrow(\mathbf{h})]\det[\mathcal{M}_\downarrow(\mathbf{h})]}$ 
        Metropolis step
        Draw random number  $r \in [0, 1]$ 
        if  $r \leq \min(1, a_{l,i})$  then
             $\mathbf{h} = \mathbf{h}'$ 
        10: else
             $\mathbf{h} = \mathbf{h}$ 
        end if
        Next space-time “site”
        if  $i < N - 1$  then
             $l = l, i = i + 1$ 
        15: else
            if  $l < L - 1$  then
                 $l = l + 1, i = 0$ 
            end if
        20: if  $l = L - 1$  then
             $l = 0, i = 0$ 
        end if
    end if
end for

```

The acceptance/rejection scheme leads to a rank-one update of the matrices $\mathbf{M}_\sigma(\mathbf{h})$ ³, which affords an efficient evaluation of the acceptance ratio $a_{l,i}$ [58] (see appendix B). The acceptance ratio is given in terms of determinants of the Green's matrices $\mathbf{G}(\mathbf{h}) = \mathbf{M}_\sigma^{-1}(\mathbf{h})$, but these need not be explicitly computed at each step. Instead, a *global* update of the Green's matrices at each step suffices to obtain the ratio between the determinants of the Green's matrices of the current and previous configurations. This brings the computational complexity from $\mathcal{O}(N^3)$ to $\mathcal{O}(N^2)$ at each step. Upon fixing the precision via the Trotter error $\Delta\tau$, this results in an overall cubic scaling of the algorithm, more precisely $\mathcal{O}(\beta N^3)$ (the process is repeated LN times, and $\beta \sim L$).

Suppose we start at the first imaginary-time slice, $l = 0$. Using the result of appendix B, for $i = 0$, the proposal $h'_{00} = -h_{00}$ leads to

$$r_{00} = \left[1 + \alpha_{0,\uparrow}(1 - \mathbf{e}_0^T \mathbf{M}_\uparrow^{-1}(\mathbf{h}) \mathbf{e}_0) \right] \left[1 + \alpha_{0,\downarrow}(1 - \mathbf{e}_0^T \mathbf{M}_\downarrow^{-1}(\mathbf{h}) \mathbf{e}_0) \right] \equiv d_{0,\uparrow} d_{0,\downarrow}, \quad (3.46)$$

where we defined the unit vectors $\mathbf{e}_0, \mathbf{e}_1, \dots, \mathbf{e}_{N-1}$, and the ratios of determinants

$$d_{i,\sigma} = 1 + \alpha_{i,\sigma}(1 - G_{ii}^\sigma) \quad \text{with} \quad \alpha_{i,\sigma} = e^{-2\sigma\nu h_{li}} - 1$$

The most expensive operation is the computation of the $(0,0)$ entry of $G^\sigma(\mathbf{h})$. However, this object is always computed in advance (it is the main object of the simulation!), so the computation of the acceptance ratio is essentially free. Whenever a step is accepted, the Green's matrices are updated in $\mathcal{O}(N^2)$ flops, and the acceptance ratio is recomputed as our notation suggests

$$\mathbf{G}^\sigma(\mathbf{h}) \leftarrow \mathbf{G}^\sigma(\mathbf{h}) - \frac{\alpha_{i,\sigma}}{r_{l,i}} \mathbf{u}_{i,\sigma} \mathbf{w}_{i,\sigma}^T \quad r_{l,i} = d_{i,\uparrow} d_{i,\downarrow}, \quad (3.47)$$

where $\mathbf{u}_{i,\sigma} = (\mathbf{I} - \mathbf{G}^\sigma(\mathbf{h}))\mathbf{e}_i$, and $\mathbf{w}_{i,\sigma} = [\mathbf{G}^\sigma(\mathbf{h})]^T \mathbf{e}_i$. Notice that here, \mathbf{G}^σ is the Green's matrix at slice l . If the step is accepted, the i -th column of the $\mathbf{B}_l(\tilde{\mathbf{h}}_l)$ -matrix is multiplied by $e^{-2\sigma\nu h_{li}}$.

Only one entry of each of the Green's matrices is used at each step for sampling. To improve the efficiency of our implementation, we can compute only the relevant entry that is required for sampling until a sweep of the space lattice is completed, at which point we need to update the entire Green's function (since this final update has complexity $\mathcal{O}(N^3)$, the complexity of the algorithm does not change, although some speed-up is expected). This block high rank update is a “delayed update” in the sense that we avoid unnecessary computations until they are absolutely needed.

This procedure generalizes for all other time slices. First, note that the order of the operators in Eq.(3.42) may be changed by using the cyclic property of the trace. Concomitantly, for example, when we advance to $l = 1$, we may write the \mathbf{M} -matrices by wrapping the equivalent $\widehat{\mathbf{M}}$ matrices:

$$\mathbf{M}_\sigma(\mathbf{h}) = \mathbf{B}_{0,\sigma}^{-1}(\tilde{\mathbf{h}}_0) \widehat{\mathbf{M}}_\sigma(\mathbf{h}) \mathbf{B}_{0,\sigma}(\tilde{\mathbf{h}}_0) \quad \widehat{\mathbf{M}}_\sigma(\mathbf{h}) = \mathbf{I} + \mathbf{B}_{0,\sigma}(\tilde{\mathbf{h}}_0) \mathbf{B}_{L-1,\sigma}(\tilde{\mathbf{h}}_{L-1}) \mathbf{B}_{L-2,\sigma}(\tilde{\mathbf{h}}_{L-2}) \dots \mathbf{B}_{1,\sigma}(\tilde{\mathbf{h}}_1) \quad (3.48)$$

The Metropolis ratio can be computed with $\widehat{\mathbf{M}}$, and the Green's functions are also wrapped :

$$r = \frac{\det[\mathbf{M}_\uparrow(\mathbf{h}')]\det[\mathbf{M}_\downarrow(\mathbf{h}')]}{\det[\mathbf{M}_\uparrow(\mathbf{h})]\det[\mathbf{M}_\downarrow(\mathbf{h})]} = \frac{\det[\widehat{\mathbf{M}}_\uparrow(\mathbf{h}')]\det[\widehat{\mathbf{M}}_\downarrow(\mathbf{h}')]}{\det[\widehat{\mathbf{M}}_\uparrow(\mathbf{h})]\det[\widehat{\mathbf{M}}_\downarrow(\mathbf{h})]} \quad \widehat{\mathbf{G}}^\sigma(\tilde{\mathbf{h}}_0) = \mathbf{B}_{0,\sigma}(\tilde{\mathbf{h}}_0) \mathbf{G}^\sigma(\mathbf{h}) \mathbf{B}_{0,\sigma}^{-1}(\tilde{\mathbf{h}}_0) \quad (3.49)$$

³We will see that it is actually more convenient to work with their inverses, the Green's matrices.

The wrapping trick makes $B_{1,\sigma}(\tilde{\mathbf{h}}_1)$ appear at the position of the $\widehat{\mathbf{M}}$ -matrix where $\mathbf{B}_{0,\sigma}(\tilde{\mathbf{h}}_0)$ appeared for $l = 0$. Thus, we can use everything that was derived for $l = 0$ with the wrapped Green's functions $\widehat{\mathbf{G}}^\sigma$. This is repeated consecutively as we advance in imaginary-time.

Since the cost of wrapping is $\mathcal{O}(N^3)$, the cost of computing r is essentially that of updating the Green's matrices. Each update requires $2N^2$ elementary operations, so that a sweep through the HS-matrix \mathbf{h} costs $2N^3L$ flops. One must pay attention to the efficiency (by delayed updates), and stability of the updating and wrapping of the Green's matrices. When numerically divergent scales are present, the instability of this scheme must be controlled by computing the Green's functions from scratch periodically. When doing so, the stability of the product of the (potentially large) chain of \mathbf{B} -matrices is ensured by using QR decomposition with partial pivoting, following QUEST's implementation [58].

3.2.5 Checkerboard Breakup

In this section, we focus on the computation of the matrix exponential $\mathbf{B} = e^{t\Delta\tau\mathbf{K}}$. Although the cost of computing it is small, and it is done only once in the initialization phase of the algorithm, if it is done naively, the resulting matrix is dense. This is undesired since it is multiplied repeatedly by other matrices throughout the algorithm, which has a high cost of order $\mathcal{O}(N^3)$. Diagonalizing and exponentiating \mathbf{K} results in a dense matrix of N^2 elements. For uniform hoppings, we can use the FFT and apply the exponential of the kinetic term $e^{t\Delta\tau\mathbf{K}}$ in momentum space, in which \mathbf{K} is diagonal. The drawback of this approach is two-fold: first, the system size becomes constrained to powers of 2, so that the FFT can be applied efficiently, and, more importantly, we cannot apply it to nonuniform hoppings (which is precisely the case we are interested in in this work). A convenient, and sparse approximation of \mathbf{B} in real space is available, and it is obtained simply by applying the Trotter breakup to the exponential of the hopping:

$$e^{t\Delta\tau\mathbf{K}} = e^{t\Delta\tau \sum_{\langle i,j \rangle} \mathbf{K}^{(ij)}} = \prod_{\langle i,j \rangle} e^{t\Delta\tau \mathbf{K}^{(ij)}} + \mathcal{O}((t\Delta\tau)^2), \quad (3.50)$$

where the sparse matrices $\mathbf{K}^{(ij)}$ have only two nonzero elements: $K_{ij}^{(ij)} = K_{ji}^{(ij)} = K_{ij}$, such that the exponential may easily be computed:

$$e^{t\Delta\tau\mathbf{K}^{(ij)}} = \exp \left[t\Delta\tau \begin{pmatrix} 1 & \dots & 0 & \dots & 0 & \dots 0 \\ \vdots & & \vdots & & \vdots & \vdots \\ 0 & \dots & \cosh(t\Delta\tau K_{ij}) & \dots & \sinh(t\Delta\tau K_{ij}) & \dots 0 \\ \vdots & & \vdots & & \vdots & \vdots \\ 0 & \dots & \sinh(t\Delta\tau K_{ij}) & \dots & \cosh(t\Delta\tau K_{ij}) & \dots 0 \\ \vdots & & \vdots & & \vdots & \vdots \\ 0 & \dots & 0 & \dots & 0 & \dots 1 \end{pmatrix} \right], \quad (3.51)$$

and it is also a sparse matrix with only the ii , ij , ji , jj elements differing from the identity. Thus, the dense matrix multiplication involving \mathbf{B} and another $N \times N$ matrix becomes a series of sparse matrix multiplications, and the complexity decreases from $\mathcal{O}(N^3)$ to $\mathcal{O}(NN_b)$, where N_b is the number of bonds, a number that grows linearly with the system size for local hoppings. For example, for the square lattice, $N_b = 2N$. The checkerboard breakup is particularly useful with site-dependent hoppings (indicating for example a fixed lattice distortion or a multi-orbital model), since it is both efficient and easy to implement.

Furthermore, the computation of the inverse requires only reversing the sign of the off-diagonal elements, which saves us another $\mathcal{O}(N^3)$ computation.

3.3 Measurements

In QMC simulations, physical observables are extracted by measuring them directly over the course of the sampling of the configuration space. The single-particle (equal time) Green's Function is useful to obtain quantities such as density and kinetic energy, and is simply the inverse of the \mathbf{M} -matrix that we already compute to obtain the acceptance ratio at each step. At imaginary-time $\tau = \Delta\tau\lambda$:

$$G_{ij}^\sigma(\tau, \tau) = \left\langle c_{i,\sigma} c_{j,\sigma}^\dagger \right\rangle_{\mathbf{h}} = \left((\mathbf{I} + \prod_{l=\lambda-1}^0 \mathbf{B}_{l,\sigma}(\tilde{\mathbf{h}}_l) \prod_{l=L-1}^\lambda \mathbf{B}_{l,\sigma}(\tilde{\mathbf{h}}_l))^{-1} \right)_{ij} \equiv \left((\mathbf{I} + \mathbf{B}_{\mathbf{h}}^\sigma(\tau, 0) \mathbf{B}_{\mathbf{h}}^\sigma(\beta, \tau))^{-1} \right)_{ij} \quad (3.52)$$

The equal time Green's function is a fermion average for a given HS field configuration [88]. For a fixed HS field, the problem becomes a free fermion problem, and one may use Wick's theorem to write down expressions for more complex observables. Eq.(3.52) is easily shown, and the proof offers some insight into how other observables are written in terms of $G_{ij}^\sigma(\tau, \tau)$ through Wick's theorem. In auxiliary field QMC, we wish to compute averages of observables O by sampling \mathbf{h} configurations, and then averaging O for fixed \mathbf{h} (which is computed throughout the simulation) over these. Ignoring spin,

$$\begin{aligned} \langle O \rangle &= \frac{1}{Z} \text{Tr}[e^{-\beta\mathcal{H}} O] = \sum_{\mathbf{h}} P(\mathbf{h}) \langle O \rangle_{\mathbf{h}} + \mathcal{O}(\Delta\tau^2), \text{ where} \\ P(\mathbf{h}) &= \frac{C(\mathbf{h}) \det[\mathbf{I} + \mathbf{B}_{\mathbf{h}}(\beta, 0)]}{\sum_{\mathbf{h}} C(\mathbf{h}) \det[\mathbf{I} + \mathbf{B}_{\mathbf{h}}(\beta, 0)]} \quad \langle O \rangle_{\mathbf{h}} = \frac{\text{Tr}[U_{\mathbf{h}}(\beta, \tau) O U_{\mathbf{h}}(\tau, 0)]}{\text{Tr}[U_{\mathbf{h}}(\beta, 0)]} \end{aligned} \quad (3.53)$$

and $U_{\mathbf{h}}(\tau', \tau)$ is the imaginary-time evolution operator between τ and τ' . Introducing a fictitious coupling η to a one-body operator $O = \mathbf{c}^\dagger \mathbf{A} \mathbf{c}$ that can be taken back to zero later, we obtain

$$\begin{aligned} \langle O \rangle_{\mathbf{h}} &= \partial_\eta \left(\ln \text{Tr} [U_{\mathbf{h}}(\beta, \tau) e^{\eta O} U_{\mathbf{h}}(\tau, 0)] \right) \Big|_{\eta=0} = \partial_\eta \left(\ln \det[\mathbf{I} + \mathbf{B}_{\mathbf{h}}(\beta, \tau) e^{\eta \mathbf{A}} \mathbf{B}_{\mathbf{h}}(\tau, 0)] \right) \Big|_{\eta=0} \\ &= \partial_\eta \left(\text{Tr} [\ln(\mathbf{I} + \mathbf{B}_{\mathbf{h}}(\beta, \tau) e^{\eta \mathbf{A}} \mathbf{B}_{\mathbf{h}}(\tau, 0))] \right) \Big|_{\eta=0} = \text{Tr} [\mathbf{B}_{\mathbf{h}}(\tau, 0) (\mathbf{I} + \mathbf{B}_{\mathbf{h}}(\beta, 0))^{-1} \mathbf{B}_{\mathbf{h}}(\beta, \tau) \mathbf{A}] \\ &= \text{Tr} \left[(\mathbf{B}^{-1}(\beta, \tau) \mathbf{B}^{-1}(\tau, 0) + \mathbf{I})^{-1} (\mathbf{B}(\tau, 0) \mathbf{B}(\beta, \tau))^{-1} (\mathbf{B}(\tau, 0) \mathbf{B}(\beta, \tau)) \mathbf{A} \right] \quad (3.54) \\ &= \text{Tr} \left[(\mathbf{I} + \mathbf{B}(\tau, 0) \mathbf{B}(\beta, \tau))^{-1} (\mathbf{I} + \mathbf{B}(\tau, 0) \mathbf{B}(\beta, \tau) - \mathbf{I}) \mathbf{A} \right] \\ &= \text{Tr} \left[\left(\mathbf{I} - (\mathbf{I} + \mathbf{B}_{\mathbf{h}}(\tau, 0) \mathbf{B}_{\mathbf{h}}(\beta, \tau))^{-1} \right) \mathbf{A} \right] \end{aligned}$$

In particular, for the case of the Green's function: $O = c_i c_j^\dagger$, $A_{xy} = \delta_{ij} - \delta_{xj}\delta_{yi}$, leading to Eq.(3.52). A generalization of Eq.(3.54) for higher order derivatives allows us to obtain the connected correlation functions, or cumulants (denoted $\langle\langle \dots \rangle\rangle_{\mathbf{h}}$), revealing a connection with Wick's theorem. Defining

$$\langle\langle O_n O_{n-1} \dots O_1 \rangle\rangle_{\mathbf{h}} = \partial_{\eta_n} \partial_{\eta_{n-1}} \dots \partial_{\eta_1} \ln \text{Tr}[U_{\mathbf{h}}(\beta, \tau) e^{\eta_n O_n} e^{\eta_{n-1} O_{n-1}} \dots e^{\eta_1 O_1} U_{\mathbf{h}}(\tau, 0)] \Big|_{\eta_n=\eta_{n-1}=\dots=\eta_1=0} \quad (3.55)$$

we see a pattern emerging, relating multi-point correlators and cumulants. Omitting the subscript \mathbf{h} :

$$\begin{aligned}\langle\langle O_1 \rangle\rangle &= \langle O_1 \rangle \quad \langle\langle O_2 O_1 \rangle\rangle = \langle O_2 O_1 \rangle - \langle O_2 \rangle \langle O_1 \rangle \\ \langle\langle O_3 O_2 O_1 \rangle\rangle &= \langle O_3 O_2 O_1 \rangle - \langle O_3 \rangle \langle\langle O_2 O_1 \rangle\rangle - \langle O_2 \rangle \langle\langle O_3 O_1 \rangle\rangle - \langle O_1 \rangle \langle\langle O_3 O_2 \rangle\rangle - \langle O_1 \rangle \langle O_2 \rangle \langle O_3 \rangle \\ \langle O_n O_{n-1} \dots O_1 \rangle &= \langle\langle O_n O_{n-1} \dots O_1 \rangle\rangle + \sum_{j=1}^n \langle\langle O_n \dots \widehat{O_j} \dots O_1 \rangle\rangle \langle\langle O_j \rangle\rangle \\ &\quad + \sum_{j>i} \langle\langle O_n \dots \widehat{O_j} \dots \widehat{O_i} \dots O_1 \rangle\rangle \langle\langle O_j O_i \rangle\rangle + \dots + \langle\langle O_n \rangle\rangle \langle\langle O_{n-1} \rangle\rangle \dots \langle\langle O_1 \rangle\rangle,\end{aligned}\tag{3.56}$$

where the operators with a hat \widehat{O}_j are excluded from the sum. This is equivalent to the zero temperature version of Wick's theorem that we state in appendix A, Eq.(A.38).

We can now compute the cumulants order by order. In particular, one can show that operators of the type $\left\langle\left\langle c_{x_n}^\dagger c_{y_n} c_{x_{n-1}}^\dagger c_{y_{n-1}} \dots c_{x_1}^\dagger c_{y_1} \right\rangle\right\rangle_{\mathbf{h}}$ can always be written in terms of a linear combination of products of pair averages of the type $\langle c^\dagger c \rangle$ [60]. A case of particular relevance for the observables we shall be interested in is obtained by doing so for a four c -operator average, i.e. $n = 2$, and $A_{xy}^{(i)} = \delta_{x,x_i} \delta_{y,y_i} \dots$

Before proceeding, recall that, for an invertible matrix \mathbf{A} , the derivative of its inverse with respect to a parameter η can be obtained in terms of the derivative of the matrix itself and its inverse. The sought identity is easy to show by using $\mathbf{A}^{-1} \mathbf{A} = \mathbf{I}$ and differentiating both the LHS and the RHS: $\partial_\eta(\mathbf{A}^{-1} \mathbf{A}) = 0 \iff (\partial_\eta \mathbf{A}) \mathbf{A}^{-1} + \mathbf{A} \partial_\eta \mathbf{A}^{-1} = 0 \iff \partial_\eta \mathbf{A}^{-1} = -\mathbf{A}^{-1} (\partial_\eta \mathbf{A}) \mathbf{A}^{-1}$.

$$\begin{aligned}\langle\langle c_{x_2}^\dagger c_{y_2} c_{x_1}^\dagger c_{y_1} \rangle\rangle_{\mathbf{h}} &= \partial_{\eta_2} \partial_{\eta_1} \left(\text{Tr} \left[\ln(\mathbf{I} + \mathbf{B}_{\mathbf{h}}(\beta, \tau) e^{\eta_2 \mathbf{A}_2} e^{\eta_1 \mathbf{A}_1} \mathbf{B}_{\mathbf{h}}(\tau, 0)) \right] \right|_{\eta=0} \\ &= \partial_{\eta_2} \text{Tr} \left[(\mathbf{I} + \mathbf{B}_{\mathbf{h}}(\beta, \tau) e^{\eta_2 \mathbf{A}_2} e^{\eta_1 \mathbf{A}_1} \mathbf{B}_{\mathbf{h}}(\tau, 0))^{-1} \mathbf{B}_{\mathbf{h}}(\beta, \tau) e^{\eta_2 \mathbf{A}_2} e^{\eta_1 \mathbf{A}_1} \mathbf{A}_1 \mathbf{B}_{\mathbf{h}}(\tau, 0) \right] \Big|_{\eta=0} \\ &= \text{Tr} \left[\mathbf{B}_{\mathbf{h}}(\tau, 0) (\mathbf{I} + \mathbf{B}_{\mathbf{h}}(\beta, \tau) \mathbf{B}_{\mathbf{h}}(\tau, 0))^{-1} \mathbf{B}_{\mathbf{h}}(\beta, \tau) \mathbf{A}_2 \mathbf{A}_1 \right] \\ &\quad - \text{Tr} \left[\mathbf{B}_{\mathbf{h}}(\tau, 0) (\mathbf{I} + \mathbf{B}_{\mathbf{h}}(\beta, \tau) \mathbf{B}_{\mathbf{h}}(\tau, 0))^{-1} \mathbf{B}_{\mathbf{h}}(\beta, \tau) \mathbf{A}_2 \mathbf{B}_{\mathbf{h}}(\tau, 0) (\mathbf{I} + \mathbf{B}_{\mathbf{h}}(\beta, \tau) \mathbf{B}_{\mathbf{h}}(\tau, 0))^{-1} \mathbf{B}_{\mathbf{h}}(\beta, \tau) \mathbf{A}_1 \right] \\ &= \text{Tr}[(\mathbf{I} - \mathbf{G}) \mathbf{A}_2 \mathbf{A}_1] - \text{Tr}[(\mathbf{I} - \mathbf{G}) \mathbf{A}_2 (\mathbf{I} - \mathbf{G}) \mathbf{A}_1] = \text{Tr}[(\mathbf{I} - \mathbf{G}) \mathbf{A}_2 \mathbf{G} \mathbf{A}_1] = \langle c_{x_2}^\dagger c_{y_1} \rangle_{\mathbf{h}} \langle c_{y_2} c_{x_1}^\dagger \rangle_{\mathbf{h}},\end{aligned}\tag{3.57}$$

where, in the last step, we simply identify the only element of the matrix $(\mathbf{I} - \mathbf{G}) \mathbf{A}_2 \mathbf{G} \mathbf{A}_1$ that is on the diagonal, which is the only one that is picked up by the trace. By comparison with Eq.(3.56), we obtain an important relation we will use repeatedly:

$$\langle c_{x_2}^\dagger c_{y_2} c_{x_1}^\dagger c_{y_1} \rangle_{\mathbf{h}} = \langle c_{x_2}^\dagger c_{y_2} \rangle_{\mathbf{h}} \langle c_{x_1}^\dagger c_{y_1} \rangle_{\mathbf{h}} + \langle c_{x_2}^\dagger c_{y_1} \rangle_{\mathbf{h}} \langle c_{y_2} c_{x_1}^\dagger \rangle_{\mathbf{h}}\tag{3.58}$$

3.3.1 Obtaining observables in terms of Green's functions

The simplest observables that can be obtained from the Green's function are the (site-dependent) electron density and the double occupancy:

$$\rho_{i,\sigma} = \langle c_{i,\sigma}^\dagger c_{i,\sigma} \rangle = 1 - \langle c_{i,\sigma} c_{i,\sigma}^\dagger \rangle = 1 - G_{ii}^\sigma \quad \langle n_{i,\uparrow} n_{i,\downarrow} \rangle = (1 - G_{ii}^\uparrow)(1 - G_{ii}^\downarrow)\tag{3.59}$$

It is natural to think of averaging them over the lattice, which is justified by the fact that the Hubbard Hamiltonian is translationally invariant. Thus, $\rho_{i\sigma}$ and $\langle n_{i,\uparrow} n_{i,\downarrow} \rangle$ should be independent of the spatial site. This statement is strict when exactly solving the model, but it becomes only approximate, i.e. valid

only on average in our simulations. Thus, to reduce statistical errors, we take the averages

$$\rho = \frac{1}{N} \sum_{\sigma} \sum_{i=0}^{N-1} \rho_{i\sigma} = 2 - \frac{1}{N} \sum_{\sigma} \sum_{i=0}^{N-1} G_{ii}^{\sigma} \quad \langle n_{\uparrow} n_{\downarrow} \rangle = 1 - \frac{1}{N} \sum_{i=0}^{N-1} (G_{ii}^{\uparrow} + G_{ii}^{\downarrow} - G_{ii}^{\uparrow} G_{ii}^{\downarrow}) \quad (3.60)$$

It is implicit that $\rho_{i\sigma}$ is already averaged over the HS-field configurations that were sampled through the simulation. One must pay attention to the symmetry of the model at hand, since, say a similar model for a disordered system including randomness would not be translationally invariant anymore (the same is true for the model of TMDNRs we will ultimately consider). Now, the average kinetic energy is similarly obtained.

$$\langle \mathcal{H}_K \rangle = -t \sum_{\langle i,j \rangle, \sigma} \left\langle (c_{i\sigma}^{\dagger} c_{j\sigma} + c_{j\sigma}^{\dagger} c_{i\sigma}) \right\rangle = t \sum_{\langle i,j \rangle, \sigma} (G_{ij}^{\sigma} + G_{ji}^{\sigma}) = t \sum_{i,j,\sigma} K_{ij} (G_{ij}^{\sigma} + G_{ji}^{\sigma}), \quad (3.61)$$

where the minus sign is due to the switching of the order of the operators bringing the c^{\dagger} to the right.

3.3.2 Correlation functions

One of the most important goals of QMC simulations is to inspect the system for order of various types, and to find associated phase transitions. This is done by computing correlation functions $C_i(j)$, measuring how correlated two sites separated by a distance j are.

$$C(i,j) = \langle \mathcal{O}_{i+j} \mathcal{O}_i^{\dagger} \rangle - \langle \mathcal{O}_{i+j} \rangle \langle \mathcal{O}_i^{\dagger} \rangle, \quad (3.62)$$

where \mathcal{O} is an operator corresponding to the order parameter of the phase transition. For example, we might be looking for magnetic order, in which case the relevant operators are S_i^z , i.e. $\mathcal{O}_i = n_{i\uparrow} - n_{i\downarrow}$, $\mathcal{O}_i^{\dagger} = n_{i\uparrow} - n_{i\downarrow}$, or superconductivity, where we would like to measure correlations in fermion pair formation: $\mathcal{O}_i = c_{i\downarrow} c_{i\uparrow}$, $\mathcal{O}_i^{\dagger} = c_{i\uparrow}^{\dagger} c_{i\downarrow}^{\dagger}$. In general, we expect a high temperature disordered phase, for which correlations decay exponentially $C(i,j) \propto e^{-j/\xi}$, where ξ is a characteristic length called the correlation length. At some point, there can be a transition to a low temperature phase, where $C(i,j) \propto m^2$, where m is the order parameter for the transition. Right at the transition, that is at $T = T_c$, there might be singular behavior. In continuous phase transitions, the correlation length diverges $\xi \propto (T - T_c)^{-\nu}$, and the correlations decay slower (in fact algebraically): $C(i,j) \propto j^{-\eta}$, in an intermediate behavior between exponential decay and a constant. The *critical* exponents ν , and η are characteristic of the transition, or more accurately, of the universality class it belongs to. The behavior of all these quantities on finite lattices does not precisely correspond to the infinite system behavior. The tails of the functions, i.e. the $j \rightarrow \infty$ limit is not well captured. Finite-size scaling is a method to improve on these predictions.

To evaluate correlation functions we use Wick's theorem. Expectations of more than two fermion creation and annihilation operators reduce to products of expectations of pairs of creation and annihilation operators. For example, for spin order in the x/y direction: $C(i,j) = \langle c_{i+j,\downarrow}^{\dagger} c_{i+j,\uparrow} c_{i,\uparrow}^{\dagger} c_{i,\downarrow} \rangle = G_{i+j,i}^{\uparrow} G_{i,i+j}^{\downarrow}$.

How would one measure a correlation function experimentally? Fortunately, there is a quantity that is easy to measure called structure factor, which is just the Fourier transform of the correlation function

$$S(\mathbf{q}) = \frac{1}{N} \sum_{i,j} e^{i\mathbf{q} \cdot (\mathbf{R}_j - \mathbf{R}_i)} C(i,j) \quad (3.63)$$

The accuracy of QMC simulations can be evaluated by comparing the results for the Fourier trans-

formed correlation functions with the corresponding experimentally measured structure factors.

3.3.3 Imaginary-time displaced Green's functions and susceptibilities

By applying Wick's theorem, any “equal-time observable” may written in terms of a combination of products of certain elements of the single-particle equal-time Green's matrices $\mathbf{G}(\tau, \tau)$. Other “unequal-time” quantities, such as susceptibilities require time-displaced correlators.

$$\chi_{\mathcal{O}}(i\omega_n) = \int_0^\beta \langle \mathcal{O}^\dagger(\tau) \mathcal{O}(0) \rangle e^{i\omega_n \tau} d\tau, \quad (3.64)$$

whose $\omega = 0$ component can be Fourier transformed and represented in \mathbf{q} -space, or averaged over the lattice ($\chi(\mathbf{0}) \equiv \chi$), as we shall often do. The more general quantity $\chi(\mathbf{q}, \omega)$ describes scattering events where momentum changes by \mathbf{q} , and energy changes by ω .

$$\chi(\mathbf{q}) = \frac{1}{N} \sum_{i,j} e^{i\mathbf{q} \cdot (\mathbf{R}_j - \mathbf{R}_i)} \int_0^\beta \langle \mathcal{O}_{i+j}^\dagger(\tau) \mathcal{O}_i(0) \rangle d\tau \quad \text{or} \quad \chi = \frac{1}{N} \sum_{i,j} \int_0^\beta \langle \mathcal{O}_{i+j}^\dagger(\tau) \mathcal{O}_i(0) \rangle d\tau \quad (3.65)$$

When we apply Wick's theorem to this case, contractions between fermion operators at different time slices arise, and thus we require matrix elements of the *unequal*-time Green's function

$$\mathbf{G}(\tau', \tau) = \mathbf{B}(\tau', \tau) (\mathbf{I} + \mathbf{B}(\tau, 0) \mathbf{B}(\beta, \tau))^{-1} \quad (3.66)$$

The Green's function can also be propagated with the \mathbf{B} -matrices to obtain these unequal-time Green's matrices: $\mathbf{G}(\tau_2, \tau_1) = \mathbf{B}(\tau_2, \tau') \mathbf{G}(\tau', \tau_1)$, $\tau_2 > \tau_1$, or $\mathbf{G}(\tau_1, \tau_2) = \mathbf{G}(\tau', \tau_1) \mathbf{B}^{-1}(\tau_2, \tau')$, $\tau_2 < \tau_1$, but this procedure too becomes unstable as β or N increase, as we will discuss later.

The unequal time Green's function is defined as $G_{ij}(\tau_1, \tau_2) = \langle \mathcal{T} c_i(\tau_1) c_j^\dagger(\tau_2) \rangle_h$, i.e. for $\tau_1 > \tau_2$:

$$\langle \mathcal{T} c_i(\tau_1) c_j^\dagger(\tau_2) \rangle_h = \frac{\text{Tr}[U_h(\beta, \tau_2) U_h^{-1}(\tau_1, \tau_2) c_i U_h(\tau_1, \tau_2) c_j^\dagger U_h(\tau_2, 0)]}{\text{Tr}[U_h(\beta, 0)]} \quad (3.67)$$

Computing $U_h^{-1}(\tau_1, \tau_2) c_i U_h(\tau_1, \tau_2)$ involves computing $c_i(\tau) = e^{\tau \mathbf{c}^\dagger \mathbf{A} \mathbf{c}} c_i e^{-\tau \mathbf{c}^\dagger \mathbf{A} \mathbf{c}}$ by using the Heisenberg equation: $\partial_\tau c_i(\tau) = e^{\tau \mathbf{c}^\dagger \mathbf{A} \mathbf{c}} [\mathbf{c}^\dagger \mathbf{A} \mathbf{c}, c_i] e^{-\tau \mathbf{c}^\dagger \mathbf{A} \mathbf{c}} = -\mathbf{A} \mathbf{c}(\tau) \rightsquigarrow c_i(\tau) = (e^{-\mathbf{A}} \mathbf{c})_i$, $c_i^\dagger(\tau) = (\mathbf{c}^\dagger e^{\mathbf{A}})_i$.

Since \mathbf{A} is an arbitrary matrix, and the \mathbf{B} -matrices are matrix exponentials, we can define $\mathbf{B} = e^{-\mathbf{A}}$:

$$U_h^{-1}(\tau_1, \tau_2) c_i U_h(\tau_1, \tau_2) = (\mathbf{B}_h(\tau_1, \tau_2) \mathbf{c})_i U_h^{-1}(\tau_1, \tau_2) c_i^\dagger U_h(\tau_1, \tau_2) = (\mathbf{c}^\dagger \mathbf{B}_h^{-1}(\tau_1, \tau_2))_i, \quad (3.68)$$

and since the \mathbf{B} 's are matrices, not operators, they can come out of the trace. This leads to a Wick's theorem for time-displaced Green's functions that stems directly from the equal-time version.

$$\begin{aligned} G_{ij}(\tau_1, \tau_2) &= \langle c_i(\tau_1) c_j^\dagger(\tau_2) \rangle_h = [\mathbf{B}_h(\tau_1, \tau_2) \mathbf{G}(\tau_2)]_{ij}, \tau_1 > \tau_2 \\ G_{ij}(\tau_1, \tau_2) &= -\langle c_j^\dagger(\tau_2) c_i(\tau_1) \rangle_h = -[(\mathbf{I} - \mathbf{G}(\tau_1)) \mathbf{B}_h^{-1}(\tau_1, \tau_2)]_{ij}, \tau_1 < \tau_2 \end{aligned} \quad (3.69)$$

3.4 Stabilization

The Green's function is needed both to perform importance sampling and to make measurements. Naively, its computation would involve multiplying a long chain of \mathbf{B} -matrices, adding the identity, and then taking the inverse. We saw that this costly procedure can be substituted by a more efficient update scheme, which involves wrapping the Green's function as one sweeps between imaginary time slices. The stability of this procedure depends on the conditioning of the matrices at hand. As the temperature is

lowered, or the system size increased, round-off errors accumulate and precision is gradually lost. Thus, we must compute the Green's function from scratch "naively" once in a while.

As β increases more and more, the problem becomes so severe that the Green's function cannot be computed at all! This is an effect due to finite-precision computing. Potentially, \mathbf{B} -matrices contain largely different energy scales, and this is particularly likely as β or N are increased. As more and more of them are multiplied together, the condition number of the product increases, and the situation worsens, with the energy scales becoming exponentially divergent. Thus, computing Green's functions determinants involves taking small differences between large matrix elements, which are very inaccurate since they become dominated by the least significant bits of these matrix elements when calculated in a finite-precision computer.

Let us look at this numerical problem from a physical standpoint. For a given configuration of the HS field, the single-particle propagators $\mathbf{B}(\tau', \tau)$ amplify "low energy" states, while attenuating "high energy" ones. Moreover, the states near the intermediate "Fermi energy" of each single-particle problem are exponentially suppressed with respect to the states at the bottom of the "band". Unfortunately, the states near the Fermi energy are precisely the ones affect the behavior of fermionic systems the most.

This intuitive single-particle picture translates into correlated systems, which we simulate by considering a sum over many time-varying single-particle problems. The problem is that when computing the single-particle Green's function, we cannot extract small-scale features out of $\mathbf{B}(\beta, \tau)$ or $\mathbf{B}(\tau, 0)$.

Note that this is not a problem of representation. Both the sparse matrices making up \mathbf{B} , and the Green's matrices \mathbf{G} can be represented on finite-precision computers with sufficient precision. The loss of information occurs when propagating states to long imaginary times, which requires a multiplication of a long chain of \mathbf{B} -matrices. The precision of the resulting matrix elements tends to deteriorate rapidly. Since this does not seem to be an intrinsic problem, in principle we could devise a different scheme to multiply the propagators so as not to lose information.

The main idea is to maintain small scales explicitly, and not implicitly as inaccurate differences of large numbers. Additionally, we must combine the largely different numerical scales at the last step of the calculation of \mathbf{G} , cutting off the smallest, inconsequential scales only at the end of the computation, so that no relevant information is lost. Let us analyze this idea in the band picture. Setting the chemical potential to μ , the numerical scale associated to a single-particle state of energy E , $e^{-\beta(E-\mu)}$, either diverges, or vanishes exponentially with β . An example of a typical Green's function element is the occupation $(e^{\beta(E-\mu)} + 1)^{-1}$, which ranges from 0 to 1. By keeping the numerical scales $e^{\beta(E-\mu)}$ separated, we can cut off ill-behaved scales in the last step of the computation of \mathbf{G} by adding terms of order one. The advantage of this approach is that it focuses on stabilizing the matrix products and inversions required to obtain \mathbf{G} [27, 89, 90], while always operating with $N \times N$ matrices. Other approaches [10, 91] use higher-dimensional matrices requiring more computer time and memory.

In this section, we start by explaining how to stabilize matrix multiplications and then discuss large and small scale cut off in Green's functions computations.

3.4.1 Stable matrix multiplication

The condition number of a matrix $\mathbf{A}_{\{\alpha\}}$ that depends on a set of parameters $\{\alpha\}$ is defined as the ratio of the maximal and minimal singular values $\kappa(\mathbf{A}_{\{\alpha\}}) \equiv s_{\max}/s_{\min}$. It measures how ill-conditioned a matrix is, thus representing an upper bound on the propagation of errors when doing matrix multiplications. The higher the condition number, the more precision-related inaccuracies tend to accumulate, and when $\kappa = \infty$, the matrix is not invertible, although in practice it becomes more and more difficult to invert it numerically with precision as κ increases.

To isolate the diverging energy scales, we represent ill-conditioned matrices in the form \mathbf{QDT} , where \mathbf{D} contains the diverging singular values explicitly, and \mathbf{Q} and \mathbf{T} are sufficiently well-conditioned matrices. More precisely, these are matrices that can be multiplied without appreciable loss of precision. There are many such decompositions, based on the constraints imposed on \mathbf{Q} and \mathbf{T} . For example, if they are chosen to be orthogonal, we obtain the singular value decomposition, which is particularly stable, but numerically expensive compared to other choices [85]. The modified Gram-Schmidt factorization is faster, corresponding to the choice \mathbf{Q} orthogonal, and \mathbf{T} unit upper triangular. The matrix is decomposed in the form $\mathbf{A} = \mathbf{QR}$, with \mathbf{Q} orthogonal, and \mathbf{R} upper triangular, and then a diagonal matrix is introduced so as to make appear the unit upper triangular matrix $\mathbf{T} = \mathbf{D}^{-1}\mathbf{R}$, which is well conditioned and can be multiplied safely in simulations, even it has appreciably large numbers, without leading to numerical instabilities. Decompositions of this type explicitly separate the largely different numerical scales for a *column-stratified* matrix \mathbf{A} , as the example below shows. Matrix elements represented as x are $\mathcal{O}(1)$, while the larger sizes represent different numerical scales. A good compromise between speed and stability is the QR decomposition with column pivoting via Householder reflections [92], which is the subroutine we use in our implementation, following [27], where rigorous bounds are proven on the conditioning of the matrices obtained in this fashion.

$$\mathbf{Q}^{-1}\mathbf{AT}^{-1} = \begin{pmatrix} x & x & x & x \\ x & x & x & x \\ x & x & x & x \\ x & x & x & x \end{pmatrix} \begin{pmatrix} X & X & X & x \\ X & X & X & x \\ X & X & X & x \\ X & X & X & x \end{pmatrix} \begin{pmatrix} x & x & x & x \\ x & x & x & x \\ x & x & x & x \\ x & x & x & x \end{pmatrix} = \begin{pmatrix} X & 0 & 0 & 0 \\ 0 & X & 0 & 0 \\ 0 & 0 & X & 0 \\ 0 & 0 & 0 & x \end{pmatrix} = \mathbf{D} \quad (3.70)$$

To compute \mathbf{G} , we recall Eq.(3.52), and note that the problem boils down to numerically inverting a matrix which involves a long chain of multiplied matrices⁴ $(\mathbf{I}_N + \mathbf{B}_{\Lambda-1}\mathbf{B}_{\Lambda-2}\dots\mathbf{B}_1)^{-1}$, where \mathbf{I}_N is the $N \times N$ identity. We start by QR-decomposing $\mathbf{B}_0 = \mathbf{Q}_0\mathbf{R}_0\mathbf{P}_0$, where \mathbf{Q}_0 is orthogonal, \mathbf{R}_0 is upper triangular, and \mathbf{P}_0 is a permutation matrix resulting from column pivoting. Although it is not guaranteed, the diagonal of \mathbf{R} generally reflects the magnitudes of the singular values of \mathbf{B}_0 . Extracting the diagonal $\mathbf{D}_0 = \text{diag}(\mathbf{R}_0)$, we define $\mathbf{T}_0 = \mathbf{D}_0^{-1}\mathbf{R}_0\mathbf{P}_0$ so that

$$\mathbf{B}_0 = \mathbf{Q}_0\mathbf{R}_0\mathbf{P}_0 = \mathbf{Q}_0\mathbf{D}_0(\mathbf{D}_0^{-1}\mathbf{R}_0\mathbf{P}_0) = \mathbf{Q}_0\mathbf{D}_0\mathbf{T}_0, \quad (3.71)$$

leaving \mathbf{T}_0 well conditioned, which will be crucial in what follows.

Now, for $\lambda = 1, 2, \dots, \Lambda$, \mathbf{QRP} -decompose: $(\mathbf{B}_\lambda\mathbf{Q}_{\lambda-1})\mathbf{D}_{\lambda-1} = \mathbf{Q}_\lambda\mathbf{R}_\lambda\mathbf{P}_\lambda \equiv \mathbf{Q}_\lambda\mathbf{D}_\lambda\mathbf{T}_\lambda$, with the diagonal

⁴The imaginary time slice index goes from 0 to $\Lambda - 1$ because the \mathbf{B}_λ -matrices are already partial products of the original \mathbf{B}_l -matrices. The procedure we present is applied after multiplying together as many \mathbf{B} -matrices as possible without significantly losing precision.

matrix $\mathbf{D}_\lambda = \text{diag}(\mathbf{R}_\lambda)$, and $\mathbf{T}_\lambda = \mathbf{D}_\lambda^{-1} \mathbf{R}_\lambda \mathbf{P}_\lambda$. Note that $\mathbf{B}_\lambda \mathbf{Q}_{\lambda-1} \mathbf{D}_{\lambda-1}$ is column-stratified, so that the diagonal matrix contains explicitly separated numerical scales. Finally, the \mathbf{B} -matrix chain becomes

$$\mathbf{B}_{\Lambda-1} \dots \mathbf{B}_1 \mathbf{B}_0 = \mathbf{Q}_{\Lambda-1} \mathbf{D}_{\Lambda-2} (\mathbf{T}_{\Lambda-1} \dots \mathbf{T}_1 \mathbf{T}_0) \equiv \mathbf{QDT}, \quad (3.72)$$

which is also column-stratified since the diagonal entries are typically ordered by magnitude from largest to smallest, and the product $\mathbf{T} = \mathbf{T}_{\Lambda-1} \dots \mathbf{T}_1 \mathbf{T}_0$ is modestly well-conditioned.

Note that the \mathbf{B} -matrices we consider are already partial products of the original ones. We suppose that we can multiply L/Λ of them stably, and then decouple the numerical scales by identifying column-stratified matrices and applying the procedure above. Imagine that we have already decomposed a partial product $\mathbf{B}(\tau, 0) = \mathbf{QDT}$, and that we want to extend the single-propagator to imaginary time $\tau + \tau_0$, where τ_0 is the time we can reach by simply multiplying \mathbf{B} 's together, without affecting precision. Then, schematically, we can see that the numerical scales are explicitly separated:

$$\mathbf{B}(\tau + \tau_0, 0) = \underbrace{\mathbf{B}(\tau + \tau_0, \tau) \mathbf{QDT}}_{\mathbf{Q}'\mathbf{D}'\mathbf{T}'} = \mathbf{BQ} \begin{pmatrix} \mathbf{X} & 0 & 0 & 0 \\ 0 & \mathbf{X} & 0 & 0 \\ 0 & 0 & \mathbf{X} & 0 \\ 0 & 0 & 0 & \mathbf{X} \end{pmatrix} \mathbf{T} = \begin{pmatrix} \mathbf{X} & \mathbf{X} & \mathbf{x} & \mathbf{x} \\ \mathbf{X} & \mathbf{X} & \mathbf{x} & \mathbf{x} \\ \mathbf{X} & \mathbf{X} & \mathbf{x} & \mathbf{x} \\ \mathbf{X} & \mathbf{X} & \mathbf{x} & \mathbf{x} \end{pmatrix} \mathbf{T} = \mathbf{Q}'\mathbf{D}'(\mathbf{T}'\mathbf{T}) \quad (3.73)$$

3.4.2 Inverting to obtain the Green's function

After successive decompositions, the chain of \mathbf{B} -matrices in Eq.(3.52) takes on the form \mathbf{QDT} . Using the orthogonality condition $\mathbf{Q}^{-1} = \mathbf{Q}^T$, and decomposing $\mathbf{Q}^T \mathbf{T}^{-1} + \mathbf{D}$ in $\mathbf{Q}'\mathbf{D}'\mathbf{T}'$:

$$(\mathbf{I} + \mathbf{QDT})^{-1} = [\mathbf{Q}(\mathbf{Q}^T \mathbf{T}^{-1} + \mathbf{D})\mathbf{T}]^{-1} = \mathbf{T}^{-1} \underbrace{(\mathbf{Q}^T \mathbf{T}^{-1} + \mathbf{D})^{-1} \mathbf{Q}^T}_{\mathbf{Q}'\mathbf{D}'\mathbf{T}'} = (\mathbf{T}'\mathbf{T})^{-1} (\mathbf{D}')^{-1} (\mathbf{Q}\mathbf{Q}')^T, \quad (3.74)$$

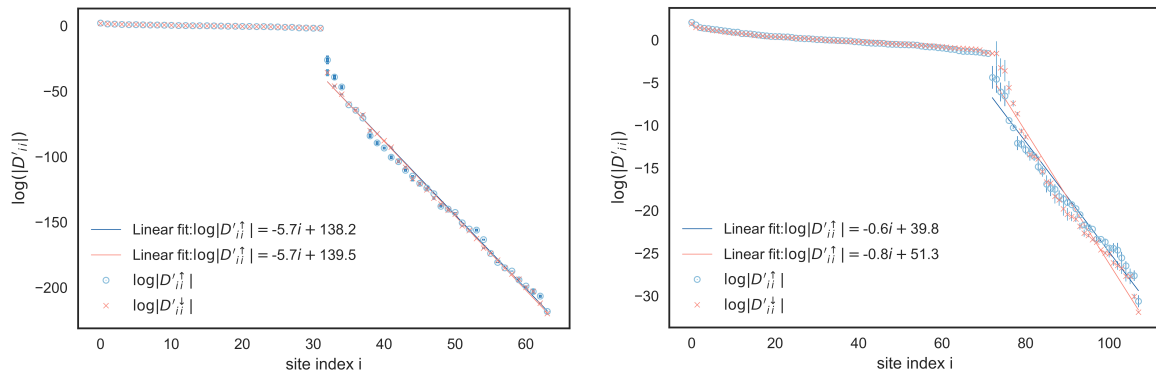


Figure 3.2: Exponentially divergent (and order one) diagonal entries of \mathbf{D}' , showing the orders of magnitude spanned by the matrix elements of the stabilized matrix product. The depicted systems are the same of Fig.(3.1).

The idea is to isolate the divergent scales in \mathbf{D} right up until they are combined with the order one elements of $\mathbf{Q}^T \mathbf{T}^{-1}$, which cut off the divergent scales. This is analogous to what happens in the band picture, where the unit term cuts off divergent scales in $e^{\beta(E-\mu)}$ when we compute the occupation of a state (which is an element of the Green's matrix). Notice that while \mathbf{Q} and \mathbf{T} are well conditioned, $\kappa(\mathbf{Q}^T \mathbf{T}^{-1} + \mathbf{D})$ and $\kappa(\mathbf{I} + \prod_l \mathbf{B}_l)$ are comparable, and the upper bound on the error in the matrix elements of the inverse $(\mathbf{Q}^T \mathbf{T}^{-1} + \mathbf{D})^{-1}$ is proportional to the condition number, which can be huge, due

to the divergent scales in \mathbf{D} .

Then, how does this procedure work? We gave an intuitive picture which we now make mathematically precise. One may safely assume that $\mathbf{Q}^T \mathbf{T}^{-1}$ has moderate magnitude and condition number, so that when we add the first many elements of the diagonal \mathbf{D} , which are typically huge, we end up with diagonally dominant matrix. Its first many rows are essentially a diagonal matrix plus a zero block on the right. The remaining rows determine the effective condition number, so that $\kappa(\mathbf{Q}^T \mathbf{T}^{-1} + \mathbf{D})$ is actually reduced and the matrix becomes better conditioned. This corresponds to defining numerical stability operationally. We maintain the numerical scales explicitly, so that the information that we lose at the end is practically irrelevant in computing the Green's function: because of the way we organized the calculation, the overwriting of small scales by unit numbers and of unit scales by big numbers does not decrease precision, instead cutting off certain well picked numerical scales.

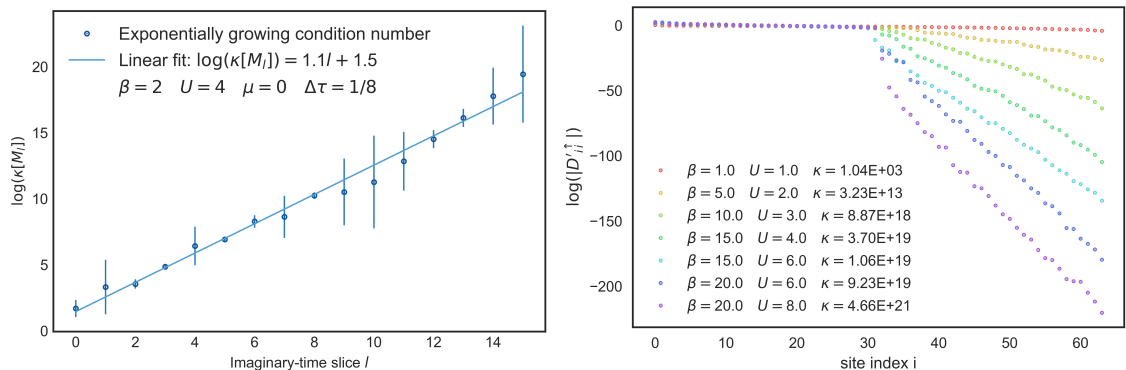


Figure 3.3: Left: Exponentially growing condition number $\kappa[\mathbf{M}_l]$ obtained by multiplying \mathbf{B} -matrices naively. Right: Absolute values of the diagonal entries of \mathbf{D}' for varying β and U and corresponding condition number of the matrix to invert to obtain the Green's function: $\kappa(\mathbf{Q}^T \mathbf{T}^{-1} + \mathbf{D})$. Here, we show that are able to stabilize a multiplication of \mathbf{B} -matrices with elements spanning about 150 orders of magnitude, as can be seen by the elements of \mathbf{D}' . Here, β is measured in units of the hopping, t .

In the band picture, our reasoning becomes particularly evident. As long as a state deep into the band is occupied, it does not matter whether it is amplified by say 10^{100} or even 10^{1000} . The same applies for high energy states, which must be cut off anyway, so there is no problem in attenuating them by 10^{-100} or 10^{-1000} . In our calculation of \mathbf{G} , this corresponds to finding the single-particle states for fixed HS field \mathbf{h} via the transformation matrices \mathbf{Q} and \mathbf{T} . The energy scales are stored in \mathbf{D} , so that when we add $\mathbf{Q}^T \mathbf{T}^{-1}$, the divergent scales are cut off, and so we can identify which states were amplified or attenuated. These do not impact the calculation of \mathbf{G} significantly, and because the computer cannot store big or small numbers anyway, it suffices to identify the big and small scales, which turn out not to contribute very much to \mathbf{G} .

A more accurate alternative proposed in [27] uses another more efficient method of separating the numerical scales. The idea is to define two diagonal matrices of big and small entries, respectively \mathbf{D}^b and \mathbf{D}^s , defined as

$$i = 0, \dots, N - 1 : D_{ii}^b = \begin{cases} D_{ii}, & \text{if } |D_{i,i}| > 1 \\ 1, & \text{otherwise} \end{cases} \quad D_{ii}^s = \begin{cases} D_{ii}, & \text{if } |D_{i,i}| \leq 1 \\ 1, & \text{otherwise} \end{cases} \quad (3.75)$$

so that $\mathbf{D} = \mathbf{D}^b \mathbf{D}^s$. Now, to compute the inverse, we can pull out \mathbf{D}^b , so that $(\mathbf{D}^b)^{-1}$ annihilates the

top many rows of \mathbf{Q}^T , while \mathbf{D}^s annihilates the bottom many rows of \mathbf{T} , isolating the relevant numerical scales, and leaving us with the fairly well conditioned matrix $(\mathbf{D}^b)^{-1}\mathbf{Q}^T + \mathbf{D}^s\mathbf{T}$ to invert.

$$(\mathbf{Q}^T\mathbf{T}^{-1} + \mathbf{D}^b\mathbf{D}^s)^{-1} = \mathbf{T}^{-1}[(\mathbf{D}^b)^{-1}\mathbf{Q}^T + \mathbf{D}^s\mathbf{T}]^{-1}(\mathbf{D}^b)^{-1} \quad (3.76)$$

The matrix elements of \mathbf{G} are computed accurately via the update scheme of Eq.(3.47), however we can only use the wrapping of Eq.(3.49) (which effectively involves multiplying \mathbf{B} -matrices) to “propagate” \mathbf{G} for L/Λ slices, after which \mathbf{G} must be recomputed from scratch using the \mathbf{QDT} decompositions. Thus, the cost of the stabilization is $\mathcal{O}(\Lambda^2) \propto \beta^2$, which may dominate at very low temperatures for certain problems. There is a great deal of recompuation involved in the stabilization, and we will present a method of storing the decomposition of the partial product of \mathbf{B} -matrices, so that the cost is reduced to $\mathcal{O}(\Lambda) \propto \beta$. In practice, it is verified that sufficiently low temperatures to study say the ground state of the Hubbard model in the square lattice can be achieved with the stabilization overhead representing only a fraction of the simulation time [59, 85].

3.4.3 Storing partial products and time-displaced Green’s function

Given the \mathbf{QRP} decomposition of a matrix, we can obtain its \mathbf{PRQ} decomposition (with partial pivoting), so that the partial products can be built up from the left through successive $\mathbf{T}_L\mathbf{D}_L\mathbf{Q}_L$ decompositions (the subscript meaning “left”). Define the row/column reversing matrix

$$\mathbf{P}_r \equiv \begin{pmatrix} & & 1 \\ & \ddots & \\ 1 & & \end{pmatrix} \text{ with } \mathbf{P}_r^T = \mathbf{P}_r \text{ and } \mathbf{P}_r^{-1} = \mathbf{P}_r^T, \quad (3.77)$$

so that \mathbf{BP}_r reverses the order of the columns of \mathbf{B} , and $\mathbf{P}_r\mathbf{B}$ reverses the order of the rows. Now \mathbf{QRP} -decompose $(\mathbf{P}_r\mathbf{B})^T = \tilde{\mathbf{Q}}\tilde{\mathbf{R}}\tilde{\mathbf{P}}$, and define $\mathbf{Q} \equiv \mathbf{P}_r\tilde{\mathbf{Q}}^T$, $\mathbf{R} \equiv \mathbf{P}_r\tilde{\mathbf{R}}^T\mathbf{P}_r$, $\mathbf{P} \equiv \mathbf{P}_r\tilde{\mathbf{P}}^T\mathbf{P}_r$, giving

$$\mathbf{B} = \underbrace{\mathbf{P}_r\mathbf{P}_r}_{\mathbf{I}}\mathbf{B} = \mathbf{P}_r(\tilde{\mathbf{Q}}\tilde{\mathbf{R}}\tilde{\mathbf{P}})^T = \mathbf{P}_r\tilde{\mathbf{P}}^T\underbrace{\mathbf{P}_r\mathbf{P}_r}_{\mathbf{I}}\tilde{\mathbf{R}}^T\underbrace{\mathbf{P}_r\mathbf{P}_r}_{\mathbf{I}}\tilde{\mathbf{Q}}^T = \mathbf{PRQ} = \mathbf{PRD}^{-1}\mathbf{DQ} \equiv \mathbf{TDQ}, \quad (3.78)$$

where we reversed the definition of \mathbf{T} , and the successive decompositions are obtained by multiplying other \mathbf{B} -matrices on the right: $\mathbf{T}(\mathbf{DQ}\mathbf{B}') = \mathbf{TT}'\mathbf{D}'\mathbf{Q}'$, and so on. At the first slice, we compute the partial products and store their decompositions

$$\overbrace{\underbrace{\mathbf{B}_{L-1}\mathbf{B}_{L-2} \dots \mathbf{B}_{L-1-L/\Lambda}}_{(\mathbf{T}_L\mathbf{D}_L\mathbf{Q}_L)_0} \mathbf{B}_{L-2-L/\Lambda} \dots \mathbf{B}_{L-2-2L/\Lambda} \dots \mathbf{B}_{L/\Lambda-1} \dots \mathbf{B}_0}_{(\mathbf{T}_L\mathbf{D}_L\mathbf{Q}_L)_{\Lambda-1}} \quad (3.79)$$

and as the \mathbf{B} -matrices are moved onto the left, we build their partial product from the right and decompose it in $\mathbf{Q}_R\mathbf{D}_R\mathbf{T}_R$, saving the resulting successive decompositions in place of the $\mathbf{T}_L\mathbf{D}_L\mathbf{Q}_L$ decompositions which become unneeded. For example, when the second partial product is on the left:

$$\underbrace{\mathbf{B}_{L/\Lambda-1} \dots \mathbf{B}_0}_{(\mathbf{Q}_R\mathbf{D}_R\mathbf{T}_R)_0} \dots \overbrace{\mathbf{B}_{L-1}\mathbf{B}_{L-2} \dots \mathbf{B}_{L-1-L/\Lambda} \dots \mathbf{B}_{2L/\Lambda-1} \dots \mathbf{B}_{L/\Lambda}}_{(\mathbf{T}_L\mathbf{D}_L\mathbf{Q}_L)_0} \quad (3.80)$$

so that at the λ -th partial product, we obtain $(\mathbf{Q}_R \mathbf{D}_R \mathbf{T}_R)_{\lambda-1} (\mathbf{T}_L \mathbf{D}_L \mathbf{Q}_L)_{\Lambda-1-\lambda}$, and generally:

$$\mathbf{G}(\tau, \tau) = [\mathbf{I} + \mathbf{B}(\tau, 0) \mathbf{B}(\beta, \tau)]^{-1} = (\mathbf{I} + \mathbf{Q}_R \mathbf{D}_R \mathbf{T}_R \mathbf{T}_L \mathbf{D}_L \mathbf{Q}_L)^{-1} = \mathbf{Q}_L^T \underbrace{(\mathbf{Q}_R^T \mathbf{Q}_L^T + \mathbf{D}_R \mathbf{T}_R \mathbf{T}_L \mathbf{D}_L)}_{\mathbf{Q}' \mathbf{D}' \mathbf{T}'}^{-1} \mathbf{Q}_R^T, \quad (3.81)$$

where we may now apply any of the two methods described in the previous section to stably compute the inverse in brackets. We will generalize the ‘‘cut off’’ method so as to obtain time-displaced Green’s functions, the price to pay being that the matrices increase their size to $2N \times 2N$.

The inverse of a matrix composed of blocks is given by the Aitken block diagonalization formula

$$\begin{pmatrix} \mathbf{A} & \mathbf{B} \\ \mathbf{C} & \mathbf{D} \end{pmatrix}^{-1} = \begin{pmatrix} (\mathbf{A} - \mathbf{B}\mathbf{D}^{-1}\mathbf{C})^{-1} & (\mathbf{C} - \mathbf{D}\mathbf{B}^{-1}\mathbf{A})^{-1} \\ (\mathbf{B} - \mathbf{A}\mathbf{C}^{-1}\mathbf{D})^{-1} & (\mathbf{D} - \mathbf{C}\mathbf{A}^{-1}\mathbf{B})^{-1} \end{pmatrix} \quad (3.82)$$

A particular choice of these matrices gives both the equal- and the unequal-time Green’s functions:

$$\begin{pmatrix} \mathbf{I} & \mathbf{B}_h(\tau, 0) \\ -\mathbf{B}_h(\beta, \tau) & \mathbf{I} \end{pmatrix}^{-1} = \begin{pmatrix} \mathbf{G}(0) & -(\mathbf{I} - \mathbf{G}(0))\mathbf{B}_h(\tau, 0) \\ \mathbf{B}_h(\tau, 0)\mathbf{G}(0) & \mathbf{G}(\tau) \end{pmatrix} = \begin{pmatrix} \mathbf{G}(0) & \mathbf{G}(0, \tau) \\ \mathbf{G}(\tau, 0) & \mathbf{G}(\tau) \end{pmatrix} \quad (3.83)$$

We can now substitute the decompositions of the partial products that we store and update throughout the algorithm, and invert while being careful in isolating the diverging scales. The method is very stable, but numerically more expensive since the matrices at hand are twice as big.

$$\begin{aligned} \begin{pmatrix} \mathbf{I} & \mathbf{T}_L \mathbf{D}_L \mathbf{Q}_L \\ \mathbf{Q}_R \mathbf{D}_R \mathbf{T}_R & \mathbf{I} \end{pmatrix}^{-1} &= \left[\begin{pmatrix} \mathbf{T}_L & 0 \\ 0 & \mathbf{Q}_R \end{pmatrix} \underbrace{\begin{pmatrix} (\mathbf{T}_R \mathbf{T}_L)^{-1} & \mathbf{D}_L \\ -\mathbf{D}_R & (\mathbf{Q}_L \mathbf{Q}_R)^{-1} \end{pmatrix}}_{\mathbf{Q} \mathbf{D} \mathbf{T}} \begin{pmatrix} \mathbf{T}_R & 0 \\ 0 & \mathbf{Q}_L \end{pmatrix} \right]^{-1} \\ &= \left[\begin{pmatrix} \mathbf{T}_R^{-1} & 0 \\ 0 & \mathbf{Q}_L^T \end{pmatrix} \mathbf{T}^{-1} \right] \mathbf{D}^{-1} \left[\mathbf{Q}^T \begin{pmatrix} \mathbf{T}_L^{-1} & 0 \\ 0 & \mathbf{Q}_R^T \end{pmatrix} \right] \end{aligned} \quad (3.84)$$

Here, \mathbf{D} contains only large scales because the matrices with order one elements, $(\mathbf{T}_R \mathbf{T}_L)^{-1}$ and $(\mathbf{Q}_L \mathbf{Q}_R)^T$, cut off the exponentially small scales in \mathbf{D}_L and \mathbf{D}_R .

This procedure of storing the decompositions of partial products is not only more efficient. It also allows us to compute any observable, whether it requires equal or unequal time Green’s functions, while still preserving the $\mathcal{O}(\beta N^3)$ complexity of the algorithm.

4

Applications and original results

Contents

4.1	One-dimensional Chain	62
4.2	Square lattice	64
4.3	Nanoribbons	66

We simulate the Hubbard model on the 1D chain and on the 2D square lattice, for which results are well established from either an analytical or numerical perspective. Then, we consider the honeycomb lattice with nanoribbon boundary conditions, and reproduce some results in the literature. We compare the obtained results and the run time with *QUEST*, the flagship implementation of auxiliary field QMC. Finally, we carry out original calculations, applying our code to a minimal model of TMD nanoribbons. We compare our QMC results with those obtained by us in the mean field (MF) approximation. The latter is formulated allowing a site and orbital-dependent mean field, and the self-consistency relation is solved iteratively. We characterize the convergence issues arising in this iterative procedure. Our original MF results suggest that in the model we consider TMD nanoribbons could host edge-magnetism at finite temperature. The obtained phase diagram shows transitions between non-magnetized and two distinct edge-magnetized configurations. We use our unbiased QMC simulations to further probe the system, searching for these or other eventual phase transitions not captured by mean field theory.

4.1 One-dimensional Chain

The analytical solution of the 1D Hubbard model at half filling indicates that the ground state is antiferromagnetic [31]. To build a physical picture of the Hubbard chain, start by considering the $\frac{U}{t} \gg 1$ limit. Then, the Hubbard model can be replaced by an effective atomic Heisenberg model defined in the Hilbert subspace with one electron per site, and antiferromagnetic (AF) order sets in. In the Hubbard model, at zero temperature, it is found that upon decreasing U , the system is not only AF for large U , but remains an AF *insulator* down to $U \rightarrow 0$, becoming a *conductor* and losing AF order only at $U = 0$. Thus, for high enough $\beta = 1/T$, we expect to see signs of AF order for all $0 < U < \infty$. Upon decreasing β , thermal fluctuations tend to completely destroy long range order. Conversely, as β is increased, we expect to see a divergence in χ , corresponding to a phase transition to the antiferromagnetic ground state. We identify it by measuring both the equal-time and time-displaced spin-spin correlation functions, $\langle S_i^z S_j^z \rangle$ and $\langle S_i^z(\tau) S_j^z(0) \rangle$ with Monte Carlo. Fourier transforming as per Eqs.(3.63,3.65), we obtain a peak at $q = \pi$ in the magnetic structure factor $S(q)$, and in the magnetic susceptibility $\chi(q)$. Both peaks increase in magnitude as temperature is decreased, and in fact, within statistical uncertainty, the “staggered” susceptibility $\chi(\pi)$ appears to diverge very near $T_c = 0$. Contrastingly, the $q = 0$ components of both the structure factor and the susceptibility go to zero as the temperature is decreased, indicating no sign of ferromagnetic ordering in the ground state (see Fig.(4.1)).

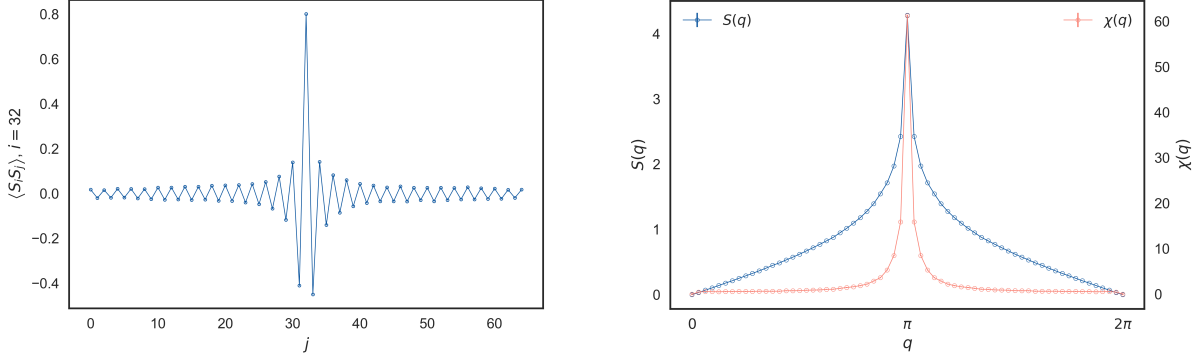


Figure 4.1: Left: Spin-spin correlation function $\langle S_i^z S_j^z \rangle$ centered on the middle of the chain. Right: Magnetic structure factor, and susceptibility for a 64-site Hubbard chain at $\beta t = 25$, for $U = 4t$, at half filling $\langle n \rangle = 1$.

In the Heisenberg limit, $U \gg t$, the staggered susceptibility $\chi_{\text{st}} \equiv \chi(\pi)$ diverges as $\chi_{\text{st}}(T) \propto 1/(T - T_c)$. Already at $U = 4t$, we find exactly this behavior with a critical temperature T_c very close to zero (see Fig.(4.2)). In fact, the ground state of the Hubbard model for the 1D chain is also antiferromagnetic, hence the divergence at $T_c = 0$ of the staggered susceptibility.

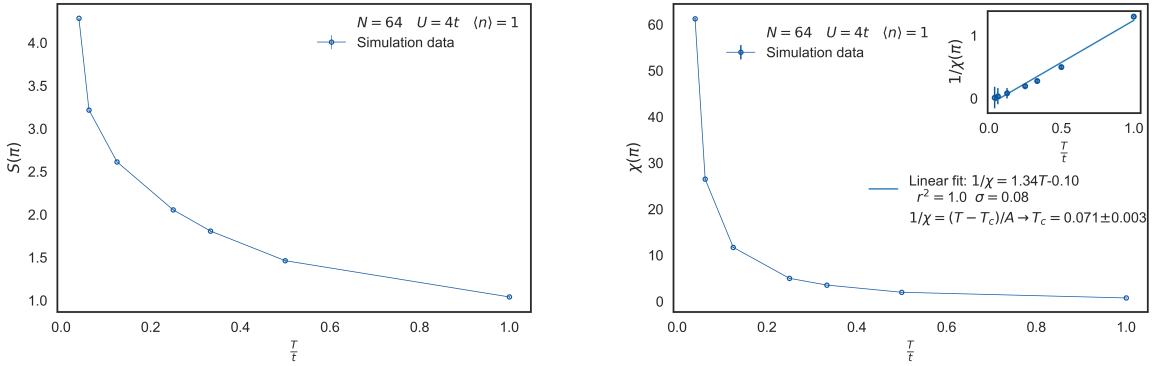


Figure 4.2: The magnetic structure factor and the susceptibility have a peak at $q = \pi$ that increases as $T \rightarrow 0$, indicating antiferromagnetic ordering. The staggered susceptibility diverges near $T_c = 0$ (not exactly 0 because the system is finite), signaling the transition to the antiferromagnetic ground state.

We ran QUEST for the same 64-site chain we simulated with our code, using $\beta t = 25$, taking a half filled chain ($\langle n \rangle = 1$), and setting $U = 4t$. We found a remarkable agreement between the measurements obtained using our code and using QUEST, namely in the magnetic structure factor, which we show in Fig.(4.3). Then, we took a small 2-site system to compare the run time and verify the scaling with the number of slices ($\mathcal{O}(LN^3)$) of the determinant Quantum Monte Carlo (QMC) algorithm. We noticed that QUEST's algorithm suffers from large overhead time if the required precision via the Trotter error $\Delta\tau$, or the inverse temperature β are large. This is due to the pre-conditioning needed to stabilize the products of the larger $LN \times LN$ matrices that are used in their algorithm (ours uses $N \times N$). For large system sizes, QUEST is better than our algorithm because their implementation uses *hybrid* QMC, which (potentially) has subcubic $\mathcal{O}(LN)$ scaling (the cost of stabilizing the matrix product required to obtain the Green's matrix with sufficient accuracy at low temperature still scales with N as $\mathcal{O}(N^3)$).

The results for the 2-site system can be compared with the results obtained using exact diagonalization, a method which can only be used for small lattice sizes, and which we outlined in chapter 2. We kept all

the parameters, changing only the system size, and verified that our results agree with a similar study carried out in [5], confirming the validity of our implementation (see Fig.(4.4)).

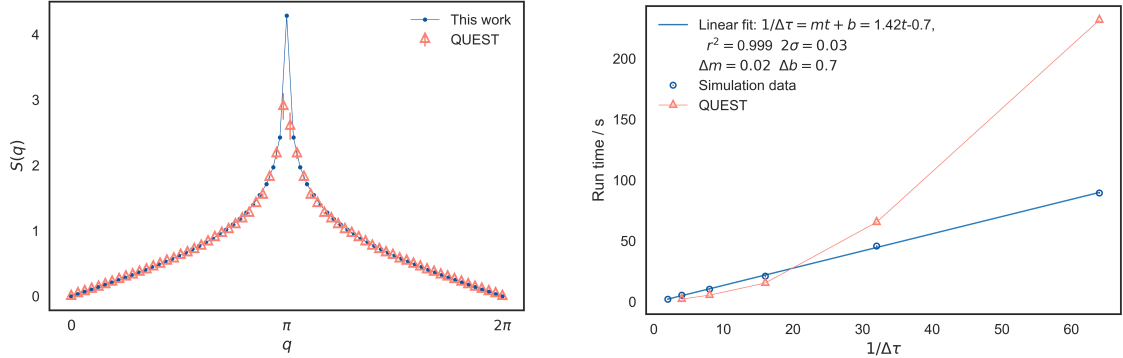


Figure 4.3: Left: Comparison of the magnetic structure factor with that obtained using **QUEST**. The used parameters are mentioned in the body of the text. Right: The run time using our code increases linearly with L , as expected. The **QUEST** algorithm initially scales linearly, but then becomes much slower due to the large overhead time associated with pre-conditioning the comparably much larger matrices they use if L is very big.

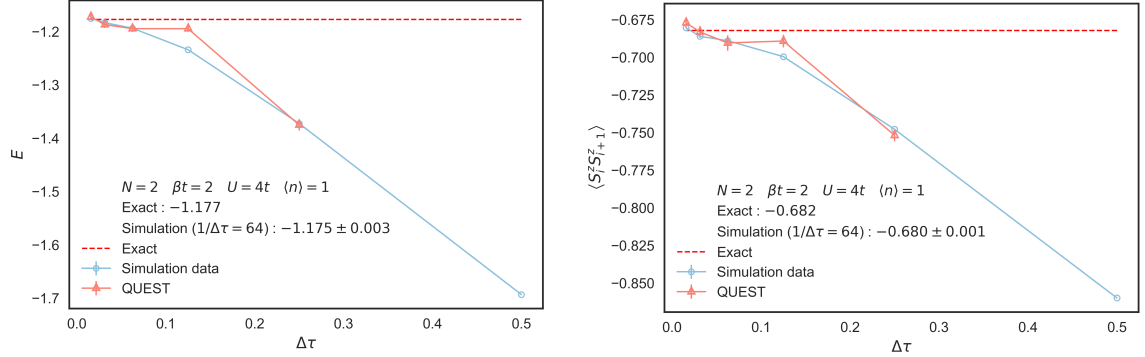


Figure 4.4: Convergence of some of the measured observables (left: total energy; right: spin-spin correlation) to the value given by exact diagonalization for $N = 2$, $\beta t = 2$, $U = 4t$. Comparison with the results of **QUEST**.

4.2 Square lattice

Similarly to what happens for the 1D case, both mean field and QMC results for the square lattice suggest that at half filling, antiferromagnetic (AF) order persists in the ground state for any value of the on-site interaction [8, 59, 93, 94]. In Fig.(4.5, left), we show the mean field phase diagram of the Hubbard model. On the right panel, we present a result for a 4×4 square lattice with PBCs at half filling ($\langle n \rangle = 1$) and $\beta t = 16$, comparing our results with those of [59].

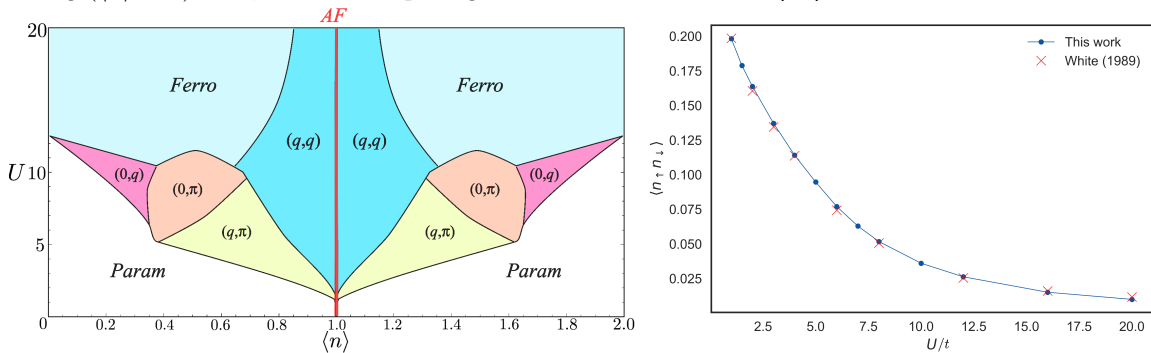


Figure 4.5: Left: MF phase diagram of the Hubbard model [94]. Right: QMC data showing the decrease of the double occupancy with increasing U , reproducing the results of [59].

Our results for a half-filled 4×4 lattice at $\beta t = 16$ clearly show antiferromagnetic (AF) spin-spin correlations - Fig.(4.6, left), which results in a peak of the magnetic structure factor $S(\mathbf{q})$ at $\mathbf{q} = (\pi, \pi)$ - Fig.(4.6, center). The susceptibility $\chi(\mathbf{q})$ is also strongly peaked at $\mathbf{q} = \pi$, again revealing long range AF order (Fig.(4.6,right)).

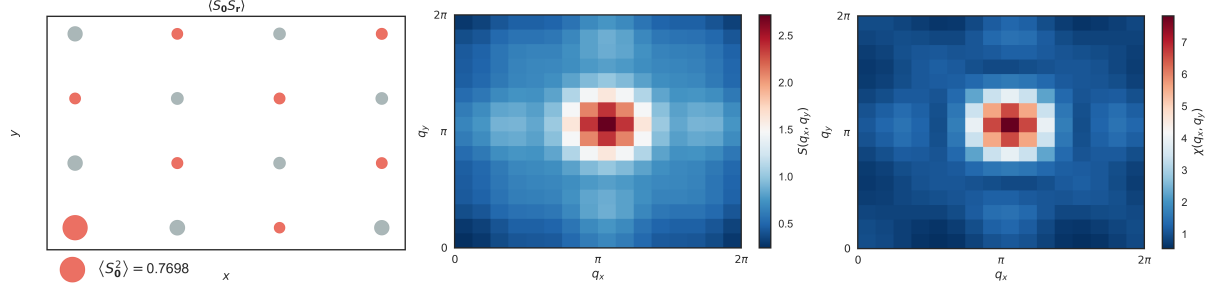


Figure 4.6: Left to right: Spin-spin correlations with respect to the point on the lower left corner of the lattice (labeled 0); color maps of the structure factor $S(\mathbf{q})$, and susceptibility $\chi(\mathbf{q})$, both showing peaks at $\mathbf{q} = \pi$.

We finish this section by characterizing AF order for varying system size and temperature, reproducing one of the main results of the seminal QMC study of White, Scalapino and Sugar [59]. In this paper, the authors report that by $\beta t = 20$, the finite temperature auxiliary field QMC algorithm is already measuring ground state properties. In fact, for $\beta t = 20$ the peaks of the magnetic structure factor, $S(\pi)$, coincide with those obtained using the projective variant of auxiliary field QMC mentioned in chapter 1.

Extrapolating to the infinite system, we verify that long range order exists, i.e. the antiferromagnetic order parameter, or staggered magnetization is finite for $N \rightarrow \infty$ (see Fig(4.7, left)). This becomes clearer by looking at Fig(4.7, right): the zero temperature extrapolation of $S(\pi)$ increases with lattice size, and inverse temperature. In fact, as per [8], for a sufficiently large lattice, at $T = 0$, we have

$$S(\pi) = N m_{\text{st}}^2 + S_c(\pi), \quad (4.1)$$

where $S_c(\pi)$ is the connected structure factor, obtained by replacing the average $\langle S_i^z S_j^z \rangle$ in the Fourier transform by $\langle S_i^z S_j^z \rangle - \langle S_i^z \rangle \langle S_j^z \rangle$, and m_{st} is the Antiferromagnetic (AF) order parameter, or staggered magnetization:

$$m_{\text{st}} = \frac{1}{N} \sum_i (-1)^{R_i} \langle n_{i,\uparrow} - n_{i,\downarrow} \rangle \quad (4.2)$$

Thus, to extrapolate the long range order, we choose $\beta t = 16$ and fit $S(\pi)/N$ by linear regression to obtain the estimate of the AF order parameter as $m_{\text{st}}^2 = 0.09$. As we increase U , this value becomes larger. According to [8] (and references therein), on a finite lattice, the AF long range order is 50% reduced from the classical Néel state due to quantum fluctuations. Thus, at $U \rightarrow \infty$, we obtain the maximum value $m_{\text{st}}^2 = 0.25$. Thus, the estimate we get for m_{st}^2 at $U = 4t$ amounts to 36% of the maximum of m_{st}^2 .

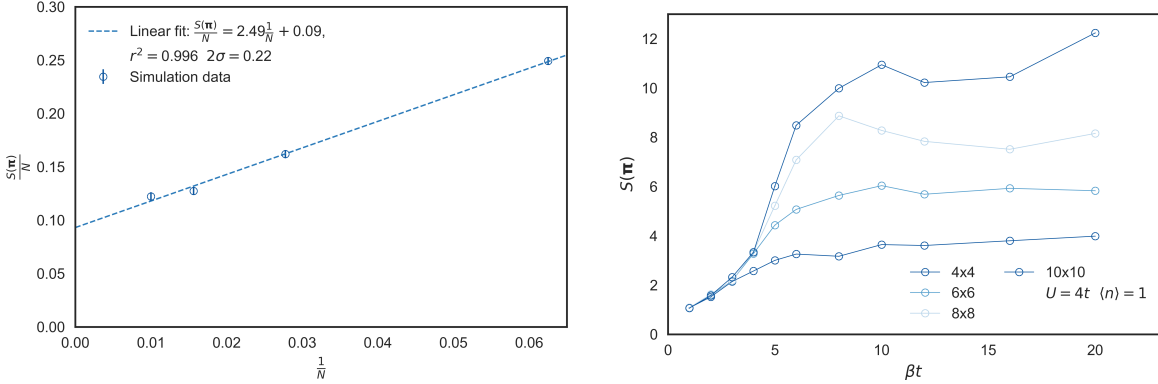


Figure 4.7: Left: Infinite system extrapolation of long range order. Right: $S(\pi)$ for varying system size and inverse temperature.

4.3 Nanoribbons

In this section, we apply our code to the honeycomb lattice of graphene and to the triangular lattice with the hoppings considered in the 3-band minimal model of TMDs with intra-orbital on-site interactions. We take boundary conditions corresponding to nanoribbons. These structures are much longer on one direction than on the other, i.e. $l \gg w$, resembling a ribbon, hence their name (see Fig.(4.8))¹. Along the longitudinal x -direction, a ribbon is normally very long, which justifies the fact that we take Periodic Boundary Conditions (PBCs). In contrast, in the narrow y -direction we take Open Boundary Conditions (OBCs). The presence of low energy electronic states on the edges of graphene nanoribbons leads to edge-magnetism [28]. This result suggests that magnetic ordering could also arise in TMD nanoribbons. As was mentioned in chapter 1, this possibility was unexplored numerically before this work [46, 47].

4.3.1 Graphene

We use three coordinates to label each site on the honeycomb lattice, by taking advantage of its bipartite nature. Looking at the honeycomb lattice as two interpenetrating triangular sublattices \mathcal{A} and \mathcal{B} , we take the axes x and y to be along the primitive vectors of each triangular sublattice. To number the sites on the ribbon, we introduce an additional coordinate labeling the sublattice: $z = 0$, if the site is in sublattice \mathcal{A} , and $z = 1$ if the site is in sublattice \mathcal{B} . We then adopt the numbering convention for the sites $i = 0, 1, \dots, 2N_x N_y - 1$ of the lattice \mathcal{L} : $i(x, y, z) = N_x N_y z + N_x y + x$, where $x = 0, \dots, N_x - 1$, $y = 0, \dots, N_y - 1$, and $z = 0, 1$ define each element $\mathbf{r} = (x, y, z) \in \mathcal{L}$.

The geometry of the system appears through the hopping matrix \mathbf{K} in our code. This numbering system makes it straightforward to find the neighbors of each site. Let us begin by considering a site that is not on a zigzag edge. There are two possible cases. For example, for $z_i = 0, y_i \neq N_y - 1, x_i \neq 0$, we have that the nearest neighbors of i are $j(i) = \{j(\mathbf{r})\}$, with \mathbf{r} in

$$\left\{ \mathbf{r}_j \in \mathcal{L} \mid z_j = 1 \wedge \left[\left(y_j = y_i \wedge (x_j = x_i \vee x_j = x_i - 1) \right) \vee \left(y_j = y_i + 1 \wedge x_j = x_i - 1 \right) \right] \right\}$$

As opposed to the sites of a honeycomb lattice with PBCs, which have 3 neighbors, the sites of the zigzag edges have only 2 neighbors. We summarize all possible cases in the following table.

¹In Fig.(4.8), this condition is, of course, not obeyed solely for the sake of giving a good visual representation of the boundary conditions, and the numbering system).

Table 4.1: Nearest neighbors on the graphene nanoribbon. The neighbors in gray are only for sites that are not on the edges. % refers to the remainder of integer division.

OBCs (PBCs)				
Case	z_j	y_j	x_j	
$z_i = 0$	1	y_i	x_i	
			$N_x - 1 - (N_x - x_i) \% N_x$	
	0	$y_i + 1$	$(x_i + 1) \% N_x$	
$z_i = 1$	0	y_i	x_i	
			$y_i - 1$	

Recall the mean field result obtained for a graphene nanoribbon we presented in chapter 1. For each sublattice, ferromagnetic order is induced by the on-site interaction along each row of the ribbon, i.e. along the longitudinal direction x . The average spin density has its maximum on the edge, decaying in the bulk. It reaches another (smaller) maximum on the other side of the ribbon, i.e., in the row next to the other sublattice's edge (see Fig.(4.13)). The spins on the other sublattice also order ferromagnetically, but point in the opposite direction. This type of global antiferromagnetic ordering (considering the two sublattices) is confirmed by QMC [46, 49]. Other recent auxiliary field QMC studies point at the possibility of strain-tuning this type of edge-magnetism in zig-zag graphene nanoribbons [50]. The authors start by introducing a reduction in the hopping along x to model strain, i.e. changing the hopping between atoms connected by red bonds in Fig.(4.8): $-t \mapsto -t + \Delta$. Then, they identify phase transitions to edge-magnetized states for varying hopping reduction ($\Delta = 0 - 0.5t$) and on-site interaction ($U = (1 - 4)t$). To do so, they fit the susceptibility at the edges, χ_{edge} , to the Curie-Weiss law:

$$\frac{1}{\chi_{\text{edge}}} = \frac{T - T_c}{A}, \quad (4.3)$$

and identify the critical temperature. By repeating this procedure for different simulations, one can find critical values of U_c and Δ for the transition to occur, and find the critical temperatures of the transitions for different values of these parameters.

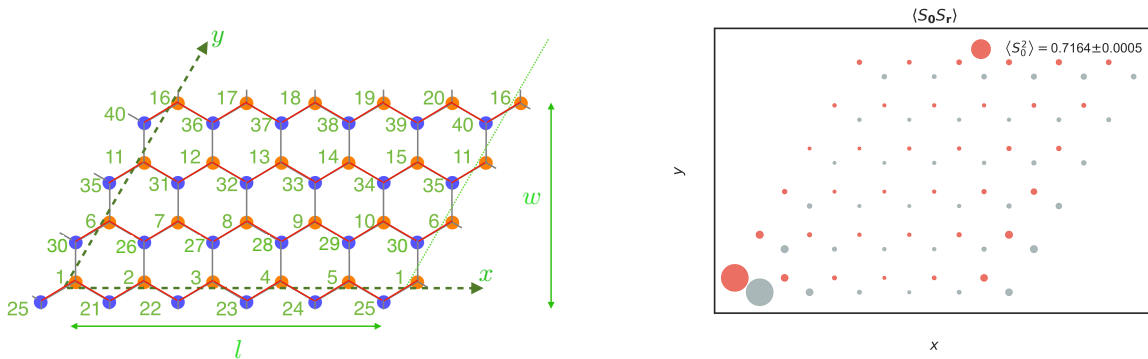


Figure 4.8: Left: Boundary conditions on the nanoribbon for $N_x = 5$, $N_y = 4$. The orange circles correspond to sublattice \mathcal{A} , and the blue circles correspond to sublattice \mathcal{B} . Right: Spin-spin correlations of a strained zig-zag graphene nanoribbon, with reduced hopping along x : $t \mapsto t - \Delta$, for $\Delta = 0.3t$ (obtained using our QMC code). The label **0** refers to the lower left site.

Any kind of mean field treatment tends to overestimate long range order. In this case, it predicts

spin correlations to decay rapidly in the edge, and then to remain constant along the x direction [46]. The QMC result of Fig.(4.8) shows us that, on the edge, it decays along the periodic x -direction with the profile shown in Fig.(4.9, left). This is a typical result for this type of nanostructure, and it generally indicates long range order. For example, in [46], it is shown that by increasing the width of ribbon, the correlations decay less and less until they almost reach the type of behavior predicted by mean field. Moreover, we study the behavior of the function $M_{\text{row}} \equiv \frac{1}{N_x} \sqrt{\sum_{(i,j) \in \text{row}} \langle S_i^z S_j^z \rangle}$, and we conclude that it is maximum in the edge row, decreases as we penetrate the bulk, and then increases again, having a smaller local maximum on the row neighboring the other sublattice's edge (see Fig.(4.9, right)). This is an indication of edge-magnetism, qualitatively similar to what is obtained in mean field. If we had more CPU time available, we could do larger scale simulations to see a more dramatic effect on *both* edges relative to the bulk. A peak at $\mathbf{q} = \mathbf{0}$ in the magnetic structure factor $S(\mathbf{q})$ suggests sublattice ferromagnetic ordering, and indeed, by studying the magnetic structure factor of each row separately, we see that it is enhanced at $\mathbf{q} = \mathbf{0}$ on the edges compared to the bulk (see Fig.(4.10)).

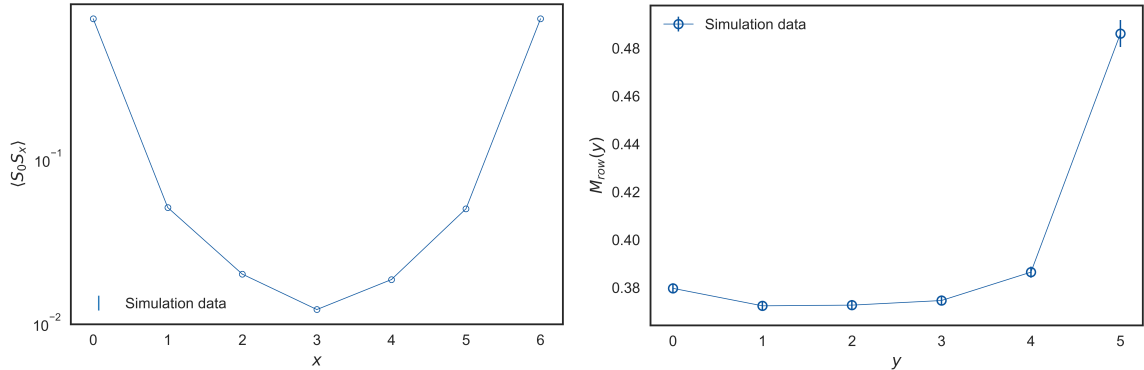


Figure 4.9: Left: Spin-spin correlation function profile along the longitudinal direction of the ribbon. Right: Magnetization parameter along each row, as a function of the transverse coordinate y , revealing the presence of magnetism localized at the edges.

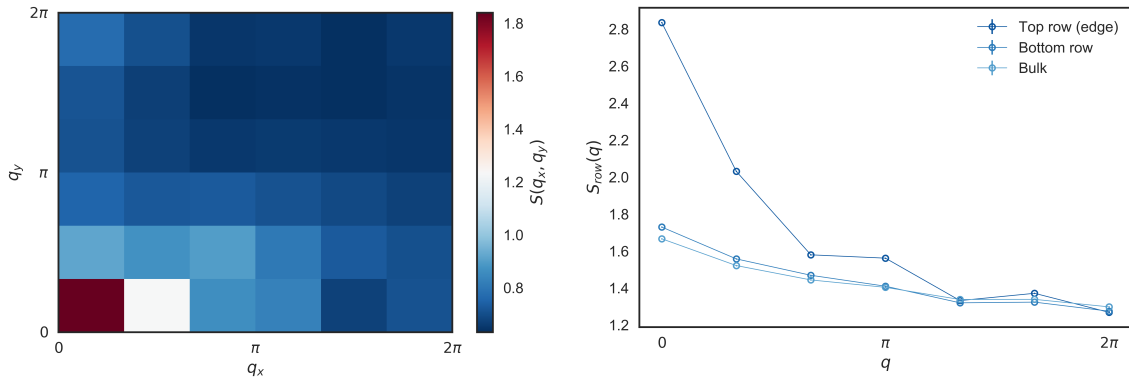


Figure 4.10: Magnetic structure factor $S(\mathbf{q})$ for a strained graphene nanoribbon: total, i.e. bulk + edges (left) and edge and bottom row compared with the innermost row of the bulk (right).

We studied the phase transition to the ordered state we described in this section by carrying out many simulations at different temperatures. By fitting the magnetic susceptibility at the *edges*, $\chi_{\text{edge}}(\mathbf{q} = \mathbf{0})$ -which diverges at the transition - to the Curie-Weiss Law, we were able to find the critical temperature $T_c = (0.017 \pm 0.003)t$, for the parameters $U = 3t$, and $\Delta = 0.3t$, a result which agrees with [50] (see Fig.(4.11)). Repeating this procedure for varying U, Δ , we could obtain a complete phase diagram of the

system.

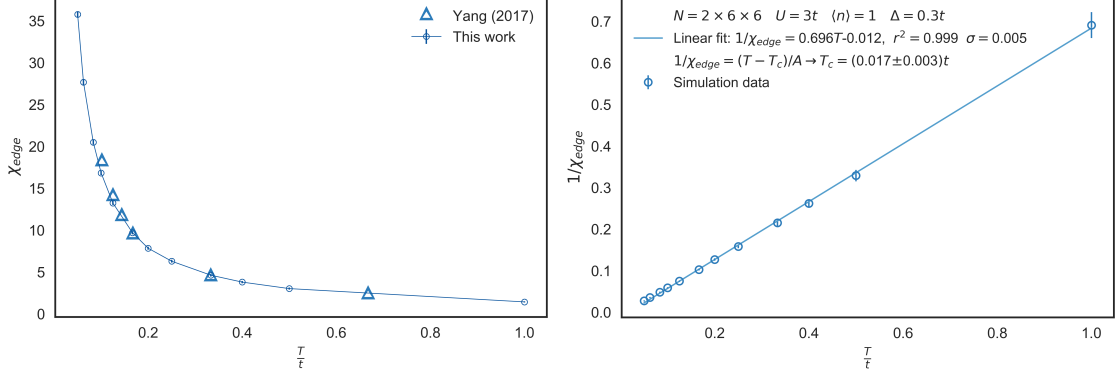


Figure 4.11: Left: Divergence of the edge susceptibility when approaching the critical temperature. Right: Linear fit used to obtain the critical temperature of the transition to the edge-magnetized phase.

4.3.2 Transition Metal Dichalcogenides (TMDs)

We start by approaching the TMDNR problem at the mean field level. Such a procedure is very useful to obtain a physical picture of the system's behavior. In particular, at a given temperature, if there is a transition between a configuration with magnetic order, and a disordered one, there is a critical on-site interaction $U = U_c$ at which the transition occurs, and it can be estimated in mean field, and compared with the more precise, unbiased QMC result (in both cases, we must sweep a certain range of interactions U to look for ordering). In the last sections we have demonstrated that we have the “tools” to carry out such a procedure. Repeating the process for different temperatures, we can obtain a complete phase diagram.

In general, our mean field formulation would involve diagonalizing an $N \times N$ matrix at each step, where $N = N_{\text{orb}}N_xN_y$ is the size of the system times the number of orbitals. However, since we consider PBCs along the x -direction, we can partially diagonalize the Hamiltonian analytically, reducing the size of the matrix to be diagonalized to $N_{\text{orb}}N_y \times N_{\text{orb}}N_y$, where N_y is the width of the ribbon, i.e. the number of MX_2 formula units.

Consider the spinless 3-band tight binding model, with unit lattice constant (see Fig.(1.2)):

$$\begin{aligned} \mathcal{H}_0 = & \sum_{\substack{m,n \\ \alpha,\beta}} \left(c_{m,n,\alpha}^\dagger t_{\alpha\beta}^0 c_{m,n,\beta} + \delta_{0,N_x} c_{m,n,\alpha}^\dagger t_{\alpha\beta}^1 c_{m+1,n,\beta} + \delta_{-\sqrt{3}/2,(N_y-1)\sqrt{3}/2} c_{m,n,\alpha}^\dagger t_{\alpha\beta}^4 c_{m-1,n,\beta} \right. \\ & + \delta_{0,N_m} \delta_{-1,(N_y-1)\sqrt{3}/2} c_{m+1/2,n-\sqrt{3}/2,\alpha}^\dagger t_{\alpha\beta}^2 c_{m,n,\beta} + \delta_{-1,(N_y-1)\sqrt{3}/2} c_{m-1/2,n-\sqrt{3}/2,\alpha}^\dagger t_{\alpha\beta}^3 c_{m,n,\beta} \\ & \left. + \delta_{N_y\sqrt{3}/2,0} c_{m+1/2,n+\sqrt{3}/2,\alpha}^\dagger t_{\alpha\beta}^6 c_{m,n,\beta} + \delta_{-1,N_x-1} \delta_{N_y\sqrt{3}/2,0} c_{m-1/2,n+\sqrt{3}/2,\alpha}^\dagger t_{\alpha\beta}^5 c_{m,n,\beta} \right) \end{aligned} \quad (4.4)$$

Fourier transforming along m : $c_{m,n,\alpha} = \frac{1}{\sqrt{N_x}} \sum_k e^{-ikm} c_{k,n,\alpha}$, with $k = \frac{2\pi}{N_x} \{-\frac{N_x}{2} + 1, -\frac{N_x}{2}, \dots, \frac{N_x}{2}\}$, we obtain

$$\begin{aligned} \mathcal{H}_0 = & \sum_{\substack{k,y \\ \alpha,\beta}} \left(c_{k,y,\alpha}^\dagger (t_{\alpha\beta}^0 + e^{ik} t_{\alpha\beta}^1 + e^{-ik} t_{\alpha\beta}^4) c_{k,y,\beta} + \delta_{-1,N_y-1} c_{k,y-1,\alpha}^\dagger (e^{ik/2} t_{\alpha\beta}^2 + e^{-ik/2} t_{\alpha\beta}^3) c_{k,y,\beta} \right. \\ & \left. + \delta_{N_y,0} c_{k,y,\alpha}^\dagger (e^{ik/2} t_{\alpha\beta}^6 + e^{-ik/2} t_{\alpha\beta}^5) c_{k,y+1,\beta} \right), \end{aligned} \quad (4.5)$$

with y defined as in Fig.(4.8). This leads to a tridiagonal block $3N_y \times 3N_y$ hopping matrix $\mathbf{H}(k)$ with

three different types of matrix elements: $\mathbf{h}_1 = \mathbf{H}_{y,y}$, $\mathbf{h}_2 = \mathbf{H}_{y,y-1}$, $\mathbf{h}_2^\dagger = \mathbf{H}_{y,y+1}$.

$$[H_{(\alpha y)(\beta y')}(k)] = \begin{pmatrix} \mathbf{h}_1 & \mathbf{h}_2^\dagger \\ \mathbf{h}_2 & \mathbf{h}_1 & \mathbf{h}_2^\dagger \\ & \mathbf{h}_2 & \mathbf{h}_1 & \ddots \\ & & \ddots & \ddots & \mathbf{h}_2^\dagger \\ & & & \ddots & \mathbf{h}_2 \\ & & & & \mathbf{h}_2 & \mathbf{h}_1 \end{pmatrix}, \quad \mathbf{h}_1 = \begin{pmatrix} \varepsilon_1 + 2t_0 \cos k & 2it_1 \sin k & 2t_2 \cos k \\ -2it_1 \sin k & \varepsilon_2 + 2t_{11} \cos k & 2it_{12} \sin k \\ 2t_2 \cos k & -2it_{12} \sin k & \varepsilon_2 + 2t_{22} \cos k \end{pmatrix}$$

$$\mathbf{h}_2 = \begin{pmatrix} 2t_0 \cos(k/2) & i \sin(k/2) \left(t_1 - \sqrt{3}t_2 \right) & -\cos(k/2) \left(\sqrt{3}t_1 + t_2 \right) \\ -i \sin(k/2) \left(t_1 + \sqrt{3}t_2 \right) & \frac{1}{2} \cos(k/2) \left(t_{11} + 3t_{22} \right) & -i \sin(k/2) \left(\frac{\sqrt{3}}{2} (t_{11} - t_{22}) + 2t_{12} \right) \\ \cos(k/2) \left(\sqrt{3}t_1 - t_2 \right) & -i \sin(k/2) \left(\frac{\sqrt{3}}{2} (t_{11} - t_{22}) - 2t_{12} \right) & \frac{1}{2} \cos(k/2) \left(3t_{11} + t_{22} \right) \end{pmatrix} \quad (4.6)$$

The energy spectrum for a ribbon with $N_y = 8$ is shown in Fig.(4.12).

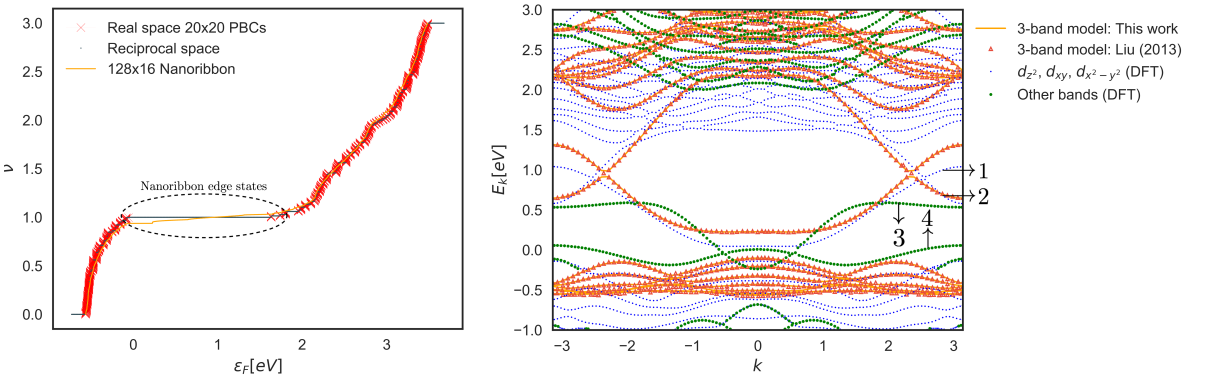


Figure 4.12: Left: Filling ν as a function of the Fermi energy ε_F for a system with PBCs, as computed by diagonalizing the input matrix of our code, and by the hopping matrix in \mathbf{k} -space. Comparison between the fillings of a nanoribbon and a periodic system. For the nanoribbon, edge states appear on the gap of the periodic system. Right: 3-band model MoS₂ zigzag edged nanoribbon energy bands (red dots and orange curve), for $N_y = 8$, using the GCA parameters. The first principles bands show the contribution from orbitals that are not considered in the 3-band model (blue: d_{z^2} , d_{xy} , $d_{x^2-y^2}$, green: others). The 3-band model reproduces the bands that correspond to the orbitals taken into account reasonably (1 and 2 correspond to the edge states from the d_{z^2} , d_{xy} , $d_{x^2-y^2}$ orbitals of the Mo atoms, while 3 and 4 correspond to the d_{yz} orbital at the Mo-terminated edge, and $p_{y,z}$ orbitals from the S-terminated edge, and are not taken into account in the 3-band model) (partially adapted from [53]).

By applying our mean field approach to solve the 3-band model with Hubbard-type interactions, we obtain solutions that are independent of x , which motivates us to reduce the number of MF parameters by choosing a translationally invariant ansatz. This is equivalent to taking $\langle n_{x,y,\alpha,\sigma} \rangle = \langle n_{y,\alpha,\sigma} \rangle \forall x$ ($6N_y$ parameters). In Fig.(4.13), we present a comparison between the mean field solutions for a finite graphene nanoribbon with dimensions 16×8 , and for a Transition Metal Dichalcogenide Nanoribbon (TMDNR) infinite along the x direction, and with width $N_y = 16$. By reducing the number of parameters, convergence is facilitated, which allows us to evaluate whether the solution of Fig.(4.13) is robust, i.e. whether it corresponds to a metastable or not. The mean field form of the interaction term with the reduced number of parameters changes, implying that the self-consistent relation of Eq.(2.60) from which

the local densities are computed changes as well.

$$\mathcal{H}_{\text{MF}} = \mathcal{H}_0 + \mathcal{H}_1 + \mathcal{C}, \text{ where } \mathcal{H}_1 = U \sum_{m,n,\alpha} \sum_{\sigma} n_{n,\alpha}^m \langle n_{m,-\sigma} \rangle, \mathcal{C} = -U \sum_{m,n,\alpha} \langle n_{n,\alpha}^{\uparrow} \rangle \langle n_{n,\alpha}^{\downarrow} \rangle \quad (4.7)$$

$$\begin{aligned} \mathcal{H}_1 + \mathcal{C} &= \frac{U}{N_x^2} \sum_{k_1 k_2} \sum_{k_3 k_4} \underbrace{\sum_m e^{i[(k_1+k_3)-(k_2+k_4)]m}}_{N_x \delta_{k_4, k_1+k_3-k_2}} \left(\sum_{\sigma} c_{n,\alpha}^{\dagger} c_{n,\alpha}^{\sigma} \underbrace{\langle c_{n,\alpha}^{\dagger} c_{n,\alpha}^{\sigma} c_{n,\alpha}^{\dagger} c_{n,\alpha}^{\sigma} \rangle}_{\delta_{k_3,k_4} \langle n_{k_3,-\sigma} \rangle} - \underbrace{\langle c_{n,\alpha}^{\dagger} c_{n,\alpha}^{\sigma} c_{n,\alpha}^{\dagger} c_{n,\alpha}^{\sigma} \rangle}_{\delta_{k_1,k_2} \langle n_{k_2,\uparrow} \rangle} \underbrace{\langle c_{n,\alpha}^{\dagger} c_{n,\alpha}^{\sigma} c_{n,\alpha}^{\dagger} c_{n,\alpha}^{\sigma} \rangle}_{\delta_{k_3,k_4} \langle n_{k_3,\downarrow} \rangle} \right) \\ &= \frac{U}{N_x} \sum_{k_2 k_3} \left(\sum_{\sigma} n_{k_2,\sigma} \langle n_{k_3,-\sigma} \rangle - \langle n_{k_2,\uparrow} \rangle \langle n_{k_3,\downarrow} \rangle \right) \equiv U \sum_{\mu} \left(\sum_{k,\sigma} n_{k,\mu,\sigma} \langle n_{\mu,-\sigma} \rangle - \langle n_{\mu,\uparrow} \rangle \langle n_{\mu,\downarrow} \rangle \right) \end{aligned} \quad (4.8)$$

where we collapsed the indexes (n, α) into a single index μ . The self-consistent relation allowing us to compute the new MF parameters at each step emerges by diagonalizing \mathcal{H}_1 in the μ -subspace:

$$\langle n_{\mu,\sigma} \rangle = \frac{1}{N_x} \sum_{q,\nu} |Q_{q\sigma\mu,\nu}|^2 f(\varepsilon_{q\nu\sigma}), \text{ where } d_{q,\sigma,\nu} = \sum_{\mu} Q_{q\sigma\mu,\nu}^* c_{q,\sigma,\mu}, \text{ and } \mathcal{H}_{\text{MF}} = \sum_{q,\nu,\sigma} \varepsilon_{q,\nu,\sigma} d_{q,\nu,\sigma}^{\dagger} d_{q,\nu,\sigma} + \mathcal{C} \quad (4.9)$$

For more details on the mean field procedure applied to the TMD nanoribbon, we refer the reader to appendix A.

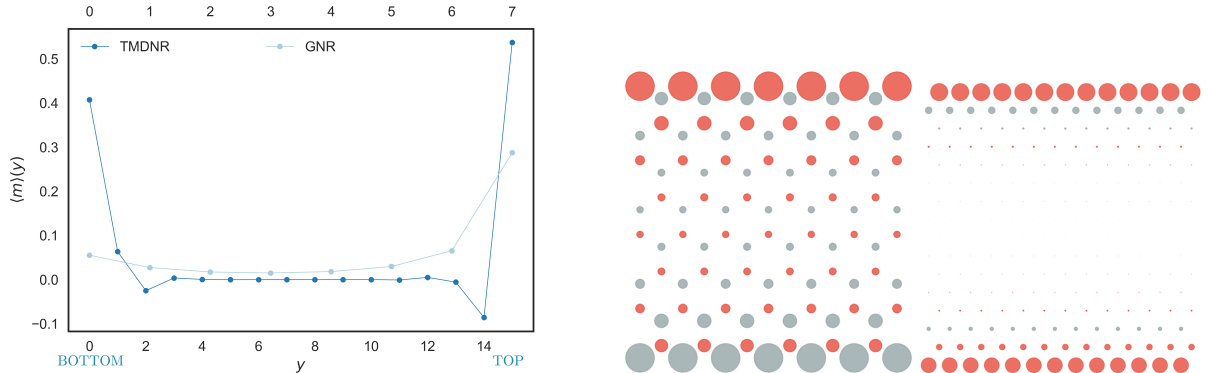


Figure 4.13: Comparison between the zero temperature MF solutions of the Hubbard model at half filling ($\langle n \rangle = 1$) for a 16×8 graphene nanoribbon (GNR) at $U = 1.2t$ and a TMDNR with $N_y = 16$ at $U = 20|t_0|$, and electron density $\langle n \rangle = 0.66$, the filling that corresponds to charge neutrality.

Left: Comparison between the spin density profile along the ribbon's transverse direction $\langle n \rangle(y)$ (the obtained solution is constant along x) for the GNR and the TMDNR. Right: Ordered phases obtained in mean field for graphene (left) and TMD nanoribbons (right). The size of the dots corresponds to the magnitude of the spin, and red stands for a positive spin, while blue stands for a negative spin. The magnetization is always normalized to the number of sites and measured in units of the Bohr magneton $\mu_B = e\hbar/2m_e$.

From now on, we take a TMDNR with $N_y = 16$, $U = 20|t_0|$ and $\langle n \rangle = 0.66$. By solving the self-consistent equation iteratively, at zero temperature, for varying U , we find two phase transitions, with respective critical on-site interactions $U_{c1} \approx 11.8|t_0|$, and $U_{c2} \approx 15.395|t_0|$.

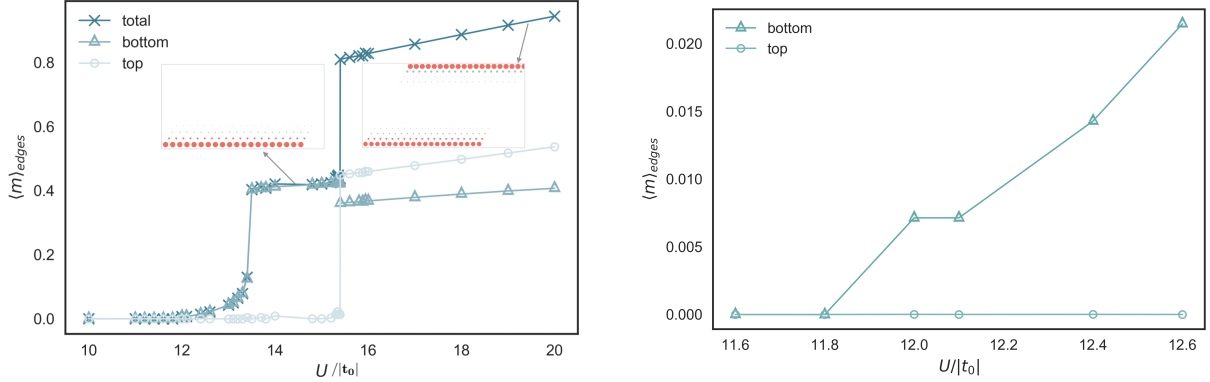


Figure 4.14: Left: Mean field phase diagram at zero temperature. Right: Zoom-in of the first phase transition.

Compare the y -scales of Figs.(4.14,4.15). One sees that the phase transition is much more abrupt in the latter than in the former, so that the first transition at $U_{c1} \approx 11.8|t_0|$ appears to be continuous, while the second one at $U_{c2} \approx 15.395|t_0|$ appears to be first order.

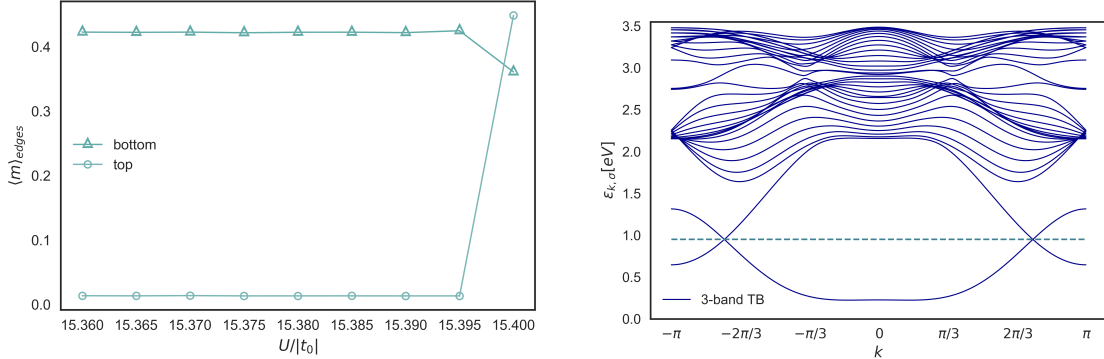


Figure 4.15: Left: Zoom-in of the second phase transition U is increased. Right: Band structure of the free-fermion problem.

To understand the effect of the on-site interaction at the mean field level, we start by comparing the band structure of the free problem to the mean field band structure, for U well within the ordered phase.

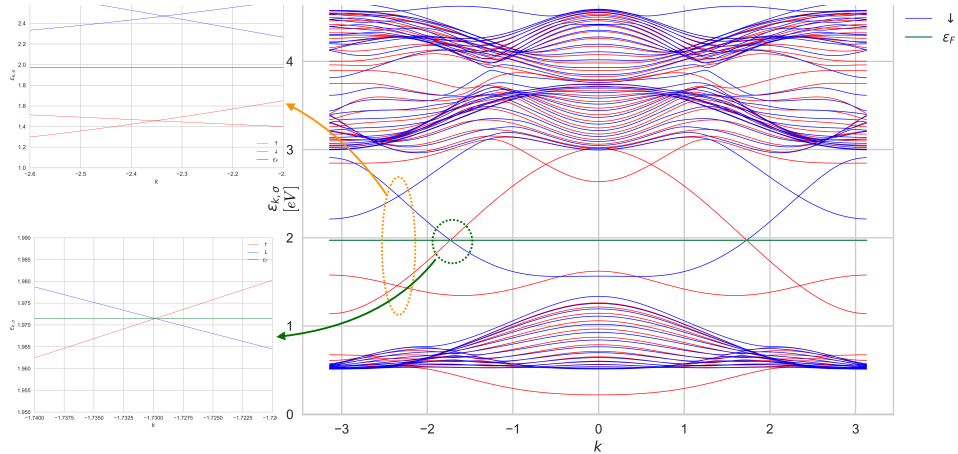


Figure 4.16: $T = 0$ mean field band structure for a TMDNR of width $N_y = 16$ in the ordered phase ($U = 20|t_0|$).

The first two aspects to notice are that spin degeneracy has been lifted, and that the shape of the

bands has been distorted. The part of the bands near the Fermi energy ε_F determines the physics of the phase. The interplay between the geometry of the tight-binding model, its parameters, the on-site interaction and temperature gives rise to different phases since it determines the shape of the bands and the location of the Fermi energy corresponding to charge neutrality.

In Fig.(4.15, right) we show the free band structure for the TMDNR with $N_y = 16$. The four bands crossing the Fermi energy (spin degeneracy only allows for 2 to be seen) correspond to edge states: two spin-degenerate bands correspond to states localized on one edge and the other two to states localized on the other edge. This explains the band crossing around $\varepsilon_{k,\sigma} \sim 1\text{eV}$, since states localized on opposite edges do not hybridize.

In Fig.(4.16), two changes with respect to the free bands of Fig.(4.15) are crucial. Firstly, we have a splitting at the K-point (circled in yellow), corresponding to a region where edge state bands with spin-up stay below the Fermi energy, while edge state bands with spin-down stay above. This leads to spin polarization of the eigenstates associated with these energies. Lastly, we have a band crossing (circled in green). Its existence implies that the edges are still metallic. As U varies, and the bands move upward or downward, and eventually distort, the states around this band crossing become either occupied or unoccupied, and since two opposite spin bands meet (*at right angles*) at this point, this leads to spin polarized states. This is a very interesting situation where at each edge we have 100% spin polarized charge carriers propagating on a background of charge at rest (completely filled bands) with opposite spin polarization.

The edge magnetization is due to the different occupation of the spin-up (in red) and spin-down bands (in blue). As the red, spin-up band near the Fermi energy rests completely below it, its electronic states are all occupied, while the corresponding spin-down states are all above ε_F , and thus are unoccupied. If these states were extended throughout the sample, a magnetization would appear in the bulk as well. However, as we show later, the wave functions corresponding to the states near the Fermi energy are heavily localized at the edges. This means that the spin polarization will be restricted to the edges. Initially, the up and down states are equally occupied. As we start increasing U , one of the bands (say, the up band) becomes more occupied than the other. The states in this band correspond only to one of the edges. Suppose it is the top edge. As we keep increasing U , the band structure changes and eventually, the up band corresponding to the bottom edge becomes more occupied than the down spin, bottom edge band, and both edges become magnetized (see Fig.(4.17)). In what follows, we explain how the two phase transitions we find can be understood in terms of the mean field picture we built.

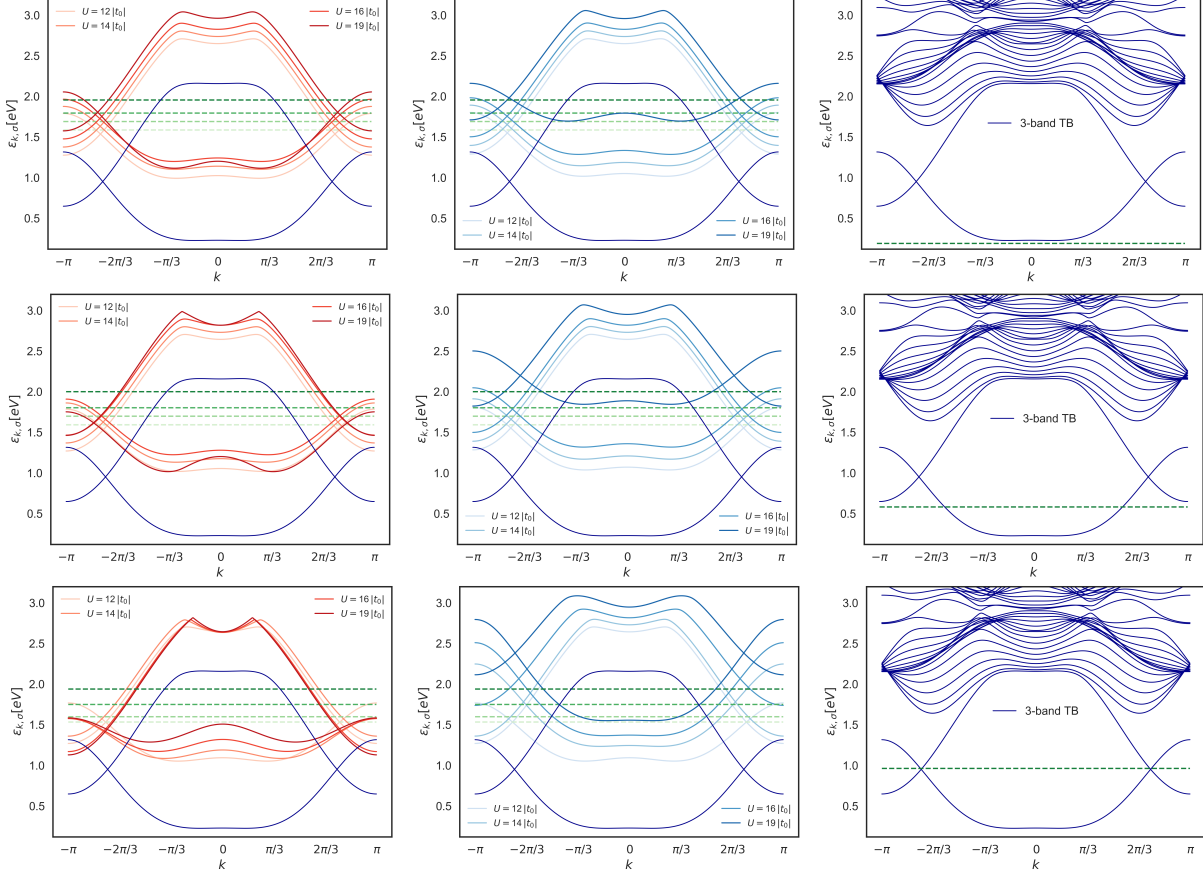


Figure 4.17: Spin-resolved band structures for varying U and β , compared with the tight-binding bands, demonstrating the changes in shape of the bands, and the change of the Fermi energy. From top to bottom, we have $\beta|t_0| = 0.5, 0.75, 4$. We can see that increasing U leads to an increase in the Fermi energy, to compensate for the states that gain more energy, and that must be occupied to ensure charge neutrality. On the rightmost figures, we represent the Fermi energy that would correspond to the considered temperature in the tight-binding case.

In Fig.(4.18), we can see that edge-magnetization has appeared on both sides of the ribbon. An important detail to notice is that when the magnetization of the bottom edge appears at $U_{c2} \approx 15.395|t_0|$, the magnetization of the top edge decreases slightly. This can be understood by looking at Fig.(4.19). The band marked "4" has now “widened” (one can see that there is white space below it), and more down spin states localized at the top edge become occupied, canceling out some of the magnetization induced by their corresponding up spin states. This effect occurs because, along with the lifting of the degeneracy, the Fermi energy increases slightly. Finally, in Fig.(4.20), we present a complete phase diagram, containing the behavior of the total edge magnetization $\langle m \rangle_{\text{edges}} = \langle m \rangle_{\text{top}} + \langle m \rangle_{\text{bottom}}$ for varying U at a number of different inverse temperatures β .

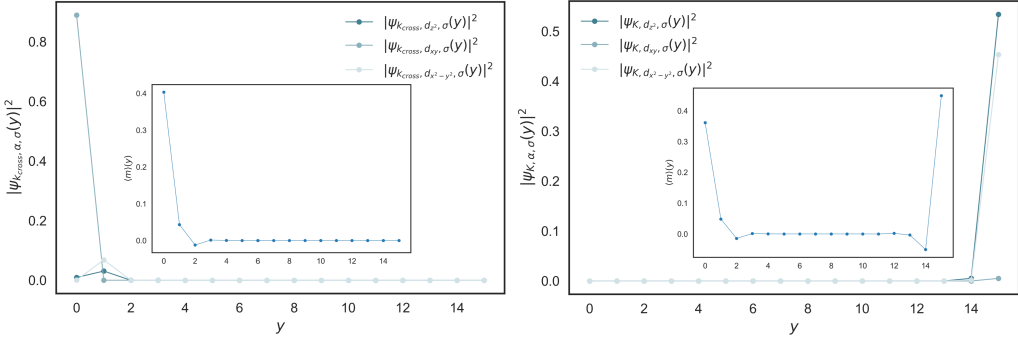


Figure 4.18: Left: Localized edge states on the top of the ribbon, at $U = 13|t_0|$ (left) and on the bottom, at $U = 15.4|t_0|$ (right) for the different orbitals. Insets: Resulting magnetization profiles along the ribbon's transverse direction due to higher spin up than spin down occupation of these states, showing, respectively top, and top-bottom edge magnetization.

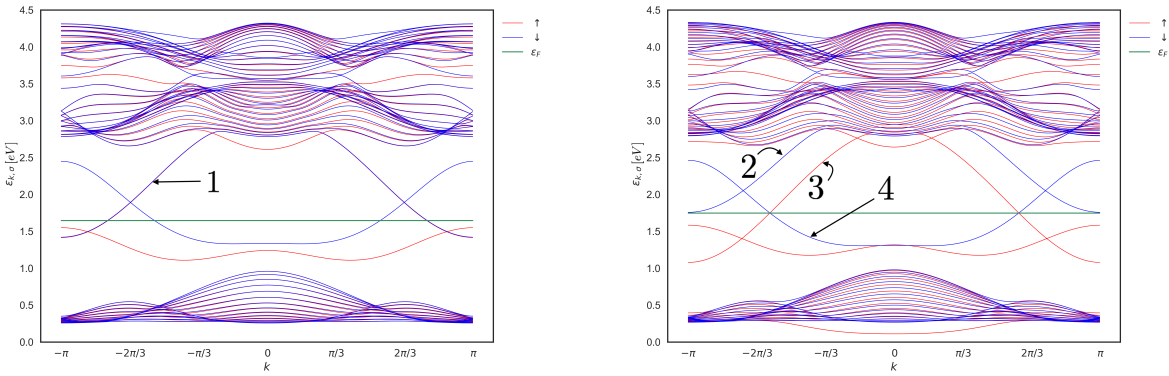


Figure 4.19: Comparison of the band structures at $U = 15.2|t_0|$ (left), and $U = 15.4|t_0|$ (right). The second phase transition occurs because the degeneracy of the bands marked as "1" below $U = 15.395|t_0|$ is lifted, leading to the appearance of two bands, marked "2", and "3". Band 2 stays above the Fermi energy. Thus, it is unoccupied. Part of band 3 becomes occupied, leading to the magnetization of the edge (the states that become occupied are localized at the bottom edge).

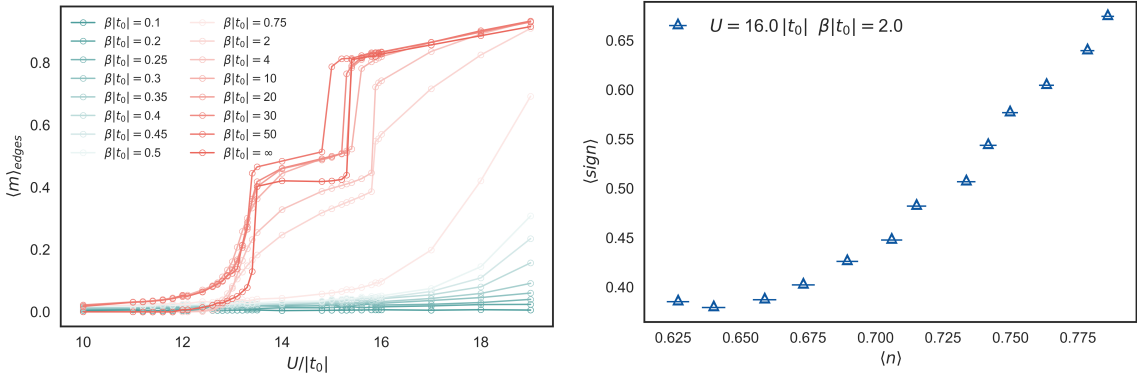


Figure 4.20: Left: Mean field phase diagram for varying U and β . Right: Average sign as a function of electron density, obtained by running our determinant QMC code for a 9×4 TMDNR at $\beta|t_0| = 2$, $U = 16|t_0|$.

Notice that in Fig.(4.20, left), the first phase transition is suppressed at inverse temperature $\beta|t_0| \lesssim 1$, and for yet higher temperatures the second transition too is suppressed. The critical on-site interactions $U_{c_{1,2}}$ vary with temperature. As β is decreased from ∞ to $\beta \sim 10/|t_0|$, the first transition occurs sooner, at about $U = 10|t_0|$, and the center plateau between the two transitions becomes shorter. By $\beta|t_0| = 2$, the plateau has disappeared, U_{c_1} returns to about its original ($\beta|t_0| = \infty$) value, and the magnetization increases smoothly until U_{c_2} (which is now higher than the original one at $\beta|t_0| = \infty$). Below $\beta|t_0| = 0.75$,

the system smoothly increases its edge magnetization starting at $U \sim 12|t_0|$, and at about $\beta|t_0| = 0.1$, both transitions seem to be completely suppressed (in this range of U).

In Figs.(4.20, right, 4.21), we show examples of the results given by our QMC code for a TMDNR. On the lattice models considered so far, we took half filling, where (in the cases we had been discussing so far - bipartite lattices and particularly symmetric Hamiltonians) there is no sign problem (see appendix B). In the model we consider, the sign problem severely restricts the range of parameters U, β, μ (or $\langle n \rangle$) that we can explore. In fact, for $\beta|t_0| > 2$, the average sign rapidly goes to zero for the range of on-site interactions where mean field predicts the existence of an ordered phase. Nonetheless, Fig.(4.20, right) gives us a particularly good combination of parameters for which mean field predicts an ordered phase, and at the relevant electron density $\langle n \rangle = 0.66$, the sign problem is not prohibitive ($\langle \text{sign} \rangle \sim 0.4$), so that our simulations can be used to extract information about the system. However, the preliminary results of Fig.(4.21) indicate that the complexity of the problem is much higher than, for example, in the case of graphene. Furthermore, recent analogous studies for graphene [46, 49, 50] suggest that one needs thicker ribbons to measure long range ordering with enough accuracy, which implies taking larger system sizes. To be conclusive about the true nature of edge-magnetism in TMDNRs, given the increased complexity of our model, this requires an enormous amount of computer time (about 20 times, or possibly more than for the analogous graphene studies), which we shall have access to very soon.

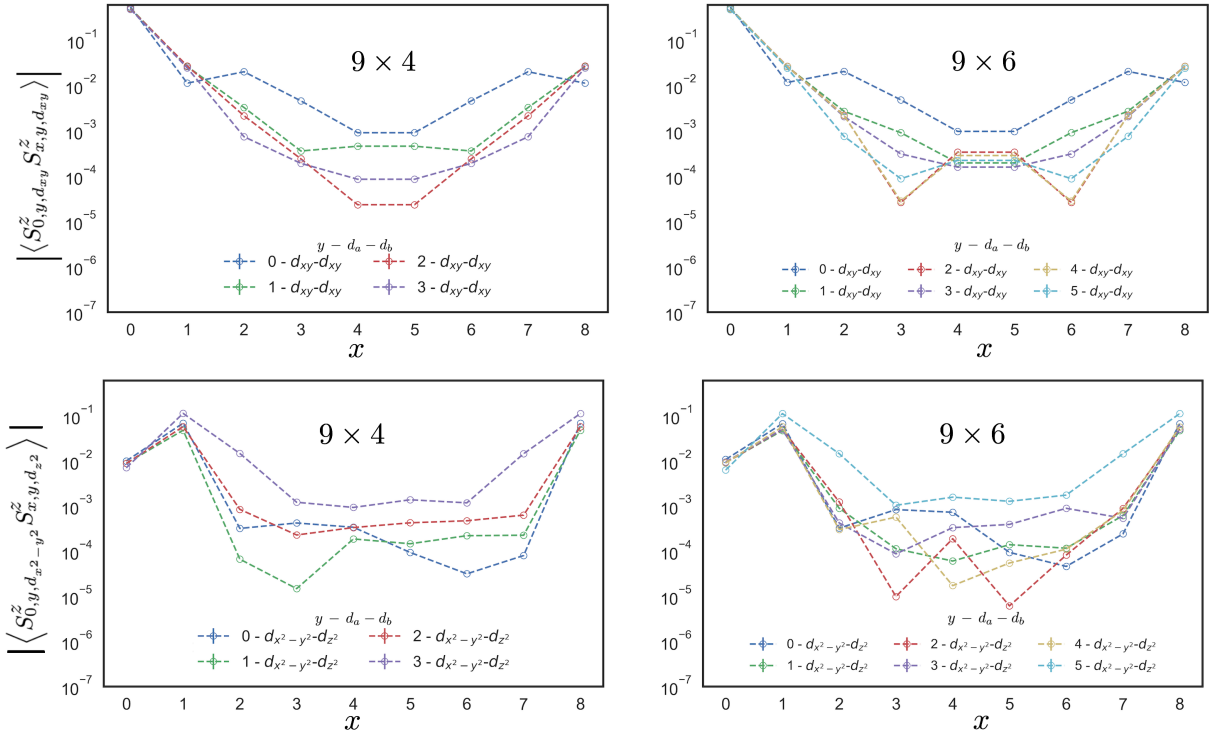


Figure 4.21: Longitudinal profile (along the x direction) of some of the orbital-resolved S^z spin-spin correlation functions for two lattice sizes 9×4 and 9×6 ($d_{x^2-y^2-d_z^2}$ and $d_{xy} - d_{xy}$). We use translational invariance along the x direction to average these correlations to improve the statistical properties of the estimator. On the left, curves 0 and 3 show correlations along the edge rows, while on the right, curves 0 and 5 correspond to the edges. $y - d_a - d_b$ means respectively, the row along which we represent the correlations, and the two orbitals considered.

5

Conclusions and Future Work

In this work, we investigated edge-magnetism in Transition Metal Dichalcogenide (TMD) nanoribbons by considering a minimal symmetry-based tight-binding model, and adding intra-orbital Hubbard-type on-site electron-electron interactions. We set up a mean field theory, arriving at a self-consistent equation, which we solved iteratively, leading to the phase diagram of Fig.(4.20). In the zero temperature case, we found two phase transitions. We explained the mechanism that is behind them by looking at how the band structure changes in mean field with the on-site intra-orbital interaction U and inverse temperature β . The obtained mean field result is very appealing, when compared to graphene for several reasons:

1. It occurs for realistic values of the interaction $U \sim 2\text{eV}$ in TMDs;
2. It shows moderately high critical temperatures at the mean field level (and true long range order at finite temperatures is possible in this system);
3. At odds with graphene, edge states in the polarized phase are metallic;
4. Magnetized edges host 100% spin polarized edge currents.

After approaching the TMD nanoribbon problem at the mean field level, we used our own implementation of the unbiased, and very accurate auxiliary field, or determinant Quantum Monte Carlo (QMC) algorithm to tackle the problem from a different, potentially more precise angle. Based on similar studies for graphene, we looked for long range magnetic order by analyzing the S^z spin-spin correlation functions (since spin-orbit coupling selects a preferred spin orientation). We found that, while the sign problem limits our simulations, it does not impede us to extract conclusions from them. However, the amount of computer time required to do so grows considerably. The fact that we consider 3 orbitals and a correspondingly less sparse hopping matrix means that both the complexity of the model, and the run time of the algorithm are increased. In practice this means that because of the presence of 3 orbitals, we must run the code for much longer to simulate systems of size comparable to the ones usually done in simulations involving graphene nanoribbons, and for which long range order can be accurately investigated. For the combination of parameters we took, this amounts to about $20\times$ more computer time than for the comparable graphene-based systems (a factor of $(3/2)^3$ due to the increased number of orbitals since the algorithm scales as $\mathcal{O}(\beta N^3)$, N being the total size of the system - sites *plus* orbitals - and a factor $\langle \text{sign} \rangle^{-2}$ due to the presence of the sign problem in the relevant region of parameter space).

Our preliminary results for the orbital-resolved spin-spin correlation functions along the rows of the ribbon are promising. Correlations along the edge rows tend to be larger than those along the bulk rows, and we notice that, while the magnetic ordering is certainly not as simple as our mean field calculation suggests, certain features of it seem to emerge, namely the fact that only one edge becomes magnetized (for example the 0 edge on the upper right panel of Fig.(4.21)). We shall continue this work by a more thorough analysis of the spin-spin correlation functions of these systems, and by carrying out larger scale simulations to characterize edge-magnetism in Transition Metal Dichalcogenide Nanoribbons (TMDNRs) in a more accurate, conclusive manner.

- Mermin, N. D. & Wagner, H. Absence of Ferromagnetism or Antiferromagnetism in One- or Two-Dimensional Isotropic Heisenberg Models. *Physical Review Letters* **17**, 1133–1136 (Nov. 28, 1966).
- Coleman, S. There are no Goldstone bosons in two dimensions. *Communications in Mathematical Physics* **31**, 259–264 (1973).
- Hohenberg, P. C. Existence of Long-Range Order in One and Two Dimensions. *Physical Review* **158**, 383–386 (June 10, 1967).
- Ajayan, P., Kim, P. & Banerjee, K. Two-dimensional van der Waals materials. *Physics Today* **69**, 38 (Aug. 31, 2016).
- Hirsch, J. Discrete Hubbard-Stratonovich transformation for fermion lattice models. *Physical Review B* **28**, 4059–4061 (June 16, 1983).
- Hirsch, J. E., Sugar, R. L., Scalapino, D. J. & Blankenbecler, R. Monte Carlo simulations of one-dimensional fermion systems. *Physical Review B* **26**, 5033–5055 (Nov. 1, 1982).
- Blankenbecler, R., Scalapino, D. J. & Sugar, R. L. Monte Carlo calculations of coupled boson-fermion systems. I. *Physical Review D* **24**, 2278–2286 (Oct. 15, 1981).
- Hirsch, J. E. Two-dimensional Hubbard model: Numerical simulation study. *Physical Review B* **31**, 4403–4419 (Apr. 1, 1985).
- Hirsch, J. E. Monte Carlo Study of the Two-Dimensional Hubbard Model. *Physical Review Letters* **51**, 1900–1903 (Nov. 14, 1983).
- Hirsch, J. E. Stable monte carlo algorithm for fermion lattice systems at low temperatures. *Physical Review B* **38**, 12023–12026 (Dec. 1, 1988).
- Hirsch, J. E. & Tang, S. Antiferromagnetism in the Two-Dimensional Hubbard Model. *Physical Review Letters* **62**, 591–594 (Jan. 30, 1989).
- Dumitrescu, P. T., Serbyn, M., Scalettar, R. T. & Vishwanath, A. Superconductivity and nematic fluctuations in a model of doped FeSe monolayers: Determinant quantum Monte Carlo study. *Physical Review B* **94**, 155127 (Oct. 17, 2016).
- Berg, E., Lederer, S., Schattner, Y. & Trebst, S. Monte Carlo Studies of Quantum Critical Metals. <http://arxiv.org/abs/1804.01988> (2018) (Apr. 5, 2018).
- Beyl, S., Goth, F. & Assaad, F. F. Revisiting the hybrid quantum Monte Carlo method for Hubbard and electron-phonon models. *Physical Review B* **97**, 085144 (Feb. 22, 2018).
- Chang, C.-C., Gogolenko, S., Perez, J., Bai, Z. & Scalettar, R. T. Recent advances in determinant quantum Monte Carlo. *Philosophical Magazine* **95**, 1260–1281 (Apr. 23, 2015).
- Esterlis, I. *et al.* Breakdown of the Migdal-Eliashberg theory: A determinant quantum Monte Carlo study. *Physical Review B* **97**, 140501 (Apr. 2, 2018).
- Mondaini, R., Ying, T., Paiva, T. & Scalettar, R. T. Determinant quantum Monte Carlo study of the enhancement of d-wave pairing by charge inhomogeneity. *Physical Review B* **86**, 184506 (Nov. 7, 2012).
- Meng, Z. Y., Hung, H.-H. & C. Lang, T. The characterization of topological properties in Quantum Monte Carlo simulations of the Kane-Mele-Hubbard model. *Modern Physics Letters B* **28**. doi:10.1142/S0217984914300014 (Jan. 10, 2014).
- Kung, Y. F. *et al.* Characterizing the three-orbital Hubbard model with determinant quantum Monte Carlo. *Physical Review B* **93**, 155166 (Apr. 29, 2016).
- Johnston, S. *et al.* Determinant quantum Monte Carlo study of the two-dimensional single-band Hubbard-Holstein model. *Physical Review B* **87**, 235133 (June 24, 2013).
- Rademaker, L., Johnston, S., Zaanen, J. & van den Brink, J. Determinant quantum Monte Carlo study of exciton condensation in the bilayer Hubbard model. *Physical Review B* **88**, 235115 (Dec. 16, 2013).
- Ying, T. *et al.* Determinant quantum Monte Carlo study of d-wave pairing in the plaquette Hubbard hamiltonian. *Physical Review B* **90**, 075121 (Aug. 13, 2014).
- Scalettar, R. T. *Numerical Studies of Disordered Tight-Binding Hamiltonians* in. Lectures on the Physics of Strongly Correlated Systems XI. **918** (June 1, 2007), 111–202. doi:10.1063/1.2751991. <http://adsabs.harvard.edu/abs/2007AIPC..918..111S> (2018).
- Zhou, Z., Cai, Z., Wu, C. & Wang, Y. Quantum Monte Carlo simulations of thermodynamic properties of SU(2N) ultracold fermions in optical lattices. *Physical Review B* **90**, 235139 (Dec. 22, 2014).
- Jiang, C., Bai, Z. & Scalettar, R. *A Fast Selected Inversion Algorithm for Green's Function Calculation in Many-Body Quantum Monte Carlo Simulations* in 2016 IEEE International Parallel and Distributed Processing Symposium (IPDPS) 2016 IEEE International Parallel and Distributed Processing Symposium (IPDPS) (May 2016), 463–472. doi:10.1109/IPDPS.2016.69.
- Lee, C. R., Chung, I. H. & Bai, Z. *Parallelization of DQMC simulation for strongly correlated electron systems* in 2010 IEEE International Symposium on Parallel Distributed Processing (IPDPS) 2010 IEEE International Symposium on Parallel Distributed Processing (IPDPS) (Apr. 2010), 1–9. doi:10.1109/IPDPS.2010.5470484.
- Bai, Z., Lee, C., Li, R.-C. & Xu, S. Stable solutions of linear systems involving long chain of matrix multiplications. *Linear Algebra and its Applications. Special Issue: Dedication to Pete Stewart on the occasion of his 70th birthday* **435**, 659–673 (Aug. 1, 2011).
- Yazyev, O. V. Emergence of magnetism in graphene materials and nanostructures. *Reports on Progress in Physics* **73**, 056501 (2010).
- Anderson, P. W. More Is Different. *Science* **177**, 393–396 (Aug. 4, 1972).
- Wen, X. G. Topological orders in rigid states. *International Journal of Modern Physics B* **04**, 239–271 (Feb. 1, 1990).
- Lieb, E. H. & Wu, F. Y. Absence of Mott Transition in an Exact Solution of the Short-Range, One-Band Model in One Dimension. *Physical Review Letters* **20**, 1445–1448 (June 17, 1968).
- Hubbard, J. Electron correlations in narrow energy bands. *Proc. R. Soc. Lond. A* **276**, 238–257 (Nov. 26, 1963).
- Novoselov, K. S. *et al.* Electric Field Effect in Atomically Thin Carbon Films. *Science* **306**, 666–669 (Oct. 22, 2004).
- Katsnelson, M. I. Graphene: carbon in two dimensions. *Materials Today* **10**, 20–27 (Jan. 1, 2007).

35. *The Nobel Prize in Physics 2010 - Advanced Information* https://www.nobelprize.org/nobel_prizes/physics/laureates/2010/advanced.html (2018).
36. Castro Neto, A. H., Guinea, F., Peres, N. M. R., Novoselov, K. S. & Geim, A. K. The electronic properties of graphene. *Reviews of Modern Physics* **81**, 109–162 (Jan. 14, 2009).
37. Wang, Q. H., Kalantar-Zadeh, K., Kis, A., Coleman, J. N. & Strano, M. S. Electronics and optoelectronics of two-dimensional transition metal dichalcogenides. *Nature Nanotechnology* **7**, 699–712 (Nov. 2012).
38. Roldán, R. *et al.* Electronic properties of single-layer and multilayer transition metal dichalcogenides MX₂ (M = Mo, W and X = S, Se). *Annalen der Physik* **526**. doi:10.1002/andp.201400128 (Oct. 1, 2014).
39. Xu, X., Yao, W., di, X. & Heinz, T. Spin and pseudospins in layered transition metal dichalcogenides. *Nature Physics* **10**. doi:10.1038/nphys2942 (Apr. 30, 2014).
40. Manzeli, S., Ovchinnikov, D., Pasquier, D., V. Yazyev, O. & Kis, A. 2D transition metal dichalcogenides. *Nature Reviews Materials* **2**. doi:10.1038/natrevmats.2017.33 (June 13, 2017).
41. Hsu, Y.-T., Vaezi, A., Fischer, M. H. & Kim, E.-A. Topological superconductivity in monolayer transition metal dichalcogenides. *Nature Communications* **8**, 14985 (Apr. 11, 2017).
42. Braz, J. E. H., Amorim, B. & Castro, E. V. Valley polarized magnetic state in hole-doped mono layers of transition metal dichalcogenides. <http://arxiv.org/abs/1712.07157> (2018) (Dec. 19, 2017).
43. Splendiani, A. *et al.* Emerging photoluminescence in monolayer MoS₂. *Nano Letters* **10**, 1271–1275 (Apr. 14, 2010).
44. Mohanty, N. *et al.* Nanotomy-based production of transferable and dispersible graphene nanostructures of controlled shape and size. *Nature Communications* **3**, 844 (May 15, 2012).
45. Chen, Y. *et al.* Fabrication of MoSe₂ nanoribbons via an unusual morphological phase transition. *Nature Communications* **8**, 15135 (May 4, 2017).
46. Feldner, H. *et al.* Dynamical Signatures of Edge-State Magnetism on Graphene Nanoribbons. *Physical Review Letters* **106**, 226401 (May 31, 2011).
47. Golor, M., Lang, T. C. & Wessel, S. Quantum Monte Carlo studies of edge magnetism in chiral graphene nanoribbons. *Physical Review B* **87**, 155441 (Apr. 30, 2013).
48. Cheng, S., Yu, J., Ma, T. & Peres, N. M. R. Strain-induced edge magnetism at the zigzag edge of a graphene quantum dot. *Physical Review B* **91**, 075410 (Feb. 11, 2015).
49. Raczkowski, M. & Assaad, F. F. Interplay between the edge-state magnetism and long-range Coulomb interaction in zigzag graphene nanoribbons: Quantum Monte Carlo study. *Physical Review B* **96**, 115155 (Sept. 26, 2017).
50. Yang, G., Li, B., Zhang, W., Ye, M. & Ma, T. Strain-tuning of edge magnetism in zigzag graphene nanoribbons. *Journal of Physics: Condensed Matter* **29**, 365601 (2017).
51. Davelou, D., Kopidakis, G., Kaxiras, E. & Remediakis, I. N. Nanoribbon edges of transition-metal dichalcogenides: Stability and electronic properties. *Physical Review B* **96**, 165436 (Oct. 27, 2017).
52. Yazyev, O. V. & Katsnelson, M. I. Magnetic Correlations at Graphene Edges: Basis for Novel Spintronics Devices. *Physical Review Letters* **100**, 047209 (Jan. 31, 2008).
53. Liu, G.-B., Shan, W.-Y., Yao, Y., Yao, W. & Xiao, D. Three-band tight-binding model for monolayers of group-VIB transition metal dichalcogenides. *Physical Review B* **88**, 085433 (Aug. 26, 2013).
54. Braz, J. E. H. *Electronic Properties of Single-layered Transition Metal Dichalcogenides* PhD thesis (IST Lisbon, Nov. 2015).
55. Troyer, M. & Wiese, U.-J. Computational Complexity and Fundamental Limitations to Fermionic Quantum Monte Carlo Simulations. *Physical Review Letters* **94**, 170201 (May 4, 2005).
56. Kosztin, I., Faber, B. & Schulten, K. Introduction to the diffusion Monte Carlo method. *American Journal of Physics* **64**, 633–644 (May 1, 1996).
57. Toulouse, J., Assaraf, R. & Umrigar, C. J. in *Advances in Quantum Chemistry* (eds Hoggan, P. E. & Ozdogan, T.) 285–314 (Academic Press, Jan. 1, 2016). doi:10.1016/bs.aiq.2015.07.003. <http://www.sciencedirect.com/science/article/pii/S0065327615000386> (2018).
58. Bai, Z., Chen, W., Scalettar, R. & Yamazaki, I. in Hou, T. Y., Liu, C. & Liu, J.-G. *Series in Contemporary Applied Mathematics* 1–110 (CO-PUBLISHED WITH HIGHER EDUCATION PRESS, June 2009). ISBN: 978-981-4273-25-1 978-981-4273-26-8. doi:10.1142/9789814273268_0001. http://www.worldscientific.com/doi/abs/10.1142/9789814273268_0001 (2018).
59. White, S. R. *et al.* Numerical study of the two-dimensional Hubbard model. *Physical Review B* **40**, 506–516 (July 1, 1989).
60. F. Assaad, F., Grotendorst, J., Marx, D. & Muramatsu (Eds.), A. *Quantum Simulations of Complex Many-Body Systems: From Theory to Algorithms. Quantum Monte Carlo Methods on Lattices: The Determinantal Approach (Lecture Notes)* (2002).
61. Broecker, P., Carrasquilla, J., Melko, R. G. & Trebst, S. Machine learning quantum phases of matter beyond the fermion sign problem. *Scientific Reports* **7**, 8823 (Aug. 18, 2017).
62. Bercx, M., Goth, F., Hofmann, J. S. & Assaad, F. The ALF (Algorithms for Lattice Fermions) project release 1.0. Documentation for the auxiliary field quantum Monte Carlo code. *SciPost Physics* **3**, 013 (Aug. 16, 2017).
63. *QUEST User's Manual* Apr. 2012.
64. Fazekas, P. *Lecture Notes on Electron Correlation and Magnetism* 798 pp. ISBN: 978-981-02-2474-5 (World Scientific, Jan. 1, 1999).
65. Mahan, G. D. *Many-Particle Physics* 3rd ed. ISBN: 978-0-306-46338-9. // www.springer.com/gp/book/9780306463389 (2018) (Springer US, 2000).
66. Altland, A. & Simons, B. D. *Condensed Matter Field Theory* Cambridge Core. /core/books/condensed-matter-field-theory (2018).
67. Hayes, B. Hip-Hop Physics. *American Scientist* **97**. <https://www.americanscientist.org/article/hip-hop-physics> (2018) (Dec. 2009).
68. Bohm, D. & Pines, D. A Collective Description of Electron Interactions: III. Coulomb Interactions in a Degenerate Electron Gas. *Physical Review* **92**, 609–625 (Nov. 1, 1953).

69. Gell-Mann, M. & Brueckner, K. A. Correlation Energy of an Electron Gas at High Density. *Physical Review* **106**, 364–368 (Apr. 15, 1957).
70. Sawada, K., Brueckner, K. A., Fukuda, N. & Brout, R. Correlation Energy of an Electron Gas at High Density: Plasma Oscillations. *Physical Review* **108**, 507–514 (Nov. 1, 1957).
71. Hubbard, J. The description of collective motions in terms of many-body perturbation theory. II. The correlation energy of a free-electron gas. *Proc. R. Soc. Lond. A* **243**, 336–352 (Jan. 14, 1958).
72. Hubbard, J. The description of collective motions in terms of many-body perturbation theory III. The extension of the theory to the non-uniform gas. *Proc. R. Soc. Lond. A* **244**, 199–211 (Mar. 11, 1958).
73. Nozières, P. & Pines, D. Electron Interaction in Solids. General Formulation. *Physical Review* **109**, 741–761 (Feb. 1, 1958).
74. Editorial. The Hubbard model at half a century. *Nature Physics* **9**, 523 (Sept. 2013).
75. Ashcroft, N. W. & Mermin, N. D. *Solid State Physics* 856 pp. ISBN: 978-0-03-083993-1 (Holt, Rinehart and Winston, 1976).
76. H de Boer, J. & J W Verwey, E. Semiconductors With Partially and With Completely Filled 3d-Lattice Bands. *Proceedings of the Physical Society* **49**, 59 (1937).
77. Mott, N. F. & Peierls, R. Discussion of the paper by de Boer and Verwey. *Proceedings of the Physical Society* **49**, 72 (1937).
78. Mott, N. F. The Basis of the Electron Theory of Metals, with Special Reference to the Transition Metals. *Proceedings of the Physical Society. Section A* **62**, 416 (1949).
79. PoorLeno. *Hydrogen Density Plots* https://commons.wikimedia.org/wiki/File:Hydrogen_Density_Plots.png. Accessed: 2018-05-03.
80. Alavi, A. et al. *Quantum Materials: Experiments and Theory* ISBN: 978-3-95806-159-0 (Aug. 31, 2016).
81. Mila, F. *Physique du Solide III et IV* (École Polytechnique Fédérale de Lausanne, 2007).
82. Fetter, A. L. & Walecka, J. D. *Quantum Theory of Many-particle Systems* 646 pp. ISBN: 978-0-486-42827-7 (Courier Corporation, June 20, 2003).
83. Molinari, L. G. Notes on Wick's theorem in many-body theory. <http://arxiv.org/abs/1710.09248> (2018) (Oct. 25, 2017).
84. Huang, E. W., Mendl, C. B., Jiang, H.-C., Moritz, B. & Devereaux, T. P. Stripe order from the perspective of the Hubbard model. *npj Quantum Materials* **3**, 22 (Apr. 20, 2018).
85. Hanke, W., Kopaev, Y. V. & John, W. Electronic Phase Transitions. *Modern Problems in Condensed Matter Sciences* Vol. 32. North Holland: Amsterdam, London, New York, Tokio 1992; 336 Seiten, ISBN 0-444-88885-3. *Crystal Research and Technology* **28**, 28–28.
86. Newman, M. E. J. & Barkema, G. T. *Monte Carlo Methods in Statistical Physics* 500 pp. ISBN: 978-0-19-851797-9 (Clarendon Press, Feb. 11, 1999).
87. Müller-Krumbhaar, H. & Binder, K. Dynamic properties of the Monte Carlo method in statistical mechanics. *Journal of Statistical Physics* **8**, 1–24 (May 1, 1973).
88. Santos, R. R. d. Introduction to quantum Monte Carlo simulations for fermionic systems. *Brazilian Journal of Physics* **33**, 36–54 (Mar. 2003).
89. Baeriswyl, D. & Campbell, D. K. *Interacting Electrons in Reduced Dimensions* Google-Books-ID: k5XfBwAAQBAJ. 400 pp. ISBN: 978-1-4613-0565-1 (Springer Science & Business Media, Dec. 6, 2012).
90. Feldbacher, M. & Assaad, F. F. Efficient calculation of imaginary-time-displaced correlation functions in the projector auxiliary-field quantum Monte Carlo algorithm. *Physical Review B* **63**, 073105 (Jan. 29, 2001).
91. White, S. R., Sugar, R. L. & Scalettar, R. T. Algorithm for the simulation of many-electron systems at low temperatures. *Physical Review B* **38**, 11665–11668 (Dec. 1, 1988).
92. Newman, M. *Computational Physics* 562 pp. ISBN: 978-1-4801-4551-1 (CreateSpace Independent Publishing Platform, Charleston, SC, Nov. 7, 2012).
93. Claveau, Y., Arnaud, B. & Matteo, S. D. Mean-field solution of the Hubbard model: the magnetic phase diagram. *European Journal of Physics* **35**, 035023 (2014).
94. Gouveia, J. D. & Dias, R. G. Magnetic phase diagram of the Hubbard model in the Lieb lattice. *Journal of Magnetism and Magnetic Materials* **382**, 312–317 (May 15, 2015).
95. Gennes, P.-G. d. *Superconductivity of Metals and Alloys* 292 pp. ISBN: 978-0-7382-0101-6 (Advanced Book Program, Perseus Books, 1999).
96. Yip, E. A Note on the Stability of Solving a Rank-p Modification of a Linear System by the Sherman–Morrison–Woodbury Formula. *SIAM Journal on Scientific and Statistical Computing* **7**, 507–513 (Apr. 1, 1986).

A

Obtaining the Hubbard Model. Approximate Solutions

A.1 Hartree-Fock Approximation and the Self Consistent Field

In the mean field approximation, the quartic term of the interaction part of the Hamiltonian

$$V_{\text{int}} = \frac{1}{2} V_{\nu' \mu'}^{\nu \mu} c_{\nu}^{\dagger} c_{\mu}^{\dagger} c_{\mu'} c_{\nu'},$$

becomes a sum of all possible 2-body terms (note that terms of the type $\langle cc \rangle$ and $\langle c^{\dagger}c^{\dagger} \rangle$ must vanish since they do not conserve the number of particles).

$$c_{\nu}^{\dagger} c_{\mu}^{\dagger} c_{\mu'} c_{\nu'} \approx -\langle c_{\nu}^{\dagger} c_{\mu'} \rangle c_{\mu}^{\dagger} c_{\nu'} - \langle c_{\mu}^{\dagger} c_{\nu'} \rangle c_{\nu}^{\dagger} c_{\mu'} + \langle c_{\nu}^{\dagger} c_{\nu'} \rangle c_{\mu}^{\dagger} c_{\mu'} + \langle c_{\mu}^{\dagger} c_{\mu'} \rangle c_{\nu}^{\dagger} c_{\nu'}, \quad (\text{A.1})$$

where we ignored the constant terms which are unimportant in the Hamiltonian, in what concerns the dynamics. This Hartree-Fock, or mean field approximation is slightly tricky to obtain. It requires one to be precise about what the meaning of the mean field approximation is in terms of creation and annihilation operators. In mean field theory, we assume that the operator

$$\rho_{\mu \mu'} = c_{\mu}^{\dagger} c_{\mu'} \quad (\text{A.2})$$

is close to its average, so that we neglect second order terms in the fluctuations $\delta \rho_{\mu \mu'}$, i.e. $\rho_{\mu \mu'}$ is “large” only when its average is nonzero, otherwise it is negligibly small. Thus, for most combinations of indices, this operator will vanish. We follow the usual mean field procedure of writing the original operator as a deviation plus an average

$$c_{\nu}^{\dagger} \left(c_{\mu}^{\dagger} c_{\mu'} - \langle c_{\mu}^{\dagger} c_{\mu'} \rangle \right) c_{\nu'} + c_{\nu}^{\dagger} c_{\nu'} \langle c_{\nu}^{\dagger} c_{\nu'} \rangle \quad (\text{A.3})$$

Then we note that if $\nu' \neq \mu$, we can commute $c_{\nu'}$ with the parenthesis. But this is true except in a set of measure zero. In the thermodynamic limit $N \rightarrow \infty$, the number of allowed \mathbf{k} -states is very large, and if we take a continuum limit in which the set of possible \mathbf{k} -states becomes dense, then the commutation becomes exact. Repeating the procedure of writing (A.3) replacing $c_{\nu}^{\dagger} c_{\nu'} \mapsto c_{\nu}^{\dagger} c_{\nu'} - \langle c_{\nu}^{\dagger} c_{\nu'} \rangle + \langle c_{\nu}^{\dagger} c_{\nu'} \rangle$, we obtain

$$\underbrace{(c_{\nu}^{\dagger} c_{\nu'} - \langle c_{\nu}^{\dagger} c_{\nu'} \rangle)(c_{\mu}^{\dagger} c_{\mu'} - \langle c_{\mu}^{\dagger} c_{\mu'} \rangle)}_{\propto \delta \rho_{\mu \mu'} \delta \rho_{\nu \nu'} \rightarrow 0} + c_{\nu}^{\dagger} c_{\nu'} \langle c_{\mu}^{\dagger} c_{\mu'} \rangle + c_{\mu}^{\dagger} c_{\mu'} \langle c_{\nu}^{\dagger} c_{\nu'} \rangle - \langle c_{\mu}^{\dagger} c_{\mu'} \rangle \langle c_{\nu}^{\dagger} c_{\nu'} \rangle \quad (\text{A.4})$$

But this result is not complete. This is only the so called Hartree or direct term. Due to identical nature of the interacting electrons, we must consider an analogous contribution for $\langle c_{\nu}^{\dagger} c_{\mu'} \rangle$ finite. We start by exchanging the first two operators:

$$c_{\nu}^{\dagger} c_{\mu}^{\dagger} c_{\mu'} c_{\nu'} = -c_{\mu}^{\dagger} c_{\nu}^{\dagger} c_{\mu'} c_{\nu'} \quad (\text{A.5})$$

Then we proceed in exactly the same manner as before. The result is analogous, but a minus sign appears and we must switch $\mu \leftrightarrow \nu$:

$$-c_{\mu}^{\dagger} c_{\nu'} \langle c_{\nu}^{\dagger} c_{\mu'} \rangle - c_{\nu}^{\dagger} c_{\mu'} \langle c_{\mu}^{\dagger} c_{\nu'} \rangle + \langle c_{\nu}^{\dagger} c_{\mu'} \rangle \langle c_{\mu}^{\dagger} c_{\nu'} \rangle \quad (\text{A.6})$$

Ignoring the constant terms of the type $\langle c^\dagger c \rangle \langle c^\dagger c \rangle$, we recover equation (A.1). Now we can simply substitute the mean field expansion of equation (A.1) in the second term to obtain the last term that is subtracted in equation (2.1) (we omit the boldface on the \mathbf{k} 's solely in the following equation, but keep in mind that they are vectors):

$$\begin{aligned} & \frac{1}{2} \sum_{\substack{\mathbf{k}_1 \mathbf{k}_2 \mathbf{k}'_1 \mathbf{k}'_2 \\ \sigma_1 \sigma_2}} V_{\mathbf{k}'_1 \mathbf{k}'_2}^{k_1 k_2} \left(-\underbrace{\left\langle c_{\mathbf{k}_1 \sigma_1}^\dagger c_{\mathbf{k}'_2 \sigma_2} \right\rangle}_{\delta_{\mathbf{k}_1 \mathbf{k}'_2} \delta_{\sigma_1 \sigma_2} f_{\mathbf{k}_1}} c_{\mathbf{k}_2 \sigma_2}^\dagger c_{\mathbf{k}'_1 \sigma_1} - \underbrace{\left\langle c_{\mathbf{k}_2 \sigma_2}^\dagger c_{\mathbf{k}'_1 \sigma_1} \right\rangle}_{\delta_{\mathbf{k}_2 \mathbf{k}'_1} \delta_{\sigma_1 \sigma_2} f_{\mathbf{k}_2}} c_{\mathbf{k}_1 \sigma_1}^\dagger c_{\mathbf{k}'_2 \sigma_2} + \underbrace{\left\langle c_{\mathbf{k}_1 \sigma_1}^\dagger c_{\mathbf{k}'_1 \sigma_1} \right\rangle}_{\delta_{\mathbf{k}_1 \mathbf{k}'_1} f_{\mathbf{k}_1}} c_{\mathbf{k}_2 \sigma_2}^\dagger c_{\mathbf{k}'_2 \sigma_2} \right. \\ & \left. + \underbrace{\left\langle c_{\mathbf{k}_2 \sigma_2}^\dagger c_{\mathbf{k}'_2 \sigma_2} \right\rangle}_{\delta_{\mathbf{k}_2 \mathbf{k}'_2} f_{\mathbf{k}_2}} c_{\mathbf{k}_1 \sigma_1}^\dagger c_{\mathbf{k}'_1 \sigma_1} \right) \end{aligned} \quad (\text{A.7})$$

In the language of Hartree Fock theory, the first two terms give the exchange term, and the last two terms the direct term. Thus, apart from the $\frac{1}{2}$ factor, the term in (A.7) becomes

$$\begin{aligned} & - \sum_{\substack{\mathbf{k}_1 \mathbf{k}_2 \\ \mathbf{k}'_1 \sigma_1}} V_{\mathbf{k}'_1 \mathbf{k}_1}^{k_1 k_2} f_{\mathbf{k}_1} c_{\mathbf{k}_2 \sigma_1}^\dagger c_{\mathbf{k}'_1 \sigma_1} - \sum_{\substack{\mathbf{k}_1 \mathbf{k}_2 \\ \mathbf{k}_2 \sigma_1}} V_{\mathbf{k}_2 \mathbf{k}'_2}^{k_1 k_2} f_{\mathbf{k}_2} c_{\mathbf{k}_1 \sigma_1}^\dagger c_{\mathbf{k}'_2 \sigma_1} + \sum_{\substack{\mathbf{k}_1 \mathbf{k}_2 \mathbf{k}'_2 \\ \sigma_1 \sigma_2}} V_{\mathbf{k}_1 \mathbf{k}'_2}^{k_1 k_2} f_{\mathbf{k}_1} c_{\mathbf{k}_2 \sigma_2}^\dagger c_{\mathbf{k}'_2 \sigma_2} \\ & + \sum_{\substack{\mathbf{k}_1 \mathbf{k}_2 \mathbf{k}'_1 \\ \sigma_1 \sigma_2}} V_{\mathbf{k}'_1 \mathbf{k}'_2}^{k_1 k_2} f_{\mathbf{k}_2} c_{\mathbf{k}_1 \sigma_1}^\dagger c_{\mathbf{k}'_1 \sigma_1} = \sum_{\mathbf{k}_1 \mathbf{k}_2 \sigma_1} \left(4V_{\mathbf{k}_1 \mathbf{k}_2}^{k_1 k_2} - 2V_{\mathbf{k}_2 \mathbf{k}_1}^{k_1 k_2} \right) f_{\mathbf{k}_2} c_{\mathbf{k}_1 \sigma_1}^\dagger c_{\mathbf{k}_1 \sigma_1}, \end{aligned} \quad (\text{A.8})$$

where we used momentum conservation to eliminate a \mathbf{k}' -sum. Moreover, we used that the sum on spin ($\pm 1/2$) on the last two terms gives factors of 2, since the interaction is spin independent and thus no spin-dependent term remains after we use momentum conservation. Making $\mathbf{k}_1 \rightarrow \mathbf{k}$, $\mathbf{k}_2 \rightarrow \mathbf{k}'$, $\sigma_1 \rightarrow \sigma$, and recalling the definition in equation (2.2), we obtain the result we sought.

The procedure above is meant to serve as an intuitive derivation. Now we approach the problem more formally. In fact, the argument that allowed us to perform the commutation leading to equation A.4 seems somewhat handwaving. We should not have to take the thermodynamic limit to perform a mean field expansion. A more systematic procedure to obtain the mean field expansion of a quartic interaction term was given by Pierre de Gennes in the context of a mean field treatment of a superconductor in a magnetic field [95]. Our case is actually much simpler to analyze, but we follow the same argument as de Gennes. Consider the Hamiltonian to be given by $\mathcal{H} = \mathcal{H}_0 + \mathcal{H}_1$, where

$$\mathcal{H}_0 = \sum_{\mathbf{k}, \sigma} \varepsilon_{\mathbf{k}} c_{\mathbf{k}, \sigma}^\dagger c_{\mathbf{k}, \sigma} \quad \mathcal{H}_1 = \frac{1}{2} \sum_{\substack{\mathbf{k}_1 \mathbf{k}_2 \\ \mathbf{k}'_1 \mathbf{k}'_2 \\ \sigma_1 \sigma_2}} V_{\mathbf{k}'_1 \mathbf{k}'_2}^{k_1 k_2} c_{\mathbf{k}_1 \sigma_1}^\dagger c_{\mathbf{k}_2 \sigma_2}^\dagger c_{\mathbf{k}'_2 \sigma_2} c_{\mathbf{k}'_1 \sigma_1} \quad (\text{A.9})$$

We would like to find an effective Hamiltonian that is quadratic in the fermion operators:

$$\mathcal{H}_{\text{eff}} = \sum_{\mathbf{k}, \sigma} (\varepsilon_{\mathbf{k}} + v_{\mathbf{k}}) c_{\mathbf{k}, \sigma}^\dagger c_{\mathbf{k}, \sigma} \quad (\text{A.10})$$

This effective Hamiltonian is diagonal, so assuming we know $v_{\mathbf{k}}$ (which is what we are trying to determine in the first place), we can compute its eigenstates $\{|\phi\rangle\}$, and compute the average of the actual Hamiltonian \mathcal{H} using the basis $\{|\phi\rangle\}$:

$$\langle \mathcal{H} \rangle = \frac{\sum_{\phi} \langle \phi | \mathcal{H} | \phi \rangle e^{-\beta E_{\phi}}}{\sum_{\phi} e^{-\beta E_{\phi}}} \quad (\text{A.11})$$

Our criterion to determine \mathcal{H}_{eff} is the requirement that the free energy $F = \langle \mathcal{H} \rangle - TS$, with the average

computed with the eigenstates of \mathcal{H}_{eff} be stationary, i.e. $\delta F = 0$. Thus, we find the mean field form of the quartic term invoking only a variational principle without any need to resort to the thermodynamic limit. In fact, we never even have to explicitly compute the average in equation (A.11). In terms of pairs of fermion operator averages, we have

$$\langle \mathcal{H} \rangle = \sum_{\mathbf{k}, \sigma} \varepsilon_{\mathbf{k}} \left\langle c_{\mathbf{k}, \sigma}^\dagger c_{\mathbf{k}, \sigma} \right\rangle + \frac{1}{2} \sum_{\substack{\mathbf{k}_1, \mathbf{k}_2 \\ \mathbf{k}'_1, \mathbf{k}'_2 \\ \sigma_1, \sigma_2}} V_{\mathbf{k}'_1 \mathbf{k}'_2}^{k_1 k_2} \left\langle c_{\mathbf{k}_1 \sigma_1}^\dagger c_{\mathbf{k}_2 \sigma_2}^\dagger c_{\mathbf{k}'_2 \sigma_2} c_{\mathbf{k}'_1 \sigma_1} \right\rangle, \quad (\text{A.12})$$

where the last term can be reduced to products of averages of pairs of fermion operators by Wick's theorem:

$$\begin{aligned} \left\langle c_{\mathbf{k}_1 \sigma_1}^\dagger c_{\mathbf{k}_2 \sigma_2}^\dagger c_{\mathbf{k}'_2 \sigma_2} c_{\mathbf{k}'_1 \sigma_1} \right\rangle &= \left\langle c_{\mathbf{k}_1 \sigma_1}^\dagger c_{\mathbf{k}'_1 \sigma_1} \right\rangle \left\langle c_{\mathbf{k}_2 \sigma_2}^\dagger c_{\mathbf{k}'_2 \sigma_2} \right\rangle - \left\langle c_{\mathbf{k}_1 \sigma_1}^\dagger c_{\mathbf{k}'_2 \sigma_2} \right\rangle \left\langle c_{\mathbf{k}_2 \sigma_2}^\dagger c_{\mathbf{k}'_1 \sigma_1} \right\rangle \\ &+ \left\langle c_{\mathbf{k}_1 \sigma_1}^\dagger c_{\mathbf{k}_2 \sigma_2} \right\rangle \left\langle c_{\mathbf{k}'_2 \sigma_2} c_{\mathbf{k}'_1 \sigma_1} \right\rangle \end{aligned} \quad (\text{A.13})$$

The computation is now done by using the rules (for all \mathbf{k} and σ).

$$\begin{aligned} \left\langle c_{\mathbf{k}, \sigma}^\dagger c_{\mathbf{k}', \sigma'} \right\rangle &= \delta_{\mathbf{k}, \mathbf{k}'} \delta_{\sigma, \sigma'} f_{\mathbf{k}} \\ \left\langle c_{\mathbf{k}, \sigma}^{(\dagger)} c_{\mathbf{k}', \sigma'}^{(\dagger)} \right\rangle &= 0, \end{aligned} \quad (\text{A.14})$$

where $f_{\mathbf{k}} = (e^{\beta(\varepsilon_{\mathbf{k}} - \mu)} + 1)^{-1}$ is the Fermi-Dirac function.

Since the original Hamiltonian is quadratic, again we have that terms of the type $\langle cc \rangle$ and $\langle c^\dagger c^\dagger \rangle$ do not contribute. Hence, varying the free energy, we obtain

$$\begin{aligned} \delta F = \delta \langle \mathcal{H} \rangle - T \delta S &= \sum_{\mathbf{k}, \sigma} \varepsilon_{\mathbf{k}} \delta \left\langle c_{\mathbf{k}, \sigma}^\dagger c_{\mathbf{k}, \sigma} \right\rangle + \frac{1}{2} \sum_{\substack{\mathbf{k}_1, \mathbf{k}_2 \\ \mathbf{k}'_1, \mathbf{k}'_2 \\ \sigma_1, \sigma_2}} V_{\mathbf{k}'_1 \mathbf{k}'_2}^{k_1 k_2} \left(\left\langle c_{\mathbf{k}_1 \sigma_1}^\dagger c_{\mathbf{k}'_1 \sigma_1} \right\rangle \delta \left\langle c_{\mathbf{k}_2 \sigma_2}^\dagger c_{\mathbf{k}'_2 \sigma_2} \right\rangle + \right. \right. \\ &\left. \left. \delta \left\langle c_{\mathbf{k}_1 \sigma_1}^\dagger c_{\mathbf{k}'_1 \sigma_1} \right\rangle \left\langle c_{\mathbf{k}_2 \sigma_2}^\dagger c_{\mathbf{k}'_2 \sigma_2} \right\rangle - \left\langle c_{\mathbf{k}_1 \sigma_1}^\dagger c_{\mathbf{k}'_2 \sigma_2} \right\rangle \delta \left\langle c_{\mathbf{k}_2 \sigma_2}^\dagger c_{\mathbf{k}'_1 \sigma_1} \right\rangle - \delta \left\langle c_{\mathbf{k}_1 \sigma_1}^\dagger c_{\mathbf{k}'_2 \sigma_2} \right\rangle \left\langle c_{\mathbf{k}_2 \sigma_2}^\dagger c_{\mathbf{k}'_1 \sigma_1} \right\rangle \right) - T \delta S, \end{aligned} \quad (\text{A.15})$$

which can be simplified exactly in the same manner as in equation (A.7), i.e. by using the rules of equation (A.14), and that the occupation of a given momentum state \mathbf{k} is given by the Fermi-Dirac function:

$$\delta F = \sum_{\mathbf{k}, \sigma} \varepsilon_{\mathbf{k}} \delta \left\langle c_{\mathbf{k}, \sigma}^\dagger c_{\mathbf{k}, \sigma} \right\rangle + \sum_{\mathbf{k}, \mathbf{k}', \sigma} \left(2V_{\mathbf{k} \mathbf{k}'}^{kk'} - V_{\mathbf{k}' \mathbf{k}}^{kk'} \right) f_{\mathbf{k}'} c_{\mathbf{k} \sigma} \delta \left\langle c_{\mathbf{k}, \sigma}^\dagger c_{\mathbf{k}, \sigma} \right\rangle \quad (\text{A.16})$$

We can now compare $\delta F = \delta \langle \mathcal{H} \rangle - T \delta S$ and $\delta F' = \delta \langle \mathcal{H}_{\text{eff}} \rangle - T \delta S$, which is simply given by

$$\delta F' = \delta \langle \mathcal{H}_{\text{eff}} \rangle - T \delta S = \sum_{\mathbf{k}, \sigma} (\varepsilon_{\mathbf{k}} + v_{\mathbf{k}}) \delta \left\langle c_{\mathbf{k}, \sigma}^\dagger c_{\mathbf{k}, \sigma} \right\rangle \quad (\text{A.17})$$

Requiring both free energies to be stationary, we find our desired result

$$v_{\mathbf{k}} = \sum_{\mathbf{k}'} \left(2V_{\mathbf{k} \mathbf{k}'}^{kk'} - V_{\mathbf{k}' \mathbf{k}}^{kk'} \right) f_{\mathbf{k}'}, \quad (\text{A.18})$$

which agrees with the result obtained from our initial more intuitive, but somewhat less rigorous argument.

A.2 Mott insulators

Band theory was found to be flawed soon after it was introduced. The picture it proposes is simple and generally works pretty well. It is based on considering the electrons to be independently moving under the constant background potential created by the ions. The solutions of the Schrödinger for free

electrons in a periodic potential $U(\mathbf{r})$, such that $U(\mathbf{r}) = U(\mathbf{r} + \mathbf{R})$,

$$\left[-\frac{1}{2m} \nabla^2 + U(\mathbf{r}) \right] \psi(\mathbf{r}) = \varepsilon \psi(\mathbf{r}) \quad (\text{A.19})$$

are given by Bloch's theorem: $\psi_{\mathbf{k}}(\mathbf{r}) = e^{i\mathbf{k}\cdot\mathbf{r}} u_{\mathbf{k}}(\mathbf{r})$. Note that we made $\hbar = 1$. Replacing this wave function in equation (A.19), we obtain a differential equation for $u_{\mathbf{k}}(\mathbf{r})$, which has in general an infinite number of solutions. We label them with an index n , which we call the band index. To each solution there corresponds a function $\varepsilon_{n\mathbf{k}}$. The set of these functions is known as the band structure. Since electrons are taken to be independent in band theory, the N-electron eigenstates are obtained by placing an electron in each quantum state. Each state is labelled by its energy $\varepsilon_{n\mathbf{k}\sigma}$. Since our model Hamiltonian does not couple spins (via an electron interaction, for example) and assuming there is no external magnetic field and that the system has an inversion center, we have $\varepsilon_{n\mathbf{k}\uparrow} = \varepsilon_{n\mathbf{k}\downarrow}$. In general there might be energies for which there is no corresponding $\varepsilon_{n\mathbf{k}\sigma}$. These form intervals called forbidden bands¹. Thus, the ground state of our model may be obtained by filling the energy levels starting from the lowest energy state. Two cases are particularly relevant:

- Every band is either fully occupied or empty. The first excited state differs from the ground state by Δ , the separation between the last fully occupied band and the first empty band. It is then impossible to induce the motion of the electrons by applying an arbitrarily small voltage. This is what it means to be an *insulator*. Since there $2N$ states per band, this is not possible unless the number of electrons per unit cell is an even integer.
- One or more of the bands are partially filled. The energy of occupied state of higher energy is named the Fermi energy ε_F . In this case, the separation between the ground state and the first excited state tends to 0 in the thermodynamic limit, $N \rightarrow \infty$. The system may then respond to infinitesimal excitations, which is the definition of a metal.

Band theory made it possible to predict whether a solid would be a metal or an insulator. However, its success rests crucially on the independent electron approximation. Thus, it is not surprising that for compounds with strongly correlated electrons the theory might fail [81]. The Coulomb interaction is in general non negligible, and the effects it leads to are not captured by a mean field approach. One must resort to many-body theory. An example of a many-body effect that band theory doesn't capture is superconductivity. However, this does not deem band theory useless. In fact, the superconducting phase arises due to an instability of a state that is itself well described by band theory [95]. A far greater failure of band theory is that predicts certain compounds with an odd number of electrons per unit cell, such as NiO and La₂CuO₄, to be metals, while in fact they turn out to be (Mott) insulators. Mott devised a simple argument to justify this failure. It is based on considering the elementary electronic excitations of a solid composed by hydrogen atoms as a function of the distance between atoms.

Consider a hypothetical solid consisting of a square lattice with hydrogen atoms on its points. Each unit cell has one hydrogen atom, and consequently one electron. Band theory would predict such a solid to be a metal. However, if the lattice parameter a is large enough, the solid cannot remain a metal.

¹We disregard surface states that may have energies that fall in the forbidden bands of band theory.

There must be some value of the lattice parameter $a = a_c$ for which the system becomes an insulator. When current flows through a sample of this solid, electrons hop consecutively, reaching positions that can be quite far on the lattice. For a metal, this process occurs even when exciting the system with an infinitesimal amount of energy. How much energy do we need to provide for this process to occur?

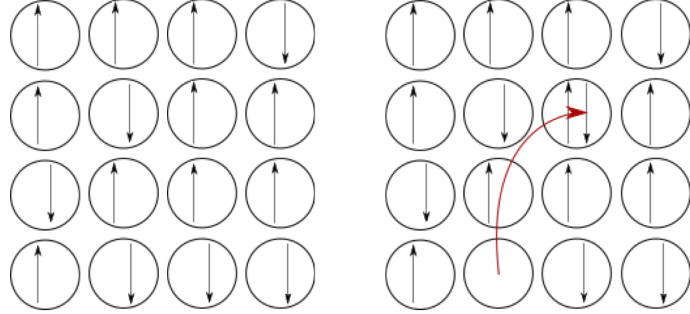


Figure A.1: On the right, a configuration of hydrogen atoms on a square lattice with a hole and a doubly occupied site obtained by delocalization of the spin down electron on the left.

If a is large, we have essentially one electron per site at the start. When an electron is displaced, we end up with a hole and a doubly occupied site. The potential energy of such a state is

$$E_{H^-} + E_{H^+} - 2E_H \quad (\text{A.20})$$

Due to the Coulomb repulsion between the two electrons in H^- , this quantity is strictly positive. Call it $U > 0$. On the other hand, the system also has kinetic energy: both the hole and the doubly occupied site can delocalize. Let W be the bandwidth corresponding to the delocalization of an electron on the lattice. Both the hole and the doubly occupied will stay at the bottom of the band and gain an energy $W/2$ (assuming that this delocalization is of the same order of magnitude). The dominant transfer integral $-t$ is between nearest neighbors. The dispersion relation then reads

$$\varepsilon_{\mathbf{k}} = -2t(\cos k_x + \cos k_y) \quad (\text{A.21})$$

The bandwidth is then $W = 8t$. The energy of a configuration with a hole and a doubly occupied site is

$$\Delta_c = U - W, \quad (\text{A.22})$$

where U is practically independent of the lattice parameter a . The bandwidth W , however, depends strongly on a . When $a \gg a_0$, where a_0 is the Bohr radius, the transfer integral is exponentially small, because only the exponential tails of the wave functions are relevant. In this limit, $\Delta_c \approx U$ is a large, positive number, and the system is an insulator. This type of insulator is called a Mott insulator, and Δ_c is called the charge gap. As a decreases, t increases, and there must be a critical value $a_c \sim a_0$, for which $U = W$. Below this value, the computation of Δ_c is not valid anymore because the gap cannot be negative. Thus, there must be a metal-insulator transition. It is possible to see this transition if we apply enough pressure to a Mott insulator so as to decrease a and increase t . A transition of this type was first seen in the 1970's for V_2O_3 ². There is a fundamental difference between a band insulator and

²Of course, the transition is not so easy to describe. We should consider the Hubbard model! However, this simple argument provides an intuitive picture.

a Mott insulator. While we must pay an energy Δ_c to make a charge excitation, there is no cost for making a spin excitation: we can flip the spin of an electron without creating a doubly occupied site. The fluctuations of both charge and spin due to the electron interactions may then lead to magnetic behavior characteristic of correlated systems.

A.3 Computing the partition function for a quadratic Hamiltonian

Let us start by restating the result we want to prove.

If $\mathcal{H} = \mathbf{c}^\dagger \mathbf{H} \mathbf{c}$, where \mathbf{H} is a $N \times N$ Hermitian matrix, then we have that

$$\text{Tr}[e^{-\beta \mathcal{H}}] = \prod_{i=1}^N (1 + e^{-\beta \lambda_i}), \quad (\text{A.23})$$

where λ_i are the eigenvalues of \mathbf{H} .

We will now prove equation (A.23). Without loss of generality, let us consider \mathbf{H} to be diagonal. Then, its eigenvalues coincide with the diagonal entries, so that $\mathbf{H} = \text{diag}(\lambda_i)$. The quadratic Hamiltonian may then be diagonalized

$$\mathcal{H} = \mathbf{c}^\dagger \text{diag}(\lambda_1, \lambda_2, \dots, \lambda_N) \mathbf{c} = \sum_{i=1}^N \lambda_i n_i$$

We continue by induction. When $N = 1$, we have

$$\text{Tr}(e^{-\beta \mathcal{H}}) = \langle 0 | e^{-\beta \lambda_1 n_1} | 0 \rangle + \langle 1 | e^{-\beta \lambda_1 n_1} | 1 \rangle = 1 + e^{-\beta \lambda_1} \quad (\text{A.24})$$

Assuming that for $N - 1$:

$$\text{Tr}[e^{-\beta \sum_{i=1}^{N-1} \lambda_i n_i}] = \prod_{i=1}^{N-1} (1 + e^{-\beta \lambda_i})$$

we can compute the trace for i going up to N .

$$\begin{aligned} \text{Tr}[e^{-\beta \sum_{i=1}^{N-1} \lambda_i n_i}] &= \sum_{i=1}^N \left\langle \psi_1^{\lambda_1} \psi_2^{\lambda_2} \dots \psi_N^{\lambda_N} \middle| e^{-\beta \sum_{i=1}^N \lambda_i n_i} \middle| \psi_1^{\lambda_1} \psi_2^{\lambda_2} \dots \psi_N^{\lambda_N} \right\rangle \\ &= \sum_{i=1}^{N-1} \left(\left\langle \{\psi_i^{\lambda_i}\} 0 \middle| e^{-\beta \sum_{i=1}^N \lambda_i n_i} e^{-\beta \lambda_N n_N} \middle| \{\psi_i^{\lambda_i}\} 0 \right\rangle + \left\langle \{\psi_i^{\lambda_i}\} 1 \middle| e^{-\beta \sum_{i=1}^N \lambda_i n_i} e^{-\beta \lambda_N n_N} \middle| \{\psi_i^{\lambda_i}\} 1 \right\rangle \right) \\ &= (1 + e^{-\beta \lambda_N}) \sum_{i=1}^{N-1} \left\langle \{\psi_i^{\lambda_i}\} \middle| e^{-\beta \lambda_i n_i} \middle| \{\psi_i^{\lambda_i}\} \right\rangle \\ &= (1 + e^{-\beta \lambda_N}) \prod_{i=1}^{N-1} (1 + e^{-\beta \lambda_i}) \\ &= \prod_{i=1}^N (1 + e^{-\beta \lambda_i}) \end{aligned}$$

To complete the proof we note that for any \mathbf{H} , there exists a unitary matrix \mathbf{Q} , such that $\mathbf{Q}^T \mathbf{H} \mathbf{Q} = \mathbf{\Lambda} = \text{diag}(\lambda_i)$. Let $\tilde{\mathbf{c}} = \mathbf{Q} \mathbf{c}$, and $\tilde{n}_i = \tilde{c}_i^\dagger \tilde{c}_i$. Then, we find

$$\mathcal{H} = \mathbf{c}^\dagger \mathbf{H} \mathbf{c} = \tilde{\mathbf{c}}^\dagger \mathbf{\Lambda} \tilde{\mathbf{c}} = \sum_{i=1}^N \lambda_i \tilde{n}_i$$

The trace is independent of the choice of basis functions. Thus, we have

$$\begin{aligned}\text{Tr}(e^{-\beta\mathcal{H}}) &= \text{Tr}\left(\prod_{i=1}^N e^{-\beta\lambda_i\tilde{n}_i}\right) \\ &= \prod_{i=1}^N \left(1 + e^{-\beta\lambda_i}\right) \quad \square\end{aligned}$$

A.4 Density of states for a 1D tight binding model

Using the definition of the density of states

$$N(E) = \frac{1}{N} \sum_{\mathbf{k}} \delta_{E, \varepsilon_{\mathbf{k}}} \rightarrow \frac{1}{(2\pi)^d} \int d\mathbf{k} \delta(E - \varepsilon_{\mathbf{k}}) \text{ when } N \rightarrow \infty. \quad (\text{A.25})$$

with $\varepsilon_k = -2t \cos k$, in the thermodynamic limit we obtain

$$N(E) = \frac{1}{2\pi} \int dk \delta(E + 2t \cos k) \quad (\text{A.26})$$

Now we use a well known property of the delta function

$$\delta(g(x)) = \sum_{\{i|g(x_i)=0\}} \frac{\delta(x - x_i)}{|g'(x_i)|} \quad (\text{A.27})$$

Noting that $g'(k) = -2t \sin k$, and that the roots of g (there are two in the first Brillouin zone, to which the integral is restricted) satisfy $\cos k_i = -E/2t$, so that $\sin k_i = \pm\sqrt{1 - E^2/4t^2}$, we obtain

$$\delta(E + 2t \cos k) = \frac{1}{\sqrt{4t^2 - E^2}} \left(\delta(k - k_1) + \delta(k - k_2) \right) \quad (\text{A.28})$$

leading to the sought result

$$N(E)_{1d} = \frac{1}{\pi\sqrt{4t^2 - E^2}} \quad (\text{A.29})$$

A.5 Effective Heisenberg model as the atomic limit of the Hubbard model

To obtain the effective Hamiltonian in the $U/t \gg 1$ limit of the Hubbard model to second order in degenerate perturbation theory, we start with its general form

$$\langle m | \mathcal{H}_{\text{eff}} | n \rangle = \sum_{|k\rangle} \frac{\langle m | \mathcal{H}_0 | k \rangle \langle k | \mathcal{H}_0 | n \rangle}{E_0 - E_k} = -\frac{1}{U} \sum_{|k\rangle} \langle m | \mathcal{H}_0 | k \rangle \langle k | \mathcal{H}_0 | n \rangle, \quad (\text{A.30})$$

where $|k\rangle$ are the states that are not in the ground state subspace. The identity operator in the subspace of states with one doubly occupied site $\sum_{|k\rangle} |k\rangle\langle k|$ may be written in a more conveniently in the representation: $\sum_j n_{j,\sigma} n_{j,-\sigma}$, so that the effective Hamiltonian is

$$\mathcal{H}_{\text{eff}} = -\mathcal{H}_0 \frac{\sum_j n_{j,\sigma} n_{j,-\sigma}}{U} \mathcal{H}_0 \quad (\text{A.31})$$

For each element j of the sum, only terms of the type

$$\sum_{i(j)} c_{j,\sigma}^\dagger c_{i,\sigma}$$

contribute. Here $\sum_{i(j)}$ is a sum over the set of neighbors i of site j . A term of the effective Hamiltonian

\mathcal{H}_{eff} corresponding to the j -th element in the sum reads

$$-\frac{t^2}{U} \sum_{i(j), \sigma_1, \sigma_2} c_{i, \sigma_1}^\dagger c_{j, \sigma_1} n_{j, \sigma} n_{j, -\sigma} c_{j, \sigma_2}^\dagger c_{i, \sigma_2}$$

There are only four cases in which the contribution of a term of this type is nonzero.

- $\sigma = \sigma_1 = \sigma_2$

The operator in the sum then becomes

$$c_{i, \sigma}^\dagger c_{j, \sigma} n_{j, \sigma} n_{j, -\sigma} c_{j, \sigma}^\dagger c_{i, \sigma} = n_{i, \sigma} n_{j, -\sigma} c_{j, \sigma} n_{j, \sigma} c_{j, \sigma}^\dagger$$

Now, we use a fermionic operator identity:

$$\begin{aligned} cn &= cc^\dagger c = (1 - c^\dagger c)c = c \\ \implies c_{j, \sigma} n_{j, \sigma} c_{j, \sigma}^\dagger &= c_{j, \sigma} c_{j, \sigma}^\dagger = 1 - n_{j, \sigma} \end{aligned}$$

The term of the Hamiltonian corresponding to this first case then takes on the form

$$n_{i, \sigma} n_{j, -\sigma} (1 - n_{j, \sigma})$$

We can further simplify this term by noting that in the subspace where \mathcal{H}_{eff} acts, every site is occupied by only a single electron so that

$$n_{j, \sigma} + n_{j, -\sigma} = 1 \iff 1 - n_{j, \sigma} = n_{j, -\sigma}$$

Since, for fermions we have that $\hat{n} = \hat{n}^k$, whichever the power $k \in \mathbb{N}$, the final form of the sought term of the Hamiltonian is

$$n_{i, \sigma} n_{j, -\sigma}$$

- $-\sigma = \sigma_1 = \sigma_2$

The contribution to the Hamiltonian is exactly of the same form but making $\sigma \mapsto -\sigma$:

$$n_{i, -\sigma} n_{j, \sigma}$$

- $\sigma = -\sigma_1 = \sigma_2$

We can use the same reasoning as we did for the first term to obtain

$$\begin{aligned} &c_{i, -\sigma}^\dagger c_{j, -\sigma} n_{j, \sigma} n_{j, -\sigma} c_{j, \sigma}^\dagger c_{i, \sigma} \\ &= c_{i, -\sigma}^\dagger c_{i, \sigma} \underbrace{c_{j, -\sigma} n_{j, -\sigma}}_{c_{j, -\sigma}} \underbrace{n_{j, \sigma} c_{j, \sigma}^\dagger}_{c_{j, \sigma}^\dagger} \\ &= -c_{i, -\sigma}^\dagger c_{i, \sigma} c_{j, \sigma}^\dagger c_{j, -\sigma} \end{aligned}$$

- $-\sigma = -\sigma_1 = \sigma_2$

Analogously, the contribution to the Hamiltonian is

$$\begin{aligned} &c_{i, \sigma}^\dagger c_{j, \sigma} n_{j, \sigma} n_{j, -\sigma} c_{j, -\sigma}^\dagger c_{i, -\sigma} \\ &= -c_{i, -\sigma}^\dagger c_{i, \sigma} c_{j, \sigma}^\dagger c_{j, -\sigma} \end{aligned}$$

Grouping all these four terms, we obtain

$$\mathcal{H}_{\text{eff}} = \frac{2t^2}{U} \sum_{\langle i,j \rangle, \sigma} (-n_{i,\sigma} n_{j,-\sigma} + c_{i,-\sigma}^\dagger c_{i,\sigma} c_{j,\sigma}^\dagger c_{j,-\sigma}), \quad (\text{A.32})$$

where the factor of 2 appears because for each pair of nearest neighbors $\langle i,j \rangle$, a term comes from the term $n_{j,\sigma} n_{j,-\sigma}$ of the sum $\sum_j n_{j,\sigma} n_{j,-\sigma}$, and another term from $n_{i,\sigma} n_{i,-\sigma}$.

Recall the second quantized form of the spin operators:

$$\begin{cases} S_i^z = \frac{1}{2}(n_{i,\uparrow} - n_{i,\downarrow}) \\ S_i^+ = c_{i,\uparrow}^\dagger c_{i,\downarrow} \\ S_i^- = c_{i,\downarrow}^\dagger c_{i,\uparrow}, \end{cases} \quad (\text{A.33})$$

Using these relations and that the density operator is $n_i = n_{i,\uparrow} + n_{i,\downarrow}$, the following relations hold

$$\begin{aligned} S_i^z S_j^z - \frac{1}{4} n_i n_j &= -\frac{1}{2}(n_{i,\uparrow} n_{j,\downarrow} + n_{i,\downarrow} n_{j,\uparrow}) \\ S_i^+ S_j^- + S_i^- S_j^+ &= c_{i,\uparrow}^\dagger c_{i,\downarrow} c_{j,\downarrow}^\dagger c_{j,\uparrow} + c_{i,\downarrow}^\dagger c_{i,\uparrow} c_{j,\uparrow}^\dagger c_{j,\downarrow} \end{aligned} \quad (\text{A.34})$$

Thus, we may rewrite the effective Hamiltonian:

$$\mathcal{H}_{\text{eff}} = \frac{4t^2}{U} \sum_{\langle i,j \rangle} \left(S_i^z S_j^z - \frac{1}{4} n_i n_j + \frac{1}{2}(S_i^+ S_j^- + S_i^- S_j^+) \right) \quad (\text{A.35})$$

But $S_i^z S_j^z + \frac{1}{2}(S_i^+ S_j^- + S_i^- S_j^+) = \mathbf{S}_i \cdot \mathbf{S}_j$ and $n_i = n_j = 1$ in the ground state subspace, so the effective Hamiltonian becomes

$$\mathcal{H}_{\text{eff}} = \frac{4t^2}{U} \sum_{\langle i,j \rangle} \left(\mathbf{S}_i \cdot \mathbf{S}_j - \frac{1}{4} \right), \quad (\text{A.36})$$

which corresponds to the antiferromagnetic Heisenberg model: $\mathcal{H}_{\text{Heis}} = J \sum_{\langle i,j \rangle} \mathbf{S}_i \cdot \mathbf{S}_j$, with $J = 4t^2/U$.

A.6 On Wick's theorem

A product of operators containing k factors c_i^\dagger and $n - k$ factors c_i is brought into *normal ordering* by the operator \mathcal{N} (also written $: \cdot :$) defined as

$$\mathcal{N}[c_1^{(\dagger)} c_2^{(\dagger)} \dots c_n^{(\dagger)}] =: c_1^{(\dagger)} c_2^{(\dagger)} \dots c_n^{(\dagger)} : \equiv (-1)^P c_{i_1}^\dagger c_{i_2}^\dagger \dots c_{i_k}^\dagger c_{i_{k+1}} c_{i_{k+2}} \dots c_{i_n}, \quad (\text{A.37})$$

where P is the parity of the permutation $1, 2, \dots, n \mapsto i_1, i_2, \dots, i_n$.

It is straightforward to simplify a product of two operators: $C_1 C_2 = \mathcal{N}[C_1 C_2] + \{C_1^-, C_2^+\}$, using the anti-commutation rules. Here C_i^{\pm} is a combination of fermionic creation (annihilation) operators. The last term is a c-number by assumption. Defining a contraction as $\overline{C_1 C_2} \equiv C_1 C_2 - \mathcal{N}[C_1 C_2]$, we obtain $\overline{C_1 C_2} = \{C_1^-, C_2^+\}$. The definition of a contraction holds even there are other operators between the two contracted ones $C_{1,2}$. Wick's theorem generalizes the result for a product of two operators, giving an expression for the product of an arbitrary number of operators.

Let us state the zero temperature version of Wick's theorem for generic operators $C_i = C_i^+ + C_i^-$.

$$C_1 C_2 \dots C_n = \mathcal{N}[C_1 C_2 \dots C_n] + \sum_{(ij)} \mathcal{N}[C_1 C_2 \dots \overline{C_i \dots C_j} \dots C_n] + \sum_{(ij),(lm)} \mathcal{N}[C_1 C_2 \dots \overline{C_i \dots C_l} \dots \overline{C_j \dots C_m} \dots C_n] + \dots, \quad (\text{A.38})$$

where the first sum is over single contractions of pairs, the second one on double contractions, and so

on. For odd n , the last term contains single unpaired operators. Otherwise, they are just products of contractions, which are c-numbers.

A general rule follows from the fact that the average of a normally ordered operator vanishes in the ground state. Two-point correlation functions determine all n -point correlation functions. In particular, for the case of 4 operators, using a self-explanatory abbreviated notation:

$$\langle gs|1234|gs\rangle = \langle 12\rangle\langle 34\rangle - \langle 13\rangle\langle 24\rangle + \langle 14\rangle\langle 23\rangle \quad (\text{A.39})$$

Of course, in the finite temperature case, Wick's theorem is not an operator identity because there is no non ambiguous way of defining normal ordering. However, for non-interacting particles, the thermal average of a product of one-particle operators is still a sum over all possible contractions of pairs. All that changes is the definition of the contraction, which is now defined in terms of the thermal average of the product of a pair of operators. Additionally, the theorem generalizes for time-ordered products, simply by replacing the thermal averages of the pair products by time-ordered pair averages.

In particular, for a free theory, the n -particle Green's function, defined by the field operators $\hat{\psi}(x)$,

$$\mathcal{G}(x_1, x_2, \dots, x_n; y_1, y_2, \dots, y_n) \equiv \left\langle \mathcal{T}\hat{\psi}(x_1)\hat{\psi}(x_2)\dots\hat{\psi}(x_n)\hat{\psi}^\dagger(y_1)\hat{\psi}^\dagger(y_2)\dots\hat{\psi}^\dagger(y_n) \right\rangle \quad (\text{A.40})$$

is determined solely by the set of all one-particle Green's functions. Here x and y denote both the complete set of quantum numbers describing the system's degrees of freedom, and imaginary time.

Applying Wick's theorem to the set of non-interacting (and thus independent) particles, we obtain

$$\mathcal{G}(x_1, x_2, \dots, x_n; y_1, y_2, \dots, y_n) = \sum_P (-1)^P \mathcal{G}^0(x_1; y_{i_1}) \mathcal{G}^0(x_2; y_{i_2}) \dots \mathcal{G}^0(x_n; y_{i_n}), \quad (\text{A.41})$$

which corresponds to evaluating the determinant of the matrix \mathbf{G} , defined as $G_{ij} \equiv \mathcal{G}^0(x_i; x_j)$ for $i, j = 1, 2, \dots, n$, where the \mathcal{G}^0 are the free-particle Green's functions, also called propagators.

A.7 Mean field theory and the variational principle

In section A.1, we derived the Hartree-Fock form of the Hubbard Hamiltonian. Here we explain how it arises as a mean field theory prone to studying spontaneous symmetry breaking, generally by resorting to a self-consistent procedure. This is useful as a first approach to investigate the tendency towards long range ordering, for example in ferromagnetic, or antiferromagnetic phases.

The starting point is the Gibbs-Bogoliubov-Feynman (GBF) inequality

$$\mathcal{F} \leq \langle \mathcal{H} \rangle_{\text{MF}} - T\mathcal{S}_{\text{MF}}, \quad (\text{A.42})$$

which is saturated when $\mathcal{H}_{\text{MF}} = \mathcal{H}$, and in general serves as a variational principle to find a simpler, non-interacting form for the Hamiltonian. \mathcal{F} is the system's free energy, T is the temperature and the mean field averages are computed as per Eq.(A.10), while the entropy is computed for the thermal distribution $\rho_{\text{MF}} = e^{-\beta\mathcal{H}_{\text{MF}}}$. Defining $\mathcal{F}_{\text{MF}} = \langle \mathcal{H}_{\text{MF}} \rangle_{\text{MF}} - T\mathcal{S}_{\text{MF}}$, we may recast Eq.(A.42) as

$$\mathcal{F} \leq \mathcal{F}_{\text{MF}} + \langle \mathcal{H} - \mathcal{H}_{\text{MF}} \rangle_{\text{MF}} \equiv F \quad (\text{A.43})$$

We seek a quadratic Hamiltonian that minimizes F , i.e. $\delta F = 0$, of the form

$$\mathcal{H}_{\text{MF}} = \mathcal{H}_K + \sum_{i,j,\sigma} \varepsilon_{ij} c_{i,\sigma}^\dagger c_{j,\sigma}, \quad (\text{A.44})$$

which corresponds to the possibility of the appearance of spin polarization along the quantization axis. and by varying $\varepsilon_{ij} \mapsto \varepsilon_{ij} + \delta\varepsilon_{ij}$, we can compute δF and show that it is minimized ($\delta F = 0$) for the mean field Hubbard Hamiltonian in much the same way as we did in section A.1.

Since the Hamiltonian of Eq.(A.44) is quadratic in the fermion operators, we have that $\langle n_{i,\uparrow} n_{i,\downarrow} \rangle_{\text{MF}} = \langle n_{i,\uparrow} \rangle_{\text{MF}} \langle n_{i,\downarrow} \rangle_{\text{MF}}$, and we must vary ε_{ij} in the following term

$$\langle \mathcal{H} - \mathcal{H}_{\text{MF}} \rangle_{\text{MF}} = \sum_{i,j,\sigma} \left(\frac{U}{2} \langle n_{i,\sigma} \rangle_{\text{MF}} \langle n_{j,-\sigma} \rangle_{\text{MF}} \delta_{ij} - \varepsilon_{ij} \langle c_{i,\sigma}^\dagger c_{j,\sigma} \rangle_{\text{MF}} \right), \quad (\text{A.45})$$

leading to

$$\delta \langle \mathcal{H} - \mathcal{H}_{\text{MF}} \rangle_{\text{MF}} = \sum_{i,j,\sigma} \left(U \langle n_{i,\sigma} \rangle_{\text{MF}} \delta \langle n_{j,-\sigma} \rangle_{\text{MF}} \delta_{ij} - \delta \varepsilon_{ij} \langle c_{i,\sigma}^\dagger c_{j,\sigma} \rangle_{\text{MF}} - \varepsilon_{ij} \delta \langle c_{i,\sigma}^\dagger c_{j,\sigma} \rangle_{\text{MF}} \right) \quad (\text{A.46})$$

The mean field free energy term can be obtained by introducing the variation $\mathcal{H} \mapsto \mathcal{H} + \delta\mathcal{H}$.

$$\begin{aligned} \text{Tr}[e^{-\beta(\mathcal{H} + \delta\mathcal{H})}] &= \text{Tr} \left[\sum_n \frac{(-\beta)^n}{n!} (\mathcal{H} + \delta\mathcal{H})^n \right] \\ &= 1 + \text{Tr} \left[\sum_{n=1}^{\infty} \frac{(-\beta)^n}{n!} \mathcal{H}^n \right] \\ &\quad + \text{Tr} \left[\sum_{n=1}^{\infty} \frac{(-\beta)^n}{n!} (\delta\mathcal{H} \mathcal{H}^{n-1} + \mathcal{H} \delta\mathcal{H} \mathcal{H}^{n-2} + \mathcal{H}^2 \delta\mathcal{H} \mathcal{H}^{n-3} + \dots \mathcal{H}^{n-1} \delta\mathcal{H}) \right] + \mathcal{O}(\delta\mathcal{H}^2), \\ &= \text{Tr}[e^{-\beta\mathcal{H}}] + \text{Tr} \left[\delta\mathcal{H} \sum_{n=1}^{\infty} \frac{(-\beta)^n}{(n-1)!} \mathcal{H}^{n-1} \right] + \mathcal{O}(\delta\mathcal{H}^2) \\ &= \text{Tr}[e^{-\beta\mathcal{H}}] - \beta \text{Tr} \left[\delta\mathcal{H} e^{-\beta\mathcal{H}} \right] + \mathcal{O}(\delta\mathcal{H}^2) \end{aligned} \quad (\text{A.47})$$

which, in turn, implies that

$$\delta \text{Tr}[e^{-\beta\mathcal{H}}] = -\beta \text{Tr}[e^{-\beta\mathcal{H}} \delta\mathcal{H}] \quad (\text{A.48})$$

and, using the definition of the mean field free energy:

$$\delta\mathcal{F}_{\text{MF}} = -\frac{1}{\beta} \delta \left(\ln(\text{Tr}[e^{-\beta\mathcal{H}_{\text{MF}})]) \right) = -\frac{1}{\beta} \frac{\delta(\text{Tr}[e^{-\beta\mathcal{H}_{\text{MF}}}])}{\text{Tr}[e^{-\beta\mathcal{H}_{\text{MF}}}]}, \quad (\text{A.49})$$

and replacing Eq.(A.48) in Eq.(A.49), we may gather all the terms to finally arrive at

$$\begin{aligned} \delta F &= \delta\mathcal{F}_{\text{MF}} + \delta \langle \mathcal{H} - \mathcal{H}_{\text{MF}} \rangle_{\text{MF}} \\ &= \sum_{i,j,\sigma} \left(U \langle n_{i,-\sigma} \rangle_{\text{MF}} \delta \langle n_{j,\sigma} \rangle_{\text{MF}} \delta_{ij} - \varepsilon_{ij} \delta \langle c_{i,\sigma}^\dagger c_{j,\sigma} \rangle_{\text{MF}} \right) \\ &= \sum_{i,j,\sigma} \left(U \langle n_{i,-\sigma} \rangle_{\text{MF}} \delta \langle c_{i,\sigma}^\dagger c_{j,\sigma} \rangle_{\text{MF}} \delta_{ij} - \varepsilon_{ij} \delta \langle c_{i,\sigma}^\dagger c_{j,\sigma} \rangle_{\text{MF}} \right) = 0 \\ &\implies \varepsilon_{ij} = U \langle n_{i,-\sigma} \rangle_{\text{MF}} \delta_{ij} \end{aligned} \quad (\text{A.50})$$

leading to the mean field approximation for the Hubbard model:

$$\mathcal{H}_{\text{MF}} = \mathcal{H}_K + U \sum_{i,\sigma} \langle n_{i,-\sigma} \rangle_{\text{MF}} n_{i,\sigma} \quad (\text{A.51})$$

Although the mean field equations can be obtained both from $\delta\mathcal{F}_{\text{MF}} = 0$ and from $\delta F = 0$, this only means that they both have a vanishing functional derivative at a given (common) configuration of the system. There may be other configurations at which $\delta\mathcal{F}_{\text{MF}}$ vanishes, but we have only an extremum. Thus, we must be cautious when analyzing self-consistent solutions to confirm that they indeed correspond to a minimum of the functional F , and not only an extremum of \mathcal{F}_{MF} .

On a final note, we remark that this procedure can be generalized to the Grand-canonical ensemble (GCE) by considering the GBF inequality for the grand potential Ω_G :

$$\Omega_G \leq \Omega_{\text{MF}} + \langle \mathcal{H} - \mathcal{H}_{\text{MF}} \rangle_{\text{MF}} \equiv \Omega, \quad (\text{A.52})$$

where we defined $\Omega_{\text{MF}} = \langle \mathcal{H}_{\text{MF}} \rangle_{\text{MF}} - T\mathcal{S}_{\text{MF}} - \mu \langle \mathcal{N} \rangle_{\text{MF}}$, \mathcal{N} being the total number operator.

For example, for the TMD nanoribbon of chapter 4, at iteration I we have that

$$\begin{aligned} \Omega_{\text{MF},I} &= -\frac{1}{\beta} \sum_{q,\nu,\sigma} \ln \left(1 + e^{-\beta[\varepsilon_{\nu,\sigma}(q)]_I} \right) \\ \langle \mathcal{H} - \mathcal{H}_{\text{MF}} \rangle_{\text{MF},I} &= UN_x \left(\sum_{\mu} \langle n_{\mu,\uparrow} \rangle_I \langle n_{\mu,\downarrow} \rangle_I - \sum_{\mu,\sigma} \langle n_{\mu,\sigma} \rangle_{I-1} \langle n_{\mu,-\sigma} \rangle_I \right) \end{aligned} \quad (\text{A.53})$$

The iterative scheme we use to solve the self consistent equation is not a minimization algorithm. However, if it does not get stuck in a metastable state, it tends to take steps towards minimizing the functional Ω . This is illustrated in Fig.(A.2). The data was obtained by solving the self consistent equation for the generalized intra-orbital version of the Hubbard model we use throughout. The model is obtained from the 3-band tight binding Hamiltonian of the first chapter, and by adding an on-site and intra-orbital interaction. In this case, we consider a TMD nanoribbon with $N_y = 16$, at inverse temperature $\beta|t_0| = 2$, at $U = 20|t_0|$, where U is an on-site interaction that only occurs if the electrons occupy the same d -orbital. Thus, only double occupancy of a site *and an orbital* is penalized.

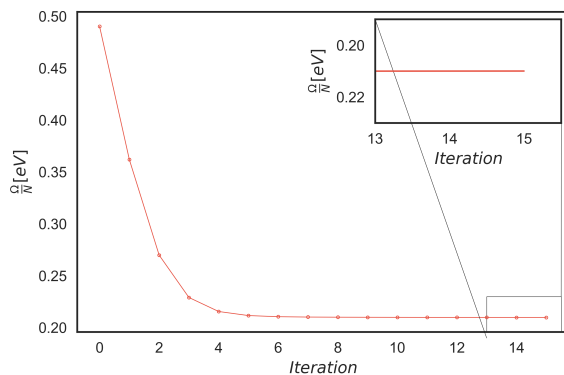


Figure A.2: Example of the minimization of the grandpotential functional per particle in units of $|t_0|$, Ω/N , for a TMD nanoribbon of width $N_y = 16$, at inverse temperature $\beta|t_0| = 2$, at $U = 20|t_0|$. N is the total number of sites in the system.

B

Formulating Auxiliary Field Quantum Monte Carlo

B.1 Casting the fermionic trace as a determinant

Let the two arbitrary real matrices be \mathbf{M} and \mathbf{N} . Then, a particular case of the identity (3.42) is

$$\text{Tr} [e^{-c_i^\dagger M_{ij} c_j} e^{-c_i^\dagger N_{ij} c_j}] = \det(\mathbf{I} + e^{-\mathbf{M}} e^{-\mathbf{N}}), \quad (\text{B.1})$$

where a summation over repeated indices is implied, as it will be throughout this proof.

To prove this identity, we start by proving that

$$e^{-c_i^\dagger M_{ij} c_j} e^{-c_i^\dagger N_{ij} c_j} = e^{-\sum_\nu c_\nu^\dagger \rho_\nu c_\nu}, \quad (\text{B.2})$$

where $\lambda_\nu = e^{-\rho_\nu}$ are the eigenvalues of the matrix $e^{-\mathbf{M}} e^{-\mathbf{N}}$.

The proof consists of showing that any many-particle state are propagated in the same way when acted upon by any of these two operators, i.e. the LHS operator leads the system to the same state as the RHS operator.

A generic single-particle state reads

$$|\phi\rangle = \sum_j a_j c_j^\dagger |0\rangle, \quad (\text{B.3})$$

where a_j are arbitrary coefficients, and $|0\rangle$ is the vacuum state.

Let $\{|\mu\rangle\}$ be the basis in which the matrix \mathbf{N} is diagonal. Using Dirac notation, we then have

$$\mathbf{N} = \sum_\mu |\mu\rangle n_\mu \langle \mu| \quad (\text{B.4})$$

Define new fermionic operators

$$c_\mu = \sum_j \langle \mu | j \rangle c_j \quad c_\mu^\dagger = \sum_j \langle j | \mu \rangle c_j^\dagger, \quad (\text{B.5})$$

which may be inverted to obtain

$$c_j = \sum_\mu \langle j | \mu \rangle c_\mu \quad c_j^\dagger = \sum_\mu \langle \mu | j \rangle c_\mu^\dagger, \quad (\text{B.6})$$

Now we prove yet another identity that goes into proving equation (B.2).

$$e^{-c_i^\dagger N_{ij} c_j} = \prod_\mu [1 + (e^{-n_\mu} - 1)c_\mu^\dagger c_\mu] \quad (\text{B.7})$$

$$\exp(-c_i^\dagger N_{ij} c_j) = \exp\left(-\sum_{\mu\nu} \langle\mu|i\rangle c_\mu^\dagger N_{ij} \langle j|\nu\rangle c_\nu\right) = \exp\left(-\sum_{ij} \sum_{\mu\nu\sigma} \langle\mu|i\rangle \langle i|\sigma\rangle c_\mu^\dagger n_\sigma \langle\sigma|j\rangle \langle j|\nu\rangle c_\nu\right),$$

(using the closure relation $\sum_i |i\rangle \langle i| = \mathbb{1}$)

$$\begin{aligned} &= \exp\left(-\sum_{\mu\nu\sigma} \overbrace{\langle\mu|\sigma\rangle}^{\delta_{\mu\sigma}} c_\mu^\dagger n_\sigma \overbrace{\langle\sigma|\nu\rangle}^{\delta_{\sigma\nu}} c_\nu\right) = \exp\left(-\sum_\mu c_\mu^\dagger n_\mu c_\mu\right) = \prod_\mu e^{-n_\mu \hat{n}_\mu} \\ &= \prod_\mu [\mathbb{1} + (-n_\mu \hat{n}_\mu + \frac{n_\mu^2}{2!} \hat{n}_\mu^2 - \frac{n_\mu^3}{3!} \hat{n}_\mu^3 + \dots)] = \prod_\mu [\mathbb{1} + (-n_\mu + \frac{n_\mu^2}{2!} - \frac{n_\mu^3}{3!} + \dots) \hat{n}_\mu] \end{aligned}$$

(since $\hat{n} = \hat{n}^k$ for all $k \in \mathbb{N}$ for fermions since $n = 0, 1$)

$$= \prod_\mu [\mathbb{1} + (e^{-n_\mu} - 1) c_\mu^\dagger c_\mu] \quad \square$$

Let $|\phi\rangle = \sum_j a_j c_j^\dagger |0\rangle$ be an arbitrary many-particle state.

Now we use the previous identity to prove that applying the operator of equation (B.7) to $|\phi\rangle$ we obtain

$$e^{-c_i^\dagger N_{ij} c_j} |\phi\rangle = \sum_j a'_j c_j^\dagger |0\rangle, \quad (\text{B.8})$$

with

$$a'_j = \sum_i (e^{-\mathbf{N}})_{ji} a_i \quad (\text{B.9})$$

We start by writing $|\phi\rangle$ in the basis $\{|\mu\rangle\}$ (in which \mathbf{N} is diagonal).

$$|\phi\rangle = \sum_{i,\mu} a_i \langle\mu|i\rangle c_\mu^\dagger |0\rangle \quad (\text{B.10})$$

Then, we apply the RHS of equation (B.7) to $|\phi\rangle$ written in this basis.

$$\begin{aligned} \sum_\nu \left[\mathbb{1} + (e^{-n_\mu} - 1) c_\nu^\dagger c_\nu \right] c_\mu^\dagger |0\rangle &= \left[\mathbb{1} + (e^{-n_\mu} - 1) c_\mu^\dagger c_\mu \right] c_\mu^\dagger |0\rangle \\ &= c_\mu^\dagger |0\rangle + (e^{-n_\mu} - 1) c_\mu^\dagger |0\rangle c_\mu^\dagger e^{-n_\mu} |0\rangle \end{aligned} \quad (\text{B.11})$$

$$\begin{aligned} \sum_\nu \left[\mathbb{1} + (e^{-n_\mu} - 1) c_\nu^\dagger c_\nu \right] |\phi\rangle &= \sum_{i\mu} \langle\mu|i\rangle a_i e^{-n_\mu} c_\mu^\dagger \\ &= \sum_{j\mu i} \langle j|\mu\rangle e^{-n_\mu} \langle\mu|i\rangle a_i |j\rangle = \underbrace{\sum_{ji} \sum_{\mu\nu} \langle j|\mu\rangle}_{(e^{-\mathbf{N}})_{ji}} \underbrace{e^{-N_{\mu\nu}} \langle\nu|i\rangle a_i |j\rangle}_{(\nu|i\rangle)} \\ &= \sum_j a'_j c_j^\dagger |0\rangle \end{aligned} \quad (\text{B.12})$$

Similarly, by repeating the procedure performing a change of basis to the eigenbasis of \mathbf{M} , we obtain the more general relation

$$\begin{aligned} e^{-c_i^\dagger M_{ij} c_j} e^{-c_i^\dagger N_{ij} c_j} |\phi\rangle &= \sum_j a''_j c_j^\dagger |0\rangle \\ a''_j &= \sum_i (e^{-\mathbf{M}} e^{-\mathbf{N}})_{ji} a_i \end{aligned} \quad (\text{B.13})$$

The amplitude of a propagated state is given by multiplying the initial amplitude by the matrix $e^{-\mathbf{M}} e^{-\mathbf{N}}$, whichever the basis we choose. Then, since equation (B.13) holds in particular for the choice

of the eigenbasis of $e^{-\mathbf{M}}e^{-\mathbf{N}}$ as our basis of single-particle states, if we start with an eigenstate

$$|\phi\rangle = c_\nu^\dagger |0\rangle, \quad (\text{B.14})$$

then the amplitude of the propagated state will be given by

$$(e^{-\mathbf{M}}e^{-\mathbf{N}})_{\nu\nu} = e^{-\rho_\nu}, \quad (\text{B.15})$$

the same as we would obtain from equation (B.2). Clearly, if we start with a state that is an arbitrary combination of states of the eigenbasis, we would obtain the identity (B.2).

The identity was proven for a single-particle state. Does it generalize to more than one particle? As we did before, we start with propagation by a single factor $e^{-\mathbf{N}}$. Take a two-particle state

$$|\phi\rangle = c_{\mu_1}^\dagger c_{\mu_2}^\dagger |0\rangle \quad (\text{B.16})$$

Now propagate it with \mathbf{N} , i.e.

$$\begin{aligned} e^{-c_i^\dagger N_{ij} c_j} |\phi\rangle &= \prod_\mu \left[1 + (e^{-n_\mu} - 1) c_\mu^\dagger c_\mu \right] c_{\mu_1}^\dagger c_{\mu_2}^\dagger |0\rangle \\ &= e^{-n_{\mu_1}} e^{-n_{\mu_2}} c_{\mu_1}^\dagger c_{\mu_2}^\dagger |0\rangle, \end{aligned} \quad (\text{B.17})$$

where we simply note that by similar reasoning to the previous case, we would in equation (B.11) keep two terms corresponding to $\mu_1 \neq \mu_2$. If $\mu_1 = \mu_2$, then both sides are equal to zero due to Pauli's exclusion principle and the equality holds trivially. This reasoning clearly generalizes to an arbitrary superposition of many-particle states. Moreover, we proved the result for a product of two factors $e^{-\mathbf{M}}e^{-\mathbf{N}}$, but it is also easy to see that by successive changes of basis, we could extend our result to an arbitrary number of factors.

To complete our proof of the identity (B.1) that is so crucial in formulating AFQMC, we use the auxiliar identity we just proved (B.2).

$$\begin{aligned} \text{Tr} \left[e^{-\sum_\nu c_\nu^\dagger \rho_\nu c_\nu} \right] &= \text{Tr} \left[\prod_\nu e^{-c_\nu^\dagger \rho_\nu c_\nu} \right] \text{ since } [\hat{n}_\mu, \hat{n}_\nu] = 0 \\ &= \prod_\nu (1 + e^{-\rho_\nu}) = \det[\mathbf{I} + e^{-\mathbf{M}}e^{-\mathbf{N}}], \quad \square \end{aligned} \quad (\text{B.18})$$

where the last equality stems from the fact that the determinant of a diagonal matrix is just the product of the eigenvalues.

B.2 Rank-one updates of the Green's function

Consider two matrices $\mathbf{A}_1, \mathbf{A}_2$ written in the form

$$\mathbf{A}_{1,2} = \mathbf{I} + \mathbf{F} \mathbf{V}_{1,2}, \quad (\text{B.19})$$

where \mathbf{F} is some matrix. $\mathbf{V}_{1,2}$ are diagonal and non-singular and differ only in the $(1, 1)$ entry, so that

$$\mathbf{V}_1^{-1} \mathbf{V}_2 = \mathbf{I} + \alpha_1 \mathbf{e}_1 \mathbf{e}_1^T, \quad (\text{B.20})$$

where \mathbf{e}_1 is a vector corresponding to the first column of the identity matrix \mathbf{I} , and

$$\alpha_1 = \frac{V_2(1, 1)}{V_1(1, 1)} - 1 \quad (\text{B.21})$$

Then, \mathbf{A}_2 is clearly a rank-one update of \mathbf{A}_1 .

$$\begin{aligned}\mathbf{A}_2 &= \mathbf{I} + \mathbf{FV}_1 + \mathbf{FV}_1(\mathbf{V}_1^{-1}\mathbf{V}_2 - \mathbf{I}) \\ &= \mathbf{A}_1 + \alpha_1(\mathbf{A}_1 - \mathbf{I})\mathbf{e}_1\mathbf{e}_1^T \\ &= \mathbf{A}_1[\mathbf{I} + \alpha_1(\mathbf{I} - \mathbf{A}_1^{-1})\mathbf{e}_1\mathbf{e}_1^T]\end{aligned}\quad (\text{B.22})$$

To find an expression for the ratio of the determinants of \mathbf{A}_1 and \mathbf{A}_2 , we shall need to make use of the Sylvester's determinant identity $\det(\mathbf{I} + \mathbf{AB}) = \det(\mathbf{I} + \mathbf{BA})$. To prove it, consider the matrices

$$\mathbf{P} = \begin{pmatrix} \mathbf{I} & -\mathbf{A} \\ \mathbf{B} & \mathbf{I} \end{pmatrix} \quad \mathbf{Q} = \begin{pmatrix} \mathbf{I} & \mathbf{A} \\ \mathbf{0} & \mathbf{I} \end{pmatrix} \quad (\text{B.23})$$

Using the identity $\det(\mathbf{MN}) = \det(\mathbf{M})\det(\mathbf{N})$ applied to these two matrices, we can clearly see that the determinants of the two matrices coincide, i.e.

$$\det(\mathbf{P}) = \det\begin{pmatrix} \mathbf{I} & -\mathbf{A} \\ \mathbf{B} & \mathbf{I} \end{pmatrix} \det\begin{pmatrix} \mathbf{I} & \mathbf{A} \\ \mathbf{0} & \mathbf{I} \end{pmatrix} \quad \det(\mathbf{Q}) = \det\begin{pmatrix} \mathbf{I} & \mathbf{A} \\ \mathbf{0} & \mathbf{I} \end{pmatrix} \det\begin{pmatrix} \mathbf{I} & -\mathbf{A} \\ \mathbf{B} & \mathbf{I} \end{pmatrix} \quad (\text{B.24})$$

The sought identity is obtained by computing the determinants explicitly.

$$\det(\mathbf{P}) = \det\begin{pmatrix} \mathbf{I} & \mathbf{0} \\ \mathbf{B} & \mathbf{I} + \mathbf{BA} \end{pmatrix} = \det(\mathbf{I} + \mathbf{BA}) \quad \det(\mathbf{Q}) = \det\begin{pmatrix} \mathbf{I} + \mathbf{AB} & \mathbf{0} \\ \mathbf{B} & \mathbf{I} \end{pmatrix} = \det(\mathbf{I} + \mathbf{AB}) \quad (\text{B.25})$$

A corollary of Sylvester's identity for any two column vectors: $\det[\mathbf{I} + \mathbf{xy}^T] = 1 + \mathbf{y}^T\mathbf{x}$ may be used with $x \mapsto (\mathbf{I} - \mathbf{A}_1^{-1})\mathbf{e}_1$, $y \mapsto \mathbf{e}_1$ to write the ratio of the determinants of matrices \mathbf{A}_1 and \mathbf{A}_2 as

$$r_1 = \frac{\det[\mathbf{A}_2]}{\det[\mathbf{A}_1]} = 1 + \alpha_1(1 - \mathbf{e}_1^T \mathbf{A}_1^{-1} \mathbf{e}_1), \quad (\text{B.26})$$

which reduces the computation of the ratio r_1 to computing the (1, 1) entry of \mathbf{A}^{-1} .

Now we generalize this idea for a sequence of matrices $\mathbf{A}_1, \mathbf{A}_2, \dots, \mathbf{A}_i, \dots, \mathbf{A}_n$ generated by successive rank-one updates: $\mathbf{A}_{i+1} = \mathbf{I} + \mathbf{FV}_{i+1}$, $i = 1, 2, \dots, n-1$, with

$$\mathbf{V}_i^{-1}\mathbf{V}_{i+1} = \mathbf{I} + \alpha_i\mathbf{e}_i\mathbf{e}_i^T \quad \alpha_i = \frac{\mathbf{V}_{i+1}(1, 1)}{\mathbf{V}_i(1, 1)} - 1 \quad (\text{B.27})$$

That is accomplished by use of the Sherman-Morrison-Woodbury formula, or simply Woodbury matrix identity:

$$(\mathbf{A} + \mathbf{BCD})^{-1} = \mathbf{A}^{-1} - \mathbf{A}^{-1}\mathbf{B}(\mathbf{C}^{-1} + \mathbf{DA}^{-1}\mathbf{B})^{-1}\mathbf{DA}^{-1}, \quad (\text{B.28})$$

where $\dim(\mathbf{A}) = N \times N$, $\dim(\mathbf{B}) = N \times K$, $\dim(\mathbf{C}) = K \times K$, $\dim(\mathbf{D}) = K \times N$, and N and K are integers. To prove the identity, we use two simple identities, from which the proof easily follows.

$$\mathbf{B} + \mathbf{BCDA}^{-1}\mathbf{B} = (\mathbf{A} + \mathbf{BCD})\mathbf{A}^{-1}\mathbf{B} \quad (\mathbf{A} + \mathbf{BCD})^{-1}\mathbf{BC} = \mathbf{A}^{-1}\mathbf{B}(\mathbf{C}^{-1} + \mathbf{DA}^{-1}\mathbf{B})^{-1} \quad (\text{B.29})$$

$$\begin{aligned}\mathbf{A}^{-1} &= (\mathbf{A} + \mathbf{BCD})^{-1}(\mathbf{A} + \mathbf{BCD})\mathbf{A}^{-1} = (\mathbf{A} + \mathbf{BCD})^{-1}(\mathbf{I} + \mathbf{BCDA}^{-1}) \\ &= (\mathbf{A} + \mathbf{BCD})^{-1} + (\mathbf{A} + \mathbf{BCD})^{-1}\mathbf{BCDA}^{-1} \\ &= (\mathbf{A} + \mathbf{BCD})^{-1} + \mathbf{A}^{-1}\mathbf{B}(\mathbf{C}^{-1} + \mathbf{DA}^{-1}\mathbf{B})\mathbf{DA}^{-1} \quad \square\end{aligned}\quad (\text{B.30})$$

The Woodbury identity applied to Eq.(B.22) gives an expression for \mathbf{A}_2^{-1} as a rank-one update of

\mathbf{A}_1^{-1} .

$$\begin{aligned}
\mathbf{A}_2^{-1} &= \mathbf{A}_1^{-1} - \alpha_1(\mathbf{I} - \mathbf{A}_1^{-1}) \underbrace{\left[\mathbf{e}_1 + \mathbf{e}_1^T \mathbf{A}_1^{-1} \alpha_1 (\mathbf{A}_1 - \mathbf{I}) \right]}_{\mathbf{e}_1 \times, \times \mathbf{e}_1 \text{ (multiply left and right)}}^{-1} \mathbf{e}_1^T \mathbf{A}_1^{-1} \\
&= \mathbf{A}_1^{-1} - \alpha_1(\mathbf{I} - \mathbf{A}_1^{-1}) \mathbf{e}_1 \left[1 + \alpha_1(1 - \mathbf{e}_1^T \mathbf{A}_1^{-1} \mathbf{e}_1) \right]^{-1} \mathbf{e}_1^T \mathbf{A}_1^{-1} \\
&= \mathbf{A}_1^{-1} - \frac{\alpha_1}{r_1} \mathbf{u}_1 \mathbf{w}_1^T,
\end{aligned} \tag{B.31}$$

where the operation on the first step does not affect the term in parentheses, and we defined $\mathbf{u}_1 = (\mathbf{I} - \mathbf{A}_1^{-1})\mathbf{e}_1$ $\mathbf{w}_1 = (\mathbf{A}_1^{-1})^T \mathbf{e}_1$.

Using Eqs.(B.26,B.31) successively, we find the updates

$$\begin{aligned}
r_i &= \frac{\det[\mathbf{A}_{i+1}]}{\det[\mathbf{A}_i]} = 1 + \alpha_i(1 - \mathbf{e}_i^T \mathbf{A}_i^{-1} \mathbf{e}_i), \text{ and} \\
\mathbf{A}_{i+1}^{-1} &= \mathbf{A}_i^{-1} - \frac{\alpha_i}{r_i} \mathbf{u}_i \mathbf{w}_i^T,
\end{aligned} \tag{B.32}$$

where $\mathbf{u}_i = (\mathbf{I} - \mathbf{A}_i^{-1})\mathbf{e}_i$ and $\mathbf{w}_i = (\mathbf{A}_i^{-1})^T \mathbf{e}_i$.

It is possible to generalize this procedure to compute the inverse of \mathbf{M}_k as a rank- $(k-1)$ update of \mathbf{A}_1^{-1} to devise a delayed update scheme that is more efficient:

$$\mathbf{M}_k^{-1} = \mathbf{M}_1^{-1} - \mathbf{U}_{k-1} \mathbf{D}_k \mathbf{W}_{k-1}^T, \tag{B.33}$$

where

$$\mathbf{U}_k = [\mathbf{u}_1, \mathbf{u}_2, \dots, \mathbf{u}_{k-1}] \quad \text{and} \quad \mathbf{W} = [\mathbf{w}_1, \mathbf{w}_2, \dots, \mathbf{w}_{k-1}], \tag{B.34}$$

and $\mathbf{D}_k = \text{diag}(\alpha_1/r_1, \alpha_2/r_2, \dots, \alpha_{k-1}/r_{k-1})$.

In [96], precise bounds are given on the conditioning of the matrices obtained via such type of Sherman-Morrison updates. In practice, if the Green's functions are sufficiently well-conditioned, no precision-related issues arise. Numerical instabilities may arise when the Green's matrices comprise divergent energy scales, and care must be taken to ensure that the algorithm converges.

B.3 Particle-hole symmetry and the sign problem

To a greater or lesser extent, all Quantum Monte Carlo methods are plagued by the sign problem. If the average of the sign is not too small, i.e. $\langle \text{sign} \rangle \rightarrow 0$, one can simply take more measurements and increase runs proportionally to $\langle \text{sign} \rangle^{-2}$ to achieve an accuracy comparable to that of the sign problem-free case. The case of the square lattice is very special because it can be proven that there is no sign problem at half filling. This is related to Particle-hole symmetry (PHS).

When approaching other models, one must carry out preliminary studies to evaluate whether the sign problem impedes accurate measurements or not, and to set the chemical potential correctly to get the desired filling of the lattice. In the following figures we give examples of this procedure for a Hubbard chain and for a TMD nanoribbon.

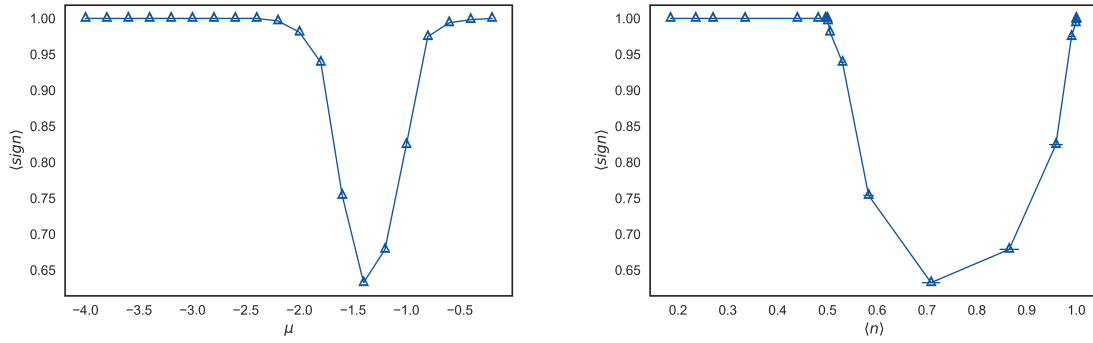


Figure B.1: Average sign as a function of chemical potential (left)/electron density (right) for a 4-site Hubbard chain with $U = 4t$ and $\beta t = 8$.

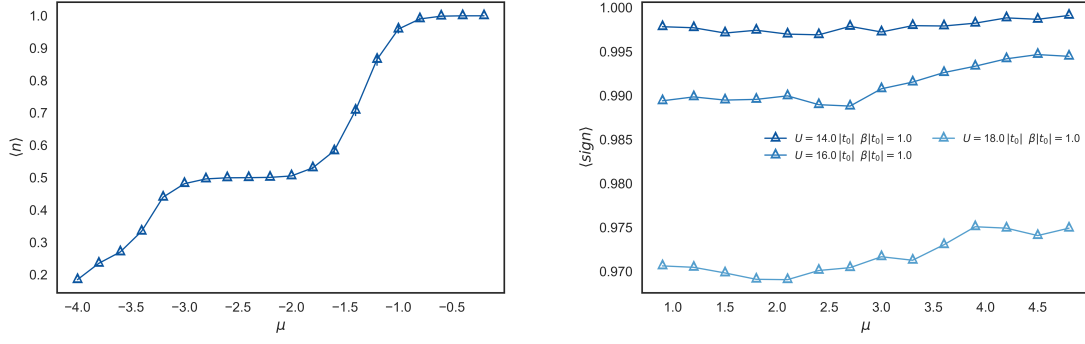


Figure B.2: Left: Electron density as a function of chemical potential for a 4-site Hubbard chain with $U = 4t$ and $\beta t = 8$. Right: Average sign as a function of chemical potential for a simulation of a 9×4 TMD nanoribbon using the minimal model described in chapter 2 at $\beta|t_0| = 1$ and $U = (14, 16, 18)|t_0|$. The sign problem worsens as U is increased.

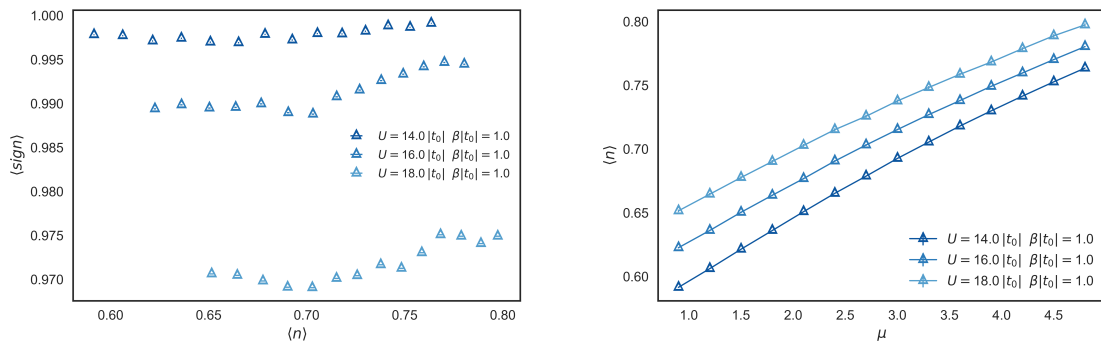


Figure B.3: Left: Average sign as a function of electron density for the minimal Hubbard model of TMDNRs. Right: Electron density as a function of chemical potential.

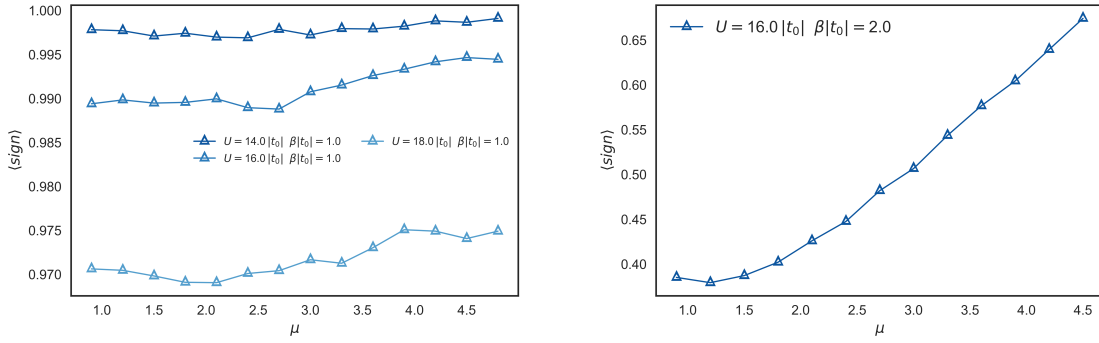


Figure B.4: Average sign as a function of chemical potential for the same system (left), and for a system at lower temperature ($\beta |t_0| = 2$), and fixed on-site/orbital interaction $U = 16|t_0|$ (right).

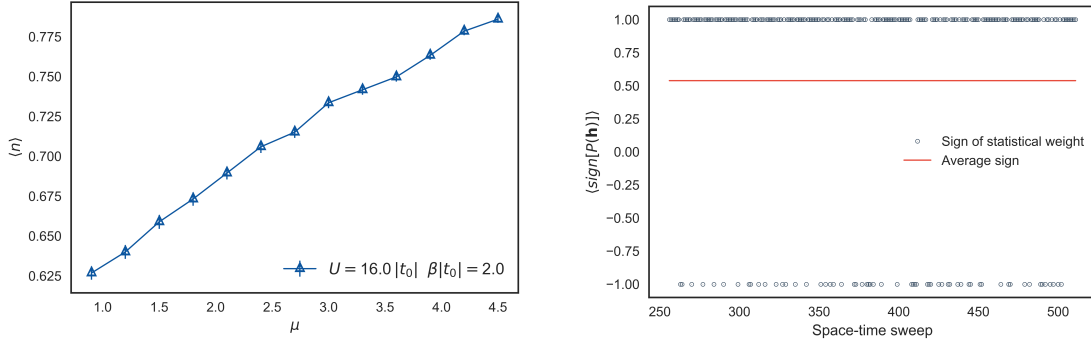


Figure B.5: Left: Electron density as a function of the chemical potential for the 9×4 TMD nanoribbon, with $\beta |t_0| = 2$ and $U = 16|t_0|$. Right: Sign of the accepted configuration as a function for a few space-time sweeps of the algorithm; the red line is the local average of the sign.

To prove that the half filled square lattice is sign problem-free we start by invoking two well known identities. Respectively, for any non-singular matrix \mathbf{A} , and for symmetric, non-singular matrices $\mathbf{A}_{l=1,\dots,m}$:

$$(\mathbf{I} + \mathbf{A}^{-1})^{-1} = \mathbf{I} - (\mathbf{I} + \mathbf{A})^{-1} \quad (\mathbf{I} + \mathbf{A}_m^{-1} \mathbf{A}_{m-1}^{-1} \dots \mathbf{A}_1^{-1})^{-1} = \mathbf{I} - [(\mathbf{I} + \mathbf{A}_m \mathbf{A}_{m-1} \dots \mathbf{A}_1)^{-1}]^T \quad (\text{B.35})$$

Moreover, given any two matrices \mathbf{A} and \mathbf{B} , there exists a third one $\mathbf{\Pi}$, which anti-commutes with \mathbf{A} , i.e. $\mathbf{\Pi}\mathbf{A} + \mathbf{A}\mathbf{\Pi} = 0$, and commutes with \mathbf{B} , i.e. $\mathbf{\Pi}\mathbf{B} - \mathbf{B}\mathbf{\Pi} = 0$ (or vice-versa). Then, the following two relations hold:

$$\begin{aligned} (\mathbf{I} + e^{\mathbf{A}-\mathbf{B}})^{-1} &= \mathbf{I} - \mathbf{\Pi}^{-1}(\mathbf{I} + e^{\mathbf{A}+\mathbf{B}})^{-1}\mathbf{\Pi} \\ \det[\mathbf{I} + e^{\mathbf{A}-\mathbf{B}}] &= e^{\text{Tr}[\mathbf{A}-\mathbf{B}]} \det[\mathbf{I} + e^{\mathbf{A}+\mathbf{B}}] \end{aligned} \quad (\text{B.36})$$

The first is proven by using the first identity of Eq.(B.35):

$$\begin{aligned} (\mathbf{I} + e^{\mathbf{A}-\mathbf{B}})^{-1} &= \mathbf{I} - (\mathbf{I} + e^{-\mathbf{A}+\mathbf{B}})^{-1} = \mathbf{I} - (\mathbf{I} + e^{\mathbf{\Pi}^{-1}(\mathbf{A}+\mathbf{B})\mathbf{\Pi}})^{-1} \\ &= \mathbf{I} - (\mathbf{I} + \mathbf{\Pi}^{-1}e^{\mathbf{A}+\mathbf{B}}\mathbf{\Pi})^{-1} = \mathbf{I} - \mathbf{\Pi}^{-1}(\mathbf{I} + e^{\mathbf{A}+\mathbf{B}})^{-1}\mathbf{\Pi} \end{aligned} \quad (\text{B.37})$$

The proof of the second uses the commutation relations:

$$\begin{aligned}
\mathbf{I} + e^{\mathbf{A}-\mathbf{B}} &= e^{\mathbf{A}-\mathbf{B}}(\mathbf{I} + e^{-(\mathbf{A}-\mathbf{B})}) = e^{\mathbf{A}-\mathbf{B}}(\mathbf{I} + e^{-\mathbf{A}+\mathbf{B}}) \\
&= e^{\mathbf{A}-\mathbf{B}}(\mathbf{I} + e^{\mathbf{\Pi}^{-1}\mathbf{A}\mathbf{\Pi} + \mathbf{\Pi}^{-1}\mathbf{B}\mathbf{\Pi}}) = e^{\mathbf{A}-\mathbf{B}}(\mathbf{I} + \mathbf{\Pi}^{-1}e^{\mathbf{A}+\mathbf{B}}\mathbf{\Pi}) \\
&= e^{\mathbf{A}-\mathbf{B}}\mathbf{\Pi}^{-1}(\mathbf{I} + e^{\mathbf{A}+\mathbf{B}})\mathbf{\Pi} \\
\rightarrow \det[\mathbf{I} + e^{\mathbf{A}-\mathbf{B}}] &= \det[e^{\mathbf{A}-\mathbf{B}}]\det[\mathbf{\Pi}^{-1}]\det[\mathbf{I} + e^{\mathbf{A}+\mathbf{B}}]\det[\mathbf{\Pi}] \\
&= e^{\text{Tr}[\mathbf{A}-\mathbf{B}]}\det[\mathbf{I} + e^{\mathbf{A}+\mathbf{B}}]
\end{aligned} \tag{B.38}$$

Similarly, we can prove that for symmetric matrices \mathbf{A} , \mathbf{B} , if we can find a non singular matrix $\mathbf{\Pi}$ that commutes with \mathbf{A} and anti-commutes with \mathbf{B} , then: $\det[\mathbf{I} + e^{\mathbf{A}}e^{-\mathbf{B}}] = e^{\text{Tr}[\mathbf{A}-\mathbf{B}]}\det[\mathbf{I} + e^{\mathbf{A}}e^{\mathbf{B}}]$ and

$$(\mathbf{I} + e^{\mathbf{A}}e^{-\mathbf{B}})^{-1} = \mathbf{I} - [\mathbf{\Pi}^{-1}]^T[(\mathbf{I} + e^{\mathbf{A}}e^{\mathbf{B}})^{-1}]^T[\mathbf{\Pi}^{-1}]^T \tag{B.39}$$

This theorem generalizes for the products we use in our code: $\mathbf{M}_\sigma = \mathbf{I} + e^{\mathbf{A}}e^{\sigma\mathbf{B}_k}e^{\mathbf{A}}e^{\sigma\mathbf{B}_{k-1}}\dots e^{\mathbf{A}}e^{\sigma\mathbf{B}_1}$.

If we can find a non singular matrix $\mathbf{\Pi}$, such that $\{\mathbf{\Pi}, \mathbf{A}\} = 0$ and $[\mathbf{\Pi}, \mathbf{B}_l] = 0$, then we have

$$\mathbf{M}_\downarrow^{-1} = \mathbf{I} - [\mathbf{\Pi}^{-1}]^T[\mathbf{M}_\uparrow^{-1}]^T\mathbf{\Pi}^T \quad \text{and} \quad \det[\mathbf{M}_\downarrow] = e^{k\text{Tr}[\mathbf{A}] - \sum_{l=1}^k \text{Tr}[\mathbf{B}_l]}\det[\mathbf{M}_\uparrow] \tag{B.40}$$

Since $\det[\mathbf{M}_\downarrow]$ is then proportional to $\det[\mathbf{M}_\uparrow]$, and $e^{k\text{Tr}[\mathbf{A}] - \sum_{l=1}^k \text{Tr}[\mathbf{B}_l]}$ is positive, the weight of the classical spin configuration $\det[\mathbf{M}_\uparrow]\det[\mathbf{M}_\downarrow]$ will always be positive, and there will be no sign problem. Now, it turns out that this is only possible at half filling. Away from half filling, we cannot find a $\mathbf{\Pi}$ obeying these conditions.

The matrix $\mathbf{\Pi}$ is intimately related to the particle hole transformation. In fact, for the 1D chain, or the square lattice, if we take $\mathbf{\Pi}_{x(y)} = \text{diag}(1, -1, 1, -1, \dots)$, then the particle-hole transformation of the Green's function reads

$$\mathbf{G}^\downarrow = \mathbf{I} - \mathbf{\Pi}_x(\mathbf{G}^\uparrow)^T\mathbf{\Pi}_x \text{ for the chain and } \mathbf{G}^\downarrow = \mathbf{I} - \mathbf{\Pi}(\mathbf{G}^\uparrow)^T\mathbf{\Pi} \text{ for the square lattice,} \tag{B.41}$$

where $\mathbf{\Pi} = \mathbf{\Pi}_x \otimes \mathbf{\Pi}_y$, the tensor (Kronecker) product of the two matrices.

This reasoning is not only valid for the chain and square lattice, but actually holds for any bipartite lattice, such as the honeycomb lattice. Unfortunately, for example for the triangular lattice, it does not. This makes simulations on the triangular lattice (such as the one in this work) and other non bipartite lattices potentially much harder to control.